

University of Warwick institutional repository: <http://go.warwick.ac.uk/wrap>

**A Thesis Submitted for the Degree of PhD at the University of Warwick**

<http://go.warwick.ac.uk/wrap/67088>

This thesis is made available online and is protected by original copyright.

Please scroll down to view the document itself.

Please refer to the repository record for this item for information to help you to cite it. Our policy information is available from the repository home page.

Crystallisation and Characterisation  
of Bimetallic- and Lanthanide-  
Organic Frameworks

By

Matthew I. Breeze

Supervisor: Richard I. Walton

---

Thesis submitted for the degree of  
Doctor of Philosophy in Chemistry

Department of Chemistry, University of Warwick  
September 2014



## Contents

### 1. Introduction

1.1.	Introduction.....	0
1.2.	Definitions .....	0
1.3.	History of Metal-Organic Frameworks .....	2
1.4.	Metal-Organic Frameworks.....	4
1.4.1.	Structures.....	4
1.4.2.	Synthesis of Metal-Organic Frameworks .....	6
1.4.3.	Isorecticular Synthesis of Metal-Organic Frameworks.....	8
1.4.4.	Post-synthetic modification of metal-organic frameworks .....	10
1.4.5.	Dynamic Metal-Organic Frameworks .....	10
1.4.6.	Potential Applications .....	12
1.5.	Heterometallic-Organic Frameworks .....	14
1.5.1.	Introduction .....	14
1.5.2.	Intercalated Nano-Particles@MOFs .....	16
1.5.3.	MOFs with counter-ions .....	17
1.5.4.	Intercalated Polyoxometalates .....	17
1.5.5.	Polyoxometalate-organic frameworks.....	17
1.5.6.	Metallo-ligands .....	18
1.5.7.	Heterometallic sites .....	19
1.5.8.	Homometallic sites.....	19
1.6.	MIL-53 ( $M^{III}(OH)(BDC)$ ) .....	20



1.6.1.	Introduction .....	20
1.6.2.	Structure and Properties.....	21
1.6.3.	Effect of the Metal Centre on MIL-53 on its dynamic behaviour .....	22
1.6.4.	Notable non-trivalent analogues of MIL-53.....	23
1.6.5.	Mixed-Metal MIL-53 .....	24
1.7.	Lanthanide-Organic Frameworks .....	25
1.7.1.	Introduction .....	25
1.7.2.	Diversity of Structures.....	26
1.7.3.	Applications of lanthanide-organic frameworks.....	30
1.8.	Aims of this work.....	31
1.9.	References.....	33
2.	Experimental	
2.1.	Introduction.....	40
2.2.	Sample Preparation.....	40
2.2.1.	Solvothermal synthesis .....	40
2.2.2.	Thermal activation of metal-organic frameworks .....	41
2.3.	Powder X-ray Diffraction .....	42
2.3.1.	Introduction .....	42
2.3.2.	Laboratory powder XRD.....	52
2.3.3.	D5000.....	52
2.3.4.	D8 .....	52
2.3.5.	Panalytical X’Pert Pro MPD .....	53

2.3.6.	High-resolution powder XRD .....	53
2.3.7.	PXRD Refinement.....	54
2.3.8.	EDXRD .....	54
2.3.9.	<i>In Situ</i> XRD Crystallisation Studies .....	56
2.4.	Single Crystal X-ray Diffraction .....	57
2.5.	X-ray Absorption Spectroscopy .....	58
2.5.1.	Introduction .....	58
2.5.2.	X-Ray Absorption Near Edge Spectroscopy .....	58
2.5.3.	Extended X-ray Absorption Fine Spectra .....	59
2.5.4.	Beamline B18 .....	59
2.6.	Other Characterisation Techniques.....	60
2.6.1.	Infrared Spectroscopy.....	60
2.6.2.	Raman Spectroscopy.....	61
2.6.3.	Thermogravimetric Analysis .....	61
2.6.4.	Elemental Analysis .....	62
2.6.5.	Mössbauer Spectroscopy.....	62
2.6.6.	Photoluminescence studies .....	64
2.7.	References .....	65
3. Mixed-Metal MIL-53		
3.1.	Introduction.....	66
3.2.	[(Fe, V)(BDC)(DMF, F)] .....	67
3.2.1.	Synthesis .....	67

3.2.2.	Structure and Composition .....	68
3.2.3.	XANES .....	71
3.2.4.	$^{57}\text{Fe}$ Mössbauer Spectroscopy .....	72
3.2.5.	Thermal Behaviour .....	75
3.2.6.	Infrared Spectroscopy of $(\text{Fe}_{0.88}\text{V}_{0.12})(\text{BDC})(\text{OH}, \text{F})$ .....	77
3.3.	$[(\text{Fe}, \text{V})(\text{BDC})(\text{OH}, \text{F})]^{0.5-} \cdot 0.5\text{DMA}^+$ .....	78
3.3.1.	Synthesis .....	78
3.3.2.	Structure and Composition .....	79
3.3.3.	XANES .....	81
3.3.4.	$^{57}\text{Fe}$ Mössbauer Spectroscopy .....	83
3.3.5.	Thermal Behaviour .....	85
3.3.6.	Infrared and Raman Spectroscopy .....	87
3.4.	MIL-53(Fe, V) .....	90
3.4.1.	Synthesis .....	90
3.4.2.	Structure and Composition .....	91
3.4.3.	XANES .....	93
3.4.4.	$^{57}\text{Fe}$ Mössbauer Spectroscopy .....	96
3.4.5.	Infrared and Raman Spectroscopy .....	97
3.4.6.	Thermal Behaviour .....	100
3.4.7.	Sorption of Ethanol by MIL-53( $\text{Fe}_{0.74}\text{V}_{0.26}$ ) .....	102
3.4.8.	Porosity Studies of MIL-53(Fe, V) .....	104
3.4.9.	Xylene sorption studies of MIL-53( $\text{Fe}_{0.74}\text{V}_{0.26}$ ) .....	105

3.5.	$[(\text{Fe}, \text{Co})(\text{BDC})(\text{OH}, \text{F})]^{0.5-} \cdot 0.5\text{DMA}^+$ .....	106
3.5.1.	Synthesis .....	106
3.5.2.	Structure .....	107
3.5.3.	Calcination .....	108
3.5.4.	XANES.....	109
3.6.	MIL-53(Fe, Cr).....	110
3.6.1.	Introduction .....	110
3.6.2.	Fitting Model.....	111
3.6.3.	EXAFS Analysis of MIL-53( $\text{Cr}_{0.6}\text{Fe}_{0.4}$ ) .....	113
3.7.	Summary.....	117
3.8.	References.....	119
4.	Ytterbium-Organic Frameworks	
4.1.	Introduction.....	121
4.2.	MB2 – $[\text{Yb}_2(\text{BDC})_3(\text{DMF})_2] \cdot 2\text{H}_2\text{O}$ .....	123
4.2.1.	Synthesis .....	123
4.2.2.	Structure .....	123
4.2.3.	Thermal Behaviour of MB2 .....	129
4.2.4.	Porosity Studies of MB2.....	138
4.2.5.	Infrared Spectra of MB2 and Its Calcination Products.....	139
4.2.6.	Synthesis of MB2 with other lanthanides .....	142
4.2.7.	Doping of MB2 with other lanthanides.....	143
4.3.	MB3 – $[\text{Yb}_2(\text{BDC})_3(\text{DMF})_2(\text{H}_2\text{O})_2]$ .....	150

4.3.1.	Synthesis .....	150
4.3.2.	Structure of MB3.....	150
4.3.3.	Thermal Behaviour of MB3 .....	154
4.3.4.	Gas Adsorption Studies of MB3.....	162
4.3.5.	Infrared Spectra of MB3 and Its Calcined Products.....	163
4.4.	Synthesis of Isoreticular Analogues of MB2 and MB3 .....	166
4.4.1.	Synthesis .....	166
4.4.2.	MB5 – $[\text{Yb}_2(\text{NDC})_3(\text{H}_2\text{O})_4] \cdot 4\text{H}_2\text{O}$ .....	168
4.4.3.	Thermal Behaviour of MB5 .....	172
4.5.	Summary.....	175
4.6.	References.....	177
5.	Crystallisation of Metal-Organic Frameworks	
5.1.	Introduction.....	179
5.2.	Experimental Set-Up.....	181
5.3.	Crystallisation of MB2 ( $[\text{Yb}_2(\text{BDC})_3(\text{DMF})_2] \cdot 2\text{H}_2\text{O}$ ) .....	183
5.3.1.	<i>In Situ</i> Studies.....	183
5.3.2.	<i>Ex Situ</i> Study.....	191
5.4.	Crystallisation of MB3 - ( $[\text{Yb}_2(\text{BDC})_3(\text{DMF})_2(\text{H}_2\text{O})_2]$ ) .....	197
5.5.	Crystallisation of interpenetrated MOF-5 .....	202
5.5.1.	MOF-5 and its interpenetrated form .....	202
5.5.2.	Synthesis of MOF-5int.....	204
5.5.3.	An <i>In Situ</i> Study of MOF-5int Crystallisation.....	208

5.6.	Summary.....	212
5.7.	References.....	214
6. Conclusions		
6.1.	Summary.....	216
6.2.	Future Work .....	218
6.3.	References.....	219
A. Appendix		
A.1.	Precious Metal-Organic Frameworks.....	220
A.2.	Synthesis of Iridium-Organic Frameworks.....	220
A.3.	Synthesis of Ruthenium-Organic Frameworks.....	224
A.4.	Synthesis of Precious Metal Doped MOFs.....	223
A.5.	Summary.....	230
A.6.	References.....	231

# Acknowledgements

---

My first and most important acknowledgement has to go to my supervisor, Richard I. Walton. For the last 8 years I've been at the University of Warwick, his support has guided me through my undergraduate and the thesis project. These last four years I've been able to travel about Europe, play with some fancy bits of kits and actually gather enough data to sum up in this thesis-book thing. So, thanks Richard for this, it's been great.

Secondly, I'd like to thank the members of the Walton group, past and present, for your help and advice over the years. Far too many sleepless nights spent with you guys collecting data at synchrotrons. Special mentions to Luke Daniels for collecting TGA data for many of the compounds featured, Helen Playford for getting me up to scratch with GSAS, Craig Hiley for some of the worst puns imaginable and especially Alexis Munn, fellow HASYLAB survivor and cofounder of the shortly-lived but totally awesome Team MOF.

Special thanks to Guy Clarkson who solved the crystal structures of the lanthanide materials. Without your expertise, there wouldn't be much of a fourth chapter to this thing.

I am exceedingly grateful to MACADEMIA for three years of funding towards this PhD and whom without, this PHD never would have happened. MACADEMIA has allowed me to travel about Europe and collaborate with researchers from universities across the EU. Many of these people have collected data for us and I would like to thank Franck Millange (Université de Versailles) for measurement of gas adsorption data, Marco Daturi and his group (Université de Caen Basse-Normandie) for IR and Raman spectroscopy, Jean-Marc Greneche (Université du Maine, Le Mans) for Mössbauer spectroscopy and Ben Van de Voorde (K.U. Leuven) for xylene sorption data.

I'd like to thank my family. Not sure if you ever understood any of what I was doing but you were still proud of me anyway

Special mention goes to Robert 'Cookie' Cook. It's been a weird few years (living with you certainly hasn't helped) but it's never been boring. You also introduced me to Warwick Rock Soc, some of the friendliest and weirdest people I've ever met and I'm all the better for ever having known. I'd especially like to thank Lee Burton and Jeremy Brown for all the drunken weekends all over the place – good for the soul, maybe not the liver.



# Declaration

---

This thesis is submitted to the University of Warwick in support of my application for the degree of Doctor of Philosophy. It has been compiled by myself and has not been submitted in any previous applications for my degree.

The work presented (including data generation and analysis) was carried out by the author except in the cases outlined below:

Various contributions have been made to this work by other researchers and MACADEMIA partners. These have been indicated clearly within the text

Parts of this thesis have been published by the author:

Nouar, F.; Devic, T.; Chevreau, H.; Guillou, N.; Gibson, E.; Clet, G.; Daturi, M.; Vimont, A.; Grenèche, J. M.; Breeze, M. I.; Walton, R. I.; Llewellyn, P. L.; Serre, C.: "Tuning the breathing behaviour of MIL-53 by cation mixing" *Chem. Commun. (Cambridge, U. K.)* **2012**, 48, 10237-10239

Breeze, M. I.; Clet, G.; Campo, B. C.; Vimont, A.; Daturi, M.; Grenèche, J.-M.; Dent, A. J.; Millange, F.; Walton, R. I.: "Isomorphous Substitution in a Flexible Metal–Organic Framework: Mixed-Metal, Mixed-Valent MIL-53 Type Materials" *Inorg. Chem.* **2013**, 52, 8171-8182.

# Abstract

---

Several new mixed-metal analogues of MIL-53 have been synthesised using iron and vanadium. The properties of the mixed-metal materials are affected greatly by the ratio of the two metals. Analysis of the EXAFS spectra of a mixed-metal MIL-53(Fe, Cr) sample was performed supporting the homogeneity of the material. The investigation of mixed iron-cobalt materials was also studied.

Several new lanthanide-organic frameworks are described. Through mediation of the reaction solvent and subsequent calcinations, several new ytterbium-organic frameworks have been synthesised and their properties investigated. Using a solvent mixture of between 1:0 and 6:4 DMF to water leads to the formation of MB2,  $[\text{Yb}_2(\text{BDC})_3(\text{DMF})_2] \cdot 2\text{H}_2\text{O}$ , which contains ytterbium-carboxylate chains. Calcination of MB2 creates  $\text{Yb}_2(\text{BDC})_3$ , a material that exhibits permanent porosity. Further decreasing the DMF to water ratio in synthesis leads to the formation of MB3,  $[\text{Yb}_2(\text{BDC})_3(\text{DMF})_2(\text{H}_2\text{O})_2]$ , which contains ytterbium-carboxylate dimers. Although sharing similar chemical formulae, MB2 and MB3 vary greatly in terms of structure and properties. Despite of this, both MB2 and MB3 can be calcined into the same  $\text{Yb}_2(\text{BDC})_3$  material, seen from the calcination of MB2. Attempts to create analogues of MB2 and MB3 using other lanthanides were unsuccessful with the exception of lutetium. In spite of this, doping of MB2(Yb) with other lanthanides was successful and their luminescence properties studies. Synthesis of isorecticular analogues of MB2 and MB3 were partially successful with an isorecticular analogue of MB3, MB5, being formed.

Crystallisation of several metal-organic frameworks were followed using both *ex situ* and *in situ* methods and it was shown these two sets of techniques can complement one another to enable the pathways of MOF formation to be monitored.

# 1. Introduction

---

## 1.1. Introduction

Metal-organic frameworks are a relatively new class of porous material, consisting of metal-ion or metal-ion clusters linked by polydentate organic ligands. Their discovery and the realisation of their stability and properties represented a new development at the interface between coordination chemistry and materials science. Many of these metal-organic frameworks have been shown to exhibit properties that outweigh those of conventional porous materials, such as gas adsorption and selectivity.<sup>1,2</sup> The purpose of this chapter is to give a brief introduction into metal-organic frameworks with particular focus on bimetallic and lanthanide materials, which are the topic of this thesis. There are now many review articles and books on metal-organic frameworks, to which the reader is referred for further information.<sup>3-7</sup>

## 1.2. Definitions

Owing to the rapid expansion of research into metal-organic frameworks in the past 10 years, large discrepancies in the nomenclature used to report these materials can be seen in the literature. The terms ‘metal-organic framework’, ‘coordination polymer’ and ‘coordination network’ have often been used interchangeably. Further confusion has arisen from inconsistencies in naming of materials between research groups. In 2013, the International Union of Pure and Applied Chemistry (IUPAC) proposed guidelines on the correct nomenclature to be used in the reporting of such materials.<sup>8</sup> The term ‘coordination polymer’ is defined as ‘a coordination compound with repeating coordination entities extending in 1, 2 or 3 dimensions.’ The term ‘coordination network’ refers to coordination compounds that extend through repeating coordination entities with cross

links between two or more individual coordination entities. Metal-organic frameworks exist as a further subset of this, defined as 'a coordination network with organic ligands containing potential voids.' Although metal-organic frameworks may appear to be non-porous initially, many of these materials show changes in porosity when exposed to temperature, pressure or other external stimuli. In order to be referred to as metal-organic frameworks, a coordination polymer must be shown to have potential porosity via experimental or theoretical means.

The large number of research groups working on metal-organic frameworks and the relative newness of the field, has meant that no clear guidelines on the naming and structural characteristics of these materials at present exist. Some groups choose to use the IUPAC recommended nomenclature for coordination compounds, *e.g.*, Poly[hexa-aqua-bis( $\mu^2$ -terephthalato)( $\mu^2$ -terephthalato)dytterbium(III)].<sup>9</sup> This method, although useful for compositional analysis, gives little information about the structure itself (such as coordination environment of the metal or porosity) and makes identification of analogues difficult. Other groups tend to use acronyms or abbreviations. The Yaghi group uses the MOF-XX notation (XX is a number used to denote a particular framework),<sup>10</sup> whereas other groups choose to use an acronym referring to the institution where the materials were synthesised, such as MIL-XX (Matériaux Institut Lavoisier),<sup>11</sup> UiO-XX (Universitetet i Oslo)<sup>12</sup> or STAM-XX (St Andrews MOF).<sup>13</sup> This notation can be expanded to make identification of materials and structural analogues easy; for example, NH<sub>2</sub>-MIL-53(Al) refers to the MIL-53 structure containing framework aluminium and amino-substituted 1,4-benzenedicarboxylate as linker.<sup>14</sup> The use of this system, however, gives little information about this composition and structure of the material without prior knowledge has led to several groups reporting the same material. A classic example of this is HKUST-1 that has also been reported as MOF-199 and Cu-BTC.

As well as the chemical composition, another important factor in the description of metal-organic frameworks is the dimensionality and connectivity of the materials. Metal-organic frameworks and similar materials can be connected by organic or inorganic moieties. Cheetham, Rao and Feller described a nomenclature where materials could be categorised in terms of their dimensionality through their connectivity by either organic or inorganic groups.<sup>15</sup> Inorganic connectivity, *i.e.* M-X-M where X = O, OH, F, *etc.*, is denoted by 'I' and organic connectivity through the ligands is given by 'O'. This leads to the notation  $I^mO^n$  where m and n refer to the number of dimensions the connectivity is propagated for inorganic and organic connectivity, respectively. For example, a chain coordination polymer with only organic connectivity would be described as  $I^0O^1$ , whereas three-dimensional zeolites would be described as  $I^3O^0$ . Metal-organic frameworks can also contain mixtures of both inorganic and organic connectivities. For example, the structure of MIL-53 contains one-dimensional inorganic metal-oxide chains connected to one another in two dimensions by the linkers with gives an overall three-dimensional system with the classification  $I^1O^2$ .<sup>11</sup> Although the notation gives little information with regards to the structure itself (such as metal coordination), it provides a useful way of comparing the connectivity of different metal-organic frameworks, when used alongside other nomenclature.

### 1.3. History of Metal-Organic Frameworks

Although not known as such, coordination polymers have been used throughout history. A classic example can be found in the tanning process used to preserve animal skins as leather. During the process, chromium (III) ions are incorporated into the collagen of the hide, leading to cross-linking of the collagen and the metal-ions via ololation.<sup>16</sup> These crude coordination polymers help the material to resist decay and weathering that affect non-treated hides.<sup>17</sup> Another well known historical coordination polymer is Prussian Blue,  $Fe_4[Fe(CN)_6]_3 \cdot xH_2O$ , containing iron linked in three dimensions by the cyanide ligands.

The first porous coordination polymer i.e. a metal-organic framework was reported by Hoffman *et al.* who described the synthesis of  $[\text{Ni}(\text{CN})_4\text{Ni}(\text{NH}_3)_2] \cdot 2\text{C}_6\text{H}_6$ .<sup>18</sup> The structure of this material was determined by Rayner *et al.* using X-ray diffraction.<sup>19</sup> Using the Cheetham-Rao-Feller notation, the structure can be described as  $\text{I}^2\text{O}^0$  with layered square nets of  $\text{Ni}(\text{CN})_2$  with amines coordinated perpendicular to the nets. Between these layers, the extra-framework benzene is found. Since the benzene occupies what could be classed as a pore in the material, it can be successfully argued that this material is indeed a metal-organic framework. Although other similar materials were reported, relatively little interest was taken in the field of coordination polymers until 1990.

In 1990, Hoskins, Robson and co-workers published a series of articles outlining a net based approach to the design of coordination polymers.<sup>20-23</sup> This work outlined how three-dimensional structures could be designed using octahedral and tetrahedral centres linked by 'rod-like units'. Through this design approach, they rationalised that materials could be engineered with characteristics such as porosity and catalytic activity assuming that the synthesis could be perfected.

The term 'metal-organic framework' was coined by Yaghi *et al.* in 1995 who reported the design and synthesis of a layered material containing 1,3,5-benzenetricarboxylate, pyridine and cobalt.<sup>24</sup> Since this material displayed selective and reversible adsorption of aromatic compounds, it was argued that the properties of the material could be altered via modification of the functionality of the frameworks. Since 1995, research into metal-organic frameworks has expanded rapidly.<sup>4</sup> Interest has been driven by the sheer versatility of these materials synthesised from a vast range of metals and linkers.

## 1.4. Metal-Organic Frameworks

### 1.4.1. Structures

Metal-organic frameworks can be thought of as a structures comprising of 'joints' and 'struts'. The 'joints' (or 'nodes') are typically metal-oxide polyhedra and are often referred to as secondary building units (SBUs) with the term 'primary building units' (PBUs) referring to the coordination about the metal centre itself. SBUs may also be clusters of metal atoms linked by oxide. The number of points of extension (i.e. where co-ordination occurs) control the geometry of the framework and can take a large range of values depending on the cluster.<sup>25</sup> The 'struts' are polydentate organic ligands (or 'linkers') often with oxygen or nitrogen donor atoms, commonly carboxylates, pyridine or imidazoles. These linkers can take a variety of shapes, rigidities, size and number of and position of donor atoms.<sup>26</sup> The 'struts' control the geometry, the size of the pores and the pore environment in combination with the 'joints' that may be metals with some preferred coordination environment. The frameworks can be connected in one, two or three dimensions by both the inorganic and the organic components (Figure 1.4.1).<sup>27</sup>

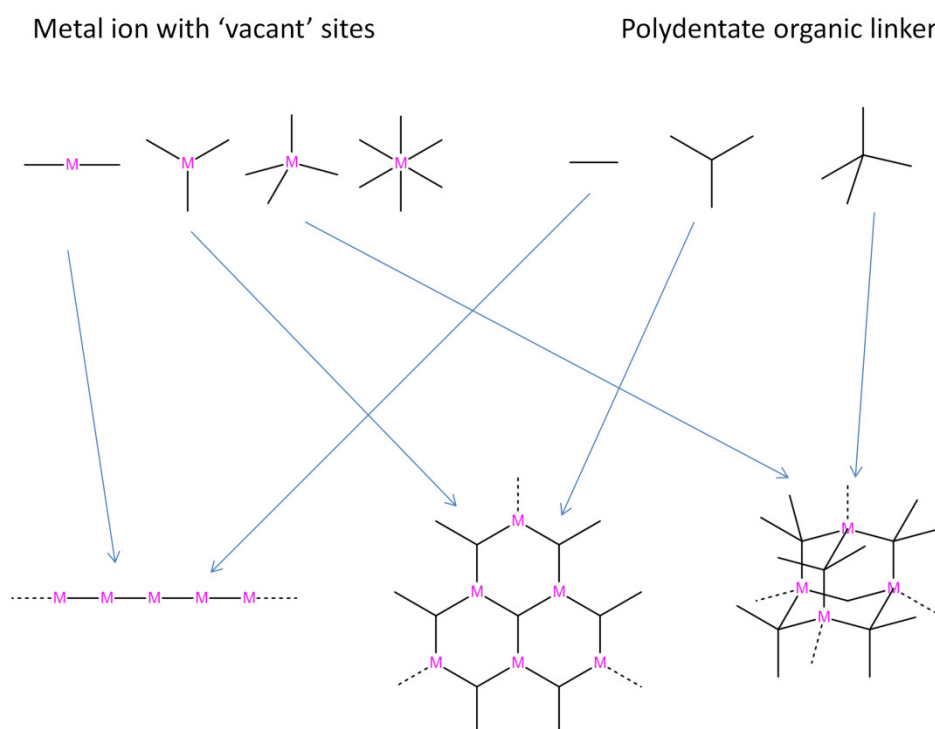


**Figure 1.4.1: How one, two and three-dimensional metal-organic frameworks can be created using a range of generic secondary building units and linkers**

The structures of metal-organic frameworks are often compared to those of zeolites since they may share similar extended networks with microporous structures. For example, ZIF-8 (ZIF – zeolitic imidazolate framework) shares the SOD-type framework as sodalite.<sup>28</sup> The pore-size in metal-organic frameworks, however, is not limited to the microporous range (less than 2 nm in dimension); several metal-organic frameworks have been reported to have pores in the mesoporous range (2-50 nm).<sup>29-31</sup> Several other potential advantages of using metal-organic frameworks are apparent. During the synthesis of zeolites, additional molecules or ions are often required to 'template' the structure (and which must be removed later), whereas metal-organic framework synthesis generally does not require additional reagents. Zeolite frameworks are either anionic (aluminosilicate) or neutral (siliceous). Metal-organic frameworks do not have this limitation – cationic, anionic and neutral frameworks have all been reported. Functionalisation of metal-organic frameworks is relatively facile, often simply requiring substitution of a non-functionalised



linker for a functionalised variant during the synthesis, or after synthesis to allow reactive groups to be added. By comparison, functionalisation of zeolites often requires harsh post-synthetic modification, high temperatures and long reaction times.<sup>32</sup> The use of organic linkers has additional benefits – hydrophilic and hydrophobic regions can be incorporated into a material, modifying the adsorption ability of the material. The use of linkers containing chiral functional groups allows for the formation of chirally-selective frameworks – a feat impossible using zeolites.<sup>33</sup> In contrast to supramolecular chemistry, the organic and inorganic components of metal-organic frameworks are covalently bonded, giving rise to thermally robust and chemically resistant materials. The applications of MOFs will be described in more detail below in Section 1.4.6.

### **1.4.2. Synthesis of Metal-Organic Frameworks**

Metal-organic frameworks are typically synthesised using solvothermal conditions. Solvothermal synthesis involves heating a sealed reaction vessel above the boiling point of the solvent used (see Figure 1.4.2 for example of typical laboratory-scale reaction vessel).<sup>34</sup> This generates autogenous pressure which can help to increase the rate of reaction and dissolve poorly soluble reagents. Metal-organic frameworks can also be synthesised under reflux, biphasic, electro-deposition and mechano-chemical conditions.<sup>26,35-37</sup>

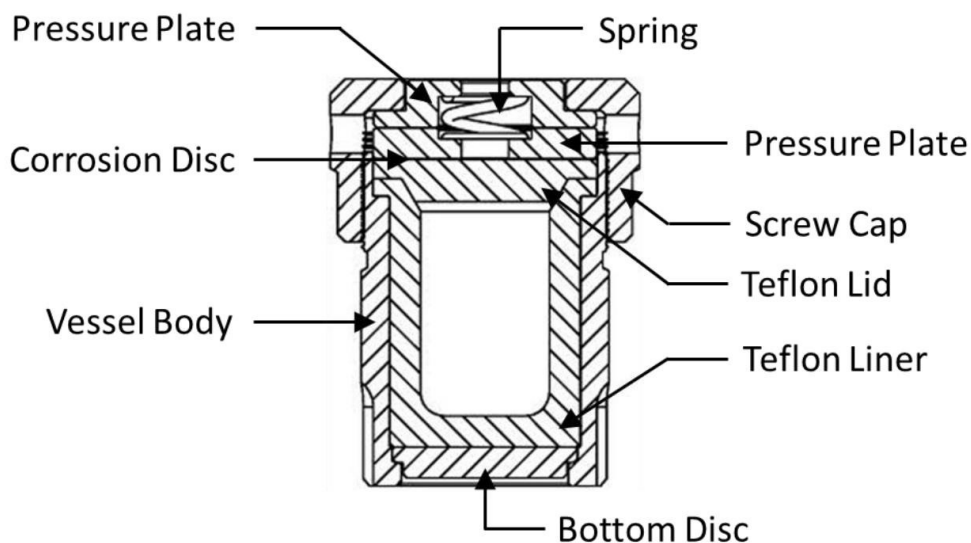


Figure 1.4.2: Schematic diagram of an autoclave typically used in the laboratory to perform solvothermal synthesis

During the synthesis of metal-organic frameworks, solvent molecules and unreacted linker are often incorporated into the material as extra-framework entities. These can generally be removed through heating, reduced pressure, or substitution with other guest molecules to generate porous materials, a step often described as 'activation'.

Although ligand geometry and choice of metal have a huge effect on the metal-organic framework formed, equally important are the reaction conditions and reagents chosen. McKinstry *et al.* investigated the synthesis of MOF-5 and found that reaction temperature, duration of reaction and stirring affected both the purity and final product itself.<sup>38</sup> Ahnfeldt *et al.* described changing the aluminium salt from the nitrate to the chloride leading to the formation of the unrelated frameworks, MIL-53(Al)-NH<sub>2</sub> and CAU-1 respectively.<sup>39</sup>

### 1.4.3. Isorecticular Synthesis of Metal-Organic Frameworks

Assuming that the geometries of the linker molecule and the metal 'joint' remain consistent, the linker can be extended or modified and the metal substituted while maintaining the overall topology of the system. This can lead to the synthesis of large ranges of structurally similar analogous materials. The substitution of the metal or the linker during synthesis while maintaining the overall topology is known as isorecticular synthesis.<sup>40</sup> This term was first coined by the Yaghi group to describe how the structure of MOF-5 could be modified using functionalised terephthalate (BDC) linkers or extended by using longer linkers such as biphenyldicarboxylate (BPDC) or terphenyldicarboxylate (TPDC). Another example of isorecticular synthesis is the use of functionalised linkers to give a family of materials with the same structure; this was shown for MIL-47(V) by Biswas *et al.* using six different functionalised terephthalates.<sup>41</sup>

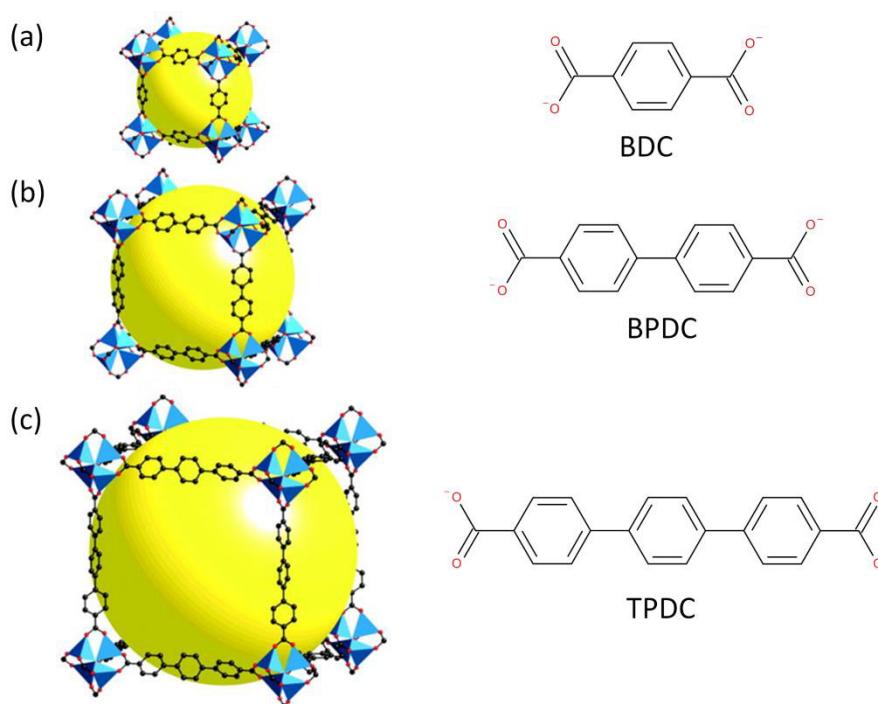


Figure 1.4.3: Isorecticular analogues of MOF-5 using extended linkers: (a) 1,4-benzenedicarboxylate (BDC), (b) biphenyldicarboxylate (BPDC) and (c) terphenyldicarboxylate<sup>42</sup>

Ma *et al.* described the synthesis of a series of mixed-component metal-organic frameworks formulated  $\text{ZnL}_2\text{L}'\cdot\text{solvent}$ .<sup>43</sup> These materials contain two different types of ligands: one dicarboxylate and the other with bi-pyridyl functionality. Both of these ligands could be substituted for extended analogues with a 1500 % increase in free volume between the fumarate-bipyridine and the biphenyldicarboxylate- di(4-pyridyl)-1,4,5,8-naphthalenetetracarboxydiimide systems. Furthermore since materials constructed from pyridyl ligands alone are often thermally unstable the use of carboxylate co-ligands was found to increase the stability of the materials.

The concept of isorecticular synthesis involves complete substitution of one linker for another. A more selective approach would be partial substitution of the linker. If the uptake of the two or more linkers could be controlled, i.e. similar to the initial reactant ratio, it may be possible to vary the properties of the material linearly with regards to the linker ratio. This 'mixed-component' approach to metal-organic synthesis may be similar to the 'solid solution' approach seen in inorganic chemistry, if both single ligand end-members can be prepared, or may be analogous to doping if one ligand is added in small amounts compared to a predominant ligand.<sup>44</sup> It is worth noting the terminology 'mixed-component' when used with regards to ligands refers to ligands that share the same coordination modes with the metal, but with differing functionality.

The first example of a mixed-component metal-organic framework prepared in this way was described by Chun *et al.* who used a 1:1 ratio of 1,4-benzenedicarboxylate (BDC) and tetramethyl-1,4-benzenedicarboxylate (TMBDC) with zinc and 1,4-diazabicyclo[2.2.2]octane (DABCO) to form  $[\text{Zn}_2(\text{BDC})(\text{TMBDC})(\text{DABCO})]$ .<sup>45</sup> This mixed-component metal-organic framework was found to be isomorphous with both of the single component products and it displayed greater hydrogen adsorption, aptly displaying the potential of investigating mixed-component systems. Mixed-component techniques may

allow for the incorporation of functionality that is difficult by conventional means. Yaghi and co-workers reported the incorporation of nitro-1,4-benzenedicarboxylate into the MOF-5 system.<sup>46</sup> The synthesis of  $[\text{Zn}_4\text{O}(\text{BDC})_{2.14}(\text{BDC-NO}_2)_{0.86}]$  is particularly interesting – using nitro-1,4-benzenedicarboxylate as the sole linker does not form  $[\text{Zn}_4\text{O}(\text{BDC-NO}_2)_3]$ . Mixed-component syntheses of metal-organic frameworks do not solely pertain to the substitution of linkers with substitution of metals also possible. This will be discussed later in section 1.5.

#### 1.4.4. Post-synthetic modification of metal-organic frameworks

Owing to the relative robustness of metal-organic frameworks towards temperature and solvents, reactions can be performed upon the framework itself. This is typically achieved via functional group interconversion on the bridging ligands. The first example of post-synthetic modification of metal-organic frameworks was reported by Seo *et al.* who reported a two-dimensional homochiral metal-organic framework, POST-1, for enantioselective separation and catalysis.<sup>47</sup> Uncoordinated pyridyl groups in POST-1 were converted to N-methylpyridinium ions through reaction with excess methyl iodide at room temperature. Since then, a wide range of post-synthetic modifications through covalent transformations have been reported including amide coupling,<sup>48</sup> imine condensation,<sup>49</sup> urea formation,<sup>50</sup> N-alkylation,<sup>47</sup> bromination,<sup>51</sup> reduction,<sup>52</sup> click reactions<sup>53,54</sup> and protonation.<sup>55</sup> Post-synthetic modifications of metal-organic frameworks involving tandem reactions have also been reported.<sup>56-61</sup>

#### 1.4.5. Dynamic Metal-Organic Frameworks

Many metal-organic frameworks are rigid, displaying little to no changes in the framework dimensions after removal of solvent molecules. Some metal-organic frameworks, however, display distinct structural changes upon the influence of external

stimuli e.g. temperature, pressure and gas adsorption. This is accompanied by a reversible expansion or contraction of framework – a property often referred to as ‘breathing’ and such materials that display this property termed as ‘dynamic.’<sup>7,62</sup> This property is not unique to metal-organic frameworks and has been reported for zeolites and perovskites,<sup>63,64</sup> but the ability of metal-organic frameworks to reversibly expand and contract far exceeds that of conventional solid state materials with atomic displacements of several Ångströms possible.<sup>7</sup>

This breathing effect is most pronounced in the MIL-88 family of isoreticular analogues, first reported by Férey and co-workers.<sup>65-67</sup> The MIL-88 series,  $[M_3O(H_2O)_3(XDC)_3] \cdot \text{guest}$  where  $M = \text{Cr(III)}, \text{Fe(III)}, \text{V(III)}$  and  $XDC = \text{fumarate (MIL-88A)}, 1,4\text{-benzenedicarboxylate (MIL-88B)}, 2,6\text{-naphthalenedicarboxylate (MIL-88C)}$  and  $4\text{-4'-biphenyldicarboxylate (MIL-88D)}$ , display a massive breathing effect with an increase of up to 270 % seen upon solvent adsorption. This expansion is achieved through rotation of the linker molecule around the dicarboxylate group, leads to a massive increase in the porosity of the material (Figure 1.4.4). Such behaviour is also known for hydrated MIL-53,  $[M(\text{BDC})(\text{OH})] \cdot \text{H}_2\text{O}$ , where dehydration of the material leads to a reversible expansion of the structure by around 30 %.<sup>68</sup> The dynamic breathing behaviour of MIL-53 will be discussed further in Section 1.6.

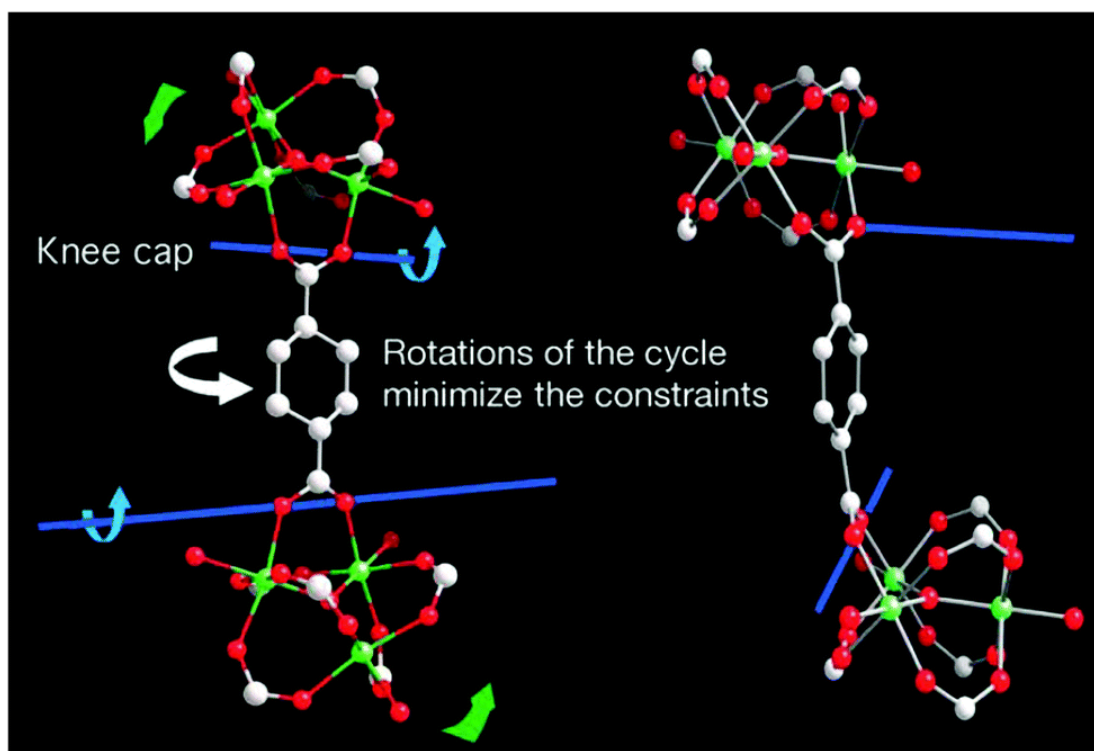


Figure 1.4.4: Rotation about the carboxylate group seen in MIL-88B<sup>66</sup>

### 1.4.6. Potential Applications

The accessible porosity of metal-organic frameworks is the driving factor in research into potential applications for these materials. The well-defined porosity of metal-organic frameworks is a characteristic shared by zeolites and indeed many of the potential applications studied mirror this.

The ability of metal-organic frameworks to reversibly absorb molecules makes them candidates for adsorption and storage of molecules. Species such as gases, liquids, drug molecules, metals and inorganic nano-particles can be introduced into metal-organic frameworks.<sup>34,69,70</sup> Sorption of gases is one of most widely studied area of metal-organic framework research. Metal-organic frameworks can adsorb considerable quantities of gases such as CH<sub>4</sub>, NO<sub>2</sub>, CO<sub>2</sub>, O<sub>2</sub> and H<sub>2</sub>.<sup>42,71-75</sup> The storage of hydrogen is being studied extensively for the purpose of providing efficient high capacity, environmentally friendly energy storage materials.<sup>5,72,76-79</sup>

The shape and definition of porosity of metal-organic frameworks make them ideal candidates for size-selective separation of mixtures of molecules, similar to zeolite systems. Selective adsorption based mainly on the molecular sieving effect has been confirmed in several metal-organic frameworks.<sup>80</sup> This property has been used to separate both mixtures of gases and liquids.<sup>81-83</sup>

A particular advantage of metal-organic frameworks is separation of mixtures based upon their interaction with the framework itself. Combined with the ability to modify the functionality of the linkers through isorecticular synthesis, there is the potential to customise metal-organic frameworks with regards to the separation required. Separation of two or more components is achieved by exploiting the differing affinities of the adsorbates to the framework itself. Gas-phase separations investigated include resolution of CO<sub>2</sub> from CH<sub>4</sub>,<sup>71</sup> C<sub>2</sub>H<sub>6</sub> from C<sub>2</sub>H<sub>4</sub>,<sup>84</sup> and MeOH over MeCN.<sup>85</sup> Liquid-phase studies include resolution of xylene mixtures and removal of nitrogen and sulphur heterocycles from fuel mixtures.<sup>86-89</sup> The difficulties in separating xylene isomers arise from their similar boiling points making techniques such as fractional distillation inefficient.<sup>90</sup> Since techniques used industrially such as fractional crystallisation are energy intensive, a simplistic adsorption based separation technique would be of benefit from a cost perspective. The MIL-53 series of materials display high selectivity for individual xylene isomers which has been used by Alaerts *et al.* and by El Osta *et al.* to resolve mixtures of xylene isomers into their separate components under close to ambient conditions.<sup>87,88</sup> Use of chiral linkers affords the ability to separate racemic mixtures into their separate enantiomers.<sup>47,91,92</sup>

Separation of isotopes cannot be achieved using molecular sieving effects due to their identical adsorption profiles from the almost identical sizes of molecules involving different isotopes of a particular element. Some metal-organic frameworks, however, have used 'quantum sieving' to resolve hydrogen / deuterium mixtures. Quantum sieving is



based upon the preferential adsorption of heavier isotopes when confined in very narrow spaces or channels. Chen *et al.* reported the ability of  $\text{Zn}_3(\text{bdc})_3[\text{Cu}(\text{Pyen})]$  ( $\text{H}_2\text{Pyen}$  = 5-methyl-4-oxo-1,4-dihydro-pyridine-3-carbaldehyde) to preferentially adsorb hydrogen over deuterium onto unsaturated Cu(II) sites present in micro-pores.<sup>93</sup> Similar behaviour was seen for  $[\text{Cu}(4,4'\text{-bipyridine})_2(\text{CF}_3\text{SO}_3)_2]$  by Noguchi *et al.*<sup>94</sup> Deliberate engineering of metal-organic framework to contain extremely narrow pores would have benefits for this and other applications.

The ability of metal-organic frameworks to adsorb molecules into their structure makes them suitable for potential use as 'sensors.' This can typically be monitored via changes in their photoluminescent properties. Li *et al.* reported the sensing of DMF by  $[\text{Eu}_2\text{L}_3(\text{H}_2\text{O})_4]$  ( $\text{L}$ =2',5'-bis(methoxymethyl)-[1,1':4',1''-terphenyl]-4,4''-dicarboxylate) that displayed a fast and strong response when exposed to DMF vapour.<sup>95</sup> Wang *et al.* described how the luminescence of  $[\text{Cd}(\text{NH}_2\text{-BDC})(\text{H}_2\text{O})_2]$  was quenched when exposed to nitroaromatic compounds.<sup>96</sup> The ability to detect nitroaromatics simply and effectively is of great importance to detection of explosives.

## 1.5. Heterometallic-Organic Frameworks

### 1.5.1. Introduction

Heterometallic-organic frameworks (HMOFs) contain two or more metals incorporated into the same metal-organic framework. With the majority of isorecticular syntheses involve complete substitution of either the ligand or the metal, it stands to reason that a more selective process would involve the partial substitution of the substituents – a mixed-component approach.<sup>44</sup> Mixed-ligand and mixed-metal MOFs could be considered to be 'molecular substitutional alloys' where the properties of the material could be varied between those of the two single component extremes or potentially display properties

unlike those of either single component materials. Incorporation of two or more metals into the same materials could lead to interesting optical, magnetic and catalytic properties for example.

Heterometallic-organic frameworks can be separated into two main groups: extra-framework or intra-framework. Extra-framework HMOFs contain one metal incorporated into the framework with further metals existing in the pores of the materials in one of three ways: counter-ions, nano-particles or as polyoxometalate clusters (Figure 1.5.1). Intra-framework HMOFs have both metals incorporated into the framework as either the secondary building unit or into the linker itself (Figure 1.5.2).

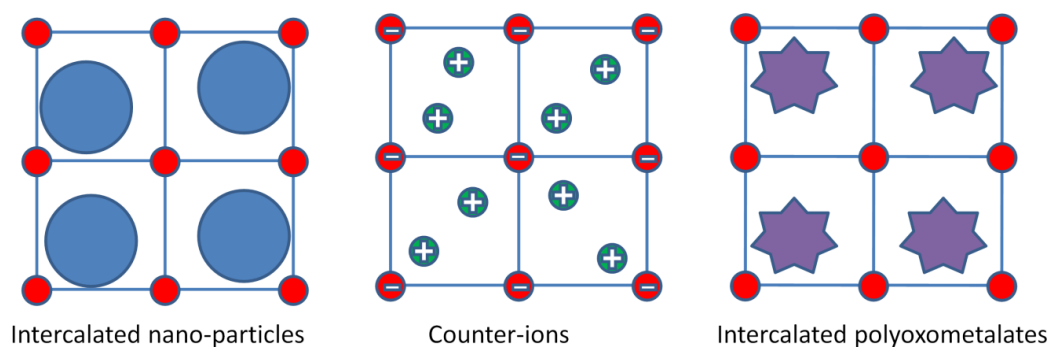


Figure 1.5.1: Examples of extra-framework heterometallic-organic frameworks

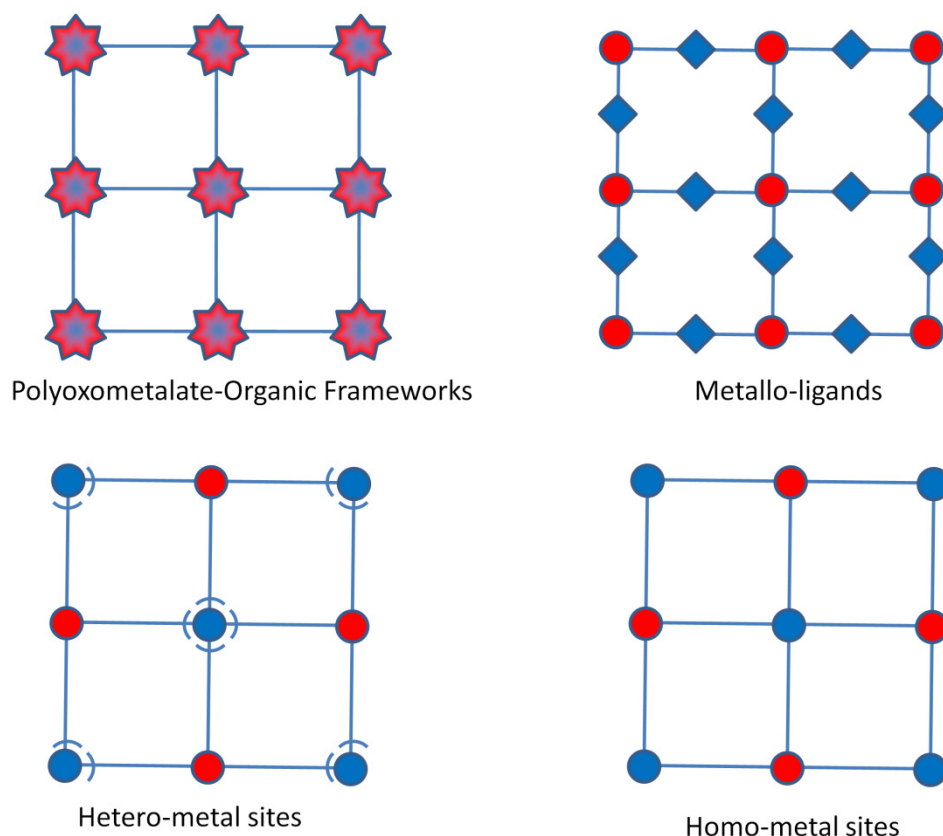


Figure 1.5.2: Examples of intra-framework heterometallic-organic frameworks

### 1.5.2. Intercalated Nano-Particles@MOFs

Because of their well defined and large pore structure, metal-organic frameworks can be used to stabilise and control the formation of metal nano-particles within their structure.<sup>97</sup> The incorporation of active metal nano-particles into metal-organic frameworks is relevant for a number of potential applications involving heterogeneous catalysis and gas storage.<sup>98,99</sup> Intercalation is usually achieved via decomposition of volatile organic precursors although it can be achieved using wetness impregnation, mechanical and co-precipitation methods.<sup>98,100-106</sup> Schroeder *et al.* described how Pd-Ru nanoparticles were incorporated into MOF-5 using chemical vapour deposition.<sup>107</sup> The presence of Pd-Ru nanoparticles was confirmed by TEM and XRD. El-Shall *et al.* reported the incalation of Cu, Pd and Pd-Cu nano-particles into MIL-101.<sup>108</sup> These materials exhibited enhanced catalytic

activity towards CO oxidation greater than that of either MIL-101 or the surface-mounted nano-particles allowing for efficient low temperature reactions.

### 1.5.3. MOFs with counter-ions

Unlike zeolites which solely have anionic or neutral frameworks, metal-organic frameworks can also have cationic frameworks. In both of the non-neutral cases, counter-ions are required to balance this charge. In many cases, simple alkali metal cations are present to neutralise anionic frameworks.<sup>109-111</sup> Cation exchange has been reported for several metal-organic frameworks.<sup>112-114</sup> Yaghi *et al.* reported the synthesis of MOF-235,  $[\text{Fe}_3\text{O}(\text{BDC})_6(\text{H}_2\text{O})_3]\text{FeCl}_4$ , an example of a cationic framework with a metallic counter-ion ( $[\text{FeCl}_4]^-$ ).<sup>115</sup>

### 1.5.4. Intercalated Polyoxometalates

Polyoxometalates (POMs) are well known for their thermal stability, reversible reduction, magnetism, and luminescent properties.<sup>116</sup> Incorporation of polyoxometalates into metal-organic frameworks may lead to interesting magnetic and catalytic properties. Ribeiro *et al.* described the encapsulation of  $[\text{PW}_{12}\text{O}_{40}]^{3-}$  into the chromium analogue of MIL-101 with the material showing promise as a catalyst for oxidative desulfurisation of S-heterocycles.<sup>117</sup> Polyoxometalates can also be using as templating agent as was seen by Bajpe *et al.* who reported the accelerated formation of HKUST-1 with encapsulation of Keggin polyoxometalates within its pores.<sup>118</sup>

### 1.5.5. Polyoxometalate-organic frameworks

Polyoxometalate-organic frameworks (POMOFs) are MOFs constructed using polyoxometalates as the secondary building units. The wide range of polyoxometalate structures and geometries comprised of a variety of metals combined with the 'customisability' of organic ligands makes them ideal partners for incorporation into the

same framework and may lead to interesting catalytic and magnetic properties.<sup>119</sup> POMOFs can be linked in several ways, typically through transition/lanthanide metals and/or organic linkers.<sup>120</sup> When heteropolyoxometallates are used as nodes then heterometallic MOFs are produced. Zheng *et al.* reported a collection of frameworks that could be constructed using a nickel-substituted phosphotungstate and a variety of carboxylate linkers including 1-D chains and 2-D layered structures depending on the geometry of the linker.<sup>121</sup> Zhang *et al.* described the synthesis of a POMOF constructed by  $[\text{GeMo}_{12}\text{O}_{40}]^{4-}$  and  $[\text{Ln}(\text{NMP})_4(\text{H}_2\text{O})_4]^{4+}$  (Ln = Ce(IV), Pr(IV) and Nd(III), NMP = *N*-methyl-2-pyrrolidone) with a 2-D porous structure that displayed photochromic behaviour upon radiation with UV light.<sup>122</sup>

### 1.5.6. Metallo-ligands

The linkers of metal-organic frameworks can be designed as such to allow coordination of metals into the linker itself as well as coordinating to node metals. Zhou and co-workers reported the synthesis of PCN-224, a zirconium metal-organic framework containing metalloporphyrin-functionalised ligands which themselves include coordinated metals.<sup>123</sup> Several analogous PCN-224 materials were synthesised containing divalent iron, nickel and cobalt, and display high catalytic activity towards the  $\text{CO}_2$ /propylene oxide coupling reaction. Zou *et al.* described the reaction of metalated  $\text{MH}_4\text{TCPP}$  (M =  $\text{Co}^{\text{II}}$ ,  $\text{Ni}^{\text{II}}$ ,  $\text{Cu}^{\text{II}}$  and  $\text{V}^{\text{IV}}\text{O}$ ) ( $\text{H}_6\text{TCPP}$  = 5,10,15,20-tetracarboxyphenylporphyrin) with lead nitrate leading to the formation of several metallo-ligand metal-organic frameworks with associated blue-shifts in the photoluminescence spectra.<sup>124</sup> Wang *et al.* reported the reaction of  $\text{ALL}_3$  (L = 3-(4-pyridyl)acetylacetonate) with  $\text{MCl}_2$  (M = Zn, Cd, Hg) where the choice of divalent metal has pronounced effects on the topology of the metal-organic framework synthesised due to the coordination of the divalent metal by 3-(4-pyridyl)acetylacetonate.<sup>125</sup> Incorporation of the metal into the metallo-ligand can also be achieved post-synthesis. Kaye *et al.* reported the post-synthetic metallation of MOF-5 using  $\text{Cr}(\text{CO})_6$  giving rise to the formation

of (BDC)Cr(CO)<sub>3</sub> organometallic species attached to the framework.<sup>126</sup> Photolysis of the Cr-CO bands in H<sub>2</sub> or N<sub>2</sub> environments led to the appearance of Cr(CO)<sub>2</sub>X<sub>2</sub> species that displayed enhanced thermal stability when compared to molecular analogues generated in frozen gas matrices or supercritical fluids. A recent review article on post-synthetic metalation of metal-organic frameworks has been published by Evans *et al.*<sup>127</sup>

### 1.5.7. Heterometallic sites

One-pot syntheses using two or more metals may result in the formation of a single-phase framework with both metals incorporated into the framework albeit at crystallographically distinct sites. This is particularly pronounced for reactions with metals from different groups. A commonly used method to achieving this is through use of a bifunctional ligand containing differing functional groups to act as hard and soft binding points for two different metals. An example of a ligand used is nicotinic acid that contains both carboxylate and pyridine functionality. This linker was used by Lian *et al.* to synthesise a mixed neodymium-silver MOF containing neodymium-carboxylate subunits and silver centres, both solely coordinated to the carboxylate or pyridine functionality respectively.<sup>128</sup> Examples include heterometallic metal-organic frameworks containing transition and lanthanide metals,<sup>129-132</sup> lanthanide and actinide metals,<sup>133,134</sup> transition and main group metals,<sup>135,136</sup> lanthanide and alkali metals<sup>137</sup> and, alkali and main group metals.<sup>138</sup>

### 1.5.8. Homometallic sites

Unlike metal-organic frameworks containing heterometallic sites which are crystallographically distinct, bimetallic-organic frameworks containing homometallic sites contain identical sites for both metals. These materials could be described as solid solutions and would ideally display characteristics of both the single metal analogues. Truly mixed-metal organic frameworks are rare in the literature due to preferential crystallisation of

single metal phases rather than a mixed phase, due to the differing reactivities of two, or more, metals in the chemical precursors used in synthesis, often as solvated cations. One way to overcome this is to use lanthanide metals where the reactivity across the series is similar,<sup>139-141</sup> and the ability to easily create mixed-lanthanide porous materials has potential in the fields of molecular sensing and molecular ‘barcodes’.<sup>142-144</sup> Because of the similarity of the two metals used in this situation, careful analysis is needed to prove that the two metals are truly present as mixtures within individual crystals.

Several mixed-metal organic frameworks have been reported. Munn *et al.* reported a range of  $[M^{\text{II}}(\text{BDC})(\text{PNO})]$  ( $M = \text{Mn, Co, Ni}$ ; PNO = pyridine N-oxide) analogues where solid solutions of composition  $[(M_{1-x}M'_x)(\text{BDC})(\text{PNO})]$  were prepared and identified as single phase by high resolution XRD.<sup>145</sup> Yaghi and co-workers synthesised mixed-metal analogues of MOF-74 containing 2, 4, 6, 8 and 10 different divalent metals with inclusion of all metals supported by elemental analysis with reproducible results suggesting true mixing of the material.<sup>146</sup> Several mixed-metal analogues of MIL-53,  $M(\text{BDC})(\text{OH})$ , have been reported, some during the course of the work described in this thesis, and will be discussed in the following section.

## 1.6. MIL-53 ( $M^{\text{III}}(\text{OH})(\text{BDC})$ )

### 1.6.1. Introduction

MIL-53,  $M^{\text{III}}(\text{BDC})(\text{OH},\text{F})$ , displays a range of interesting and unique properties including flexibility and selectivity. MIL-53 can be synthesised using a range of metals and the choice of metal has great influence on the properties of the material. Controlled uptake of two or more metals into the MIL-53 structure could lead to tuning of properties of the materials. In Chapter 3 of this thesis, the synthesis and characterisation of mixed-metal MIL-53 and the effect of metal content on its properties will be described.

### 1.6.2. Structure and Properties

MIL-53 has the general chemical composition  $M^{III}(BDC)(OH)$  and consists of 1-D chains of *trans* linked metal-oxide octahedra chains cross-linked to one another by 1,4-benzenedicarboxylate (BDC) dianions, Figure 1.6.1. In this simplest form of the material, the metal is trivalent and in an octahedral environment, coordinated to four oxygens from 1,4-benzenedicarboxylates and two from the *trans* bridging  $\mu_2$ -hydroxyl groups. The interconnectivity of the 1-D metal-oxide chains with the BDC linkers leads to a structure with one-dimensional, diamond-shaped channels running parallel to the hydroxide chains.

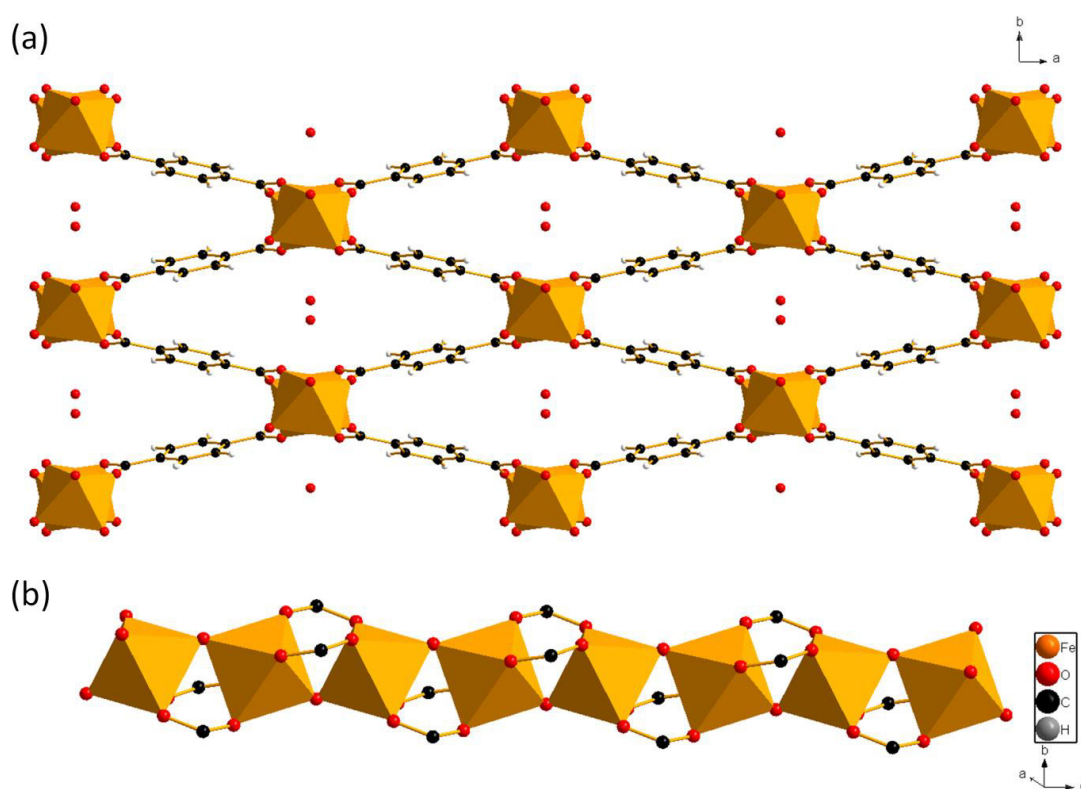


Figure 1.6.1: (a) Crystal structure of hydrated MIL-53(Fe) viewed down the *c*-axis; (b) Metal-oxide chains running along the *c*-axis in MIL-53



### 1.6.3. Effect of the Metal Centre on MIL-53 on its dynamic behaviour

The first example of the MIL-53-type structure reported was in fact a related vanadium material, MIL-47, which contains bridging oxy groups ( $O^{2-}$ ) along the inorganic backbone of the structure, instead of hydroxyl ( $OH^-$ ) groups.<sup>147</sup> Now several analogues of the material have been reported, containing either solely transition metals (Cr,<sup>11</sup> Fe,<sup>148</sup> Sc,<sup>149</sup>) or Group 13 metals (Al,<sup>150</sup> Ga,<sup>151</sup> In<sup>152</sup>), and in these cases the metal is in the +3 oxidation state and the bridging groups are usually hydroxyls, or may be partially replaced by fluoride, as in the case of MIL-53(Fe),<sup>153</sup> or completely replaced to give a fully fluorinated materials, as for MIL-53(Al).<sup>154</sup> Upon heating the as-made MIL-53(V<sup>III</sup>) in air to remove unreacted 1,4-benzenedicarboxylic acid from the pores, it undergoes irreversible oxidation of vanadium from 3+ to 4+ with associated dehydrogenation of the bridging hydroxyl groups to oxy groups to produce MIL-47. This leads to a permanently fully open structure of the type shown in Figure 1c. Later, utilising a careful activation technique, Leclerc *et al.* isolated an evacuated vanadium MIL-53(V<sup>III</sup>) analogue that did display reversible flexibility upon heating, but only in the absence of air.<sup>155</sup> Despite being isostructural in nature, the flexibility of the MIL-53 materials varies greatly from metal to metal.<sup>26</sup> Typically, MIL-53 materials have a closed hydrated form at room temperature, Figure 1.6.2(a) and (b), and upon heating the extra-framework water is removed. At this point, the chromium and aluminium materials convert to a fully open, or 'LP' (large pore) structure, Figure 1.6.2(c) and (d), with a large increase in pore volume, whereas the iron analogue undergoes a slight contraction of its structure.<sup>11,156</sup> Even upon heating further, MIL-53(Fe) only slightly expands, essentially remaining in the 'NP' (narrow pore) structure. The chromium and aluminium materials return to the closed form upon cooling to 5 K,<sup>157</sup> or upon rehydration.<sup>11</sup> The chromium material also shows 'superhydration', giving full expansion in the presence of excess water, unlike the iron analogue which remains in the small-pore

form.<sup>68</sup> This differing behaviour found for isostructural materials cannot be easily explained using factors such as the strength of the hydrogen bonding from the metal backbone, the ionic radii of the metal or the electronic structure of the metal, and is still a matter of debate in the literature.

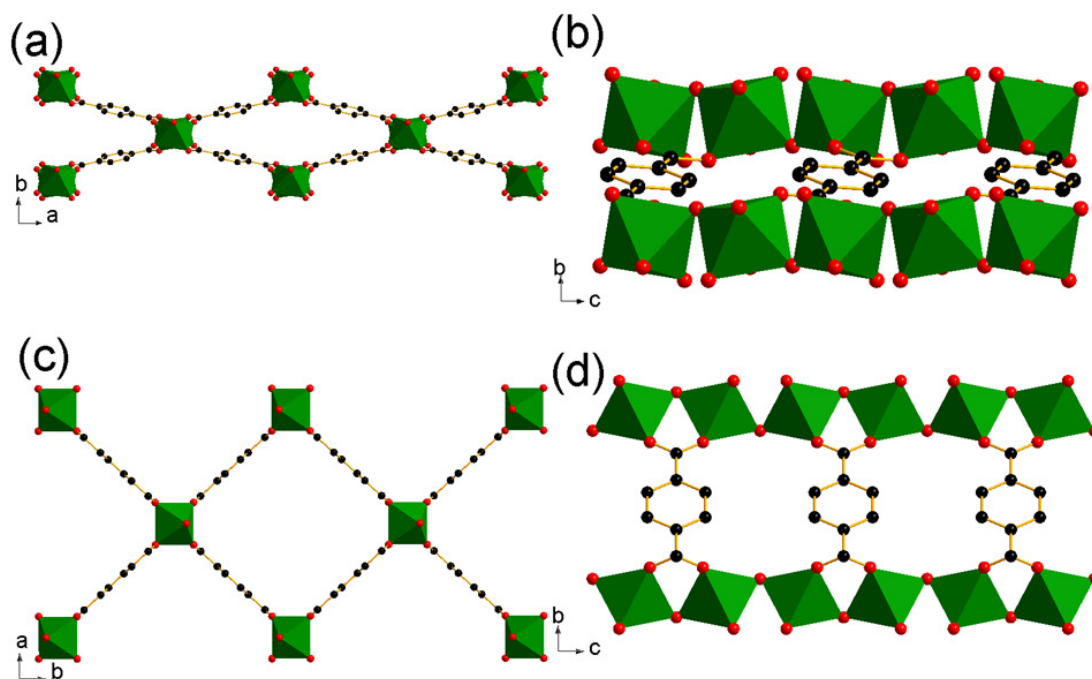


Figure 1.6.2: Two views of closed and open forms of the MIL-53 structure. The closed form (a) and (b) can be reversibly converted into the open form (c) and (d) by removal or addition of guest molecules, and in some cases by application of temperature and pressure. The structures were drawn using the published crystal structures of hydrated and dehydrated MIL-53(Cr), respectively.<sup>68</sup>

#### 1.6.4. Notable non-trivalent analogues of MIL-53

As noted for MIL-47(V<sup>IV</sup>), the MIL-53 framework is capable of stabilising valance states other than the usual trivalent state. In order to vary the oxidation state of the metal centres, either the bridging ligand must be substituted or a counter-ion introduced to balance the overall charge.

Substitution of the bridging hydroxyl ligand for the doubly anionic oxide group allows for the stabilisation of tetravalent vanadium in MIL-47(V<sup>IV</sup>). In a similar manner, substitution of the anionic hydroxyl group for a neutral ligand stabilises the presence of divalent metal in the MIL-53 structure. Whitfield *et al.* reported the synthesis of

Fe(BDC)(DMF) which contains divalent iron with coordinated neutral  $\mu^2$ -N,N'-dimethylformamide. The use of pyridine-N-oxide ligands has facilitated the synthesis of  $M^{II}(\text{BDC})(\text{PNO})$  ( $M = \text{Co}, \text{Ni}, \text{Mn}$ ).<sup>145,158,159</sup> These materials are analogous to MIL-53 and incorporate metals that cannot be used to synthesise trivalent MIL-53,  $M^{III}(\text{BDC})(\text{OH})$ .

An alternative to ligand substitution is to balance the charge using a counter-ion. This can be done pre- or post-synthesis. Medina *et al.* reported the synthesis of a mixed-valent MIL-53(Fe) analogue,  $[\text{Fe}^{III}_{0.5}\text{Fe}^{II}_{0.5}(\text{BDC})(\text{OH}, \text{F})]^{0.5-} \cdot 0.5\text{DMA}^+$ , that contains alternating  $\text{Fe}^{III} / \text{Fe}^{II}$  along the metal-oxide chains.<sup>160</sup> The anionic framework's charge is balanced by the presence of dimethylammonium ( $\text{DMA}^+$ ) cations. Heating of this material to 300 °C allows for removal of the dimethylammonium cations and subsequent oxidation of the framework to generate MIL-53(Fe). Férey and co-workers introduced lithium into MIL-53(Fe) post-synthetically, reducing around 60 % of the trivalent iron to iron(II).<sup>109</sup> Around 0.6 lithium atoms were incorporated per formula unit and the material studied for its potential use as a cathode in a Li-ion battery. It was found that the material could be reversibly charged and discharged, consistent with uptake / removal of  $\text{Li}^+$  and the reversible reduction of  $\text{Fe}^{III}$  into  $\text{Fe}^{II}$ .

### 1.6.5. Mixed-Metal MIL-53

Attempts to modify the 'flexibility' and absorption properties of MIL-53 materials have primarily focused on modifying the organic linkers with varying functional groups.<sup>161</sup> However, a simpler and more intuitive method of modifying MIL-53 behaviour would be the synthesis of bimetallic MIL-53 materials. A mixed metal analogue,  $[\text{Fe}_{0.28}\text{V}_{0.72}(\text{OH})_{0.8}(\text{BDC})] \cdot 0.53\text{H}_2\text{BDC} \cdot (\text{NH}_4)_{0.2}$ , was reported by Whitfield *et al.*,<sup>162</sup> but attempts to remove the disordered extra-framework 1,4-benzenedicarboxylic acid and ammonium ions were unsuccessful, with the structure decomposing upon heating. At the start of the work described in this thesis no further work had been reported on mixed-

metal MIL-53, but during the course of the work, some work appeared in the literature (see Chapter 3). MIL-53( $\text{Cr}_{0.6}\text{Fe}_{0.4}$ ) was reported by Nouar *et al.*<sup>163</sup> where the reactivity of the Fe(III) salt during synthesis was tempered to match the slower reactivity of Cr(III) salts by instead using iron metal, while small amounts (1 %) of Cr(III) were introduced into MIL-53(Al) by Mendt *et al.*<sup>164</sup> Kozachuk *et al.* reported the synthesis of  $[\text{Al}_{1-x}\text{V}_x(\text{BDC})(\text{OH})_{1-x}\text{O}_x]$  ( $0 < x < 1$ ), a solid solution of MIL-53( $\text{Al}^{\text{III}}$ ) and MIL-47( $\text{V}^{\text{IV}}$ ).<sup>165</sup> As the vanadium content was increased, the material's rigidity increased, consistent with the substitution of hydroxyl groups for oxide.

## 1.7. Lanthanide-Organic Frameworks

### 1.7.1. Introduction

Unlike metal-organic frameworks containing transition metals where the framework geometry is primarily dependent on electronic configuration, lanthanides with their shielded f-orbitals act as hard acids making cation size the main factor in coordination. Coupled with the larger radii of lanthanide ions, with preferences for higher coordination number (7,8 and 9 are not uncommon), leading to novel framework structures not seen for the transition metals. The formation of isostructural lanthanide MOF series is also therefore easier with several examples of both single metal and doped series having been reported.<sup>141,166-172</sup> A common feature of lanthanide-organic frameworks is their higher thermal stability against framework decomposition, often up to around 600°C due to stronger ionic interactions between the linkers and the lanthanide ions. The synthesis and characterisation of new lanthanide-organic frameworks may lead to the discovery of materials with unique optical, magnetic and catalytic properties. Chapter 4 is focused on the synthesis and discussion of new lanthanide-organic frameworks.

The trivalent lanthanide ions are characterised by filling of the 4f orbitals from 4f<sup>0</sup> (La<sup>3+</sup>) to 4f<sup>14</sup> (Lu<sup>3+</sup>). These electronic [Xe]4f<sup>x</sup> configurations, (x = 0 – 14) can generate a wide range of luminescent emissions ranging from ultraviolet to near infrared. Lanthanide electronic transitions are forbidden by parity (Laporte) selection rules, leading to weak absorbance and low quantum yields. This problem can be overcome by using ligands that can participate in energy transfer processes with the lanthanide ion. This is known as ‘luminescence sensitisation’ or the ‘antenna effect’ and has been exploited in several lanthanide-organic frameworks.<sup>173,174</sup>

### 1.7.2. Diversity of Structures

Lanthanide metals have several properties that make them more difficult to form metal-organic frameworks with predictable structures. Bonding in f-block metals is predominately ionic in character, leading to coordination geometries dependent on the steric demands of the ligands themselves rather than the directive electronic effects driving coordination geometry in transition metals.<sup>4</sup> Owing to the vast range of lanthanide-organic frameworks reported, only the structures of materials containing heavier lanthanides coordinated by 1,4-benzenedicarboxylate will be discussed here as this is most relevant to the work described in this thesis. These lanthanide-organic frameworks are of particular use to this work for their use in identifying new materials and their decomposition products.

Carboxylate-based ligands are of particular use in synthesis of lanthanide-organic frameworks due to the oxophilic nature of the lanthanide cations. The range of potential binding modes relates well to the lack of any preferential coordination geometry of 4f metals. Carboxylate ligands can coordinate singly ( $\eta^1$ ) or act in a bridging ( $Z, Z' - \mu^1 \eta^1$ ) or chelating ( $\eta^2$ ) manner (Figure 1.7.1). A single carboxylate can act in a simultaneous bridging and chelating binding mode ( $\mu^2 - \eta^2 : \eta^1$ ). For simplicity, these coordination modes have been denoted Type I, II *etc.*, and this will be the terminology used for the remainder of this work.

A list of structurally relevant lanthanide-BDC frameworks that have been reported in the literature and structurally investigated is given in Table 1.7.1 with the variety of reaction conditions required for synthesis given in Table 1.7.2. This considers the later lanthanides which are relevant for the work in this thesis.

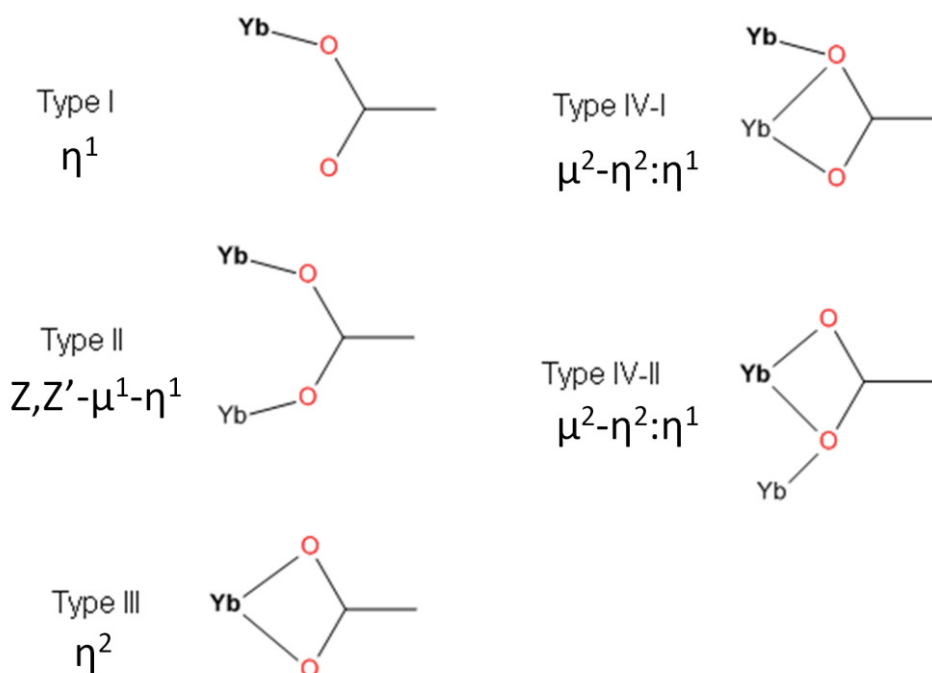


Figure 1.7.1: Examples of coordination modes known for ytterbium dicarboxylates using the notation outlined by Batten *et al.*<sup>4</sup> Principal ytterbium atom is in bold

**Table 1.7.1 : Connectivity and coordination of selected lanthanide (Ln)-BDC frameworks reported in the literature. Connectivity about Ln refers to the number of coordination points about the Ln centre and how the ligands coordinate to the metal centre. The sum of coordination points from singly and doubly coordinating ligands allows the coordination number (C.N.) to be calculated**

Name	Space group	Ln C.N.	Connectivity about Ln	Ref
[Yb <sub>2</sub> (BDC) <sub>3</sub> (H <sub>2</sub> O) <sub>2</sub> ]	$P\bar{1}$	6	1(I), 5(II)	140
		7	5(II), 2H <sub>2</sub> O	
[Yb <sub>2</sub> (BDC) <sub>3</sub> (H <sub>2</sub> O) <sub>6</sub> ]	$P\bar{1}$	8	1(I), 2(II), 1(III), 3H <sub>2</sub> O	9,140
[Yb <sub>2</sub> (BDC) <sub>3</sub> (H <sub>2</sub> O) <sub>8</sub> ]·2H <sub>2</sub> O	$P\bar{1}$	8	2(I), 1(III), 4H <sub>2</sub> O	140
[Lu <sub>2</sub> (BDC) <sub>3</sub> (H <sub>2</sub> O) <sub>8</sub> ]·2H <sub>2</sub> O	$P\bar{1}$	8	2(I), 1(III), 4H <sub>2</sub> O	174
[Er <sub>2</sub> (BDC) <sub>3</sub> (H <sub>2</sub> O) <sub>8</sub> ]·2H <sub>2</sub> O	$P\bar{1}$	8	2(I), 1(III), 4H <sub>2</sub> O	175
[Yb <sub>3</sub> (BDC) <sub>4.5</sub> (DMF) <sub>2</sub> (H <sub>2</sub> O) <sub>3</sub> ]·2H <sub>2</sub> O	$P\bar{1}$	8	3(II), 2(III), H <sub>2</sub> O	176
		8	5(II), 2H <sub>2</sub> O, DMF	
		8	4(II), 1(IV-I), 1(IV-II), DMF	
[Yb <sub>3</sub> (BDC) <sub>3.5</sub> (OH) <sub>2</sub> (H <sub>2</sub> O) <sub>2</sub> ]·H <sub>2</sub> O	$P1$	8	4(II), 1(IV-II), 1μ <sub>3</sub> -OH, H <sub>2</sub> O	177
		8	3(II), 2(IV-I), 3μ <sub>3</sub> -OH,	
		8	3(II), 1(IV-II), 2μ <sub>3</sub> -OH, H <sub>2</sub> O	
[Tb <sub>2</sub> (BDC) <sub>3</sub> (H <sub>2</sub> O) <sub>4</sub> ]	$P\bar{1}$	8	6(II), 2H <sub>2</sub> O	178
[Tm <sub>2</sub> (BDC) <sub>3</sub> (H <sub>2</sub> O) <sub>2</sub> ]	$C2/c$	7	6(II), H <sub>2</sub> O	179
·DMF·2C <sub>2</sub> H <sub>5</sub> OH·4H <sub>2</sub> O				
[Tm <sub>2</sub> (BDC) <sub>3</sub> (H <sub>2</sub> O)(DMF)]	$P\bar{1}$	7	6(II), H <sub>2</sub> O	179
·DMF·H <sub>2</sub> O				
		7	6(II), DMF	
[Er <sub>2</sub> (BDC) <sub>3</sub> (H <sub>2</sub> O) <sub>6</sub> ]	$P\bar{1}$	8	3(I), 1(III), 3H <sub>2</sub> O	180
[Er <sub>2</sub> (BDC) <sub>3</sub> (H <sub>2</sub> O) <sub>6</sub> ]·2H <sub>2</sub> O	$P2_1/c$	8	1(I), 2(II), 1(III), 3H <sub>2</sub> O	175
[Er <sub>2</sub> (BDC) <sub>3</sub> (H <sub>2</sub> O) <sub>6</sub> ]·2H <sub>2</sub> O	$C2/c$	8	1(I), 2(II), 1(III), 3H <sub>2</sub> O	175
[Er <sub>2</sub> (BDC) <sub>3</sub> (H <sub>2</sub> O) <sub>6</sub> ]·H <sub>2</sub> O	$P\bar{1}$	8	1(I), 2(II), 1(III), 3H <sub>2</sub> O	175
		8	2(II), 1(III), 4H <sub>2</sub> O	
[Er <sub>2</sub> (BDC) <sub>3</sub> ]·6H <sub>2</sub> O	$Pbca$	8	1(I), 5(II), 2H <sub>2</sub> O	181
		7	5(II), 2H <sub>2</sub> O	
		7	6(II), H <sub>2</sub> O	
[Er <sub>2</sub> (BDC) <sub>3</sub> (DMF) <sub>2</sub> ]	$C2/c$	7	6(II), DMF	182
[Er <sub>2</sub> (BDC) <sub>3</sub> (DMF) <sub>2</sub> (H <sub>2</sub> O) <sub>2</sub> ]	$P\bar{1}$	8	2(II), 2(III), DMF, H <sub>2</sub> O	183

Table 1.7.2: Reaction conditions used to synthesise lanthanide-organic frameworks given in Table 1.7.1

Name	Synthesis method	Reaction Conditions	
		Temperature / °C	Time
[Yb <sub>2</sub> (BDC) <sub>3</sub> (H <sub>2</sub> O) <sub>2</sub> ]	Hydrothermal	170	4 days
[Yb <sub>2</sub> (BDC) <sub>3</sub> (H <sub>2</sub> O) <sub>6</sub> ]	Hydrothermal	170	4 weeks
[Yb <sub>2</sub> (BDC) <sub>3</sub> (H <sub>2</sub> O) <sub>8</sub> ]·2H <sub>2</sub> O	Hydrothermal	160	4 weeks
[Lu <sub>2</sub> (BDC) <sub>3</sub> (H <sub>2</sub> O) <sub>8</sub> ]·2H <sub>2</sub> O	Hydrothermal	180	20 hours
[Er <sub>2</sub> (BDC) <sub>3</sub> (H <sub>2</sub> O) <sub>8</sub> ]·2H <sub>2</sub> O	TMOS gel	R.T.	Several weeks
[Yb <sub>3</sub> (BDC) <sub>4.5</sub> (DMF) <sub>2</sub> (H <sub>2</sub> O) <sub>3</sub> ]·2H <sub>2</sub> O	Solvothermal	60	6 days
[Yb <sub>3</sub> (BDC) <sub>3.5</sub> (OH) <sub>2</sub> (H <sub>2</sub> O) <sub>2</sub> ]·H <sub>2</sub> O	Hydrothermal	190	3 days
[Tb <sub>2</sub> (BDC) <sub>3</sub> (H <sub>2</sub> O) <sub>4</sub> ]	Hydrothermal	140	12 hours
[Tm <sub>2</sub> (BDC) <sub>3</sub> (H <sub>2</sub> O) <sub>2</sub> ] ·DMF·2C <sub>2</sub> H <sub>5</sub> OH·4H <sub>2</sub> O	Solvothermal	50	7 days
[Tm <sub>2</sub> (BDC) <sub>3</sub> (H <sub>2</sub> O)(DMF)]·DMF·H <sub>2</sub> O	Solvothermal	R.T.	6 weeks
[Er <sub>2</sub> (BDC) <sub>3</sub> (H <sub>2</sub> O) <sub>6</sub> ]	TEOS gel	R.T.	1 month
[Er <sub>2</sub> (BDC) <sub>3</sub> (H <sub>2</sub> O) <sub>6</sub> ]·2H <sub>2</sub> O	TMOS gel	R.T.	Several weeks
[Er <sub>2</sub> (BDC) <sub>3</sub> (H <sub>2</sub> O) <sub>6</sub> ]·2H <sub>2</sub> O	Agar gel	R.T.	Several weeks
[Er <sub>2</sub> (BDC) <sub>3</sub> (H <sub>2</sub> O) <sub>6</sub> ]·H <sub>2</sub> O	TEOS gel	R.T.	Several weeks
[Er <sub>2</sub> (BDC) <sub>3</sub> ]·6H <sub>2</sub> O	Hydrothermal	160	3 days
[Er <sub>2</sub> (BDC) <sub>3</sub> (DMF) <sub>2</sub> ]	Solvothermal	85	60 hours
[Er <sub>2</sub> (BDC) <sub>3</sub> (DMF) <sub>2</sub> (H <sub>2</sub> O) <sub>2</sub> ]	Solvothermal	80	40 hours

Zehnder *et al.* reported a series of [Yb<sub>2</sub>(BDC)<sub>3</sub>(H<sub>2</sub>O)<sub>x</sub>] (x = 2, 6, 8), illustrating the wide range of structures possible with a simple set of components.<sup>141</sup> These three lanthanide-organic frameworks exhibit structurally unrelated frameworks with [Yb<sub>2</sub>(BDC)<sub>3</sub>(H<sub>2</sub>O)<sub>2</sub>] assembling in a 3-D network with two crystallographically distinct ytterbium positions, [Yb<sub>2</sub>(BDC)<sub>3</sub>(H<sub>2</sub>O)<sub>6</sub>] forming 2-D layers linked by hydrogen bonds and [Yb<sub>2</sub>(BDC)<sub>3</sub>(H<sub>2</sub>O)<sub>8</sub>] consisting of 1-D chains that interact via hydrogen bonds. Erbium and lutetium analogues of [Yb<sub>2</sub>(BDC)<sub>3</sub>(H<sub>2</sub>O)<sub>8</sub>] have also been reported.<sup>175,185</sup>

The wide range of possible coordination modes in a single material was illustrated by Na *et al.* who described the structure of [Yb<sub>3</sub>(BDC)<sub>4.5</sub>(DMF)<sub>2</sub>(H<sub>2</sub>O)<sub>3</sub>]·2H<sub>2</sub>O that contains 8-



coordinated ytterbium in three distinct coordination environments.<sup>177</sup> Weng *et al.* reported the synthesis of  $[\text{Yb}_3(\text{BDC})_{3.5}(\text{OH})_2(\text{H}_2\text{O})_2]\cdot\text{H}_2\text{O}$  that also contains three unique coordination environments and the presence of bridging  $\mu^3\text{-OH}$ , rarely seen in lanthanide-organic frameworks.<sup>178</sup>

Analogous lanthanide-organic frameworks sharing the same framework connectivity albeit with differing coordinating solvents are seen for  $[\text{Tm}_2(\text{BDC})_3(\text{H}_2\text{O})_2]\cdot\text{DMF}\cdot 2\text{C}_2\text{H}_5\text{OH}\cdot 4\text{H}_2\text{O}$ ,  $[\text{Tm}_2(\text{BDC})_3(\text{H}_2\text{O})(\text{DMF})]\cdot\text{DMF}\cdot\text{H}_2\text{O}$ ,<sup>186</sup> and  $[\text{Er}_2(\text{BDC})_3(\text{DMF})_2]$ .<sup>183</sup> These three materials all share the same connectivity with 1-D lanthanide-carboxylate chains cross-linked by BDC to form 1-D diamond shaped channels. They differ, however, in the ratio of water to DMF with  $[\text{Tm}_2(\text{BDC})_3(\text{H}_2\text{O})_2]\cdot\text{DMF}\cdot 2\text{C}_2\text{H}_5\text{OH}\cdot 4\text{H}_2\text{O}$  and  $[\text{Er}_2(\text{BDC})_3(\text{DMF})_2]$  solely coordinating  $\text{H}_2\text{O}$  and DMF respectively and  $[\text{Tm}_2(\text{BDC})_3(\text{H}_2\text{O})(\text{DMF})]\cdot\text{DMF}\cdot\text{H}_2\text{O}$  coordinating water or DMF in a 1:1 ratio.

### 1.7.3. Applications of lanthanide-organic frameworks

The combination of inherent porosity and luminescent properties in lanthanide-organic frameworks have been shown to sensing of small organic molecules,<sup>187,188</sup> anions,<sup>189</sup> metal ions,<sup>112,190</sup> nitro-aromatics,<sup>96,191,192</sup> dyes,<sup>193,194</sup> and polyoxometalates<sup>195</sup> via changes in their photoluminescence spectra.

The luminescence properties of lanthanide-organic frameworks can be exploited for other means. White light emitting materials have attracted significant attraction due to their broad applications in displays and lighting. Although no lanthanide can emit white light, a combination of two or more lanthanides could produce an emissive profile close to that of white light through combination of red, green and blue emissions. Incorporating europium(III) and terbium(III) into the same material could achieve this result since these two lanthanides display red and blue, and green light respectively. This was used by Rao *et*

*al.* who doped ZJU-1,  $[\text{La}_2(\text{PDA})_3(\text{H}_2\text{O})_5]$  (PDA = pyridine-2,6-dicarboxylate), with small amounts of europium and terbium to form a series of colour tuneable lanthanide-organic frameworks.<sup>196</sup> Two of these doped materials displayed emissions close to the CIE (Commission Internationale de l'Eclairage) chromaticity values for pure white light.

The emissive profile of two lanthanides was used by Cui *et al.* to form a luminescent thermometer using the mixed-lanthanide  $[(\text{Eu}_{0.0069}\text{Tb}_{0.9931})_2(\text{DMBDC})_3(\text{H}_2\text{O})_4]\cdot\text{DMF}\cdot\text{H}_2\text{O}$  (DMBDC = 2,5-methoxy-1,4-benzenedicarboxylate).<sup>197</sup> At 10 K, the intensities of the  $^5\text{D}_4 \rightarrow ^7\text{F}_5$  ( $\text{Tb}^{3+}$ , 545 nm) and  $^5\text{D}_0 \rightarrow ^7\text{F}_2$  ( $\text{Eu}^{3+}$ , 613 nm) transitions are approximately equal in intensity. As the temperature increases, the europium emissions range constant whereas the terbium emissions diminish which leads to a gradual change in colour of the emissive profile from green to yellow to red over the range 10 to 300 K.

## 1.8. Aims of this work

The objective of this thesis were to use various X-ray diffraction techniques and other complementary studies to investigate the synthesis and crystallisation and properties of mixed-metal MIL-53, lanthanide-organic frameworks and other MOFs. MIL-53 can be synthesised using a range of metals and the properties of this material depend greatly on the metal used. Although the properties of single-metal MIL-53 have been extensively investigated, at the start of the work described herein, very little work had been done on mixed-metal analogues. It was hoped that by preparation of mixed-metal MIL-53 analogues their properties could be tuned from the single-metal materials. The synthesis and characterisation of these bimetallic materials and investigations into the effect of metal content on the properties were required to fully understand these systems. The work presented here aimed to investigate these effects.

Lanthanide-organic frameworks allow the combination of the unique properties of the lanthanide series with those of porous frameworks. Investigation of synthesis and thermal treatments are required to optimise the properties of these materials. Small changes to the synthesis of these materials can greatly change both the structure and the composition of the lanthanide-organic framework synthesised. Crystallisation of these materials can be investigated using both *in situ* and *ex situ* methods and may help to rationalise why solvent and temperature have such an effect on the lanthanide-organic framework formed. The combined use of temperature-resolved XRD and thermogravimetric analysis allows for greater understanding of the thermal decomposition of these materials. An extensive study of two lanthanide-organic frameworks formed through mediation of the reaction solvent is presented in this thesis.

Some of the work presented here in the thesis was performed as part of the MACADEMIA project (MOFS as Catalysts and Adsorbants: Discovery and Engineering of Materials for Industrial Applications). MACADEMIA was part of the European Community's Seventh Framework Programme (FP7/2007-2013). The Walton research group at the University of Warwick were responsible for the synthesis and characterisation of new MOF materials, particularly using *in situ* X-ray diffraction methods. Characterisation of these materials was aided by collaborations with other members of the MACADEMIA project. The results of these additional characterisation techniques will be summarised where relevant.

## 1.9. References

- (1) Chae, H. K.; Siberio-Perez, D. Y.; Kim, J.; Go, Y.; Eddaoudi, M.; Matzger, A. J.; O'Keeffe, M.; Yaghi, O. M. *Nature* **2004**, 427, 523.
- (2) Furukawa, H.; Go, Y. B.; Ko, N.; Park, Y. K.; Uribe-Romo, F. J.; Kim, J.; O'Keeffe, M.; Yaghi, O. M. *Inorg. Chem.* **2011**, 50, 9147.
- (3) Schröder, M. *Functional metal-organic frameworks : gas storage, separation and catalysis*; Springer: Heidelberg, 2010.
- (4) Batten, S. R.; Neville, S. M.; Turner, D. R. *Coordination polymers : design, analysis and application*; RSC Pub.: Cambridge, 2009.
- (5) Farrusseng, D. *Metal-organic frameworks : applications from catalysis to gas storage*; Wiley-VCH: Weinheim, 2011.
- (6) Furukawa, H.; Cordova, K. E.; O'Keeffe, M.; Yaghi, O. M. *Science* **2013**, 341.
- (7) Schneemann, A.; Bon, V.; Schwedler, I.; Senkovska, I.; Kaskel, S.; Fischer, R. A. *Chem. Soc. Rev.* **2014**, 43, 6062.
- (8) Batten, S. R.; Champness, N. R.; Chen, X. M.; Garcia-Martinez, J.; Kitagawa, S.; Ohrstrom, L.; O'Keeffe, M.; Suh, M. P.; Reedijk, J. *Pure Appl. Chem.* **2013**, 85, 1715.
- (9) Feng, S. *Acta Crystallogr., Sect. E: Struct. Rep. Online* **2009**, 66, m33.
- (10) Yaghi, O. M.; O'Keeffe, M.; Ockwig, N. W.; Chae, H. K.; Eddaoudi, M.; Kim, J. *Nature* **2003**, 423, 705.
- (11) Serre, C.; Millange, F.; Thouvenot, C.; Nogues, M.; Marsolier, G.; Louer, D.; Ferey, G. *J. Am. Chem. Soc.* **2002**, 124, 13519.
- (12) Katz, M. J.; Brown, Z. J.; Colon, Y. J.; Siu, P. W.; Scheidt, K. A.; Snurr, R. Q.; Hupp, J. T.; Farha, O. K. *Chem. Commun.* **2013**, 49, 9449.
- (13) Mohideen, M. I. H.; Xiao, B.; Wheatley, P. S.; McKinlay, A. C.; Li, Y.; Slawin, A. M. Z.; Aldous, D. W.; Cessford, N. F.; Düren, T.; Zhao, X.; Gill, R.; Thomas, K. M.; Griffin, J. M.; Ashbrook, S. E.; Morris, R. E. *Nat Chem* **2011**, 3, 304.
- (14) Cheng, X.; Zhang, A.; Hou, K.; Liu, M.; Wang, Y.; Song, C.; Zhang, G.; Guo, X. *Dalton Trans.* **2013**, 42, 13698.
- (15) Cheetham, A. K.; Rao, C. N. R.; Feller, R. K. *Chem. Commun.* **2006**, 4780.
- (16) Covington, A. D. *Chem. Soc. Rev.* **1997**, 26, 111.
- (17) Zuckerman, J. J.; Hagen, A. P. *Inorganic reactions and methods*; Deerfield Beach.
- (18) Hofmann, K. A. K. Z. *Z. Anorg. Chem.* **1897**, 15, 204.
- (19) Rayner, J. H.; Powell, H. M. *J. Chem. Soc.* **1952**, 319.
- (20) Hoskins, B. F.; Robson, R. *J. Am. Chem. Soc.* **1989**, 111, 5962.
- (21) Hoskins, B. F.; Robson, R. *J. Am. Chem. Soc.* **1990**, 112, 1546.
- (22) Abrahams, B. F.; Hoskins, B. F.; Liu, J. P.; Robson, R. *J. Am. Chem. Soc.* **1991**, 113, 3045.
- (23) Robson, R.; Abrahams, B. F.; Batten, S. R.; Gable, R. W.; Hoskins, B. F.; Liu, J. P. *ACS Symp. Ser.* **1992**, 499, 256.
- (24) Yaghi, O. M.; Li, G. M.; Li, H. L. *Nature* **1995**, 378, 703.
- (25) Tranchemontagne, D. J.; Mendoza-Cortes, J. L.; O'Keeffe, M.; Yaghi, O. M. *Chem. Soc. Rev.* **2009**, 38, 1257.
- (26) Czaja, A. U.; Trukhan, N.; Muller, U. *Chem. Soc. Rev.* **2009**, 38, 1284.
- (27) Park, K. S.; Ni, Z.; Côté, A. P.; Choi, J. Y.; Huang, R.; Uribe-Romo, F. J.; Chae, H. K.; O'Keeffe, M.; Yaghi, O. M. *Proc. Natl. Acad. Sci. U. S. A.* **2006**, 103, 10186.
- (28) Park, Y. K.; Choi, S. B.; Nam, H. J.; Jung, D.-Y.; Ahn, H. C.; Choi, K.; Furukawa, H.; Kim, J. *Chem. Commun.* **2010**, 46, 3086.
- (29) Lan, Y.-Q.; Jiang, H.-L.; Li, S.-L.; Xu, Q. *Adv. Mater. (Weinheim, Ger.)* **2011**, 23, 5015.

- (30) Plaza, M. G.; Ribeiro, A. M.; Ferreira, A.; Santos, J. C.; Hwang, Y. K.; Seo, Y. K.; Lee, U. H.; Chang, J. S.; Loureiro, J. M.; Rodrigues, A. E. *Microporous Mesoporous Mater.* **2012**, *153*, 178.
- (31) Senapati, S.; Zimdars, J.; Ren, J.; Koller, H. *J. Mater. Chem.* **2014**, *2*, 10470.
- (32) Pardo, E.; Train, C.; Gontard, G.; Boubekur, K.; Fabelo, O.; Liu, H. B.; Dkhil, B.; Lloret, F.; Nakagawa, K.; Tokoro, H.; Ohkoshi, S.; Verdaguer, M. *J. Am. Chem. Soc.* **2011**, *133*, 15328.
- (33) Ferey, G. *Chem. Soc. Rev.* **2008**, *37*, 191.
- (34) Forster, P. M.; Thomas, P. M.; Cheetham, A. K. *Chem. Mater.* **2002**, *14*, 17.
- (35) Garay, A. L.; Pichon, A.; James, S. L. *Chem. Soc. Rev.* **2007**, *36*, 846.
- (36) Zacher, D.; Shekhah, O.; Woell, C.; Fischer, R. A. *Chem. Soc. Rev.* **2009**, *38*, 1418.
- (37) McKinsty, C.; Cussen, E. J.; Fletcher, A. J.; Patwardhan, S. V.; Sefcik, J. *Cryst. Growth Des.* **2013**.
- (38) Ahnfeldt, T.; Gunzelmann, D.; Loiseau, T.; Hirsemann, D.; Senker, J.; Ferey, G.; Stock, N. *Inorg. Chem.* **2009**, *48*, 3057.
- (39) Yaghi, O. M. *Abstr. Pap. Am. Chem. Soc.* **2002**, *223*, A35.
- (40) Biswas, S.; Vanpoucke, D. E. P.; Verstraelen, T.; Vandichel, M.; Couck, S.; Leus, K.; Liu, Y.-Y.; Waroquier, M.; Van Speybroeck, V.; Denayer, J. F. M.; Van Der Voort, P. *J. Phys. Chem. C* **2013**, *117*, 22784.
- (41) Eddaoudi, M.; Kim, J.; Rosi, N.; Vodak, D.; Wachter, J.; O'Keeffe, M.; Yaghi, O. M. *Science* **2002**, *295*, 469.
- (42) Ma, B.-Q.; Mulfort, K. L.; Hupp, J. T. *Inorg. Chem.* **2005**, *44*, 4912.
- (43) Burrows, A. D. *CrystEngComm* **2011**, *13*, 3623.
- (44) Chun, H.; Dybtsev, D. N.; Kim, H.; Kim, K. *Chem. Eur. J.* **2005**, *11*, 3521.
- (45) Deng, H. X.; Doonan, C. J.; Furukawa, H.; Ferreira, R. B.; Towne, J.; Knobler, C. B.; Wang, B.; Yaghi, O. M. *Science* **2010**, *327*, 846.
- (46) Seo, J. S.; Whang, D.; Lee, H.; Jun, S. I.; Oh, J.; Jeon, Y. J.; Kim, K. *Nature* **2000**, *404*, 982.
- (47) Smalley, A. P.; Reid, D. G.; Tan, J. C.; Lloyd, G. O. *CrystEngComm* **2013**, *15*, 9368.
- (48) Rood, J. A.; Noll, B. C.; Henderson, K. W. *Main Group Chem.* **2009**, *8*, 237.
- (49) Bernt, S.; Guillerm, V.; Serre, C.; Stock, N. *Chem. Commun.* **2011**, *47*, 2838.
- (50) Sun, F.; Yin, Z.; Wang, Q.-Q.; Sun, D.; Zeng, M.-H.; Kurmoo, M. *Angew. Chem., Int. Ed.* **2013**, *52*, 4538.
- (51) Morris, W.; Doonan, C. J.; Furukawa, H.; Banerjee, R.; Yaghi, O. M. *J. Am. Chem. Soc.* **2008**, *130*, 12626.
- (52) Wang, Z.; Liu, J.; Arslan, H. K.; Grosjean, S.; Hagendorn, T.; Gliemann, H.; Braese, S.; Woell, C. *Langmuir* **2013**, *29*, 15958.
- (53) Zhu, W.; He, C.; Wu, X.; Duan, C. *Inorg. Chem. Commun.* **2014**, *39*, 83.
- (54) Wang, X.-S.; Ma, S.; Sun, D.; Parkin, S.; Zhou, H.-C. *J. Am. Chem. Soc.* **2006**, *128*, 16474.
- (55) Arnanz, A.; Pintado-Sierra, M.; Corma, A.; Iglesias, M.; Sánchez, F. *Adv. Synth. Catal.* **2012**, *354*, 1347.
- (56) Burrows, A. D.; Keenan, L. L. *CrystEngComm* **2012**, *14*, 4112.
- (57) Chen, C.; Allen, C. A.; Cohen, S. M. *Inorg. Chem.* **2011**, *50*, 10534.
- (58) Hindelang, K.; Vagin, S. I.; Anger, C.; Rieger, B. *Chem. Commun.* **2012**, *48*, 2888.
- (59) Jiang, D.; Keenan, L. L.; Burrows, A. D.; Edler, K. J. *Chem. Commun.* **2012**, *48*, 12053.
- (60) Lee, Y.-R.; Chung, Y.-M.; Ann, W.-S. *Rsc Advances* **2014**, *4*, 23064.

- (61) Kitagawa, S.; Uemura, K. *Chem. Soc. Rev.* **2005**, *34*, 109.
- (62) Khosrovani, N.; Sleight, A. W. *J. Solid State Chem.* **1996**, *121*, 2.
- (63) Ferey, G.; Parmentier, J. *Eur. J. Solid State Inorg. Chem.* **1994**, *31*, 697.
- (64) Surble, S.; Serre, C.; Mellot-Draznieks, C.; Millange, F.; Ferey, G. *Chem. Commun.* **2006**, 284.
- (65) Mellot-Draznieks, C.; Serre, C.; Surble, S.; Audebrand, N.; Ferey, G. *J. Am. Chem. Soc.* **2005**, *127*, 16273.
- (66) Carson, F.; Su, J.; Platero-Prats, A. E.; Wan, W.; Yun, Y.; Samain, L.; Zou, X. *Cryst. Growth Des.* **2013**.
- (67) Guillou, N.; Millange, F.; Walton, R. I. *Chem. Commun.* **2011**, *47*, 713.
- (68) Walton, R. I.; Munn, A. S.; Guillou, N.; Millange, F. *Chem. Eur. J.* **2011**, *17*, 7069.
- (69) Horcajada, P.; Serre, C.; Maurin, G.; Ramsahye, N. A.; Balas, F.; Vallet-Regi, M.; Sebban, M.; Taulelle, F.; Ferey, G. *J. Am. Chem. Soc.* **2008**, *130*, 6774.
- (70) Bourrelly, S.; Llewellyn, P. L.; Serre, C.; Millange, F.; Loiseau, T.; Ferey, G. *J. Am. Chem. Soc.* **2005**, *127*, 13519.
- (71) Lupu, D.; Ardelean, O.; Blanita, G.; Borodi, G.; Lazar, M. D.; Biris, A. R.; Ioan, C.; Mihet, M.; Misan, I.; Popeneciu, G. *Int. J. Hydrogen Energy* **2011**, *36*, 3586.
- (72) Ramsahye, N. A.; Maurin, G.; Bourrelly, S.; Llewellyn, P. L.; Devic, T.; Serre, C.; Loiseau, T.; Ferey, G. *Adsorption* **2007**, *13*, 461.
- (73) Vimont, A.; Travert, A.; Bazin, P.; Lavalley, J. C.; Daturi, M.; Serre, C.; Ferey, G.; Bourrelly, S.; Llewellyn, P. L. *Chem. Commun.* **2007**, 3291.
- (74) Collins, D. J.; Zhou, H.-C. *J. Mater. Chem.* **2007**, *17*, 3154.
- (75) Furukawa, H.; Ko, N.; Go, Y. B.; Aratani, N.; Choi, S. B.; Choi, E.; Yazaydin, A. O.; Snurr, R. Q.; O'Keeffe, M.; Kim, J.; Yaghi, O. M. *Science* **2010**, *329*, 424.
- (76) Jhung, S. H.; Khan, N. A.; Hasan, Z. *CrystEngComm* **2012**, *14*, 7099.
- (77) Klebanoff, L. E.; Keller, J. O. *Int. J. Hydrogen Energy* **2013**, *38*, 4533.
- (78) Lim, D.-W.; Chyun, S. A.; Suh, M. P. *Angew. Chem. Int. Ed.* **2014**, *53*, 7819.
- (79) Li, J.-R.; Kuppler, R. J.; Zhou, H.-C. *Chem. Soc. Rev.* **2009**, *38*, 1477.
- (80) Maji, T. K.; Uemura, K.; Chang, H.-C.; Matsuda, R.; Kitagawa, S. *Angew. Chem. Int. Ed.* **2004**, *43*, 3269.
- (81) Chen, B.; Ma, S.; Hurtado, E. J.; Lobkovsky, E. B.; Zhou, H.-C. *Inorg. Chem.* **2007**, *46*, 8490.
- (82) Xie, S.; Yuan, L. *Prog. Chem.* **2013**, *25*, 1763.
- (83) Bae, Y.-S.; Lee, C. Y.; Kim, K. C.; Farha, O. K.; Nickias, P.; Hupp, J. T.; Nguyen, S. T.; Snurr, R. Q. *Angew. Chem. Int. Ed.* **2012**, *51*, 1857.
- (84) Ghosh, S. K.; Bureekaew, S.; Kitagawa, S. *Angew. Chem. Int. Ed.* **2008**, *47*, 3403.
- (85) Alaerts, L.; Kirschhock, C. E. A.; Maes, M.; van der Veen, M. A.; Finsy, V.; Depla, A.; Martens, J. A.; Baron, G. V.; Jacobs, P. A.; Denayer, J. E. M.; De Vos, D. E. *Angew. Chem. Int. Ed.* **2007**, *46*, 4293.
- (86) Alaerts, L.; Maes, M.; Giebel, L.; Jacobs, P. A.; Martens, J. A.; Denayer, J. E. M.; Kirschhock, C. E. A.; De Vos, D. E. *J. Am. Chem. Soc.* **2008**, *130*, 14170.
- (87) El Osta, R.; Carlin-Sinclair, A.; Guillou, N.; Walton, R. I.; Vermoortele, F.; Maes, M.; de Vos, D.; Millange, F. *Chem. Mater.* **2012**, *24*, 2781.
- (88) Van de Voorde, B.; Munn, A. S.; Guillou, N.; Millange, F.; De Vos, D. E.; Walton, R. I. *Phys. Chem. Chem. Phys.* **2013**, *15*, 8606.
- (89) Daramola, M. O.; Burger, A. J.; Pera-Titus, M.; Giroir-Fendler, A.; Miachon, S.; Dalmon, J. A.; Lorenzen, L. *Asia-Pac. J. Chem. Eng.* **2010**, *5*, 815.
- (90) Zhang, L.; Zhang, J.; Li, Z. J.; Qin, Y. Y.; Lin, Q. P.; Yao, Y. G. *Chem. Eur. J.* **2009**, *15*, 989.

- (91) He, J. H.; Zhang, G. J.; Xiao, D. R.; Chen, H. Y.; Yan, S. W.; Wang, X.; Yang, J.; Yuan, R.; Wang, E. B. *J. Mol. Struct.* **2012**, *1018*, 131.
- (92) Chen, B.; Zhao, X.; Putkham, A.; Hong, K.; Lobkovsky, E. B.; Hurtado, E. J.; Fletcher, A. J.; Thomas, K. M. *J. Am. Chem. Soc.* **2008**, *130*, 6411.
- (93) Noguchi, D.; Tanaka, H.; Kondo, A.; Kajiro, H.; Noguchi, H.; Ohba, T.; Kanoh, H.; Kaneko, K. *J. Am. Chem. Soc.* **2008**, *130*, 6367.
- (94) Li, Y.; Zhang, S. S.; Song, D. T. *Angew. Chem. Int. Ed.* **2013**, *52*, 710.
- (95) Wang, Y. P.; Wang, F.; Luo, D. F.; Zhou, L.; Wen, L. L. *Inorg. Chem. Commun.* **2012**, *19*, 43.
- (96) Meilikhov, M.; Yusenko, K.; Esken, D.; Turner, S.; Van Tendeloo, G.; Fischer, R. A. *Eur. J. Inorg. Chem.* **2010**, 3701.
- (97) Hermes, S.; Schroter, M. K.; Schmid, R.; Khodeir, L.; Muhler, M.; Tissler, A.; Fischer, R. W.; Fischer, R. A. *Angew. Chem. Int. Ed.* **2005**, *44*, 6237.
- (98) Zlotea, C.; Campesi, R.; Cuevas, F.; Leroy, E.; Dibandjo, P.; Volkringer, C.; Loiseau, T.; Ferey, G.; Latroche, M. *J. Am. Chem. Soc.* **2010**, *132*, 2991.
- (99) Esken, D.; Zhang, X.; Lebedev, O. I.; Schroeder, F.; Fischer, R. A. *J. Mater. Chem.* **2009**, *19*, 1314.
- (100) Schroeder, F.; Esken, D.; Cokoja, M.; van den Berg, M. W. E.; Lebedev, O. I.; van Tendeloo, G.; Walaszek, B.; Buntkowsky, G.; Limbach, H.-H.; Chaudret, B.; Fischer, R. A. *J. Am. Chem. Soc.* **2008**, *130*, 6119.
- (101) Houk, R. J. T.; Jacobs, B. W.; El Gabaly, F.; Chang, N. N.; Talin, A. A.; Graham, D. D.; House, S. D.; Robertson, I. M.; Allendorf, M. D. *Nano Lett.* **2009**, *9*, 3413.
- (102) Jacobs, B. W.; Houk, R. J. T.; Anstey, M. R.; House, S. D.; Robertson, I. M.; Talin, A. A.; Allendorf, M. D. *Chem. Sci.* **2011**, *2*, 411.
- (103) Ishida, T.; Kawakita, N.; Akita, T.; Haruta, M. *Gold Bull.* **2009**, *42*, 267.
- (104) Ishida, T.; Nagaoka, M.; Akita, T.; Haruta, M. *Chem. Eur. J.* **2008**, *14*, 8456.
- (105) Opelt, S.; Tuerk, S.; Dietzsch, E.; Henschel, A.; Kaskel, S.; Klemm, E. *Catal. Commun.* **2008**, *9*, 1286.
- (106) Schroder, F.; Henke, S.; Zhang, X. N.; Fischer, R. A. *Eur. J. Inorg. Chem.* **2009**, 3131.
- (107) El-Shall, M. S.; Abdelsayed, V.; Khder, A. E. R. S.; Hassan, H. M. A.; El-Kaderi, H. M.; Reich, T. E. *J. Mater. Chem.* **2009**, *19*, 7625.
- (108) Ferey, G.; Millange, F.; Morcrette, M.; Serre, C.; Doublet, M. L.; Greneche, J. M.; Tarascon, J. M. *Angew. Chem. Int. Ed.* **2007**, *46*, 3259.
- (109) Karabach, Y. Y.; da Silva, M. F. C. G.; Kopylovich, M. N.; Gil-Hernandez, B.; Sanchiz, J.; Kirillov, A. M.; Pombeiro, A. J. L. *Inorg. Chem.* **2010**, *49*, 11096.
- (110) Zhang, Y. D.; Zhang, S. H.; Ge, C. M.; Wang, Y. G.; Huang, Y. H.; Li, H. P. *Synthesis and Reactivity in Inorganic Metal-Organic and Nano-Metal Chemistry* **2013**, *43*, 990.
- (111) Dang, S.; Ma, E.; Sun, Z. M.; Zhang, H. J. *J. Mater. Chem.* **2012**, *22*, 16920.
- (112) Brozek, C. K.; Cozzolino, A. F.; Teat, S. J.; Chen, Y.-S.; Dincă, M. *Chem. Mater.* **2013**.
- (113) Li, B.; Chen, X.; Yu, F.; Yu, W.; Zhang, T.; Sun, D. *Cryst. Growth Des.* **2014**, *14*, 410.
- (114) Sudik, A. C.; Cote, A. P.; Yaghi, O. M. *Inorg. Chem.* **2005**, *44*, 2998.
- (115) Katsoulis, D. E. *Chem. Rev.* **1998**, *98*, 359.
- (116) Ribeiro, S.; Barbosa, A. D. S.; Gomes, A. C.; Pillinger, M.; Goncalves, I. S.; Cunha-Silva, L.; Balula, S. S. *Fuel Process. Technol.* **2013**, *116*, 350.
- (117) Bajpe, S. R.; Breynaert, E.; Mustafa, D.; Jobbagy, M.; Maes, A.; Martens, J. A.; Kirschhock, C. E. A. *J. Mater. Chem.* **2011**, *21*, 9768.
- (118) Miras, H. N.; Vila-Nadal, L.; Cronin, L. *Chem. Soc. Rev.* **2014**, *43*, 5679.

- (119) Wang, N.; Yue, S. T.; Wu, H. Y.; Li, Z. Y.; Li, X. X.; Liu, Y. L. *Inorg. Chim. Acta* **2010**, 363, 1008.
- (120) Zheng, S.-T.; Zhang, J.; Yang, G.-Y. *Angew. Chem. Int. Ed.* **2008**, 47, 3909.
- (121) Zhang, H.; Duan, L.; Lan, Y.; Wang, E.; Hu, C. *Inorg. Chem.* **2003**, 42, 8053.
- (122) Feng, D.; Chung, W.-C.; Wei, Z.; Gu, Z.-Y.; Jiang, H.-L.; Darensbourg, D. J.; Zhou, H.-C. *J. Am. Chem. Soc.* **2013**.
- (123) Zou, C.; Xie, M.-H.; Kong, G.-Q.; Wu, C.-D. *CrystEngComm* **2012**, 14, 4850.
- (124) Li, D. J.; Mo, L. Q.; Wang, Q. M. *Inorg. Chem. Commun.* **2011**, 14, 1128.
- (125) Kaye, S. S.; Long, J. R. *J. Am. Chem. Soc.* **2007**, 130, 806.
- (126) Evans, J. D.; Sumbly, C. J.; Doonan, C. J. *Chem. Soc. Rev.* **2014**, 43, 5933.
- (127) Lian, Q. Y.; Huang, C. D.; Zeng, R. H.; Qiu, Y. C.; Mou, J. X.; Deng, H.; Zeller, M. Z. *Anorg. Allg. Chem.* **2009**, 635, 393.
- (128) Zhu, L. C.; Zhao, Y.; Yu, S. J.; Zhao, M. M. *Inorg. Chem. Commun.* **2010**, 13, 1299.
- (129) Yue, S. T.; Wei, Z. Q.; Wang, N.; Liu, W. J.; Zhao, X.; Chang, L. M.; Liu, Y. L.; Mo, H. H.; Cai, Y. P. *Inorg. Chem. Commun.* **2011**, 14, 1396.
- (130) Liu, W. J.; Li, Z. Y.; Wang, N.; Li, X. X.; Wei, Z. Q.; Yue, S. T.; Liu, Y. L. *CrystEngComm* **2011**, 13, 138.
- (131) Liang, L.; Li, G. Z.; Sun, L.; Lan, G. Q.; Zhang, L. M.; Yang, C. F.; Ma, Y. Z.; Deng, H. *Inorg. Chem. Commun.* **2012**, 20, 295.
- (132) Thuery, P. *CrystEngComm* **2008**, 10, 1126.
- (133) Mihalcea, I.; Volkringer, C.; Henry, N.; Loiseau, T. *Inorg. Chem.* **2012**.
- (134) Stork, J. R.; Thoi, V. S.; Cohen, S. M. *Inorg. Chem.* **2007**, 46, 11213.
- (135) Chen, J. X.; Liu, Z. C.; Yu, T.; Chen, Z. X.; Sun, J. Y.; Weng, L. H.; Tu, B.; Zhao, D. Y. *Chem. Lett.* **2003**, 32, 474.
- (136) Lu, H.; Li, F.; Yuan, D. Q.; Cao, R. *Polyhedron* **2007**, 26, 2979.
- (137) Chen, S. C.; Zhang, Z. H.; Zhou, Y. S.; Zhou, W. Y.; Li, Y. Z.; He, M. Y.; Chen, Q.; Du, M. *Cryst. Growth Des.* **2011**, 11, 4190.
- (138) Serre, C.; Millange, F.; Thouvenot, C.; Gardant, N.; Pelle, F.; Férey, G. J. *Mater. Chem.* **2004**, 14, 1540.
- (139) Cahill, C. L.; de Lill, D. T.; Frisch, M. *CrystEngComm* **2007**, 9, 15.
- (140) Zehnder, R. A.; Renn, R. A.; Pippin, E.; Zeller, M.; Wheeler, K. A.; Carr, J. A.; Fontaine, N.; McMullen, N. C. *J. Mol. Struct.* **2011**, 985, 109.
- (141) Takashima, Y.; Martinez, V. M.; Furukawa, S.; Kondo, M.; Shimomura, S.; Uehara, H.; Nakahama, M.; Sugimoto, K.; Kitagawa, S. *Nature Commun.* **2011**, 2.
- (142) White, K. A.; Chengelis, D. A.; Gogick, K. A.; Stehman, J.; Rosi, N. L.; Petoud, S. p. *J. Am. Chem. Soc.* **2009**, 131, 18069.
- (143) Haquin, V.; Gummy, F.; Daiguebonne, C.; Bunzli, J. C.; Guillou, O. *Eur. J. Inorg. Chem.* **2009**, 4491.
- (144) Munn, A. S.; Clarkson, G. J.; Millange, F.; Dumont, Y.; Walton, R. I. *CrystEngComm* **2013**, 15, 9679.
- (145) Wang, L. J.; Deng, H.; Furukawa, H.; Gandara, F.; Cordova, K. E.; Peri, D.; Yaghi, O. M. *Inorg. Chem.* **2014**, 53, 5881.
- (146) Barthelet, K.; Marrot, J.; Riou, D.; Férey, G. *Angew. Chem. Int. Ed.* **2001**, 41, 281.
- (147) Whitfield, T. R.; Wang, X. Q.; Liu, L. M.; Jacobson, A. J. *Solid State Sci.* **2005**, 7, 1096.
- (148) Mowat, J. P. S. M. J. P. S.; Miller, S. R.; Slawin, A. M. Z.; Seymour, V. R.; Ashbrook, S. E.; Wright, P. A. *Microporous Mesoporous Mater.* **2011**, 142, 322.
- (149) Loiseau, T.; Serre, C.; Huguenard, C.; Fink, G.; Taulelle, F.; Henry, M.; Bataille, T.; Férey, G. *Chem. Eur. J.* **2004**, 10, 1373.



- (150) Volkringer, C.; Loiseau, T.; Guillou, N.; Ferey, G.; Elkaim, E.; Vimont, A. *Dalton Trans.* **2009**, 2241.
- (151) Anokhina, E. V.; Vougo-Zanda, M.; Wang, X. Q.; Jacobson, A. J. *J. Am. Chem. Soc.* **2005**, 127, 15000.
- (152) Guillou, N.; Walton, R. I.; Millange, F. Z. *Kristallogr.* **2010**, 225, 552.
- (153) Liu, L.; Wang, X.; Jacobson, A. J. *Dalton Trans.* **2010**, 39, 1722.
- (154) Leclerc, H.; Devic, T.; Devautour-Vinot, S.; Bazin, P.; Audebrand, N.; Ferey, G.; Daturi, M.; Vimont, A.; Clet, G. *J. Phys. Chem. C* **2011**, 115, 19828.
- (155) Millange, F.; Guillou, N.; Walton, R. I.; Greneche, J.-M.; Margiolaki, I.; Férey, G. *Chem. Commun.* **2008**, 4732.
- (156) Liu, Y.; Her, J.-H.; Dailly, A.; Ramirez-Cuesta, A. J.; Neumann, D. A.; Brown, C. M. *J. Am. Chem. Soc.* **2008**, 130, 11813.
- (157) Liu, G. X.; Wang, Y.; Huang, L. F.; Kong, X. J.; Chen, H. J. *Inorg. Organomet. Polym. Mater.* **2008**, 18, 358.
- (158) Xu, G.; Zhang, X.; Guo, P.; Pan, C.; Zhang, H.; Wang, C. *J. Am. Chem. Soc.* **2010**, 132, 3656.
- (159) Medina, M. E.; Dumont, Y.; Greneche, J. M.; Millange, F. *Chem. Commun.* **2010**, 46, 7987.
- (160) Devic, T.; Horcajada, P.; Serre, C.; Salles, F.; Maurin, G.; Moulin, B.; Heurtaux, D.; Clet, G.; Vimont, A.; Greneche, J. M.; Le Ouay, B.; Moreau, F.; Magnier, E.; Filinchuk, Y.; Marrot, J.; Lavalley, J. C.; Daturi, M.; Ferey, G. *J. Am. Chem. Soc.* **2010**, 132, 1127.
- (161) Whitfield, T. R.; Wang, X. Q.; Jacobson, A. J. *MRS Proceedings*, **2003**; Vol. 755, 191.
- (162) Nouar, F.; Devic, T.; Chevreau, H.; Guillou, N.; Gibson, E.; Clet, G.; Daturi, M.; Vimont, A.; Greneche, J. M.; Breeze, M. I.; Walton, R. I.; Llewellyn, P. L.; Serre, C. *Chem. Commun.* **2012**, 48, 10237.
- (163) Mendt, M.; Jee, B.; Stock, N.; Ahnfeldt, T.; Hartmann, M.; Himsl, D.; Poppl, A. *J. Phys. Chem. C* **2010**, 114, 19443.
- (164) Kozachuk, O.; Meilikhov, M.; Yusenko, K.; Schneemann, A.; Jee, B.; Kuttatheyil, A. V.; Bertmer, M.; Sternemann, C.; Poepl, A.; Fischer, R. A. *Eur. J. Inorg. Chem.* **2013**, 2013, 4546.
- (165) Chandler, B. D.; Yu, J. O.; Cramb, D. T.; Shimizu, G. K. H. *Chem. Mater.* **2007**, 19, 4467.
- (166) Cheng, J. W.; Zheng, S. T.; Yang, G. Y. *Inorg. Chem.* **2007**, 46, 10261.
- (167) Huang, Y. G.; Wu, B. L.; Yuan, D. Q.; Xu, Y. Q.; Jiang, F. L.; Hong, M. C. *Inorg. Chem.* **2007**, 46, 1171.
- (168) Millange, F.; Serre, C.; Marrot, J.; Gardant, N.; Pelle, F.; Ferey, G. *J. Mater. Chem.* **2004**, 14, 642.
- (169) Serre, C.; Millange, F.; Thouvenot, C.; Gardant, N.; Pelle, F.; Ferey, G. *J. Mater. Chem.* **2004**, 14, 1540.
- (170) Serre, C.; Pelle, F.; Gardant, N.; Ferey, G. *Chem. Mater.* **2004**, 16, 1177.
- (171) Serre, C.; Stock, N.; Bein, T.; Ferey, G. *Inorg. Chem.* **2004**, 43, 3159.
- (172) Wang, C.; Xie, Z. G.; deKrafft, K. E.; Lin, W. B. *ACS Appl. Mater. Interfaces* **2012**, 4, 2288.
- (173) Eliseeva, S. V.; Bunzli, J.-C. G. *Chem. Soc. Rev.* **2010**, 39, 189.
- (174) Wang, P.; Li, Z. F.; Song, L. P.; Wang, C. X.; Chen, Y. *Acta Crystallogr., Sect. E: Struct. Rep. Online* **2006**, 62, M253.
- (175) Daiguebonne, C.; Kerbellec, N.; Bernot, K.; Gérault, Y.; Deluzet, A.; Guillou, O. *Inorg. Chem.* **2006**, 45, 5399.

- (176) Na, L.; Hua, R.; Zhang, L.; Zhang, W.; Ning, G. *J. Chem. Crystallogr.* **2009**, *39*, 688.
- (177) Weng, D.; Zheng, X.; Jin, L. *Eur. J. Inorg. Chem.* **2006**, *2006*, 4184.
- (178) Reineke, T. M.; Eddaoudi, M.; Fehr, M.; Kelley, D.; Yaghi, O. M. *J. Am. Chem. Soc.* **1999**, *121*, 1651.
- (179) He, H.; Ma, H.; Sun, D.; Zhang, L.; Wang, R.; Sun, D. *Cryst. Growth Des.* **2013**, *13*, 3154.
- (180) Deluzet, A.; Maudez, W.; Daiguebonne, C.; Guillou, O. *Cryst. Growth Des.* **2003**, *3*, 475.
- (181) Pan, L.; Zheng, N.; Wu, Y.; Han, S.; Yang, R.; Huang, X.; Li, J. *Inorg. Chem.* **2001**, *40*, 828.
- (182) Zhang, Y.; Yang, J.; Li, G. D.; Zhang, F.; Chen, J. S. *J. Coord. Chem.* **2008**, *61*, 945.
- (183) Chen, B.; Yang, Y.; Zapata, F.; Qian, G.; Luo, Y.; Zhang, J.; Lobkovsky, E. B. *Inorg. Chem.* **2006**, *45*, 8882.
- (184) Daiguebonne, C.; Kerbellec, N.; Guillou, O.; Bünzli, J.-C.; Gumy, F.; Catala, L.; Mallah, T.; Audebrand, N.; Gérault, Y.; Bernot, K.; Calvez, G. *Inorg. Chem.* **2008**, *47*, 3700.
- (185) He, H. Y.; Ma, H. Q.; Sun, D.; Zhang, L. L.; Wang, R. M.; Sun, D. F. *Cryst. Growth Des.* **2013**, *13*, 3154.
- (186) Wan, X.; Song, H.; Zhao, D.; Zhang, L.; Lv, Y. *Sens. Actuators, B* **2014**, *201*, 413.
- (187) Guo, Z.; Xu, H.; Su, S.; Cai, J.; Dang, S.; Xiang, S.; Qian, G.; Zhang, H.; O'Keeffe, M.; Chen, B. *Chem. Commun.* **2011**, *47*, 5551.
- (188) Chen, B.; Wang, L.; Zapata, F.; Qian, G.; Lobkovsky, E. B. *J. Am. Chem. Soc.* **2008**, *130*, 6718.
- (189) Chen, B.; Wang, L.; Xiao, Y.; Fronczek, F. R.; Xue, M.; Cui, Y.; Qian, G. *Angew. Chem. Int. Ed.* **2009**, *48*, 500.
- (190) Ding, S.-B.; Wang, W.; Qiu, L.-G.; Yuan, Y.-P.; Peng, F.-M.; Jiang, X.; Xie, A.-J.; Shen, Y.-H.; Zhu, J.-F. *Mater. Lett.* **2011**, *65*, 1385.
- (191) Wang, W.; Qiu, L. G.; Shao, G. Q.; Wu, Y.; Wang, Y. *Asian J. Chem.* **2012**, *24*, 4041.
- (192) Qin, J.-S.; Zhang, S.-R.; Du, D.-Y.; Shen, P.; Bao, S.-J.; Lan, Y.-Q.; Su, Z.-M. *Chem. Eur. J.* **2014**, *20*, 5625.
- (193) Sun, C.-Y.; Wang, X.-L.; Qin, C.; Jin, J.-L.; Su, Z.-M.; Huang, P.; Shao, K.-Z. *Chem. Eur. J.* **2013**, *19*, 3639.
- (194) Bo, Q.-B.; Zhang, H.-T.; Wang, H.-Y.; Miao, J.-L.; Zhang, Z.-W. *Chem. Eur. J.* **2014**, *20*, 3712.
- (195) Rao, X.; Huang, Q.; Yang, X.; Cui, Y.; Yang, Y.; Wu, C.; Chen, B.; Qian, G. *J. Mater. Chem.* **2012**, *22*, 3210.
- (196) Cui, Y.; Xu, H.; Yue, Y.; Guo, Z.; Yu, J.; Chen, Z.; Gao, J.; Yang, Y.; Qian, G.; Chen, B. *J. Am. Chem. Soc.* **2012**, *134*, 3979.

## 2. Experimental

---

### 2.1. Introduction

The details of all experimental procedures and characterisation techniques that were used throughout this work are summarised in this chapter. Some details presented here are brief where further information is provided in later chapters.

### 2.2. Sample Preparation

#### 2.2.1. Solvothermal synthesis

Solvothermal synthesis is a method widely used for the low temperature ( $< 240\text{ }^{\circ}\text{C}$ ) synthesis of inorganic and hybrid inorganic-organic materials.<sup>1-5</sup> Reagents are placed in solvents that are heated above their boiling points in a sealed vessel to generate autogenous pressure. These conditions are used to induce reactions between dissolved or suspended chemical reagents allowing for precise control of both particle size and morphology, and often the stoichiometry of the products, although this can be difficult to predict since reagents can remain in solution after crystallisation.<sup>6,7</sup> In the work described in this thesis,  $20\text{ cm}^3$  Teflon lined autoclaves were used for the majority of experiments with typical reactions using between 5 and  $10\text{ cm}^3$  of solvent. The maximum reaction temperature used for these vessels is around  $250\text{ }^{\circ}\text{C}$  due to the higher coefficient of thermal expansion of the Teflon liner compared to that of the steel vessel. At this temperature or below, a spring-loaded closure is able to maintain a constant pressure on the liner. A schematic of a typical Teflon lined autoclave is given in Figure 2.2.1.

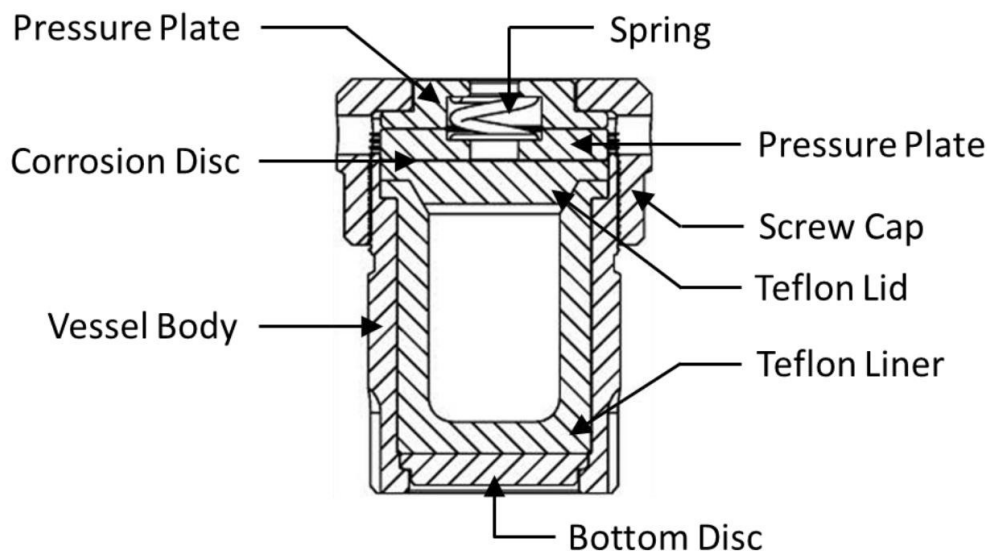


Figure 2.2.1: Schematic of a Teflon-lined autoclave

All reagents were obtained from chemical vendors and were used without any further purification.

For the reactions outlined in Chapter 5, either PEEK autoclaves or glass culture tubes were used as reaction vessels. Since these reaction vessels were tightly sealed and held at reaction temperatures, these reactions can also be described as solvothermal.

### 2.2.2. Thermal activation of metal-organic frameworks

Many of the metal-organic frameworks described in this work contain either organic counter-ions or directly coordinated solvent molecules. In order to fully realise the porosity of these materials, these moieties can be removed. Owing to the strong interactions between the framework and these molecules, typical MOF activation methods such as stirring the metal-organic framework in the presence of excess volatile solvent are unsuccessful. Additional energy is required to break coordination bonds, to allow structural rearrangement or to oxidise the framework. Heating a metal-organic framework below its decomposition temperature can remove trapped or coordinated solvent molecules. For the purposes of this thesis, this technique is described as calcination.

In a typical *ex situ* calcination, the sample was heated in tube furnace in air, held at elevated temperatures and cooled back to room temperature using a heating and cooling rate of  $1\text{ }^{\circ}\text{C}\cdot\text{min}^{-1}$ . Post-calcination, the samples were washed in methanol or DMF for MIL-53(Fe, V) and the lanthanide-organic frameworks respectively and then dried in air. For *in situ* diffraction studies, the heating and cooling rate was  $10\text{ }^{\circ}\text{C}\cdot\text{s}^{-1}$ .

## 2.3. Powder X-ray Diffraction

### 2.3.1. Introduction

Various X-ray diffraction (XRD) techniques were used to characterise the structural properties of the metal-organic frameworks studies in this work. These were performed under both static and dynamic conditions.

Powder X-ray diffraction (PXRD) is a technique used to investigate the structures of crystalline materials. A crystalline material has an ordered arrangement of atoms or ions in three-dimensional space. The simplest representation of this arrangement that can be repeated by translation to give the full structure is defined as the 'unit cell'. Two examples of a unit cell for a two-dimensional array are shown in Figure 2.3.1, both A and B can be repeated by applying translational symmetry to give the complete array. However, A would be chosen as the representative unit cell as it has the smallest area.

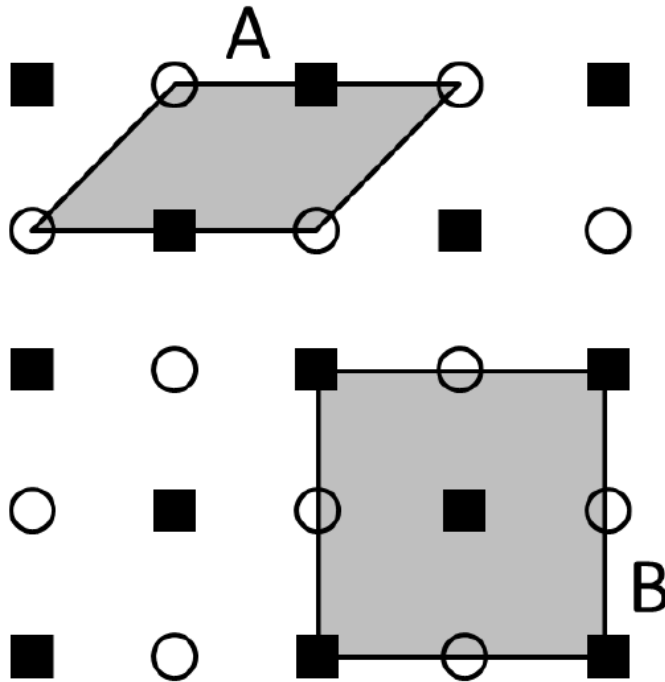


Figure 2.3.1: Two-dimensional representation of a crystalline material demonstrating the choice of unit cells, A and B.<sup>8</sup>

A three-dimensional unit cell can be defined by a parallelepiped with the side lengths denoted as  $a$ ,  $b$  and  $c$  and the internal angles denoted as  $\alpha$ ,  $\beta$  and  $\gamma$ . These are known as the 'unit cell parameters'. No relationship between cell parameters is necessary, however increasing levels of symmetry produce varying relationships which lead to the seven 'crystal classes.' These classes are summarised in Table 2.3.1.

Table 2.3.1: Summary of crystal classes

Unit cell dimensions		Crystal Class
$a = b = c$	$\alpha = \beta = \gamma = 90^\circ$	Cubic
$a = b \neq c$	$\alpha = \beta = \gamma = 90^\circ$	Tetragonal
$a = b \neq c$	$\alpha = \beta = 90^\circ, \gamma = 120^\circ$	Hexagonal
$a = b = c$	$\alpha = \beta = \gamma \neq 90^\circ$	Trigonal / Rhombohedral
$a \neq b \neq c$	$\alpha = \beta = \gamma = 90^\circ$	Orthorhombic
$a \neq b \neq c$	$\alpha = \gamma = 90^\circ, \beta \neq 90^\circ$	Monoclinic
$a \neq b \neq c$	$\alpha \neq \beta \neq \gamma \neq 90^\circ$	Triclinic

The translation symmetry that describes how the unit cell generates the complete structure is known as the 'lattice'. A lattice is defined as an array of equivalent points in one, two or three dimensions. The lattice provides no information about the actual positions of the atoms or molecules in space it only shows the translational symmetry of the material; the environment of an atom placed on a lattice point would be identical to an atom placed on any other equivalent point.

For three-dimensional crystal structures there are four types of lattice (Figure 2.3.2). The simplest lattice is known as 'primitive' (P). A unit cell with a primitive lattice contains a single lattice point *i.e.* the only purely translational symmetry is that of the unit cell; lattice points are normally located at the corners of the unit cell.

The remaining three types of lattice contain translational symmetry within the unit cell. The second lattice type is 'body centred' (I). The additional lattice point is at the cell's centre, which has the fractional coordinates  $(\frac{1}{2}, \frac{1}{2}, \frac{1}{2})$ . This means that for any atom given the fractional coordinates  $(x, y, z)$  this lattice will generate an identical atom with the fractional coordinates  $(x+\frac{1}{2}, y+\frac{1}{2}, z+\frac{1}{2})$ .

The third lattice type is known as 'face centred' (F), this lattice has additional lattice points at the centre of each face with the fractional coordinates  $(\frac{1}{2}, \frac{1}{2}, 0)$ ,  $(0, \frac{1}{2}, \frac{1}{2})$ , and  $(\frac{1}{2}, 0, \frac{1}{2})$ . Therefore, for an atom with the general position  $(x, y, z)$  three additional identical atoms will be generated with the coordinates  $(x+\frac{1}{2}, y+\frac{1}{2}, z)$ ,  $(x, y+\frac{1}{2}, z+\frac{1}{2})$  and  $(x+\frac{1}{2}, y, z+\frac{1}{2})$ .

The final lattice type is similar to the face centred lattice however it only has lattice points on one of the faces. This lattice is still known as face centred but is given the symbol C. The lattice point is normally placed at the centre of the face delineated by  $a$  and  $b$ , which has the fractional coordinates  $(x+\frac{1}{2}, y+\frac{1}{2}, z)$ . Hence, only one additional atom is generated in this lattice. The A and B face centred lattices can be obtained if the lattice points sit at

the centre of the  $bc$  or  $ac$  planes, respectively. Conventionally, the C description is always used as redefinition of the  $a$ ,  $b$  and  $c$  directions will always produce the C centred description, where the line joining the pair of lattice points on the faces runs parallel to the  $c$  axis.

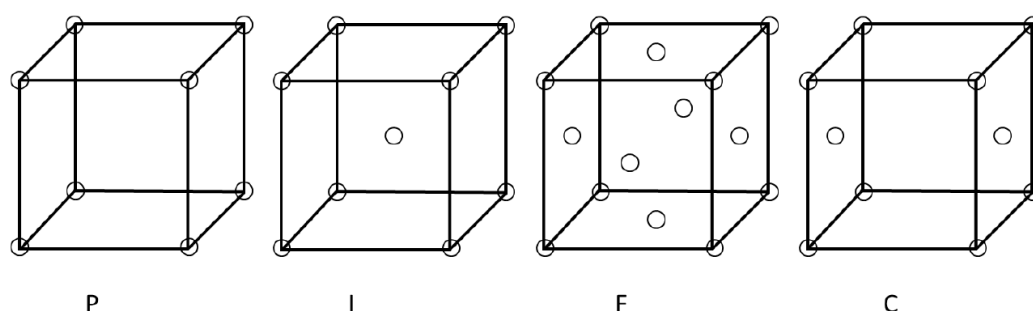


Figure 2.3.2: The four lattice types: primitive (P), body centred (I) and face centred types (F) and (C)

These lattice types can be combined with the seven crystal classes giving rise to all the possible variations which are known as the ‘Bravais lattices’ (Table 2.3.2), named after Auguste Bravais, a prominent French physicist. There are only fourteen possibilities as not all combinations give rise to a unique lattice *e.g.* a face centred tetragonal unit cell can be redefined as a body centred tetragonal unit cell.

Table 2.3.2: The fourteen Bravais lattices

Crystal class	Bravais Lattice
Cubic	P, I, F
Tetragonal	P, I
Hexagonal	P
Trigonal / Rhombohedral	P
Orthorhombic	P, C, I, F
Monoclinic	P, C
Triclinic	P

Additional symmetry operations such as rotation axes and mirror planes can be applied to the Bravais lattice descriptions to produce 230 distinct three-dimensional symmetry groups; these are known as ‘space groups’. For every unit cell a set of equally



spaced parallel planes can be defined and labelled using 'Miller indices', named after William Hallows Miller, a British mineralogist. These indices are conventionally designated as  $h$ ,  $k$  and  $l$  which relate to the unit cell directions  $a$ ,  $b$  and  $c$ . The Miller indices are given by the reciprocals of the fractional intercepts along each of the cell directions *i.e.* the fractional intercept along the unit cell  $a$  direction gives  $h$ , along  $b$  gives  $k$  and along  $c$  gives  $l$ . The  $h$ ,  $k$  and  $l$  values are always integers; they can be positive, negative or zero. For planes that are parallel to one of the unit cell directions the intercept is at infinity, the reciprocal of which is equal to zero. These indices define the Miller index for a set of parallel planes, which includes one that passes through the origin. An example of a set of lattice planes is shown in Figure 2.3.3, where the intercepts are at  $\frac{1}{2}a$ ,  $\infty b$  and  $c$  therefore the Miller indices for these planes are (201).

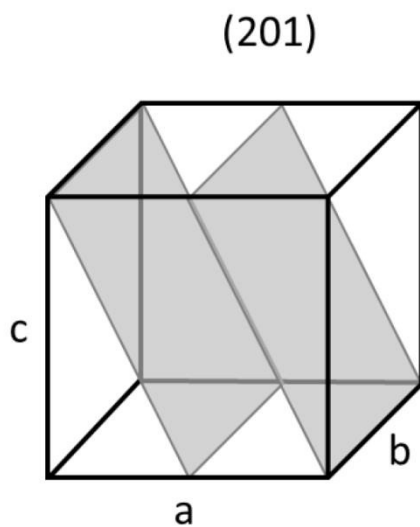


Figure 2.3.3: Two of the sets of lattice planes with Miller indices (201)

The distance between a set of lattice planes is known as the ' $d$ -spacing' and is normally denoted as  $d_{hkl}$ . The relationship between  $d$ -spacing and the lattice parameters can be determined geometrically but is dependent upon the crystal class. The relationships between the  $d$ -spacing and the Miller indices are shown in Table 2.3.3.

Table 2.3.3: Expressions for  $d$ -spacings for the different crystal classes

Crystal class	Expression for $d_{hkl}$ in terms of lattice parameters and Miller indices
Cubic	$\frac{1}{d^2} = \frac{h^2 + k^2 + l^2}{a^2}$
Tetragonal	$\frac{1}{d^2} = \frac{h^2 + k^2}{a^2} + \frac{l^2}{c^2}$
Hexagonal	$\frac{1}{d^2} = \frac{4}{3} \left( \frac{h^2 + hk + k^2}{a^2} \right) + \frac{l^2}{c^2}$
Trigonal / Rhombohedral	$\frac{1}{d^2} = \frac{(h^2 + k^2 + l^2)\sin^2\alpha + 2(hk + kl + hl)(\cos^2\alpha - \cos\alpha)}{a^2(1 - 3\cos^2\alpha + 2\cos^3\alpha)}$
Orthorhombic	$\frac{1}{d^2} = \frac{h^2}{a^2} + \frac{k^2}{b^2} + \frac{l^2}{c^2}$
Monoclinic	$\frac{1}{d^2} = \frac{1}{\sin^2\beta} \left( \frac{h^2}{a^2} + \frac{k^2}{b^2} + \frac{l^2}{c^2} - \frac{2hl \cos\beta}{ac} \right)$
Triclinic	$\frac{1}{d^2} = \frac{\left[ \frac{h^2}{a^2 \sin^2\alpha} + \frac{2kl}{bc} (\cos\beta \cos\gamma - \cos\alpha) + \frac{k^2}{b^2 \sin^2\beta} + \frac{2hl}{ac} (\cos\alpha \cos\gamma - \cos\beta) + \frac{l^2}{c^2 \sin^2\gamma} + \frac{2hk}{ab} (\cos\alpha \cos\beta - \cos\gamma) \right]}{1 - \cos^2\alpha - \cos^2\beta - \cos^2\gamma + 2\cos\alpha \cos\beta \cos\gamma}$

The distances between atoms or ions in solids are typically a few Ångströms which are comparable to the wavelength of X-rays. When X-rays collide with solid materials, they interact with the atomic electrons and are scattered in various directions. Since the atoms are separated by distances comparable to the wavelength of the X-rays, interference between scattered waves can occur. For an ordered array of atoms this scattering can give rise to interference maxima and minima which can provide information about the structure of the solid, providing a useful technique for the study of crystalline solids. This type of interference is known as diffraction. Figure 2.3.4 demonstrates diffraction from points on a set of lattice planes. When the X-rays leave the source, they are in phase but after they

have been scattered by points B and D on different lattice planes they will only remain in phase (constructive interference) if the additional path difference, equal to  $AB + BC$ , is an integral number of wavelengths *i.e.*  $AB + BC = n\lambda$ . The path difference is dependent upon the lattice spacing,  $d_{hkl}$ , and the angle of incidence of the X-ray beam,  $\theta$ . For constructive interference the following relationship can be obtained:

$$n\lambda = 2d \sin \theta$$

**Equation 2.3.1: The Bragg equation**

Where  $n$  is an integer which is related to the order of the diffracted beam and  $\lambda$  is the X ray wavelength. This expression is known as the Bragg equation, first derived by W. H. and W. L. Bragg in 1913. The derivation of this expression is shown in Figure 2.3.4, given that the angle of incidence is equal to the angle ADB.

$$\begin{aligned}\sin \theta &= \frac{AB}{BD} = \frac{BC}{BD} \\ BD &= d \\ 2\sin \theta &= \frac{AB + BC}{d} \\ n\lambda &= 2d \sin \theta\end{aligned}$$

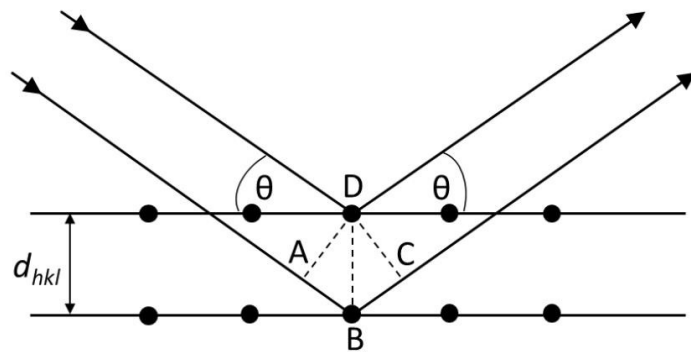


**Figure 2.3.4: Schematic showing Bragg diffraction and derivation of the Bragg equation**

An X-ray diffractometer is used to study the diffraction of X-rays by crystalline samples. An X-ray diffractometer consists of three essential components; a source of radiation, a detector and a goniometer. A source of X-rays may be generated using an X-ray tube, in which a high energy beam of electrons is accelerated towards a metal target. The target is excited and emits energy in the X-ray range.

There are two main types of detector; gas-filled and scintillation detectors. Gas-filled detectors work on the principle that X-ray photons can ionise inert gases e.g. xenon. These ions are then accelerated towards a detector which converts the electrical signal into voltage allowing it to be interpreted computationally. Scintillation detectors require a two-step process; the X-ray photons initially strike a phosphor screen which emits photons in the visible region. These photons strike a detector and are then converted to voltage pulses which are interpreted computationally. This type of detector has a poorer resolution due to the energy losses during the process however it benefits from rapid data collection. The goniometer allows for the precise angle at which Bragg diffraction occurs to be calculated.

The basic relationship between the X-ray source, the sample and the detector is shown in Figure 2.3.5. The schematic highlights the connection between the incident and reflected beams; the reflected beam will always be reflected at the angle of incidence therefore the angle between the incident beam and the reflected beam will always be equal to  $2\theta$ . Consequently, the detector will always need to be positioned at an angle of  $2\theta$  to record the Bragg diffraction for a given set of lattice planes.

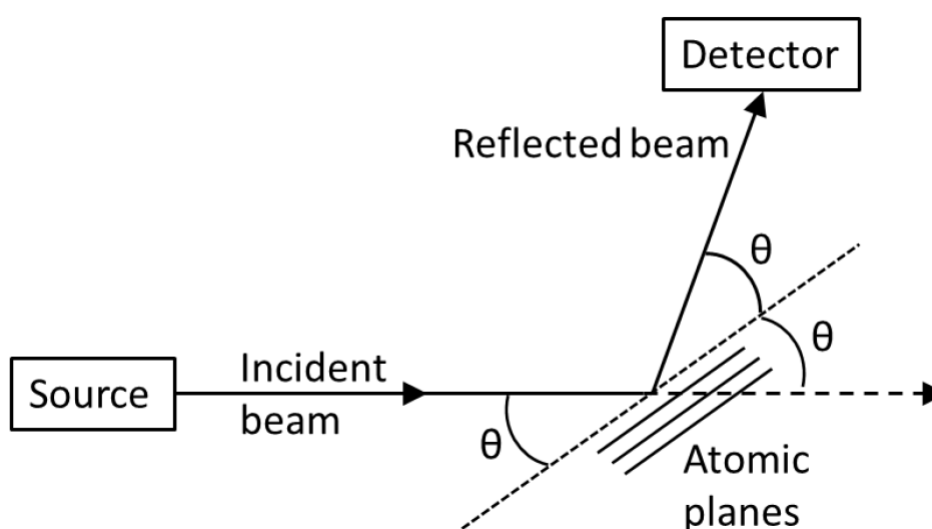


Figure 2.3.5: Typical experimental set-up for X-ray diffraction techniques

The output produced by this method is the intensity of the X-rays detected as a function of the detector angle,  $2\theta$ . X-ray diffraction (XRD) can be used to analyse both single crystals and crystalline powders. The remainder of this section will focus on powder X-ray diffraction. Figure 2.3.6 shows an example of a typical powder X-ray diffraction pattern. The positions of the reflections ( $2\theta$ ) and the X-ray wavelength can be used to determine the Miller indices for a given XRD pattern using the relationship between the Bragg equation and the expressions for the different crystal classes. The simplest example is for a cubic unit cell. Equation 2.3.2 shows the result of rearranging the Bragg equation to solve for  $d$  and substituting this into the expression for the cubic crystal class.

$$\sin^2\theta = \left\{ \frac{\lambda^2}{4a^2} h^2 + k^2 + l^2 \right\}$$

Equation 2.3.2

Equation 2.3.2 can be simplified to give Equation 2.3.3:

$$\sin^2\theta = A\{h^2 + k^2 + l^2\}$$

Equation 2.3.3

The  $\sin^2\theta$  values for a sample can be calculated using the  $2\theta$  positions observed in the diffraction pattern. The ratio between these values can be used to identify the Miller indices  $h$ ,  $k$  and  $l$ . The Miller indices can then be used to indicate the lattice planes responsible for each reflection in a diffraction pattern. Figure 2.3.6 shows an indexed powder XRD pattern for  $\text{Cu}_2\text{O}$ .

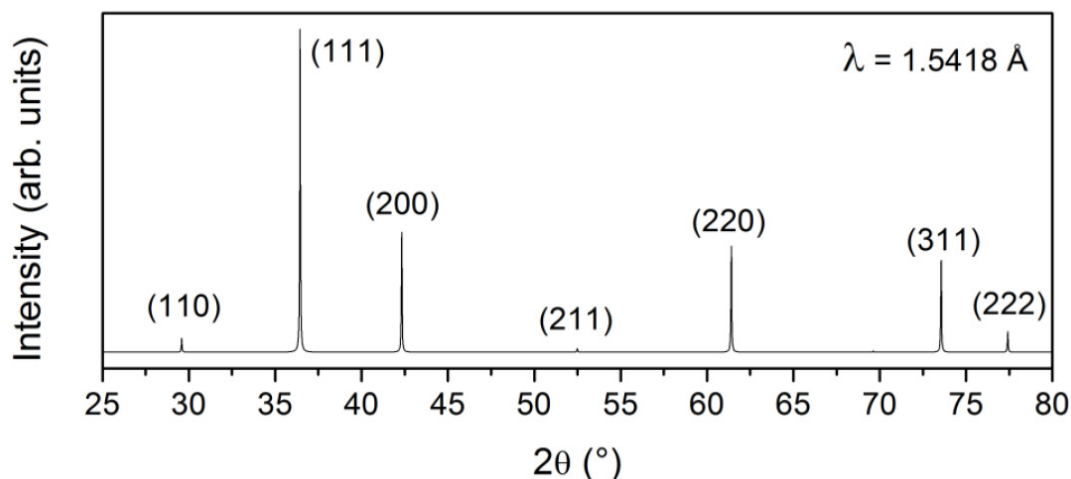


Figure 2.3.6: Indexed powder XRD pattern for the cubic structure of  $\text{Cu}_2\text{O}$

A powder diffraction pattern can be used in various ways, it can be used for identification purposes if a reference crystal structure is already known; for confirming the purity of a sample as any crystalline materials within the powder sample will contribute reflections to the diffraction pattern; it can also be used for determining or refining the unit cell parameters of a sample; refining the atomic parameters if a structural model is known; and for solving structures *ab initio* if high-resolution data are available.

Refinement of structures against PXRD patterns can be performed using structure analysis software which can process and analyse structural data. These types of software can be used to calculate an ideal diffraction pattern from existing crystal structure information which is then compared with experimental data. Through a series of parameter refinements (*i.e.* unit cell dimensions, peak intensities and widths), the comparison between the two can be improved. This type of refinement can simply provide a profile fit which contains information about the unit cell parameters but no information about atom positions (a Pawley or Le Bail analysis), or atomic positions may be refined if the peak intensities have been determined accurately (a Rietveld refinement). The relative intensities of diffraction peaks is dependent on the type and arrangement of atoms in the unit cell, related by the 'structure factor'. This will not be discussed further, since in this

work only profile refinement of powder XRD was used to prove phase purity and determined lattice parameters.

### 2.3.2. Laboratory powder XRD

Three diffractometers were used to collect XRD data in the laboratory: a Siemens D5000, a Bruker D8 Advance and a Panalytical X'Pert Pro X-Ray MPD powder diffractometer.

### 2.3.3. D5000

A Siemens D5000 diffractometer was used primarily for sample identification purposes. The X-ray source position and detector positions vary to maintain the  $2\theta$  angle. The instrument uses Cu K $\alpha$  radiation with a weighted average wavelength of 1.54184 Å (Cu K $\alpha$ 1 = 1.54056 Å and Cu K $\alpha$ 2 = 1.54439 Å). The structural database supplied by Bruker as part of the EVA software was used to identify the composition of any crystalline impurities that were present and simulated patterns from published crystallographic data were used to identify any frameworks that had been reported previously.

### 2.3.4. D8

A Bruker D8 Advance diffractometer was used to collect temperature-resolved powder X-ray diffraction data. The breathing property of flexible MOFs, such as MIL-53, means that as the framework expands the position and the intensity of the Bragg peaks change, which can be followed using X-ray diffraction. Some of these changes can be fast therefore the ability to collect data quickly is crucial. The D8 diffractometer is fitted with a VÅNTEC solid-state detector which benefits from rapid data collection (on the time scale of minutes). However, the disadvantage of this is the resolution of the data is reduced, so the structural information obtained is qualitative. Most scans were collected over a  $2\theta$  range of 6 - 30 ° for a total of approximately 300 seconds. This allowed for sufficient information

about the unit cell parameters to be obtained to enable different phases to be distinguished. This instrument uses a fixed sample position where the X-ray source (Cu K $\alpha$  radiation with a weighted average wavelength of 1.54184 Å) and detector positions are varied to maintain the 2 $\theta$  angle. For thermodiffractometry, samples were held at the required temperature for 10 minutes before initialising the scan to ensure that the sample had reached said temperature.

The D8 advance diffractometer is equipped with a sample chamber (Anton Paar XRK900) which can be pressurised to 10 bar. The chamber was modified to allow for a gas flow to pass over the sample in a continuous flow without a pressure build-up. Use of dry nitrogen allowed helped to indicated whether observed structural changes involved absorption of water or not, particularly useful in rationalising the calcination of the lanthanide-organic frameworks.

### **2.3.5. Panalytical X'Pert Pro MPD**

A Panalytical X'Pert Pro X-Ray MPD powder diffractometer was equipped with a focussing Johanson monochromator on the incident beam optics, giving very high-resolution pure Cu K $\alpha$ 1 radiation. The diffractometer was also fitted with a reflection/transmission spinner stage, diminishing the effects of preferred orientation. This allowed for collection of powder diffraction patterns of suitable quality for extraction of lattice parameters by Le Bail fitting. Profile parameters and unit cell dimensions were refined against the data using the GSAS suite of software (see below).<sup>9</sup>

### **2.3.6. High-resolution powder XRD**

High-resolution XRD data were collected using Beamline I11 at the DIAMOND Light source located in Oxfordshire in the UK. Data were collected while the samples were spun continuously in borosilicate glass capillaries. Data collection performed using this method



removes the effects of preferred orientation; a true average diffraction pattern can be obtained.

Beamline I11 uses high energy X-rays, ~15 keV ( $\lambda = 0.825174 \text{ \AA}$  for the work presented in this thesis) and has an angular range of 3-150 °2 $\theta$ . The finely ground samples were loaded into capillaries with a diameter of between 0.5- 0.7 mm and mounted onto a brass tip which fits directly on to the instrument. The standard time taken for data collection was 30 minutes. For cases where quick data collection were necessary (where beam degradation of the samples was seen) the position sensitive detector (PSD) was used. The PSD (based on Mythen-2 modules) is specified to perform fast data collection (e.g. 1 powder pattern / ms) with a 90° aperture and an intrinsic angular resolution of 0.01°.

### 2.3.7. PXRD Refinement

Refinement of PXRD patterns was performed using the General Structure Analysis System (GSAS) which uses the graphical user interface EXPGUI.<sup>9</sup> Profile parameter fits were used to obtain refined unit cell parameters for powder samples. The profile fit involves empirical fitting of peak intensities and the method used in this thesis was that developed by Le Bail *et al.*<sup>10</sup>

### 2.3.8. EDXRD

Energy dispersive X-ray diffraction (EDXRD) uses a *white beam* of X-rays to collect data over a wide range of energies. The higher energy and intensity of the beam allows the X-rays to penetrate a reaction vessel, which means solid/liquid reactions that involve crystalline samples can be followed *in situ*, giving invaluable insight into the way a reaction proceeds. Laboratory-sized vessels can be used for this method. This type of *in situ* technique has allowed for the crystallisation of different materials to be followed from nucleation to completion leading to a better understanding of the mechanisms involved. In

this thesis, the technique allowed for the investigation of the breathing behaviour of MIL-53(Fe, V).

Beamline F3 at the HASYLAB synchrotron facility in Hamburg, Germany was used to record all EDXRD data. The diagram of Beamline F3, Figure 2.3.7, highlights how the sample and detector positions are adjustable but fixed for a given experiment. Beamline F3 receives white-beam radiation with energy 13.5–65 keV and the incident X-ray beam is collimated to dimensions  $20 \times 20 \mu\text{m}^2$ . The scattered X-rays are detected using a fixed single-element germanium solid-state detector.

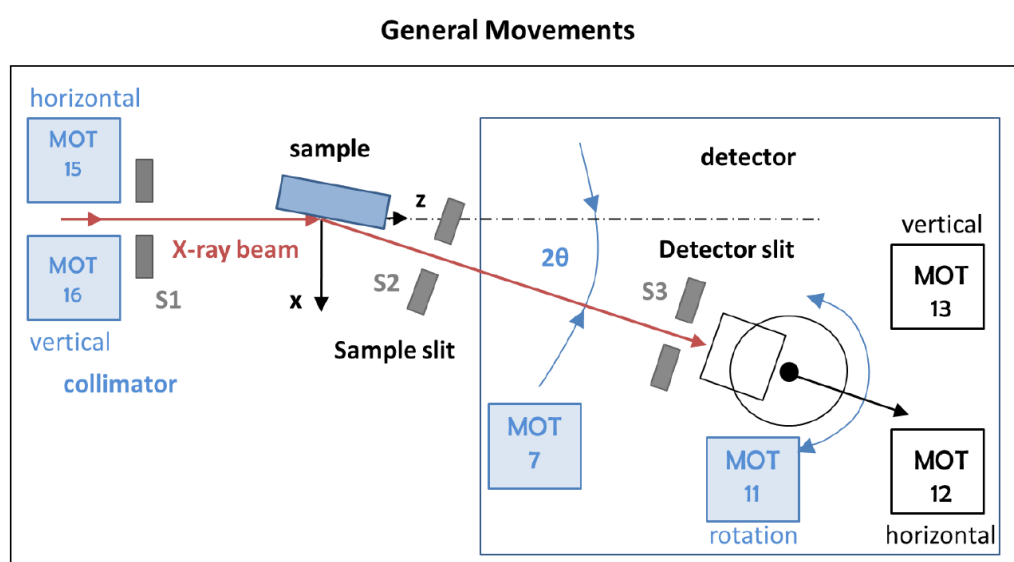


Figure 2.3.7: Schematic of Beamline F3 at HASYLAB. Schematic was drawn by A.S. Munn

The use of white beam radiation means that the data is collected as a function of energy. By substituting Equation 2.3.4, which relates energy,  $E$ , to the wavelength,  $\lambda$ , into the Bragg equation, Equation 2.3.5 can be obtained where  $h$  is Planck's constant and  $c$  is the speed of light.

$$E = \frac{hc}{\lambda}$$

Equation 2.3.4

$$E = \frac{hc}{2d \sin \theta}$$

Equation 2.3.5

The precise angle of the detector was calibrated using the Bragg peaks of a solid polycrystalline sample of MIL-53(Fe)[H<sub>2</sub>O] and the detector energy was calibrated using a glass containing heavy elements with well-separated fluorescence lines. These calibrations were performed on each visit to the beamline.

In the experiments reported here, around 400 mg of solid MIL-53(Fe, V)/MIL-53(Fe)[H<sub>2</sub>O] with ~3 cm<sup>3</sup> of water was added to a 1 cm diameter borosilicate glass tube with a Teflon coated magnetic stirrer bar. Addition of ethanol solutions was made using a syringe pump with the tube placed in a stand with continuous stirring of the solution during addition. The guest solution (10 cm<sup>3</sup>) was added drop-wise at a rate of 0.1 cm<sup>3</sup>·min<sup>-1</sup>. Data collection began as soon as the syringe pump was started. Data were recorded every 60 seconds. Due to the quick data collection time and the large range of wavelengths in the X-ray beam the resolution is poor meaning only the strongest Bragg peaks are visible. This is, however, sufficient to be able to follow the changes in symmetry as the framework expands in response to the ethanol molecules. Contour plots were made to show the growth and decay of the characteristic Bragg peaks as a function of time. These allow the expansion and contraction of the framework throughout the entire experiment to be observed.

### 2.3.9. *In Situ* XRD Crystallisation Studies

*In situ* XRD methods are non-invasive allowing for direct observation of the crystallisation process, often in real-time. These techniques often require the high intensity radiation provided by a synchrotron source to penetrate reaction vessels to directly observe syntheses. The Joint Engineering Environmental and Processing Beamline I12

(referred to as JEEP or Beamline I12) is a multipurpose, high energy X-ray with flexibility in the type and complexity of the experiments it can provide. For the work presented in this thesis, a monochromatic X-ray wavelength ( $\sim 0.2 \text{ \AA}$ ) was used to probe a PEEK reaction vessels heated using ODISC.<sup>11</sup> For further discussion of the methods used, please refer to chapter 5.

## 2.4. Single Crystal X-ray Diffraction

Single crystal X-ray diffraction operates using the same basic principles described for powder X-ray diffraction in Section 2.3. The technique differs in the instrumentation used to collect the data and the size of the sample to be studied. This technique collects data from a single unfractured, optically-clear crystal between 30 – 300 microns in size. The advantage of single-crystal XRD is that the data can be used to determine, through analysis and refinement techniques, the full crystal structure of unknown materials; this includes the location and identity of all the atoms, the bond distances and angles, and also the space group and unit cell dimensions. In powder X-ray diffraction the ability to extract this information is compromised by Bragg-peak overlap in the two-dimensional pattern so structure solution is still not routine.

Single crystal diffraction was performed using a Gemini R diffractometer from Oxford Diffraction equipped with an Oxford Cryosystems Cobra which allows for low temperature ( $>8 \text{ K}$ ) experiments to be performed. The EPSRC National Crystallography Service (NCS) was also used for data collection.<sup>12</sup> Data analysis and structure refinement was performed by G. J. Clarkson. The structures were solved by direct methods using SHELXS and refined using SHELXL 97.<sup>13</sup>

## 2.5. X-ray Absorption Spectroscopy

### 2.5.1. Introduction

X-ray Absorption Spectroscopy (XAS) is the measurement of the X-ray absorption coefficient of a material as a function of energy. X-rays of a narrow energy resolution are shone on a sample and the incident and transmitted X-ray intensity is recorded as the incident X-ray energy is increased. When the energy of the incident X-ray matches the binding energy of an electron of an atom in the sample, the amount of X-rays absorbed by the sample increases. This leads to a drop in the transmitted X-ray intensity. This results in an absorption edge. The absorption edge varies in energy depending on which core electron is ejected. For example, the absorption of a photon leading to the ejection of a 1s core electron is referred to as the K-edge. Each element has a unique set of absorption edges, allowing for XAS element selectivity. Data are normalised using the ATHENA program.<sup>14</sup>

### 2.5.2. X-Ray Absorption Near Edge Spectroscopy

X-ray Absorption Near Edge Spectroscopy (XANES) focuses on the region near to the edge, typically within the range of around 50 - 100 eV. The energy of the edge position is the energy required to eject a core electron by photoabsorption and is directly related to the attractive forces between the electron and the atom. This is essentially Coulombic in nature. An oxidised atom has a positive charge, leading to stronger attraction between remaining electrons and the nucleus. This corresponds to shift in the position of the absorption edge to higher energies. By measuring the position of the absorption edge of reference materials of known oxidation state materials, the oxidation state of an unknown sample may be elucidated. The edge position is defined in this thesis as the energy at which the normalised absorption is equal to 0.5.

### 2.5.3. Extended X-ray Absorption Fine Spectra

Extended X-Ray Absorption Fine Spectra (EXAFS) focuses on the oscillatory structure extending for hundreds of electron volts beyond the edge position, including the XANES region. This region is also known as the Kronig structure, named after Ralph Kronig who published the first theory of EXAFS in 1931.<sup>15</sup> Upon absorption of the X-ray photon, an electron is ejected from the core of the absorbing atom. Since this photoelectron has wave-like nature and the surrounding atoms act as point scatterers, a resulting interference pattern is seen between backscattered electron waves and incident X-rays. This leads to oscillations being seen in the post-edge region of EXAFS spectra. Since the interference is directly dependant on surrounding atoms, local structural information can be determined. This can be used for example to determine if the local environment of an atom changes before or after a reaction. In this work, EXAFS were fitted using the ARTEMIS software and a further discussion of the fitting procedure is given in Chapter 3.<sup>14</sup>

### 2.5.4. Beamline B18

Beamline B18 is a general purpose XAS beamline, located at the Diamond Light source. B18 has a wide range of energies between 2 and 35 keV, covering the majority of the K-edges of the elements studied in this work. The measurements were carried out using the Pt-coated branch of collimating and focusing mirrors, a Si(111) double-crystal monochromator and a pair of harmonic rejection mirrors. The samples were prepared in the form of a self-supported pellet, using polyethylene powder as the diluent, with the thickness optimised to obtain an edge jump close to one. The size of the beam at the sample position was approximately 600  $\mu\text{m}$  (horizontal)  $\times$  700  $\mu\text{m}$  (vertical). XANES data were collected at the Fe K-edge (7112 eV) and the V K-edge (5465 eV) in transmission mode with ion chambers before and behind the sample filled with appropriate mixtures of inert gases to optimise sensitivity ( $I_0$ : 300 mbar of N<sub>2</sub> and 700 mbar of He, resulting in an overall

efficiency of 10%;  $I_t$ : 150 mbar of Ar and 850 mbar of He, with 70% efficiency). Data were normalised using the program ATHENA<sup>14</sup> with a linear pre-edge and polynomial post-edge background subtracted from the raw  $\ln(I_t/I_0)$  data. In order to estimate the oxidation state of the metal in the mixed iron-vanadium materials, data for several reference materials containing the metals in known oxidation state were also collected (See Supporting Information) using the same conditions. For all edges studied, the edge position was defined as the energy at which the normalised intensity was equal to 0.5. Similar techniques were used for studies of other metals.

## 2.6. Other Characterisation Techniques

Described here briefly are the various other characterisation techniques used throughout this work.

### 2.6.1. Infrared Spectroscopy

Some data were collected by collaborators from Université de Caen Basse-Normandie as part of the MACADEMIA project. For the MIL-53(Fe, V) materials, solid samples were deposited on a silicon wafer after dilution in ethanol. The mixture was dried in air and placed in an IR quartz cell equipped with KBr windows. The cell was connected to a vacuum line for evacuation, calcinations and introduction of doses of vapours or gases. The compounds were activated in vacuum from room temperature to 350 °C, with a dwell of 30 minutes at each temperature chosen (one spectrum every 50 °C). Transmission spectra were recorded in the 500 – 5600  $\text{cm}^{-1}$  range at 4  $\text{cm}^{-1}$  resolution on a Nicolet Nexus spectrometer equipped with an extended KBr beam splitting device and a mercury cadmium telluride (MCT) cryo-detector.

For all other materials, infrared spectroscopy was measured using a PerkinElmer Spectrum 100 FTIR with an attenuated total reflectance (ATR) attachment. Spectra were acquired at  $4\text{ cm}^{-1}$  resolution in the range  $4000\text{--}450\text{ cm}^{-1}$ .

### 2.6.2. Raman Spectroscopy

These data were collected by collaborators from Université de Caen Basse-Normandie. Raman experiments were conducted on a Jobin Yvon Labram 300 confocal microscope. The solids were analysed in ambient conditions with a laser at  $532\text{ nm}$  and a  $1800\text{ lines}\cdot\text{mm}^{-1}$  grating. Laser power on sample was ca.  $0.4\text{ mW}$ , acquisition time varied from  $10\text{ s}$  to  $4\text{ min}$ . Some materials were also analysed *in situ* in an environmental chamber Linkam CCR-1000 connected to a gas flow system. The samples were then heated in the cell under  $60\text{ mL}\cdot\text{min}^{-1}$  Ar or Ar/O<sub>2</sub> (0.8/0.2).

### 2.6.3. Thermogravimetric Analysis

Combined thermogravimetric (TG) and differential scanning calorimetry (DSC) data were recorded using a Mettler Toledo TGA/DSC1 instrument. Approximately  $10\text{ mg}$  of powder were loaded into an alumina crucible; the sample was heated in air to  $1000\text{ }^{\circ}\text{C}$  at a rate of  $10\text{ }^{\circ}\text{C}\cdot\text{min}^{-1}$ .

Where the full empirical formula was not certain, *i.e.* the identity and quantity of the guest molecules was unknown, predictions were made based on the final mass of the metal oxide after complete decomposition; the mass, and consequently the number of moles, of the metal oxide was used to calculate theoretical masses of predicted empirical formulae. These masses were converted to percentage masses by dividing by the initial mass of the experimental sample. The predicted percentage masses were clearly marked on the graphs and compared to the percentage masses that correspond to the plateaus seen in the experimental data.



#### 2.6.4. Elemental Analysis

Quantitative elemental analyses (performed using ICP-MES for Fe, Schöniger flask combustion followed by titration for fluorine and by combustion analysis for CHN) was performed by Medac Ltd, UK.

#### 2.6.5. Mössbauer Spectroscopy

Nuclei in atoms undergo changes in energy levels with associated absorption or emission of a gamma-ray. This is accompanied by recoil due to conservation of momentum. This leads to a discrepancy between the energy of the gamma-ray absorbed or emitted with that of the associated nuclear transition. In addition to this, any atom that is in a free phase *i.e.* gas phase will emit a broad gamma-ray energy profile due to the Doppler Effect caused by the random thermal motion. The combination of these two effects makes generation of a resonant signal between two atoms extremely difficult.

Rudolph Mössbauer discovered that when atoms are contained in a solid matrix, the effective mass of the nucleus is now that of the whole system, making both the recoil energy and the Doppler Effect almost non-existent. This makes the energy of the emitted and the absorbed gamma-ray effectively equal, allowing for a resonant effect between two atoms. Providing a suitable radioactive source can be found *i.e.* one that shares the same atomic mass as that of the absorbing nucleus, the energy levels of the probed nucleus can be studied. The energy levels of the absorbing nuclei can be affected by its local environment. In order to observe these effects, a range of probe gamma-ray energies are required. This can be achieved through oscillation of the radioactive source, artificially generating the Doppler Effect. Since the size of the Doppler Effect is dependent on the velocity of the source, a range of gamma-ray energies can be generated from the singular energy of the source emission. It is for this reason that Mössbauer spectra are recorded as velocity ( $\text{mm}\cdot\text{s}^{-1}$ ) against counts.

If the environment of the source atom and the absorbing atom are identical, only a single peak is observed in the spectrum whereas several peaks and a shift in the peak positions can be seen if the two environments differ. The local environment of the absorbing atom can affect its energy levels in three main ways: by the isomer shift, quadrupole splitting and magnetic splitting.

The isomer shift arises from the interaction between the non-zero volume of the nucleus and the electron charge density from s-electrons within it. This generates a Coulombic interaction, changing the energy levels of the nucleus. Any difference between the s-electron density of the source and the absorbing atom generates a shift in the resonant energy of the transition leading to a corresponding shift in the position of the peaks in the Mössbauer spectra. The s-electron density can be affected by the oxidation state and the chemical environment of the atom.

Quadrupolar splitting reflects the interaction between the nuclear energy level and the non-spherical charge distribution found in nuclei with angular momentum quantum number ( $I$ ) greater than  $1/2$ . The non-spherical charge distribution produces an asymmetric electrical field that splits the nuclear energy levels, forming a nuclear quadrupole. For the case of an isotope with an  $I = 3/2$  excited state such as  $^{57}\text{Fe}$ , the excited state is split into two substates,  $m_I = \pm 1/2$  and  $m_I = \pm 3/2$ . This leads to two lines being observed in the Mössbauer spectrum.

Magnetic splitting results from the interaction between the nucleus and any surrounding magnetic field. The magnetic field splits nuclear levels with spin,  $I$ , into  $(2I + 1)$  substates. This leads to further lines observed in the spectra. Magnetic splitting can be used to determine if the material displays ordered magnetism.

Data were collected by collaborators from the Université du Maine, Le Mans. The  $^{57}\text{Fe}$  Mössbauer spectra were recorded at 300 K and 77 K using a constant acceleration spectrometer and a  $^{57}\text{Co}$  source diffused into a rhodium matrix. The powdered samples were held either under helium gas in a bath cryostat or under vacuum in a homemade cryo-furnace. Velocity calibrations were made using a  $\alpha$ -Fe foil at 300 K. The hyperfine parameters were refined using a least-square fitting using the MOSFIT program.<sup>16</sup> In addition to the number and the relative proportions of Fe species, the hyperfine parameters are the isomer shift and the quadrupolar splitting which provide relevant information on the valency state, the spin state, the coordination and the chemical nature of ligands of  $^{57}\text{Fe}$  nuclei.

#### **2.6.6. Photoluminescence studies**

Data were collected by collaborators from the Universidade de São Paulo. Photoluminescence studies allow investigation of the emissive profiles of the lanthanide ions at different wavelengths of light. This was investigated in the UV–vis region using a Fluorolog SPEX F212I fluorescence spectrometer spectrofluorometer equipped with an R928 Hamamatsu photomultiplier and a 450 W Xe lamp.

## 2.7. References

- (1) Cheng, X.; Zhang, A.; Hou, K.; Liu, M.; Wang, Y.; Song, C.; Zhang, G.; Guo, X. *Dalton Trans.* **2013**, 42, 13698.
- (2) Forster, P. M.; Thomas, P. M.; Cheetham, A. K. *Chem. Mater.* **2002**, 14, 17.
- (3) Huang, G.; Yang, P.; Wang, N.; Wu, J. Z.; Yu, Y. *Inorg. Chim. Acta* **2012**, 384, 333.
- (4) Liu, L.; Wang, X.; Jacobson, A. J. *Dalton Trans.* **2010**, 39, 1722.
- (5) Zou, H. H.; Zhang, S. H.; Xiao, Y.; Feng, C.; Wang, Y. G. *Struct. Chem.* **2011**, 22, 135.
- (6) Daiguebonne, C.; Kerbellec, N.; Guillou, O.; Bünzli, J.-C.; Gumy, F.; Catala, L.; Mallah, T.; Audebrand, N.; Gérault, Y.; Bernot, K.; Calvez, G. *Inorg. Chem.* **2008**, 47, 3700.
- (7) Jacobs, B. W.; Houk, R. J. T.; Anstey, M. R.; House, S. D.; Robertson, I. M.; Talin, A. A.; Allendorf, M. D. *Chemical Science* **2011**, 2, 411.
- (8) Weller, M. T. *Inorganic materials chemistry*; Oxford University Press: Oxford, 1994.
- (9) Toby, B. H. *J. Appl. Crystallogr.* **2001**, 34, 210.
- (10) Lebail, A.; Duroy, H.; Fourquet, J. L. *Mater. Res. Bull.* **1988**, 23, 447.
- (11) Moorhouse, S. J.; Vranješ, N.; Jupe, A.; Drakopoulos, M.; O'Hare, D. *Rev. Sci. Instrum.* **2012**, 83.
- (12) Coles, S. J.; Gale, P. A. *Chem. Sci.* **2012**, 3, 683.
- (13) Sheldrick, G. *Acta Crystallogr., Sect. A* **2008**, 64, 112.
- (14) Ravel, B.; Newville, M. J. *Synchrotron Radiat.* **2005**, 12, 537.
- (15) de L. Kronig, R.; Penney, W. G. *Proc.R. Soc. A.* **1931**, 130, 499.
- (16) Varret, F., Teillet, J. *Unpublished MOSFIT Program* **1976**.

## 3. Mixed-Metal MIL-53

### 3.1. Introduction

MIL-53 or  $M^{III}(\text{BDC})(\text{OH})$  consists of 1-D chains of metal-oxide polyhedra connected to one another by 1,4-benzenedicarboxylate (terephthalate) linkers. Each metal is typically trivalent and in an octahedral environment, coordinated to four oxygens from 1,4-benzenedicarboxylates and two from  $\mu_2$ -hydroxyl groups. The interconnectivity of the 1-D metal-oxide chains with the 1,4-benzenedicarboxylate (BDC) linkers leads to a structure with 1-D diamond shaped channels running parallel to the oxide chains (Figure 3.1.1). These channels are typically occupied by solvent or unreacted 1,4-benzenedicarboxylic acid and can be evacuated using elevated temperatures or reduced pressure.

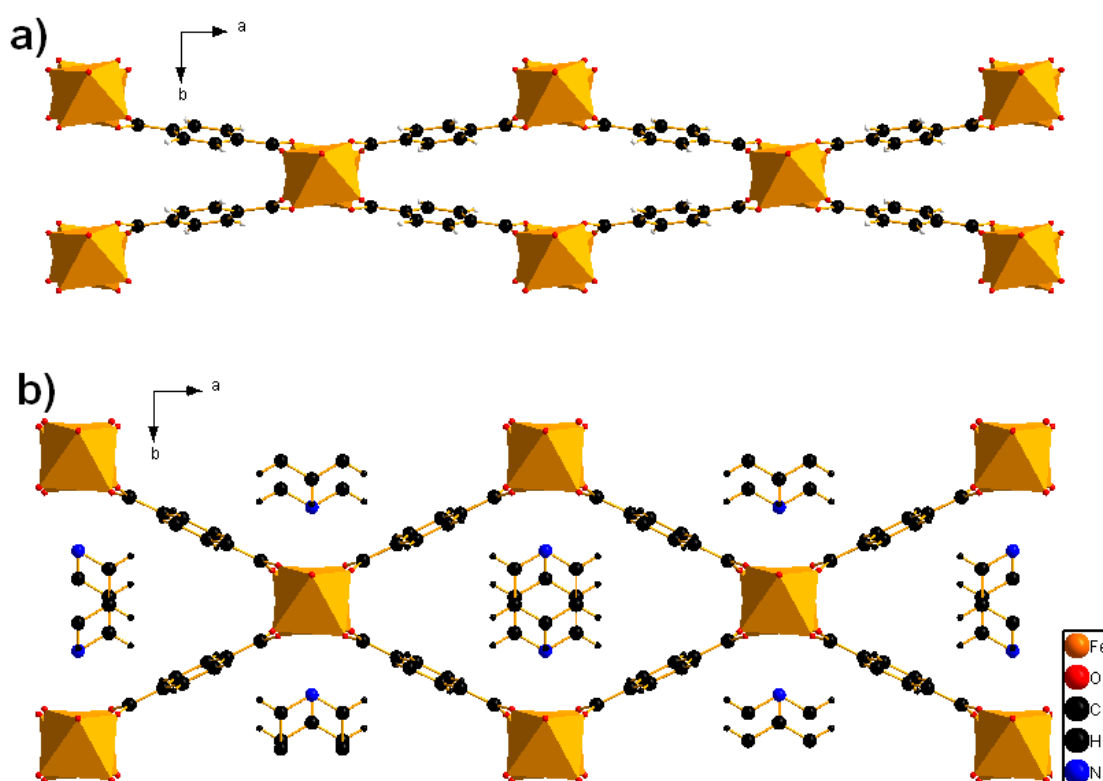


Figure 3.1.1: Closed and open forms of MIL-53(Fe). The closed hydrated form a) can be converted into the open form b) through the introduction of pyridine<sup>1</sup>

The MIL-53 series of materials have now been extensively studied for their adsorption properties for both gas-phase and liquid-phase adsorbents.<sup>2-7</sup> Attempts to modify the 'flexibility' and absorption properties of MIL-53 materials have primarily focused on modifying the organic linkers with varying functional groups, replacing hydrogen with both electropositive and electronegative groups.<sup>8</sup> However, a simpler and more intuitive method of modifying MIL-53 behaviour would be the synthesis of bimetallic MIL-53 materials. Compared to mixed-ligand systems, mixed-metal-organic frameworks where the structure is preserved upon partial metal substitution are relatively rare in the literature. This can arguably be accounted for by the preferential crystallisation of competing single metal phases rather than a mixed phase, due to the differing reactivities of two, or more, metals in the chemical precursors used in synthesis.

This chapter describes how through mediation of reaction conditions, several new mixed-metal analogues of MIL-53 have been synthesised using iron and vanadium. The properties of the mixed-metal materials are affected greatly by the ratio of the two metals. Analysis of the EXAFS spectra of a mixed-metal MIL-53(Fe, Cr) sample was performed supporting the homogeneity of the material. The investigation of mixed iron-cobalt materials was also studied.

## 3.2. [(Fe, V)(BDC)(DMF, F)]

### 3.2.1. Synthesis

Anhydrous iron (III) chloride and anhydrous vanadium (III) chloride in molar ratios 1:0, 2:1 and 1:1 (0.001 mol total metal) and H<sub>2</sub>(BDC) (0.001 mol) were dissolved into a mixture of DMF (5 cm<sup>3</sup>), H<sub>2</sub>O (0.5 cm<sup>3</sup>) and HF (0.1 cm). The mixtures were stirred at room temperature and then transferred into Teflon liners. The Teflon liners were placed in steel autoclaves, kept at 200 °C for 60 minutes and cooled to room temperature. The resulting

dark brown powders were isolated by suction filtration, washed with DMF and dried in air. This synthesis route differs from that used to form Fe(BDC)(DMF) reported by Whitfield *et al.* where iron oxy-hydroxide was used as a metal source with longer reaction times and lower temperatures used.<sup>9</sup> HF and water were also excluded. Attempts to increase the vanadium content lead to the co-formation of MIL-68(V<sup>III</sup>).<sup>10</sup>

### 3.2.2. Structure and Composition

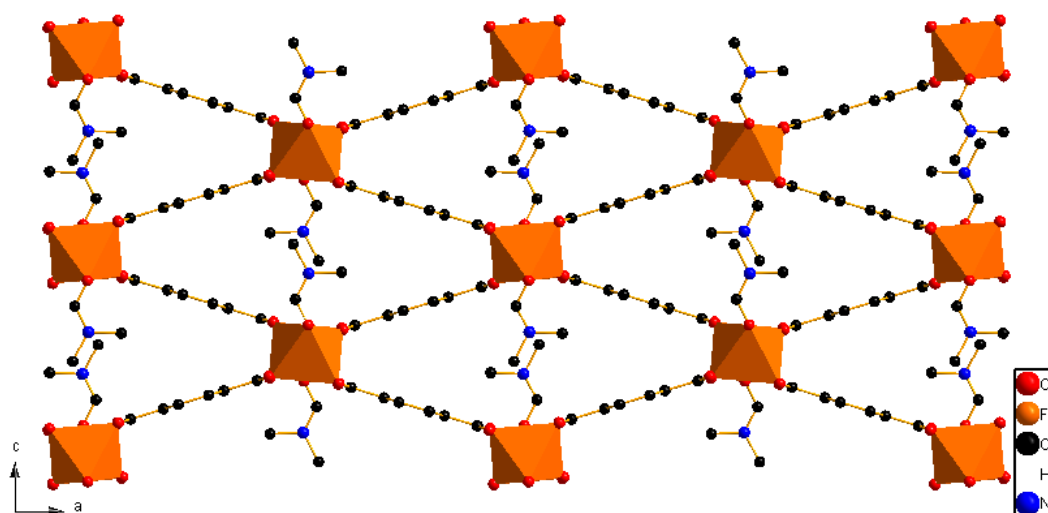


Figure 3.2.1: Crystal structure of Fe(BDC)(DMF) viewed along the *b*-axis<sup>9</sup>

The crystal structure of Fe(BDC)(DMF) is similar in connectivity to that of MIL-53(Fe<sup>III</sup>) as seen in Figure 3.2.1. The bridging anionic OH groups are replaced by neutral DMF coordinating via the carbonyl group. This has the effect of reducing the iron from a trivalent to a divalent state. The coordinated DMF has the additional effect of preventing guest-induced flexibility by occupying the pores of the material.

The three materials formed using differing iron-vanadium ratios all appeared to be isostructural sharing a structure similar to that of Fe(BDC)(DMF) as supported by XRD which can be fitted as single phases (Figure 3.2.2) and by colour (dark brown powder as opposed to the orange crystals reported by Whitfield *et al.*). The incorporation of fluoride through substitution of DMF is difficult to determine by powder XRD due to the isoelectronic nature

of  $O^{2-}$  and  $F^-$ , but all of the materials show contractions in the unit cell parameters from the reported  $Fe(BDC)(DMF)$  structure ( $Pn2_1a$ ,  $a = 19.422(2)$  Å,  $b = 7.3022(5)$  Å,  $c = 8.8468(7)$  Å,  $V = 1254.68$  Å<sup>3</sup>) (Figure 3.2.2). This is consistent with the partial substitution of the bulky DMF with smaller, highly electronegative fluoride ions. The incorporation of anionic fluoride over the neutral DMF would lead to partial oxidation of the iron and the vanadium (discussed below). Upon addition of vanadium to the materials the unit cell volumes show expansion, consistent with the slightly larger ionic radii of V(II)/V(III) ions compared to high-spin Fe(II)/Fe(III) ions.<sup>11</sup>

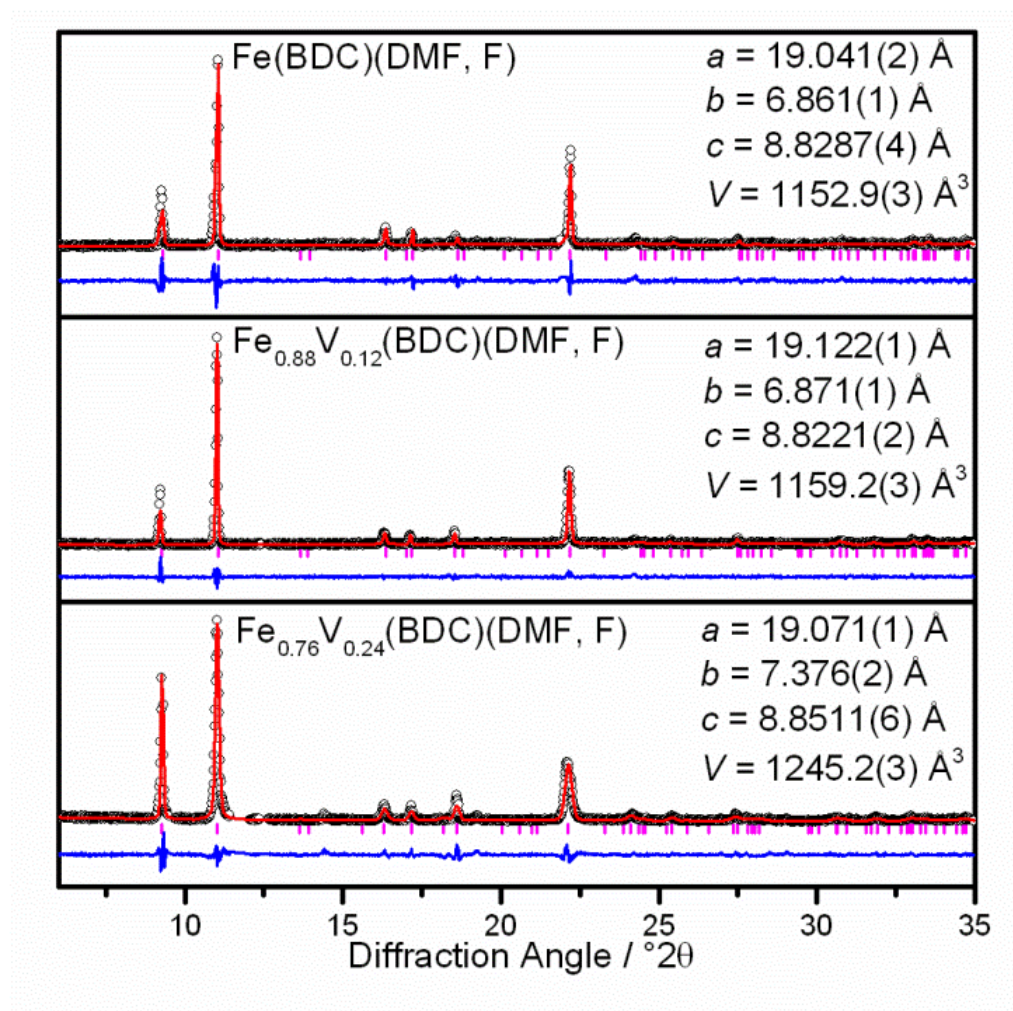


Figure 3.2.2: Profile fit of PXRD patterns of  $(Fe, V)(BDC)(DMF, F)$  at 298 K with refined parameters. Data were collected on Beamline I11 at Diamond ( $\lambda = 0.825174$  Å). Black crosses: experimental data; Green: background; Red: profile fit; Magenta lines: allowed reflections; difference: blue. Top to bottom: samples made with Fe:V ratios of 1:0, 2:1 and 1:1 respectively. Composition of these materials are discussed below



The presence and ratios of each metal in the fluorinated samples were confirmed by elemental analysis (Table 3.2.1). The ratio of Fe:V was measured as 7.3:1 and 3:1 for the samples prepared with initial Fe:V ratios of 2:1 and 1:1, respectively. Although both have lower V content than the initial reactant ratio used, there is a clear evidence for substantial vanadium inclusion in both samples, and the material prepared using a larger vanadium amount does contain more vanadium; presumably some vanadium must remain in solution after the crystallisation of the materials. Both samples contain fluorine and a lower nitrogen content expected for the non-fluorinated composition (expected: 4.78 % N for Fe(BDC)(DMF), actual: ~2.2 % N and 5.6 % F). The ratio of fluorine to nitrogen can be used to determine the degree of fluorination; both mixed metal samples display similar ratios of nitrogen to fluorine of around 45:55. Using this information, it can be deduced that the empirical formulae for the materials are  $\text{Fe}_{0.88}\text{V}_{0.12}(\text{BDC})(\text{DMF})_{0.46}\text{F}_{0.54}$  and  $\text{Fe}_{0.76}\text{V}_{0.24}(\text{BDC})(\text{DMF})_{0.44}\text{F}_{0.56}$  for the samples prepared using 2:1 and 1:1 Fe:V in synthesis, respectively.

**Table 3.2.1: Elemental analysis of (Fe, V)(BDC)(DMF). Calculated expected values for Fe(BDC)(DMF), for 33% and 50% vanadium substituted Fe(BDC)(DMF) and fully fluorinated Fe(BDC)(F) are also given.**

	Type	Synthesis Ratio	C / %	H / %	N / %	F / %	Fe / %	V / %
Meas.	(Fe, V)(BDC)(DMF, F)	2:1	40.94	2.29	3.44	5.47	17.32	2.44
		1:1	40.9	2.11	3.38	5.86	13.86	4.97
Calc.	Fe(BDC)(DMF) [*]		45.07	3.76	4.78	-	19.07	-
	$\text{Fe}_{0.67}\text{V}_{0.33}(\text{BDC})(\text{DMF})$ [*]		45.33	3.78	4.81	-	12.85	5.77
	$\text{Fe}_{0.5}\text{V}_{0.5}(\text{BDC})(\text{DMF})$ [*]		45.45	3.79	4.82	-	9.62	8.77
	Fe(BDC)(F) [*]		40.19	1.67	-	7.95	23.38	-

### 3.2.3. XANES

Iron and vanadium K-edge XANES spectra of the fluorinated samples display a clear shift in the K-edge of both metals to lower energies than for MIL-53(Fe<sup>III</sup>) or for the related material MIL-68(V<sup>III</sup>), consistent with a decrease in average oxidation state of the metals (see Figure 3.2.3). Comparison with reference materials (see Table 3.2.2) would suggest an average Fe oxidation state of around 2.7 for all the materials. This can be rationalised by partial substitution of the neutral DMF molecules for fluoride anions. The observed shift in oxidation state is not equivalent for iron and vanadium, with iron showing an oxidation state closer to +3 than for vanadium which appears to be more reduced (~2.2 on average) (Table 3.2.3). This suggests that most of the fluoride is found adjacent to iron centres in the mixed frameworks. This is consistent with the observation that no fluorinated vanadium analogues of MIL-53 type structure exist whereas MIL-53(Fe<sup>III</sup>) has been synthesised with greater than 20 % substitution of hydroxyl groups for fluoride.<sup>12</sup>

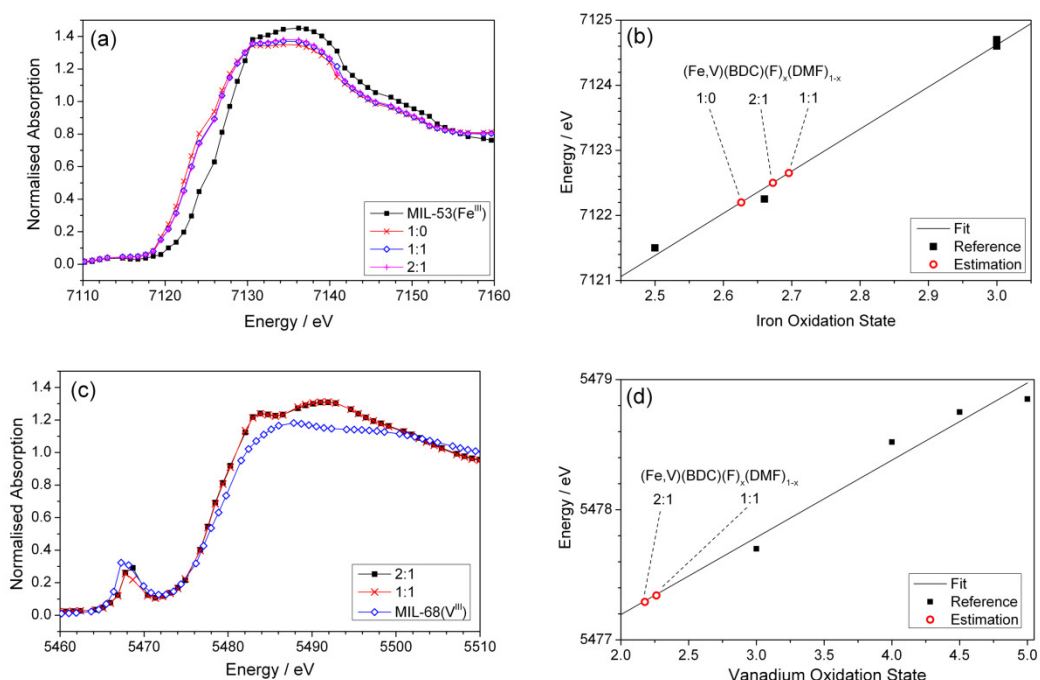


Figure 3.2.3: XANES spectra of (Fe,V)(BDC)(DMF,F) materials at (a) the iron K edge and (b) the vanadium K-edge. Estimates of the oxidation states are shown in (b) and (d) for iron and vanadium respectively. Edge positions and the reference materials used are given in Table 3.2.2 and Table 3.2.3.

**Table 3.2.2: Iron K-edge positions of reference materials and (Fe, V)(BDC)(DMF, F). Reference compound oxidation states in bold. Edge positions defined as the energy at which the normalised absorption is equal to 0.5**

Compound	Edge Position / eV	Oxidation State
Fe <sub>2</sub> O <sub>3</sub>	7124.6	<b>3</b>
Fe <sub>3</sub> O <sub>4</sub>	7122.25	<b>2.66</b>
Fe(BDC)(OH,F) (MIL-53(Fe))	7124.7	<b>3</b>
[Fe(BDC)(OH, F)] <sup>0.5-</sup> ·0.5DMA <sup>+</sup>	7121.5	<b>2.5</b>
Fe(BDC)(DMF, F)	7122.65	2.70
(Fe <sub>0.88</sub> V <sub>0.12</sub> )(BDC)(DMF, F)	7122.5	2.67
(Fe <sub>0.76</sub> V <sub>0.24</sub> )(BDC)(DMF, F)	7122.2	2.62

**Table 3.2.3: Vanadium K-edge positions of reference materials and (Fe, V)(BDC)(DMF, F). Reference compound oxidation states in bold. Edge positions defined as the energy at which the normalised absorption is equal to 0.5**

Compound	Edge Position / eV	Oxidation State
V <sub>2</sub> O <sub>5</sub>	5478.85	<b>5</b>
NaV <sub>2</sub> O <sub>5</sub>	5478.7	<b>4.5</b>
CaVO <sub>3</sub>	5478.52	<b>4</b>
V(BDC)(OH) (MIL-68(V))	5477.7	<b>3</b>
(Fe <sub>0.88</sub> V <sub>0.12</sub> )(BDC)(DMF, F)	5477.19	2.18
(Fe <sub>0.76</sub> V <sub>0.24</sub> )(BDC)(DMF, F)	5477.79	2.26

### 3.2.4. <sup>57</sup>Fe Mössbauer Spectroscopy

As is illustrated in Figure 3.2.4 and listed in Table 3.2.1, <sup>57</sup>Fe Mössbauer spectroscopy provides further insight into the both the oxidation state and the environment of iron in the (Fe, V)(BDC)(DMF, F) materials. Both mixed metal and the pure iron materials show evidence of ~30 % high spin Fe(II) and ~70 % high spin Fe(III), *i.e.*, an average Fe oxidation state of close to 2.75, entirely consistent with the XANES results.

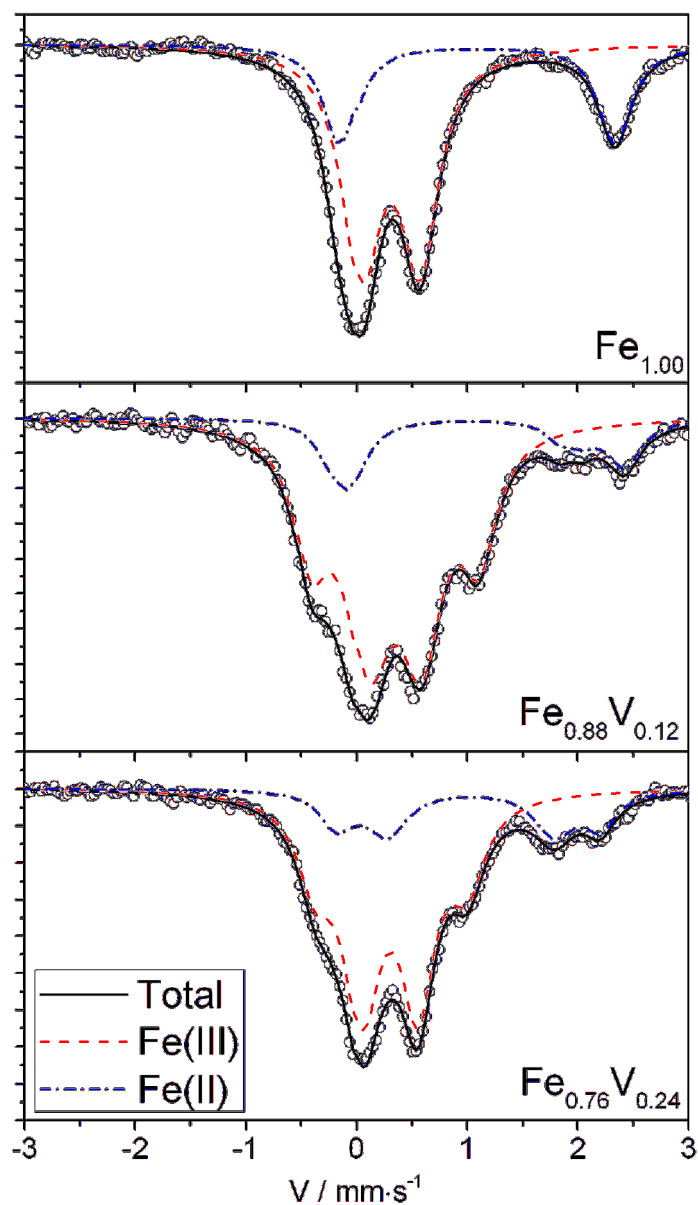


Figure 3.2.4:  $^{57}\text{Fe}$  Mössbauer spectra of  $(\text{Fe}, \text{V})(\text{BDC})(\text{DMF}, \text{F})$  materials recorded at 300 K. The amounts of each metal in each sample are indicated.

Table 3.2.4: Results of fitting of the  $^{57}\text{Fe}$  Mössbauer spectra at 300 K and 77 K for  $(\text{Fe}, \text{V})(\text{BDC})(\text{DMF}, \text{F})$  materials.

	Fe(III) / % (300K : 77K)	Fe(II) / % (300K : 77K)
$\text{Fe}(\text{BDC})(\text{DMF}, \text{F})$	$70 \pm 2 : 70 \pm 2$	$30 \pm 2 : 30 \pm 2$
$\text{Fe}_{0.88}\text{V}_{0.12}(\text{BDC})(\text{DMF}, \text{F})$	$83 \pm 2 : 82 \pm 2$	$17 \pm 2 : 18 \pm 2$
$\text{Fe}_{0.76}\text{V}_{0.24}(\text{BDC})(\text{DMF}, \text{F})$	$77 \pm 2 : 78 \pm 2$	$23 \pm 2 : 22 \pm 2$

Partial substitution of DMF by F leads to three potential iron environment where iron can be neighboured by either two DMF, one DMF and fluoride or two fluorides (Figure 3.2.5). From the elemental analysis of the (Fe, V)(BDC)(DMF, F) materials that show approximately 50 % substitution of DMF by fluoride, these three environments have the probabilities of 25 %, 50 % and 25% respectively from a purely statistical viewpoint. Since the third case of two neighbouring fluorides can be discounted due to the lack of any known fluorinated MIL-53(Fe) beyond 20%, the two remaining environments now have the probability of 33 % for DMF-Fe-DMF and 67 % for DMF-Fe-F (and F-Fe-DMF). Iron neighboured by two neutral DMF will be divalent whereas the presence of fluoride neighbouring iron leads to trivalency. The ratio of Fe(II) to Fe(III) predicted by statistical means (33:67) is close to that seen by Mössbauer spectroscopy for Fe(BDC)(DMF, F) (30:70). Substitution of iron for vanadium in primarily divalent positions leads to the overall decrease in the iron (II) ratio as seen by both XANES and Mössbauer substitution in Table 3.3.2 Table 3.3.4.

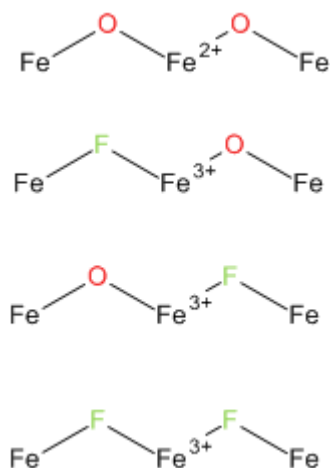


Figure 3.2.5: Potential iron environments found in Fe(BDC)(DMF, F)

In addition, the Mössbauer spectra of the 2:1 and 1:1 Fe:V materials show the presence of both Fe(II) and Fe(III) each in two differing environments as evidenced by the clear splitting of each peak (Figure 3.2.4). This can be interpreted as the presence of iron

adjacent to either one vanadium neighbours or solely iron neighbours along the inorganic chains of the MIL-53 structure; since both materials are iron rich the probability of finding iron adjacent to two vanadium neighbours is low.

### 3.2.5. Thermal Behaviour

Thermogravimetric analysis for both  $(\text{Fe,V})(\text{BDC})(\text{DMF}, \text{F})$  mixed-metal samples shows a gradual mass loss beginning at around 200°C to 400°C of approximately 14 % (see Figure 3.2.6 and Figure 3.2.7). This agrees well with the loss of coordinated DMF (13 % expected). A second, larger mass loss relating to the combustion of the BDC linkers begins at 400 °C. After this loss, total mass losses of 29.7 and 31.4 % for the  $\text{Fe}_{0.88}\text{V}_{0.12}$  and  $\text{Fe}_{0.76}\text{V}_{0.24}$  samples, respectively, were seen. These values correspond well to the theoretical composition of the residual materials of 30.8 and 31.7 %, assuming complete oxidation of the metals to mixtures of  $\text{Fe}_2\text{O}_3$  and  $\text{V}_2\text{O}_5$ .

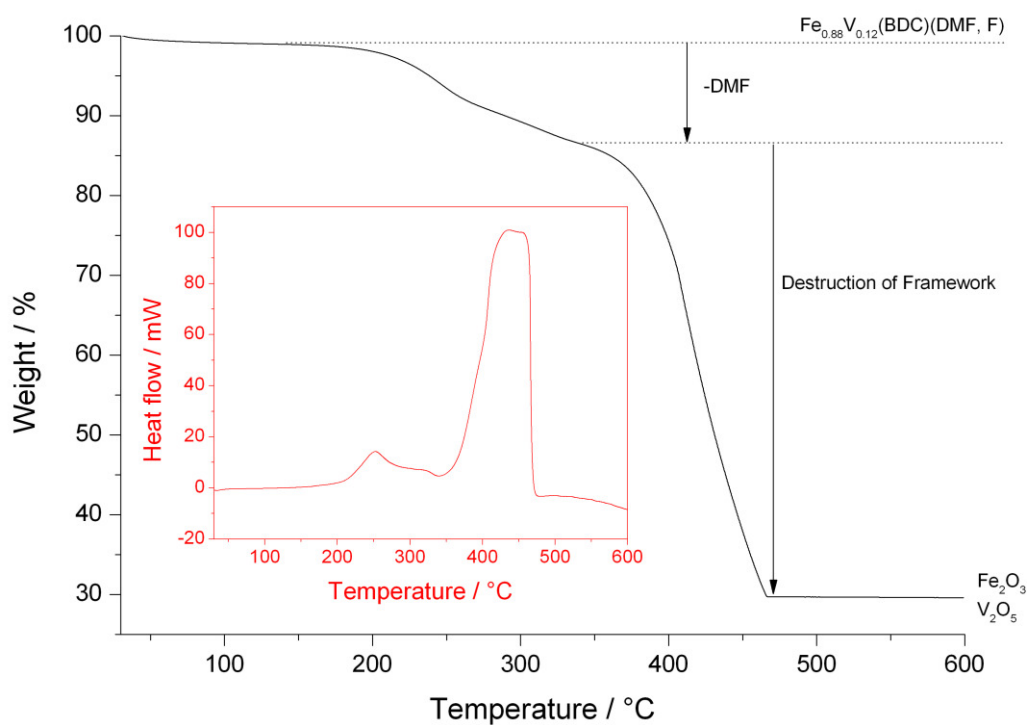


Figure 3.2.6: Main: TGA of  $(\text{Fe}_{0.88}\text{V}_{0.12})(\text{BDC})(\text{DMF}, \text{F})$  in air; Insert: DSC curve over the same temperature range

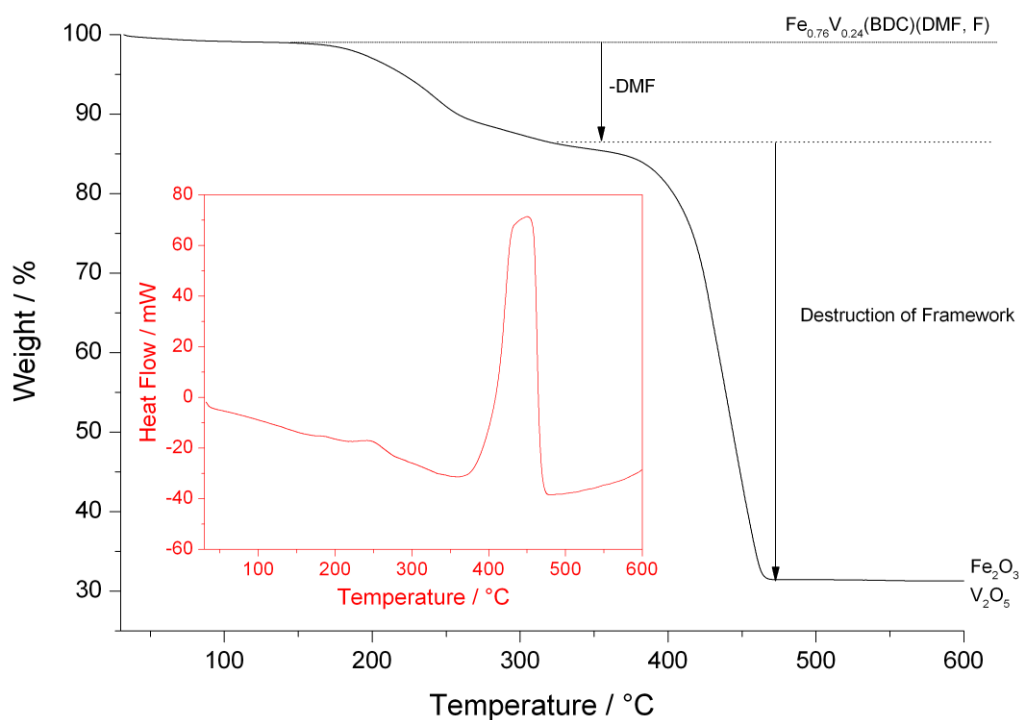


Figure 3.2.7: Main: TGA of  $(\text{Fe}_{0.76}\text{V}_{0.24})(\text{BDC})(\text{DMF}, \text{F})$  in air; Insert: DSC curve over the same temperature range

Thermodiffractometry of the  $(\text{Fe},\text{V})(\text{BDC})(\text{DMF},\text{F})$  materials (Figure 3.2.8) show the appearance of second phases at around 200 °C. The second phases are stable until 330 °C and 420 °C for the  $\text{Fe}_{0.88}\text{V}_{0.12}$  and the  $\text{Fe}_{0.76}\text{V}_{0.24}$  materials before decomposing into an amorphous material. This thermal behaviour agrees well with the TGA profiles. Large differences are seen in the XRD patterns of each material at 300 °C, but both patterns can be identified as both open and closed forms of the MIL-53 type structure. The  $\text{Fe}_{0.88}\text{V}_{0.12}$  material displays a closed form like MIL-53( $\text{Fe}^{\text{III}}$ ) whereas the  $\text{Fe}_{0.76}\text{V}_{0.24}$  material fully opens, as seen in MIL-47( $\text{V}^{\text{IV}}$ ). This suggests an effect of metal substitution on the properties of the material. The MIL-53 materials produced in this way, however, are poorly crystalline and were not studied further (see section 3.4 for synthesis of more crystalline forms of these materials).

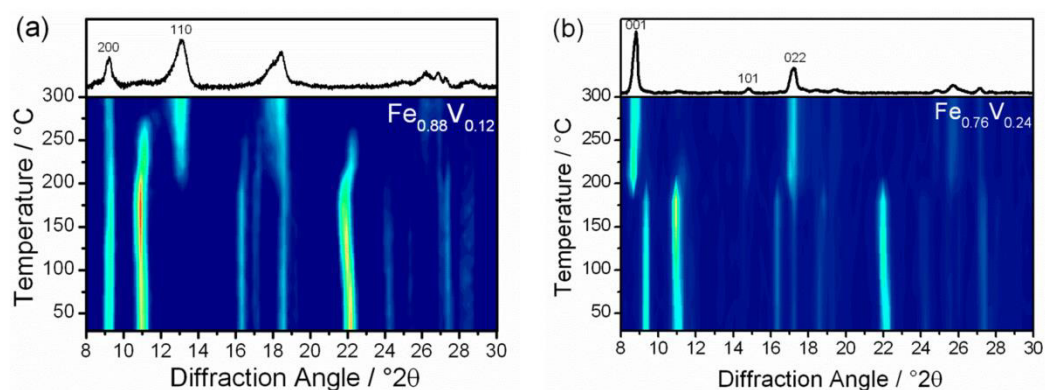


Figure 3.2.8: Thermodiffractometry of the (Fe, V)(BDC)(DMF, F) materials with the individual pattern of each material at 300°C, which can be indexed as (a) the closed *Imma* and (b) open *C/2c* forms of MIL-53(Fe,V)

### 3.2.6. Infrared Spectroscopy of (Fe<sub>0.88</sub>V<sub>0.12</sub>)(BDC)(OH, F)

IR spectroscopy of (Fe<sub>0.88</sub>V<sub>0.12</sub>)(BDC)(DMF,F)(Figure 6) further supports the observations of thermodiffractometry. Loosely adsorbed DMF and a small amount of unreacted carboxylic acid are found as impurities. The peak at 1692 cm<sup>-1</sup> indicates the presence of free carboxylic acid and this is removed at 200°C. The peak at 1663 cm<sup>-1</sup>, corresponding to free DMF, disappears at 100°C under vacuum, as well as weak associated bands at 2899 and 2805 cm<sup>-1</sup>. Metal-coordinated DMF should show a  $\nu(\text{C=O})$  band at lower wavenumber than free DMF but it is likely hidden by the carboxylate vibrations. However, it is noteworthy that  $\nu(\text{CH}_3)$  bands remain present at *ca* 2924 and 2852 cm<sup>-1</sup> up to 350°C. This confirms the presence of DMF directly, and strongly, coordinated to the MIL-53 structure. The other bands in the spectrum remain similar to those of the calcined MIL-53(Fe,V) (see below) except at 400°C where the material starts to degrade. One can also observe that the band at 3646 cm<sup>-1</sup> corresponding to  $\nu(\text{OH})$ , and the  $\delta(\text{OH})$  band at 850 cm<sup>-1</sup> (not shown) attributed to Fe-OH-Fe (see section 3) remain unchanged upon DMF removal but only vanish above 300°C. This is possible if DMF bridges preferentially to vanadium sites and that either hydroxyl or fluorine coordinate to iron.



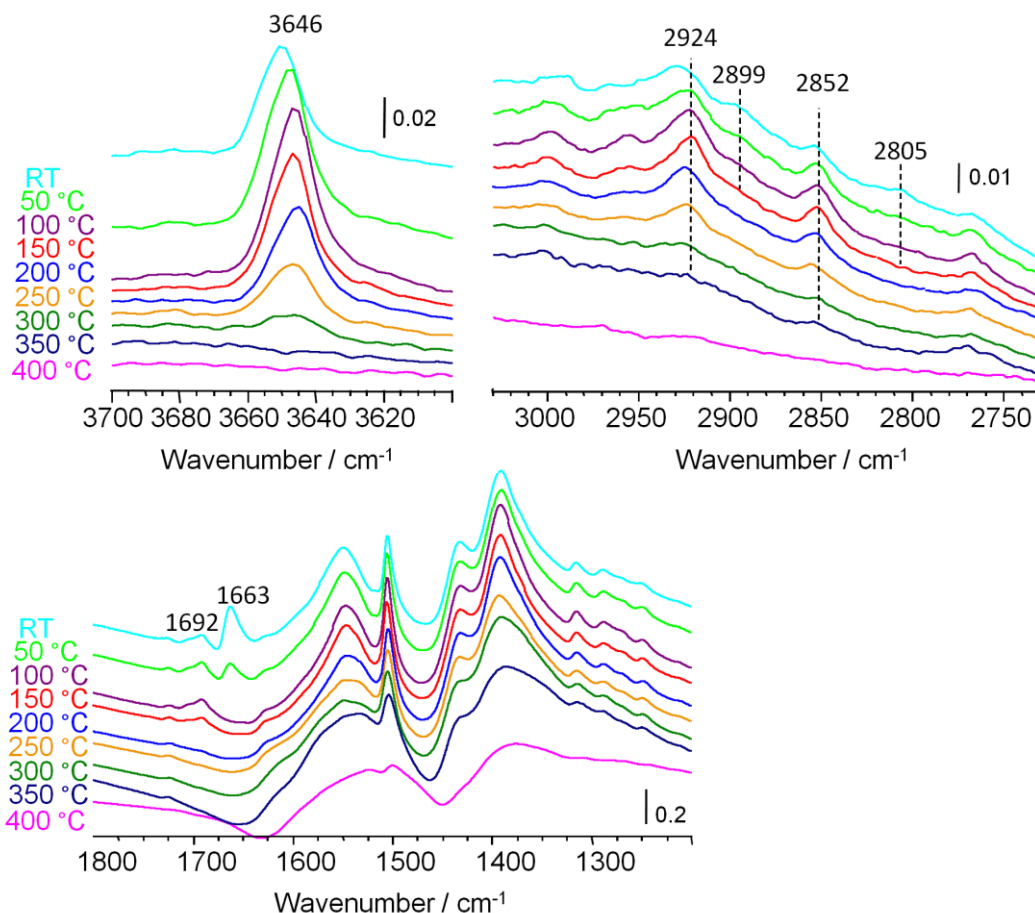


Figure 3.2.9: Three regions of the absorbance IR spectra of the  $(\text{Fe}_{0.88}\text{V}_{0.12})(\text{BDC})(\text{DMF},\text{F})$  material during heating under vacuum.

### 3.3. $[(\text{Fe}, \text{V})(\text{BDC})(\text{OH}, \text{F})]^{0.5-} \cdot 0.5\text{DMA}^+$

#### 3.3.1. Synthesis

Anhydrous iron (III) chloride and vanadium (III) chloride in ratios 2:1 and 1:1 (0.002 mol total metal) and  $\text{H}_2(\text{BDC})$  (0.002 mol) were dissolved into a mixture of DMF ( $10 \text{ cm}^3$ ),  $\text{H}_2\text{O}$  ( $0.3 \text{ cm}^3$ ) and HF (0.1 cm). The mixture was stirred at room temperature and then transferred into Teflon liners. The Teflon liners were placed in steel autoclaves, kept at  $170^\circ\text{C}$  for 72 hours and cooled to room temperature. The resulting dark brown powders were isolated by suction filtration, washed with DMF and dried in air. This synthesis route differs from that used by Medina *et al.* to form  $[\text{Fe}^{\text{III}}_{0.5}\text{Fe}^{\text{II}}_{0.5}(\text{BDC})(\text{OH}, \text{F})]^{0.5-} \cdot 0.5\text{DMA}^+$  by using longer reaction times (3 days instead of 12 hours), higher temperatures ( $170^\circ\text{C}$  over  $150^\circ\text{C}$ )

°C) and using a far larger volume of solvent (ten times as much).<sup>13</sup> These changes have the same effect of catalysing DMF hydrolysis, leading to both metal reduction and generation of the dimethylammonium ( $\text{DMA}^+$ ) counter-ion. Attempts to increase the vanadium content further lead to the formation of MIL-68.<sup>10</sup>

### 3.3.2. Structure and Composition

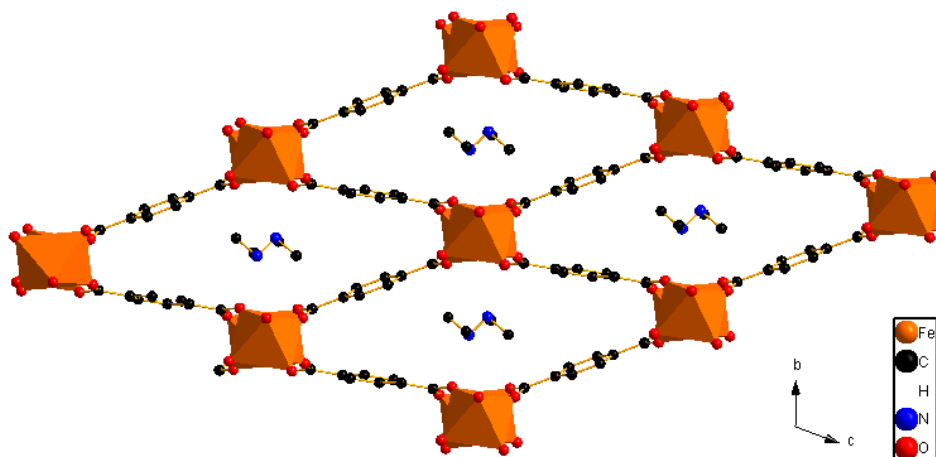


**Figure 3.3.1:** Crystal structure of  $[\text{Fe}^{\text{III}}_{0.5}\text{Fe}^{\text{II}}_{0.5}(\text{BDC})(\text{OH}, \text{F})]^{0.5-} \cdot 0.5\text{DMA}^+$  viewed along the  $a$ -axis

A profile fit of the PXRD patterns of the two  $[(\text{Fe}, \text{V})^{\text{III}}_{0.5}(\text{Fe}, \text{V})^{\text{II}}_{0.5}(\text{BDC})(\text{OH}, \text{F})]^{0.5-} \cdot 0.5\text{DMA}^+$  materials formed using initial iron-vanadium ratios of 2:1 and 1:1 show that these materials share the same structure as that of the reported  $[\text{Fe}^{\text{III}}_{0.5}\text{Fe}^{\text{II}}_{0.5}(\text{BDC})(\text{OH}, \text{F})]^{0.5-} \cdot 0.5\text{DMA}^+$  material (Figure 3.3.2). Since the purely iron analogue contains both Fe(II) and Fe(III), it must be case that the mixed iron-vanadium analogues must contain either reduced iron or vanadium or a mixture of both. For these materials, increasing vanadium content results in an increase in unit cell volume (Figure 3.3.2); for comparison the pure Fe material has triclinic cell parameters  $a = 6.9004(14) \text{ \AA}$ ,  $b = 8.554(3) \text{ \AA}$ ,  $c = 10.380(3) \text{ \AA}$ ,  $\alpha = 107.15(2)^\circ$ ,  $\beta = 100.155(17)^\circ$ ,  $\lambda = 102.095(17)^\circ$  and  $V = 553.6(2) \text{ \AA}^3$ .<sup>14</sup> This would be consistent with replacement of  $\text{Fe}^{2+}/\text{Fe}^{3+}$  with the slightly larger  $\text{V}^{2+}/\text{V}^{3+}$  cations. Further evidence for the incorporation of vanadium is given by colour; dark brown opposed to the orange reported for the iron analogue.

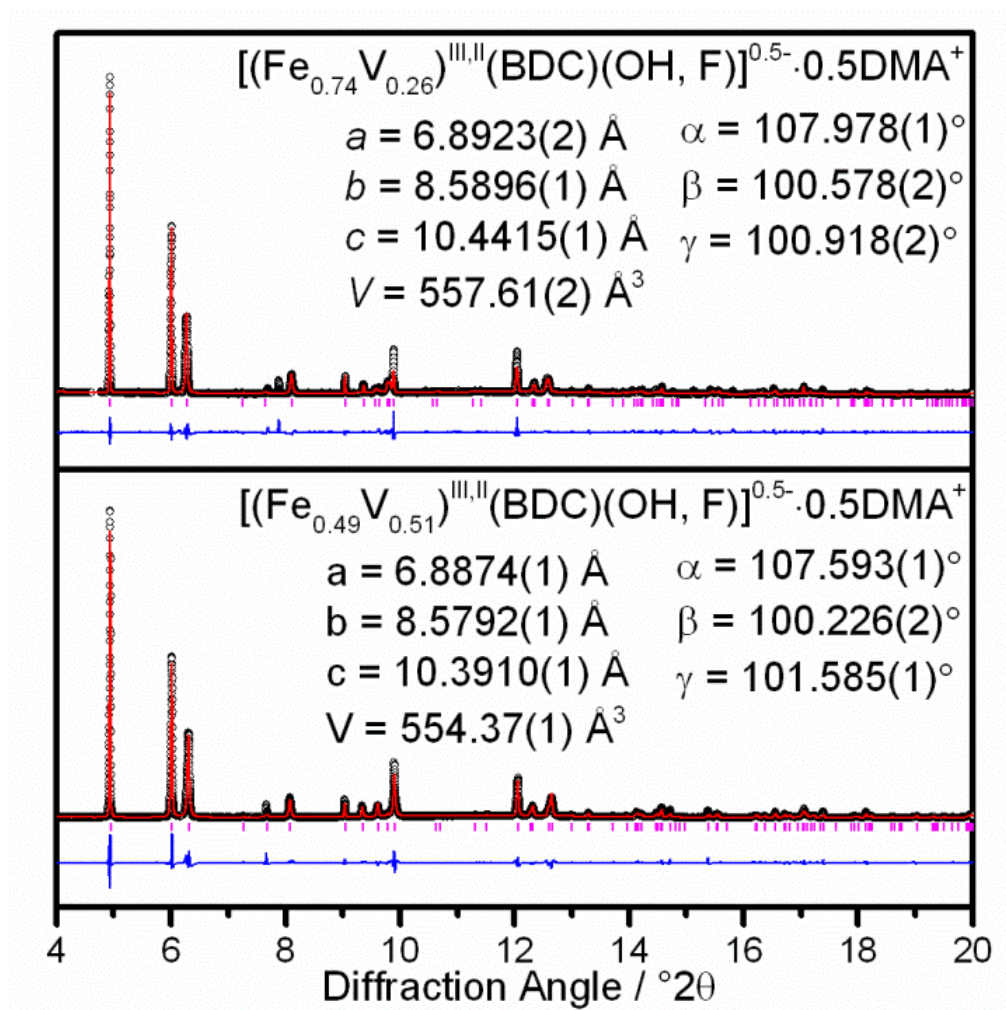


Figure 3.3.2: High resolution powder XRD patterns with profile fits and refined unit cell parameters of  $[(\text{Fe}, \text{V})(\text{BDC})(\text{OH}, \text{F})]^{0.5-} \cdot 0.5\text{DMA}^+$  materials. Data were collected on Beamline I11 at Diamond ( $\lambda = 0.825164 \text{ \AA}$ ). Raw data are black circles, the red line is the fit, and the blue line is the difference. Both materials crystallise in the *PI* space group

The amount of iron and vanadium in each sample was determined by elemental analysis: the ratio of Fe:V was found to be 2.8:1 and 0.96:1 for the materials synthesised using 2:1 and 1:1 ratios of iron to vanadium respectively, agreeing well with expected values (Table 3.2.1). A large discrepancy was seen between the theoretical and elemental results for fluorine, however. Even assuming that all the framework hydroxyl groups have been replaced, a value for fluorine content of around 7.3 % would be expected, lower than the values of 11.45 % and 9.72 % observed for the two materials. One explanation for the higher fluorine content is the presence of an amorphous fluorinated by-product. The high-resolution powder X-ray diffraction, however, shows negligible amorphous background. If

the fluorinated by-product was present inside the channels, it would also be difficult to determine by powder diffraction, and another possible explanation is the capping of the metal-oxide chains by fluoride at the crystal surface; this would be consistent with the increased fluorine values at the expense of CHN content seen in both materials.

**Table 3.3.1: Elemental analysis of  $[(\text{Fe}, \text{V})(\text{BDC})(\text{OH}, \text{F})]^{0.5} \cdot 0.5\text{DMA}^+$ . Expected values for the theoretical fully hydroxylated  $[(\text{Fe})(\text{BDC})(\text{OH})]^{0.5} \cdot 0.5\text{DMA}^+$  and fully fluorinated  $[(\text{Fe})(\text{BDC})(\text{F})]^{0.5} \cdot 0.5\text{DMA}^+$  are also given.**

	Type	Synthesis Ratio	C / %	H / %	N / %	F / %	Fe / %	V / %
Meas.	$[(\text{Fe}, \text{V})(\text{BDC})(\text{OH}, \text{F})]^{0.5} \cdot 0.5\text{DMA}^+$	2:1	36.47	2.28	3.24	11.45	16.71	4.67
		1:1	37.46	2.01	3.19	9.72	10.89	10.56
Calc.	$[(\text{Fe})(\text{BDC})(\text{OH})]^{0.5} \cdot 0.5\text{DMA}^+ [*]$	-	41.24	3.44	2.67	-	21.33	41.24
	$[(\text{Fe})(\text{BDC})(\text{F})]^{0.5} \cdot 0.5\text{DMA}^+$	-	41.24	3.06	2.67	7.26	21.33	41.24

### 3.3.3. XANES

XANES at the iron K-edge shows a clear shift to lower energies with increasing vanadium content for the two  $[(\text{Fe}, \text{V})(\text{BDC})(\text{OH}, \text{F})]^{0.5} \cdot 0.5\text{DMA}^+$  materials (Figure 3.3.3(a)). This indicates a decrease in the average iron oxidation state from the expected average value of 2.5, implying then that vanadium occupies the trivalent sites. Vanadium XANES supports this, with an average oxidation state of  $\sim 2.75$  (Figure 3.3.3(b)). This is consistent with approximately 75% of vanadium occupying the 3+ site. The preference of vanadium to be trivalent makes sense from a chemical point since vanadium(II) is a highly reducing species.<sup>15</sup>

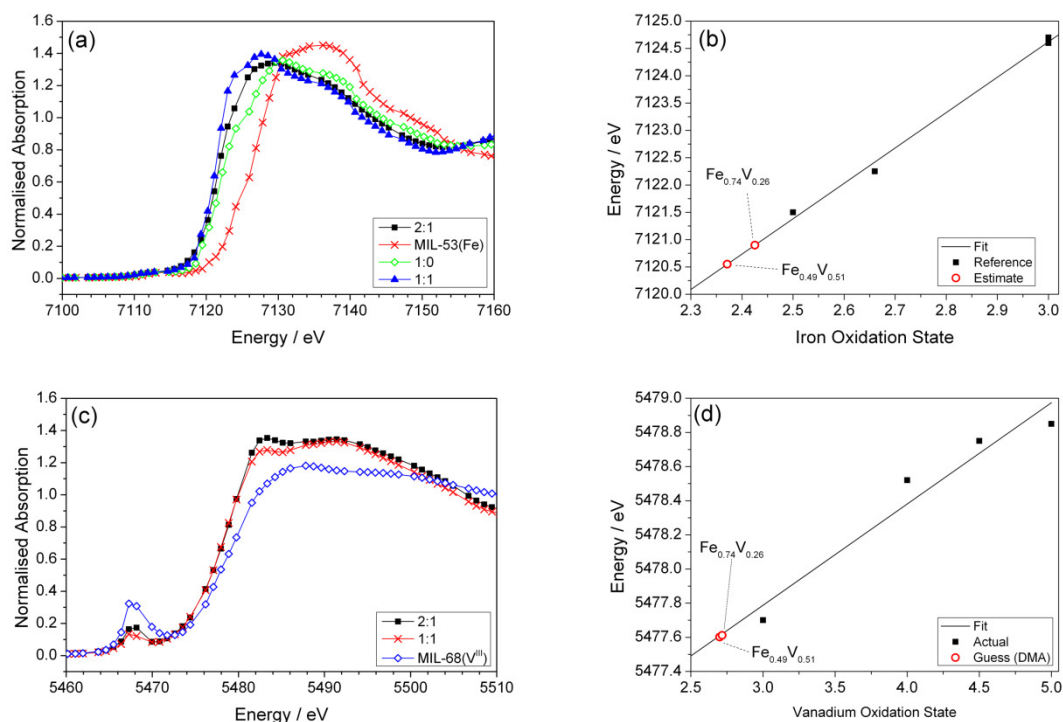


Figure 3.3.3: XANES spectra of  $[(\text{Fe}, \text{V})(\text{BDC})(\text{OH}, \text{F})]^{0.5-} \cdot 0.5\text{DMA}^+$  materials at (a) the iron K-edge and (c) the vanadium K-edge. Estimates of the oxidation states are shown in (b) and (d) for iron and vanadium respectively. Edge positions and the reference materials used are given in Table 3.3.2 and

Table 3.3.2: Iron K-edge positions of reference materials and  $[(\text{Fe}, \text{V})(\text{BDC})(\text{OH}, \text{F})]^{0.5-} \cdot 0.5\text{DMA}^+$ . Reference compound oxidation states in bold. Edge positions defined as the energy at which the normalised absorption is equal to 0.5

Compound	Edge Position / eV	Oxidation State
$\text{Fe}_2\text{O}_3$	7124.6	<b>3</b>
$\text{Fe}_3\text{O}_4$	7122.25	<b>2.66</b>
$\text{Fe}(\text{BDC})(\text{OH}, \text{F})$ (MIL-53(Fe))	7124.7	<b>3</b>
$[\text{Fe}(\text{BDC})(\text{OH}, \text{F})]^{0.5-} \cdot 0.5\text{DMA}^+$	7121.5	<b>2.5</b>
$[(\text{Fe}_{0.74}\text{V}_{0.26})(\text{BDC})(\text{OH}, \text{F})]^{0.5-} \cdot 0.5\text{DMA}^+$	7120.9	2.43
$[(\text{Fe}_{0.49}\text{V}_{0.51})(\text{BDC})(\text{OH}, \text{F})]^{0.5-} \cdot 0.5\text{DMA}^+$	7120.55	2.37

**Table 3.3.3: Vanadium K-edge positions of reference materials and  $[(\text{Fe}, \text{V})(\text{BDC})(\text{OH}, \text{F})]^{0.5-} \cdot 0.5\text{DMA}^+$ .**  
Reference compound oxidation states in bold. Edge positions defined as the energy at which the normalised absorption is equal to 0.5

Compound	Edge Position / eV	Oxidation State
$\text{V}_2\text{O}_5$	5478.85	<b>5</b>
$\text{NaV}_2\text{O}_5$	5478.7	<b>4.5</b>
$\text{CaVO}_3$	5478.52	<b>4</b>
$\text{V}(\text{BDC})(\text{OH})$ (MIL-68(V))	5477.7	<b>3</b>
$[(\text{Fe}_{0.74}\text{V}_{0.26})(\text{BDC})(\text{OH}, \text{F})]^{0.5-} \cdot 0.5\text{DMA}^+$	5477.3	2.70
$[(\text{Fe}_{0.49}\text{V}_{0.51})(\text{BDC})(\text{OH}, \text{F})]^{0.5-} \cdot 0.5\text{DMA}^+$	5477.35	2.72

### 3.3.4. $^{57}\text{Fe}$ Mössbauer Spectroscopy

$^{57}\text{Fe}$  Mössbauer spectroscopy gives results that agree completely with the expected occupation of vanadium in the trivalent sites in these materials, Figure 3.3.4. For the parent  $[\text{Fe}^{\text{III}}_{0.5}\text{Fe}^{\text{II}}_{0.5}(\text{BDC})(\text{OH}, \text{F})]^{0.5-} \cdot 0.5\text{DMA}$ , the amounts of trivalent and divalent iron is close to the value of 50:50 Fe(II):Fe(III) expected. For the  $\text{Fe}_{0.74}\text{V}_{0.26}$  material, a ratio of 26:74 Fe(III):Fe(II) is seen, rather close to the expected value of 33:66 where all of the vanadium is occupying trivalent sites, leading to a diminution of iron(III) sites by half. The  $\text{Fe}_{0.49}\text{V}_{0.51}$  material contains Fe(III):Fe(II) ratio of 28:72. This is less than the expected case where all Fe(III) sites are occupied by vanadium, suggesting that a small fraction of the vanadium is present in the divalent state, again consistent with the XANES spectroscopy.

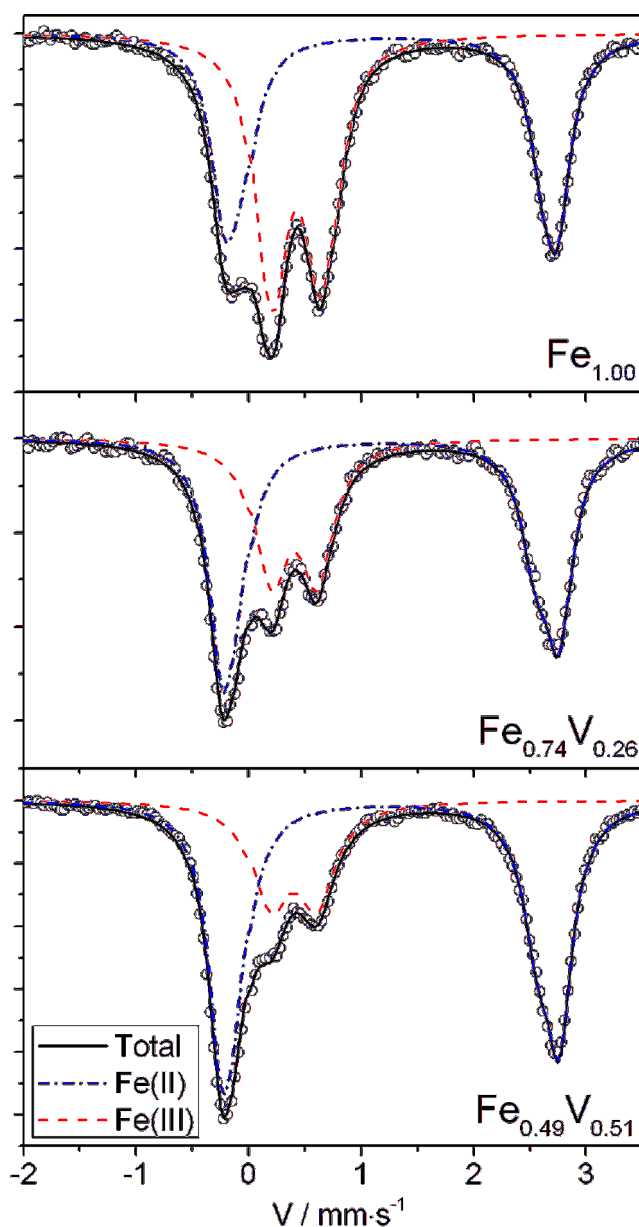


Figure 3.3.4: 77 K  $^{57}\text{Fe}$  Mössbauer spectra of the  $[(\text{Fe}, \text{V})(\text{BDC})(\text{OH}, \text{F})]^{0.5-} \cdot 0.5\text{DMA}^+$  materials

Table 3.3.4: Results of fitting of the  $^{57}\text{Fe}$  Mössbauer spectra for  $[(\text{Fe}, \text{V})(\text{BDC})(\text{OH}, \text{F})]^{0.5-} \cdot 0.5\text{DMA}^+$  at 300 K and 77 K

	Fe(III) / % (300K : 77K)	Fe(II) / % (300K : 77K)
$[(\text{Fe})(\text{BDC})(\text{OH}, \text{F})]^{0.5-} \cdot 0.5\text{DMA}^+$	$53 \pm 2 : 52 \pm 2$	$47 \pm 2 : 48 \pm 2$
$[(\text{Fe}_{0.74}\text{V}_{0.26})(\text{BDC})(\text{OH}, \text{F})]^{0.5-} \cdot 0.5\text{DMA}^+$	$40 \pm 2 : 36 \pm 2$	$60 \pm 2 : 64 \pm 2$
$[(\text{Fe}_{0.49}\text{V}_{0.51})(\text{BDC})(\text{OH}, \text{F})]^{0.5-} \cdot 0.5\text{DMA}^+$	$29 \pm 2 : 28 \pm 2$	$71 \pm 2 : 72 \pm 2$

### 3.3.5. Thermal Behaviour

Thermogravimetric analysis (Figure 3.3.5 and Figure 3.3.6) shows two major losses for each of the  $[(\text{Fe},\text{V})(\text{BDC})(\text{OH},\text{F})]^{0.5-} \cdot 0.5\text{DMA}^+$  materials. The first of around 11% at around 280°C corresponds to the loss of the DMA counter-ion (expected: 9.1%) plus residual solvent. Assuming oxidation of the framework at this point the materials will have composition  $[(\text{Fe}^{\text{III}}, \text{V}^{\text{III}})(\text{BDC})(\text{OH},\text{F})]$  and are expected to be direct analogues of MIL-53. Combustion of the framework begins at around 400°C and leads to losses of 57.9 % and 56.4 % for the  $\text{Fe}_{0.74}\text{V}_{0.26}$  and  $\text{Fe}_{0.49}\text{V}_{0.51}$  sample, respectively (expected: 56.6 % and 56.1 %).

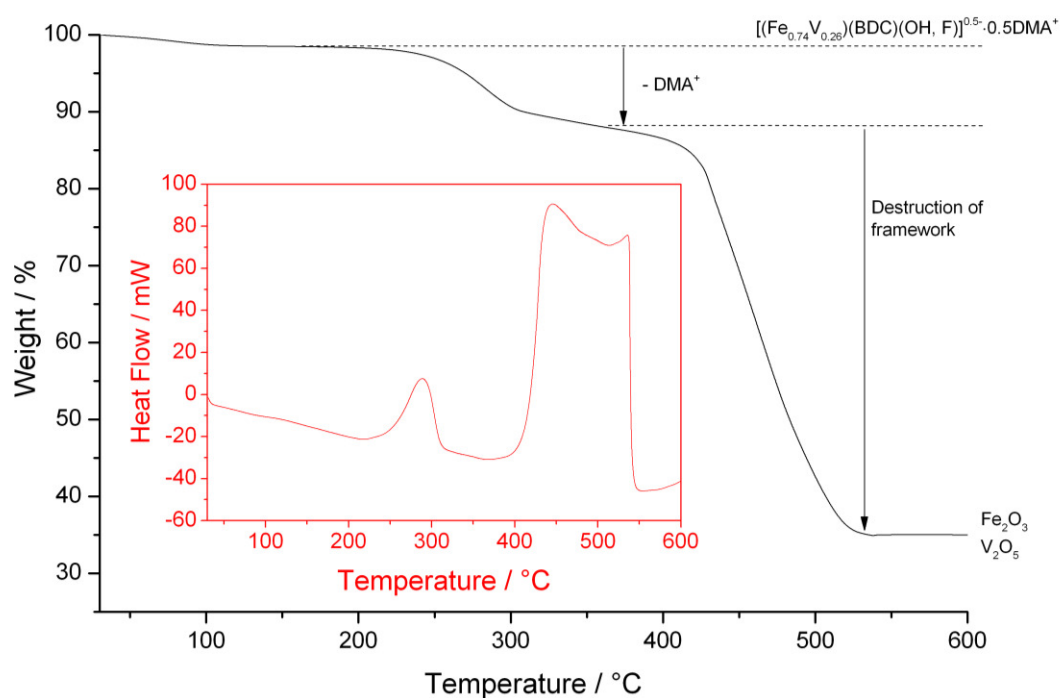


Figure 3.3.5: Main: TGA of  $[(\text{Fe}_{0.74}\text{V}_{0.26})(\text{BDC})(\text{OH}, \text{F})]^{0.5-} \cdot 0.5\text{DMA}^+$ ; Insert: DSC over the same temperature range



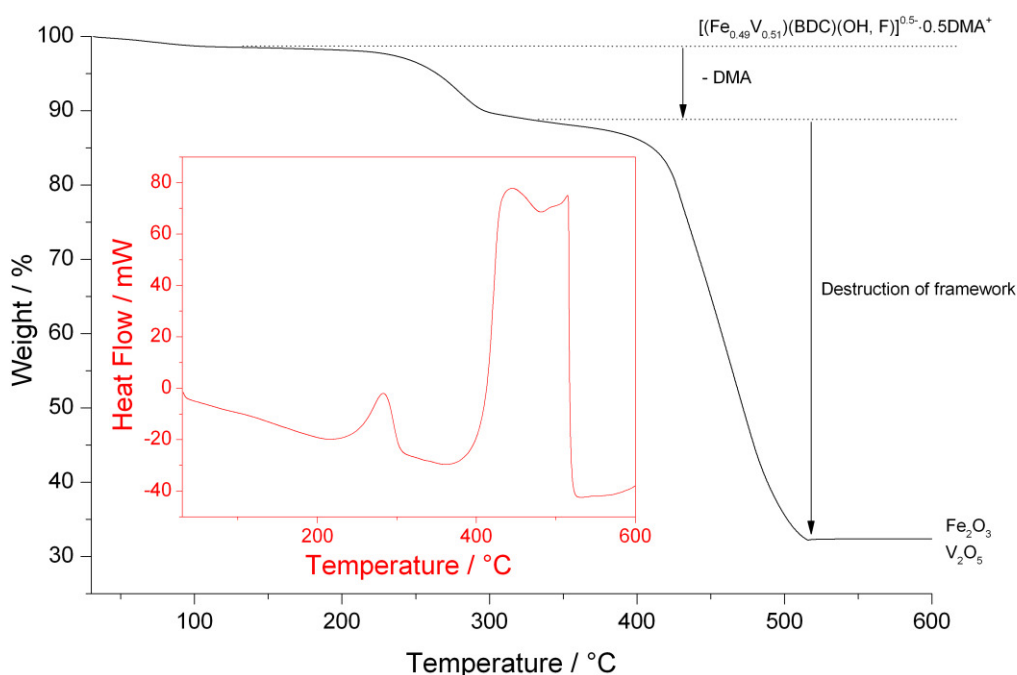


Figure 3.3.6: Main: TGA of  $[(\text{Fe}_{0.49}\text{V}_{0.51})(\text{BDC})(\text{OH}, \text{F})]^{0.5-} \cdot 0.5\text{DMA}^+$ ; Insert: DSC over the same temperature range

It has been reported that the material  $[\text{Fe}^{\text{III}}_{0.5}\text{Fe}^{\text{II}}_{0.5}(\text{BDC})(\text{OH}, \text{F})]^{0.5-} \cdot 0.5\text{DMA}^+$  loses the DMA counter ion upon heating at 300 °C in air, with oxidation of the iron to a trivalent state, leading to the formation of MIL-53( $\text{Fe}^{\text{III}}$ ).<sup>14</sup> To determine whether calcination of the mixed iron-vanadium materials would provide a means of synthesis of mixed-metal MIL-53( $\text{Fe}, \text{V}$ ) materials, thermodiffraction was measured. At 100 °C, both materials show clear changes in crystallinity, Figure 3.3.7. The result of the calcination is that both materials form a fully open structural form of MIL-53 at around 300 °C. This immediately suggests different behaviour than for the pure iron material, since the dehydrated high temperature form of MIL-53( $\text{Fe}^{\text{III}}$ ) exists in a closed form,<sup>16</sup> not open as we see with the mixed Fe,V materials. This implies that these MIL-53( $\text{Fe}, \text{V}$ ) materials are single, distinct phases containing a true mixture of the metals on an atomic scale and are not mixtures of MIL-53( $\text{Fe}^{\text{III}}$ ) and MIL-53( $\text{V}^{\text{III}}$ ), or a V-containing impurity. The presence of only a single distinct powder pattern during heating of both materials also allows us to conclude that they are truly mixed-metal materials as opposed to a mixture of two or more phases.

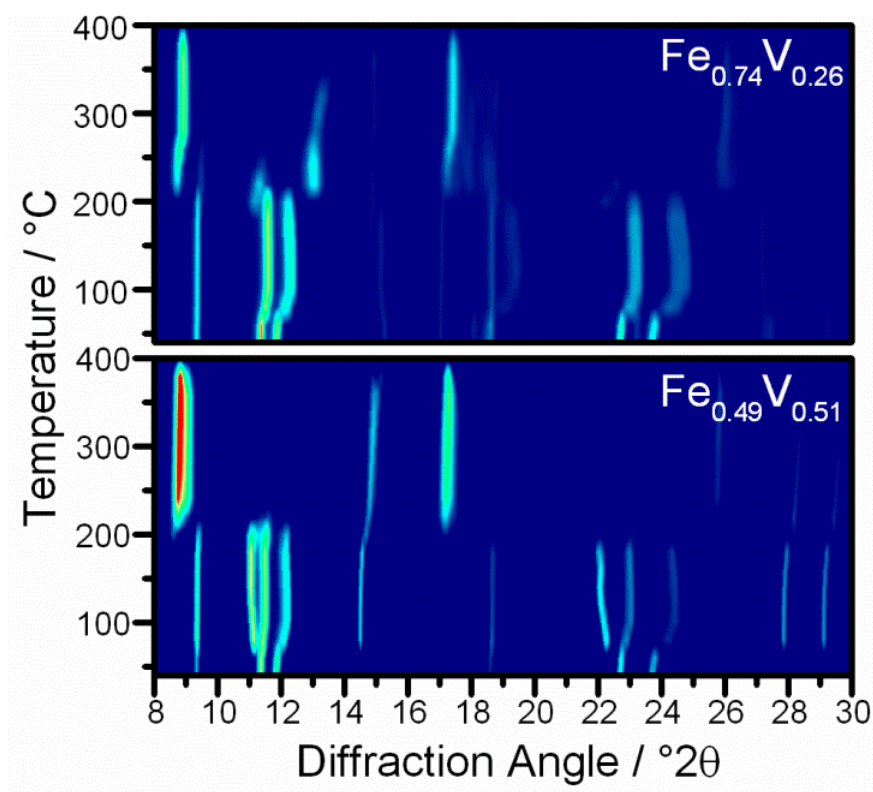
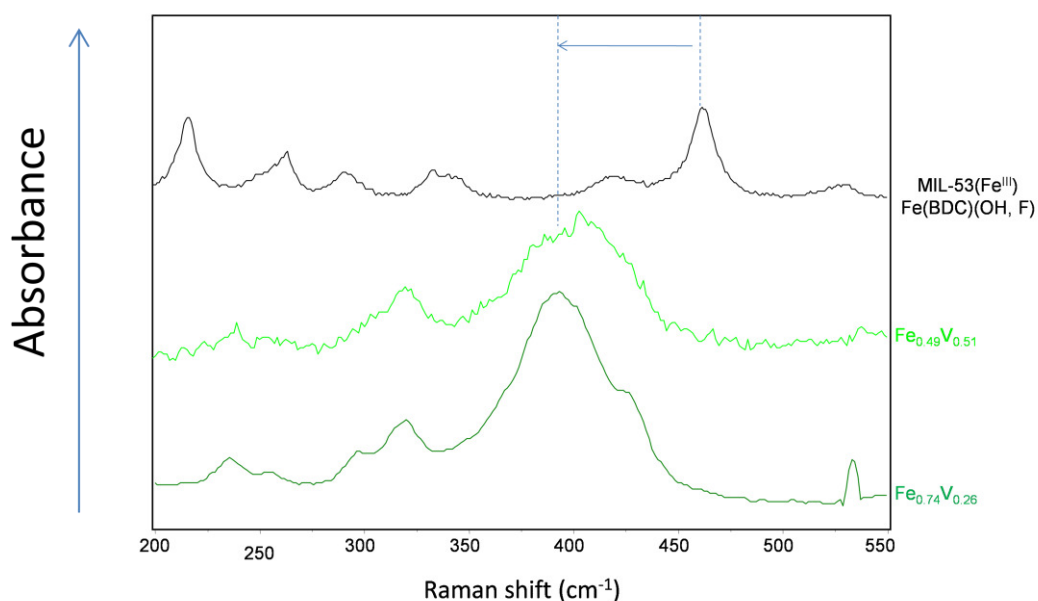


Figure 3.3.7: Thermodiffractometry of iron-vanadium DMA materials, displaying both calcination at  $\sim 250\text{ }^{\circ}\text{C}$  and eventual destruction of the framework at  $\sim 400\text{ }^{\circ}\text{C}$

### 3.3.6. Infrared and Raman Spectroscopy

Raman spectroscopy allows further investigation of the structure and calcination process of the  $[(\text{Fe},\text{V})(\text{BDC})(\text{OH},\text{F})]^{0.5-} \cdot 0.5\text{DMA}^+$  materials. Both materials show downward shifts of the Fe-O-M bond vibrations compared to MIL-53(Fe) from *ca* 460 to  $400\text{ cm}^{-1}$  (see below). This is consistent with the lengthening of Fe-O bonds suggesting the presence of divalent Fe, although signals directly attributable to Fe(II) or V(II) could not be identified unambiguously.



**Figure 3.3.8: Raman spectroscopy of DMA materials and MIL-53(Fe). Illustrated is the shift in the Fe-O-M band**

The IR spectra of both DMA containing solids show an intense broad band around 3150-3170 cm<sup>-1</sup> which was absent from the DMF containing solid (Figure 3.2.2). This band, which can be assigned to perturbed  $\nu(\text{N-H})$ , confirms the degradation of the DMF in the synthesis into DMA. Loss of DMA occurs around 350-400 °C under vacuum, *i.e.* at higher temperature than under oxygen-containing atmospheres, as evidenced by TGA or Raman spectroscopy. Figure 10 shows the presence of hydroxyl groups on  $[(\text{Fe}_{0.49}\text{V}_{0.51})(\text{BDC})(\text{OH},\text{F})]^{0.5-} \cdot 0.5\text{DMA}^+$ . These bands at 3636 and 850 cm<sup>-1</sup> which persist up to 300°C could be attributed to M-OH-M vibrations (see below).

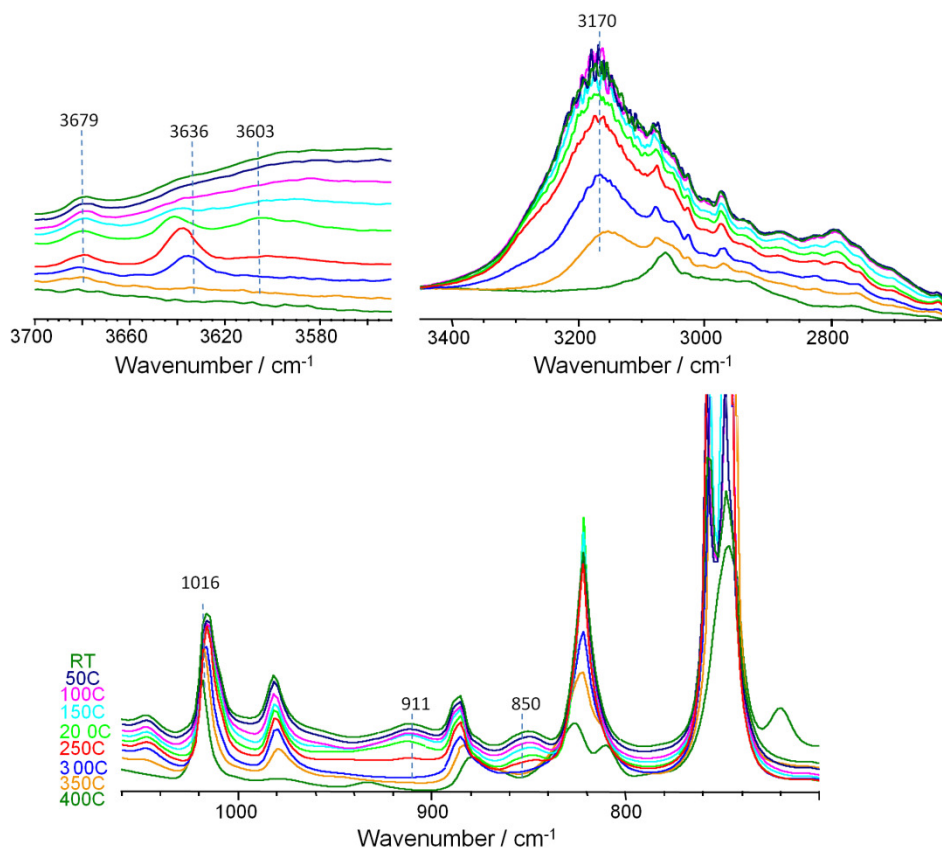


Figure 3.3.9: Three regions of the absorbance IR spectra of  $[(\text{Fe}_{0.49}\text{V}_{0.51})(\text{BDC})(\text{OH}, \text{F})]^{0.5} \cdot 0.5\text{DMA}^+$  during heating under vacuum

The calcination of these materials was also followed by Raman spectroscopy *in situ* (Figure 3.3.8). Most of DMA is first removed under argon flow at 250°C. Oxidation was then observed and the final form of MIL-53(Fe,V) was quickly obtained. The loss of DMA and oxidation of the metal centres were also ascertained by the structural change. Both materials transformed from a closed to an open structure, as evidenced by the shift of the  $\nu(\text{COO})$  band from 1421 to *ca* 1440  $\text{cm}^{-1}$ .<sup>4,17</sup>

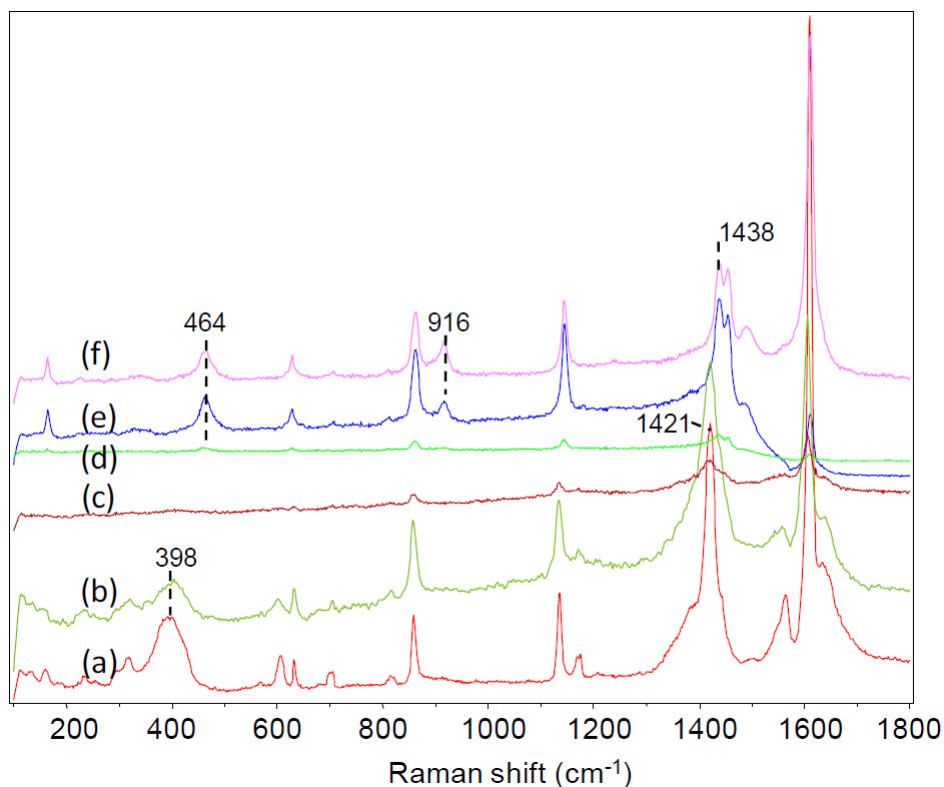


Figure 3.3.10: Raman spectra in situ of  $[(\text{Fe}_{0.49}\text{V}_{0.51})(\text{BDC})(\text{OH}, \text{F})]^{0.5-} \cdot 0.5\text{DMA}^+$  during calcination. (a) : under Ar at 20 °C ; under Ar at 250°C for 3 min (b) and 180 min (c) ; subsequently treated under Ar/O<sub>2</sub> at 250°C for 3 min (d), 11 min (e) and 63 min (f).

### 3.4. MIL-53(Fe, V)

#### 3.4.1. Synthesis

As mentioned in section 3.3.5, the pure iron analogue of the DMA materials,  $[\text{Fe}^{\text{III}}_{0.5}\text{Fe}^{\text{II}}_{0.5}(\text{BDC})(\text{OH}, \text{F})]^{0.5-} \cdot 0.5\text{DMA}^+$  could be calcined at 300°C to form the purely trivalent MIL-53(Fe) –  $\text{Fe}^{\text{III}}(\text{BDC})(\text{OH}, \text{F})$ . As seen in Figure 3.3.7, calcination of the iron-vanadium DMA materials lead to the formation of open MIL-53 type structures although it remained to be seen what would happen to these materials upon cooling. To investigate this, both iron-vanadium DMA materials were calcined at 300 °C for three hours in air then cooled back to room temperature using a ramping and cooling rate of 1 °C per minute. In both cases, MIL-53-like materials were formed.

### 3.4.2. Structure and Composition

After the calcination process, the  $\text{Fe}_{0.74}\text{V}_{0.26}$  vanadium material closes to form a structure similar to that of hydrated  $\text{MIL-53}(\text{Fe}^{\text{III}})^{26}$ , whereas the  $\text{Fe}_{0.49}\text{V}_{0.51}$  material remains fully open, as expected for  $\text{MIL-47}(\text{V}^{\text{IV}})^{18}$  (Figure 3.4.1). The presence of only a single distinct powder pattern during heating and post-calcination of both materials also allows us to conclude that they are truly mixed-metal materials as opposed to a mixture of two or more phases. The refined unit cell parameters mostly show slight decreases from those reported for  $\text{MIL-53}(\text{Fe})$  and  $\text{MIL-47}(\text{V})$ , consistent with substitution of hydroxyl and oxide groups with the smaller fluoride anion. A comparison of the values is given in Table 3.4.1.

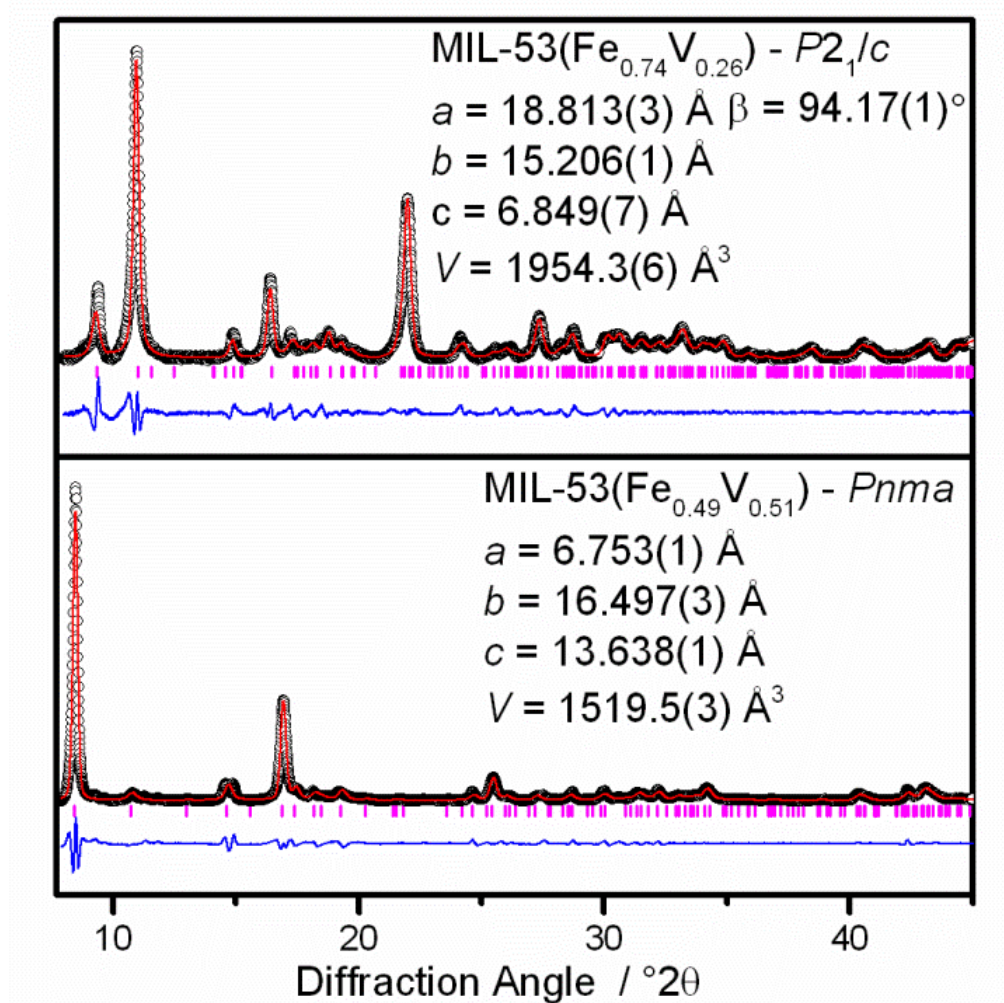
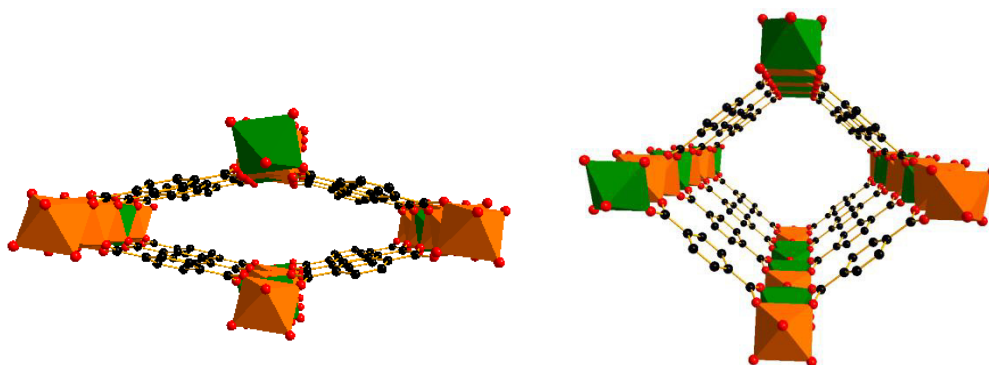


Figure 3.4.1: Profile fits to room temperature powder XRD patterns ( $\lambda = 1.5406 \text{ \AA}$ ) of  $\text{MIL-53}(\text{Fe},\text{V})$  materials prepared by calcination of  $[(\text{Fe}_x\text{V}_y)(\text{BDC})(\text{OH}, \text{F})]^{0.5-} \cdot 0.5\text{DMA}^+$  at  $300^\circ\text{C}$ . Raw data are black circles, the red line is the fit, and the blue line is the difference

**Table 3.4.1: Comparison of unit cell parameters of MIL-53(Fe, V) with those of the known MIL-53(Fe) and MIL-47(V)**

	Space group	$a / \text{\AA}$	$b / \text{\AA}$	$c / \text{\AA}$	$\beta / ^\circ$	$V / \text{\AA}^3$
MIL-53(Fe)_OH <sup>19</sup>	$P2_1/c$	19.3197	15.0362	6.8351	96.305	1973.5
MIL-53(Fe <sub>0.74</sub> V <sub>0.26</sub> )	$P2_1/c$	18.813(3)	15.206(1)	6.849(7)	94.17(1)	1954.3(6)
MIL-47(V) <sup>18</sup>	$Pnma$	6.818(1)	16.143(3)	13.939(2)	---	1534.2(5)
MIL-53(Fe <sub>0.49</sub> V <sub>0.51</sub> )	$Pnma$	6.753(1)	16.497(3)	13.638(1)	---	1519.5(3)

Although differing in structure, it seems likely that both materials display the same connectivity *i.e.* metal-oxide chains connected to one another by the BDC linkers. The differing properties of the materials could be caused by oxidation of vanadium (III) to a tetravalent state with associated dehydrogenation of the bridging hydroxyl groups to oxide, leading to an opening of the structure akin to that seen in MIL-47 or potentially introduction of vanadium into MIL-53(Fe) leads to properties unlike that of either of the pure metal analogues, explaining why the lower vanadium content material closes upon cooling. The pore structures for MIL-53(Fe<sub>0.74</sub>V<sub>0.26</sub>) and MIL-53(Fe<sub>0.49</sub>V<sub>0.51</sub>) are given in Figure 3.4.2.



**Figure 3.4.2: Pore structures for the closed MIL-53(Fe<sub>0.74</sub>V<sub>0.26</sub>) and the open MIL-53(Fe<sub>0.49</sub>V<sub>0.51</sub>) materials**

Elemental analysis confirms that the ratio of iron to vanadium remains constant after calcination of the DMA material (Fe:V 75:25 and 51:49 for the  $\text{Fe}_{0.74}\text{V}_{0.26}$  and  $\text{Fe}_{0.49}\text{V}_{0.51}$  materials, respectively). A large drop in the nitrogen content is seen, consistent with loss of the DMA counter-ion, and a large drop is also seen in the fluorine content of both materials. This would suggest that the high fluorine content seen in the uncalcined materials was due to an impurity that is either destroyed by the calcination step or removed by subsequent water/DMF washings. The fluorine content (6.1% and 3.7%) of both MIL-53 materials is within acceptable values, *i.e.* less than the value expected for complete substitution of bridging hydroxyl groups (7.9% would be found for the hypothetical pure fluorinated phase  $\text{Fe}(\text{BDC})(\text{F})$ ).

**Table 3.4.2: Elemental analysis of the MIL-53(Fe, V) materials and the values expected for non-fluorinated MIL-53(Fe),  $\text{Fe}(\text{BDC})(\text{OH})$ , and the theoretical fully fluorinated MIL-53(Fe) analogue,  $\text{Fe}(\text{BDC})(\text{F})$**

Type	Synthesis Ratio	C / %	H / %	N / %	F / %	Fe / %	V / %
(Fe, V)(BDC)(OH, F)	2:1	32.58	2.00	0.77	6.07	17.08	5.06
	1:1	38.17	2.74	0.71	3.69	10.7	9.32
$\text{Fe}(\text{BDC})(\text{OH})$	-	40.19	2.09	-	-	23.38	-
$\text{Fe}(\text{BDC})(\text{F})$	-	40.19	1.67	-	7.95	23.38	-

### 3.4.3. XANES

XANES of both MIL-53(Fe,V) materials proves an oxidation state of +3 for both metals, consistent with a MIL-53  $\text{M}^{\text{III}}(\text{OH},\text{F})(\text{BDC})$  composition. This is entirely consistent with the closed MIL-53( $\text{Fe}^{\text{III}}$ ) structure seen for the MIL-53( $\text{Fe}_{0.74}^{\text{III}}\text{V}_{0.26}^{\text{III}}$ ) material produced after cooling to room temperature is as expected. However, the presence of trivalent vanadium contrasts with that of the open structure seen for the MIL-53( $\text{Fe}_{0.49}\text{V}_{0.51}$ ) – the related fully open MIL-47( $\text{V}^{\text{IV}}$ ) only contains tetravalent vanadium sites.



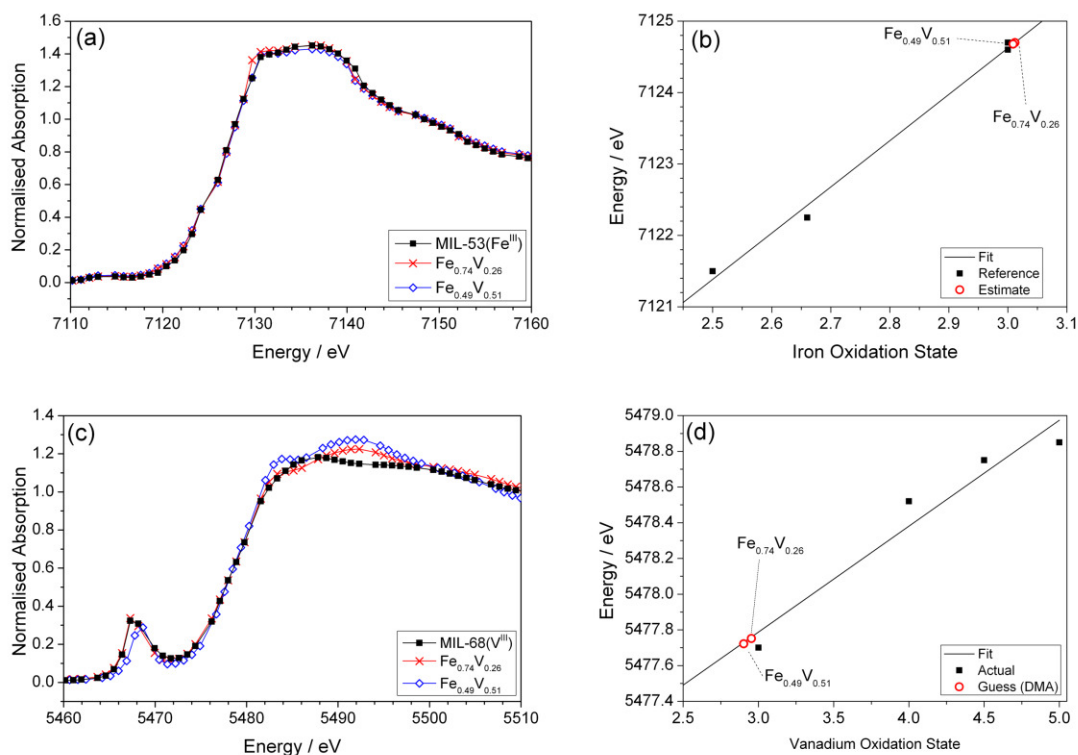


Figure 3.4.3: XANES spectra of  $[(\text{Fe}, \text{V})(\text{BDC})(\text{OH}, \text{F})]^{0.5-} \cdot 0.5\text{DMA}^+$  materials at (a) the iron K-edge and (c) the vanadium K-edge. Estimates of the oxidation states are shown in (b) and (d) for iron and vanadium respectively. Edge positions and the reference materials used are given in Tables 3.4.3 and 3.4.4.

Table 3.4.3: Iron K-edge positions of reference materials and  $[(\text{Fe}, \text{V})(\text{BDC})(\text{OH}, \text{F})]^{0.5-} \cdot 0.5\text{DMA}^+$ . Reference compound oxidation states in bold. Edge positions defined as the energy at which the normalised absorption is equal to 0.5

Compound	Edge Position / eV	Oxidation State
$\text{Fe}_2\text{O}_3$	7124.6	<b>3</b>
$\text{Fe}_3\text{O}_4$	7122.25	<b>2.66</b>
$\text{Fe}(\text{BDC})(\text{OH}, \text{F})$ (MIL-53(Fe))	7124.7	<b>3</b>
$[\text{Fe}(\text{BDC})(\text{OH}, \text{F})]^{0.5-} \cdot 0.5\text{DMA}^+$	7121.5	<b>2.5</b>
$[(\text{Fe}_{0.74}\text{V}_{0.26})(\text{BDC})(\text{OH}, \text{F})]$ (MIL-53( $\text{Fe}_{0.74}\text{V}_{0.26}$ ))	7124.7	3.01
$[(\text{Fe}_{0.49}\text{V}_{0.51})(\text{BDC})(\text{OH}, \text{F})]$ (MIL-53( $\text{Fe}_{0.49}\text{V}_{0.51}$ ))	7124.68	3.01

**Table 3.4.4: Vanadium K-edge positions of reference materials and  $[(\text{Fe}, \text{V})(\text{BDC})(\text{OH}, \text{F})]^{0.5-} \cdot 0.5\text{DMA}^+$ . Reference compound oxidation states in bold. Edge positions defined as the energy at which the normalised absorption is equal to 0.5**

Compound	Edge Position / eV	Oxidation State
$\text{V}_2\text{O}_5$	5478.85	<b>5</b>
$\text{NaV}_2\text{O}_5$	5478.7	<b>4.5</b>
$\text{CaVO}_3$	5478.52	<b>4</b>
$\text{V}(\text{BDC})(\text{OH})$ (MIL-68(V))	5477.7	<b>3</b>
$[(\text{Fe}_{0.74}\text{V}_{0.26})(\text{BDC})(\text{OH}, \text{F})]$ (MIL-53( $\text{Fe}_{0.74}\text{V}_{0.26}$ ))	5477.76	2.97
$[(\text{Fe}_{0.49}\text{V}_{0.51})(\text{BDC})(\text{OH}, \text{F})]$ (MIL-53( $\text{Fe}_{0.49}\text{V}_{0.51}$ ))	5477.73	2.95

Either via heat or exposure to oxygen, MIL-47as( $\text{V}^{\text{III}}$ ) can be irreversibly converted into MIL-47( $\text{V}^{\text{IV}}$ ) through oxidation of the bridging hydroxyl groups to oxide moieties, forcing the framework into a relatively rigid open form. In order to oxidise the hydroxyl bridging group, two or more adjacent vanadium moieties in the chain are required since the formation of Fe(IV) is chemically unlikely. In MIL-53( $\text{Fe}_{0.74}\text{V}_{0.26}$ ), the large amount of iron present makes this statistically unlikely so the vanadium remains unoxidised. However, in MIL-53( $\text{Fe}_{0.49}\text{V}_{0.51}$ ), the probability of vanadium rich regions increases, leading to the chance that some vanadium is oxidised to a certain degree. Since the average oxidation state is around +3, the presence of tetravalent vanadium is rare but significant enough that sufficient oxide groups are present to force the framework into a fully open state. This suggests that although the MIL-53( $\text{Fe}_{0.49}\text{V}_{0.51}$ ) is phase-pure evidenced by XRD, the two metals are not homogeneously distributed throughout the framework leading to metal-rich domains (Figure 3.4.4). The effect of increasing inflexibility with increasing V(IV) content has also been seen in the graduated calcination of MIL-47as( $\text{V}^{\text{III}}$ ) to MIL-47( $\text{V}^{\text{IV}}$ ) via MIL-47( $\text{V}^{\text{III}} / \text{V}^{\text{IV}}$ ) by Leclerc *et al.*<sup>17</sup>

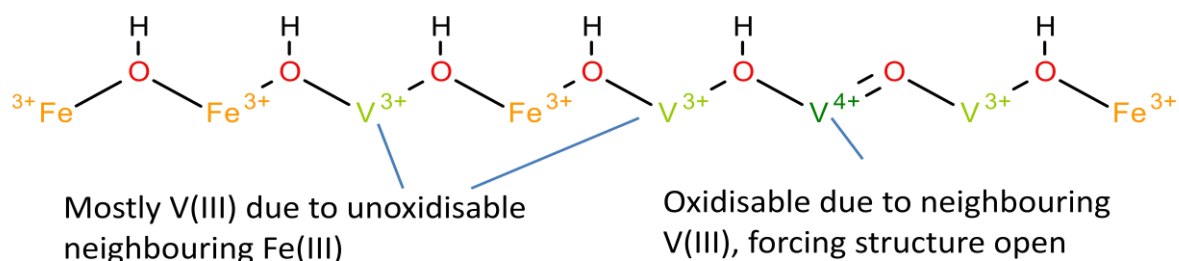


Figure 3.4.4: Rationalisation of vanadium character in MIL-53( $\text{Fe}_{0.49}\text{V}_{0.51}$ ) indicating regions where vanadium oxidation can and cannot occur

### 3.4.4. $^{57}\text{Fe}$ Mössbauer Spectroscopy

$^{57}\text{Fe}$  Mössbauer spectroscopy for both MIL-53(Fe,V) materials suggests the presence of high-spin iron(III) in two differing environments, Figure 3.4.5 (a) and (b). Comparison with a partially fluorinated sample of MIL-53(Fe) is revealing (Figure 3.4.5 (c)) since this also shows two sites for high-spin Fe(III) owing to the presence of iron surrounded either by hydroxides or by fluorides: the internal quadrupolar component is clearly attributed to Fe surrounded by more fluorine atoms than the external one taking into account on the largest (lowest) values of isomer shift, respectively (this is also confirmed by examination of the previously published spectrum of the purely hydroxylated material<sup>16</sup>). Thus it can be proposed that the major component of the signal in the Mössbauer spectra of the mixed-metal materials is due to high-spin Fe(III) surrounded by bridging fluorides because of the largest isomer shift value, while the minor component is due to the effect of neighbouring hydroxide groups. The smaller signal is either due to the proportion of iron with hydroxide neighbours, where the next metal in the chain is vanadium, or an extra degree of perturbation caused by the presence of either iron or vanadium as neighbouring metals within each chain. In either case, this is consistent with vanadium only being coordinated by hydroxides and not fluorides, as noted above.

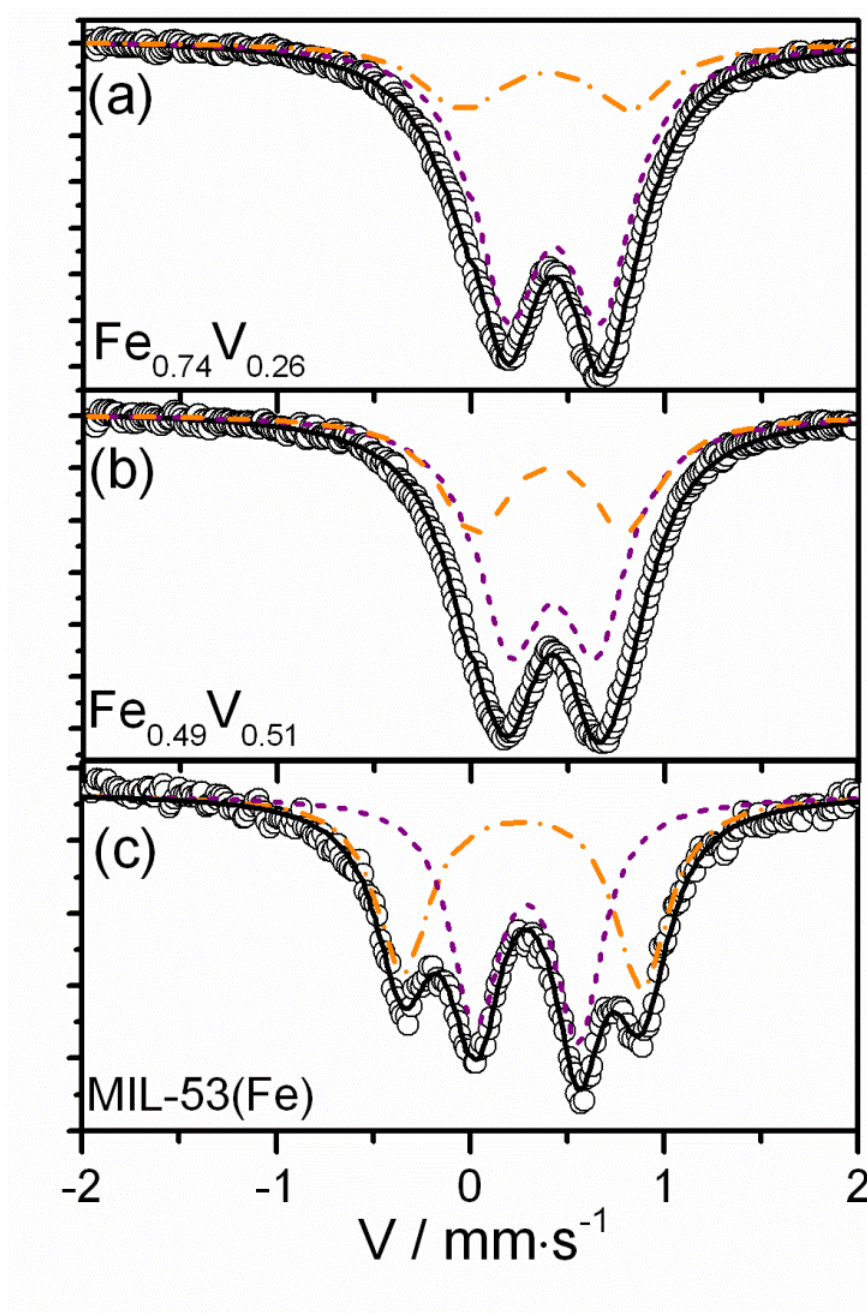


Figure 3.4.5:  $^{57}\text{Fe}$  Mössbauer spectra recorded at 77 K of (a) MIL-53( $\text{Fe}_{0.76}\text{V}_{0.24}$ ), (b) MIL-53( $\text{Fe}_{0.49}\text{V}_{0.51}$ ) and at 300K (c) partially fluorinated MIL-53(Fe)

### 3.4.5. Infrared and Raman Spectroscopy

In its infrared spectrum, Figure 3.4.6, the  $\text{Fe}_{0.76}\text{V}_{0.24}$  MIL-53 material displays a  $\nu(\text{OH})$  stretch at  $3645\text{ cm}^{-1}$ . This band is in the same range as those observed for MIL-53( $\text{Fe}^{\text{III}}$ ) ( $3644\text{ cm}^{-1}$ )<sup>8</sup> and MIL-53( $\text{V}^{\text{III}}$ ) ( $3642\text{ cm}^{-1}$ ).<sup>17</sup> In the  $\delta(\text{OH})$  region, both Fe-OH-Fe and

V-OH-V bands are seen at 850 and 899  $\text{cm}^{-1}$ , respectively, but unlike the recently reported MIL-53(Cr, Fe) material,<sup>20</sup> no intermediary product Fe-OH-V band is observed, although the presence of such a band at approximately 874  $\text{cm}^{-1}$  may be obscured by an overlapping band around 880  $\text{cm}^{-1}$ . This band indeed presents a shoulder at lower wavenumbers. Both sets of OH bands disappear when the material is heated at 300 °C. An additional band is seen at 913  $\text{cm}^{-1}$ . A similar band is observed in the range 910-920  $\text{cm}^{-1}$  on MIL-53( $\text{Fe}_{0.49}\text{V}_{0.51}$ ), as discussed below. For MIL-53( $\text{Fe}_{0.49}\text{V}_{0.51}$ ), the main  $\nu(\text{OH})$  band is observed at higher wavenumber (3656  $\text{cm}^{-1}$ ) than for the lower vanadium content material. It disappears upon heating above 300 °C. This band can thus be tentatively assigned to V-OH-V stretchings. In the  $\delta(\text{OH})$  region, both sets of single metal bands may be observed but similarly to MIL-53( $\text{Fe}_{0.76}\text{V}_{0.24}$ ), Fe-OH-V bands could not be identified due to the overlapping band at ca. 880  $\text{cm}^{-1}$ . A comparison of IR spectra, Figure 3.4.6, allows investigation of the effects of increasing vanadium concentration. In the  $\delta(\text{OH})$  region, the band at ca. 900  $\text{cm}^{-1}$  is higher on the vanadium rich solid while the band at 850  $\text{cm}^{-1}$  is intense on the iron rich solid confirming their assignment to V-OH-V and Fe-OH-Fe respectively. However, although consistent with increasing vanadium content, statistical repartition of the hydroxyls cannot be resolved with pure M-OH-M bands always more abundant than the Fe-OH-V. This suggests that iron-rich and vanadium-rich domains are present in both materials.

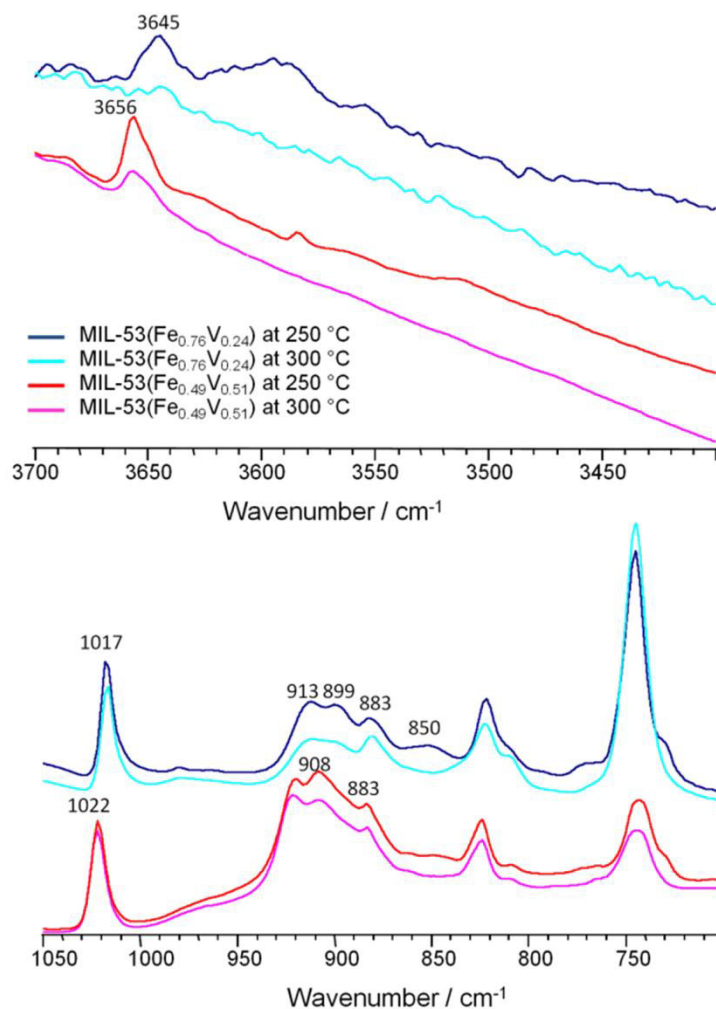


Figure 3.4.6: Absorbance IR spectra of the  $\text{Fe}_{0.76}\text{V}_{0.24}$  and  $\text{Fe}_{0.49}\text{V}_{0.51}$  MIL-53 materials recorded under vacuum at 250 °C and 300 °C

Raman spectroscopy (Figure 3.3.10) allows further investigation of both MIL-53(Fe, V) materials. The unassigned band at  $\sim 915 \text{ cm}^{-1}$  is also present on the Raman spectra for both materials. This band is similar, but much weaker, to the  $\nu(\text{V}=\text{O})$  band observed on MIL-47( $\text{V}^{\text{IV}}$ )<sup>17</sup> and can be correlated to a V-O bond of around 0.164 nm with a bond order of 1.5.<sup>21</sup> The presence of  $\text{V}^{\text{IV}}=\text{O}$  bonds are likely due to defects or chain ends, supported by the low crystallinity of both materials and the presence of some free terephthalic acid detected by FTIR on the hydrated forms of MIL-53 after DMA removal. Raman spectra also confirmed the results obtained by XRD: MIL-53( $\text{Fe}_{0.49}\text{V}_{0.51}$ ) is observed as an open structure, whereas MIL-53( $\text{Fe}_{0.74}\text{V}_{0.26}$ ) remains closed at room temperature and both structures are

open upon removal of DMA at 250 °C. The open structure of MIL-53( $\text{Fe}_{0.49}\text{V}_{0.51}$ ) at room temperature and the presence of V=O supports the idea that it contains sufficiently large pure vanadium regions which allow the pore opening even at room temperature, while this is not the case for the iron rich material. Importantly, the IR and Raman spectroscopic data show no evidence for the presence of extra-framework metal-containing species in the materials, which also supports the evidence from thermodiffraction which shows pore opening (see next section) and hence the lack of metal salts in pores of the solids.

### 3.4.6. Thermal Behaviour

Upon heating to 250°C, MIL-53( $\text{Fe}_{0.74}\text{V}_{0.26}$ ) dehydrates and reforms the fully open phase seen upon initial calcination and upon cooling reverts to the hydrated closed form. This can be repeated with little structural degradation observed (see Figure 3.4.7: Thermodiffraction of the reversible dehydration - rehydration of MIL-53( $\text{Fe}_{0.74}\text{V}_{0.26}$ ) showing the breathing property of the framework). This 'breathing' effect is found for MIL-53( $\text{Cr}^{\text{III}}$ ) and for MIL-53( $\text{Al}^{\text{III}}$ ) but, importantly, not for MIL-53( $\text{Fe}^{\text{III}}$ ).<sup>16</sup> The structural changes with heating and cooling (closed-open-closed) differ from that of MIL-53(Fe) (closed-closed (ht)-closed), lending further credence to the conclusion that the new mixed Fe/V material is indeed a distinct phase. Furthermore, the fact that the vanadium in MIL-53( $\text{Fe}_{0.74}\text{V}_{0.26}$ ) is not permanently oxidised to the +4 state, would suggest a high degree of mixing of Fe(III) and V(III) such that hydroxyls always bridge a pair of Fe and V centres, preventing oxidation of vanadium since iron is unlikely to be oxidised to the +4 oxidation state.

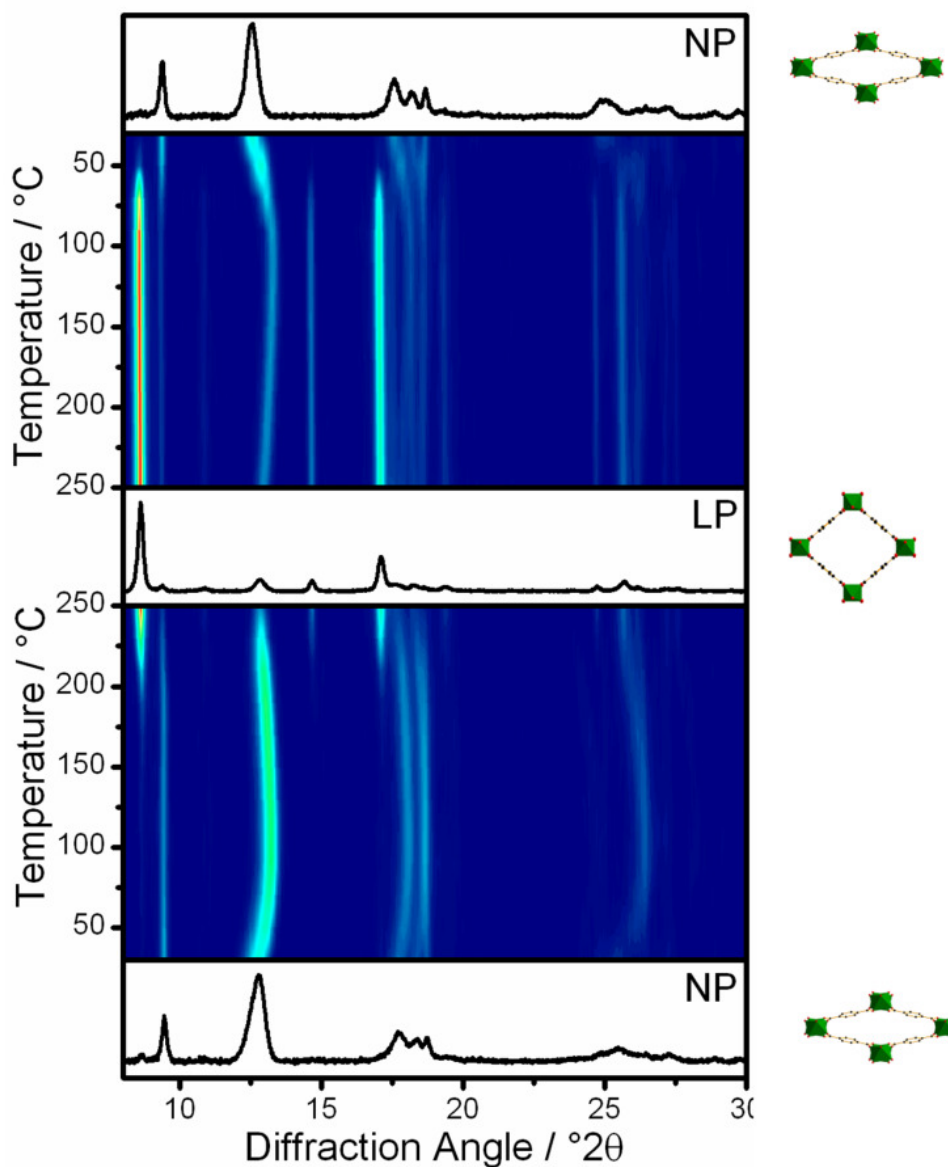


Figure 3.4.7: Thermodiffractometry of the reversible dehydration - rehydration of MIL-53( $\text{Fe}_{0.74}\text{V}_{0.26}$ ) showing the breathing property of the framework

This breathing behaviour is not observed for MIL-53( $\text{Fe}_{0.49}\text{V}_{0.51}$ ) where the fully open LP structure is maintained both during and after cooling (see Figure 3.4.8). This is consistent with MIL-47(V)-like behaviour with the bridging oxide groups forcing the structure into an open form.



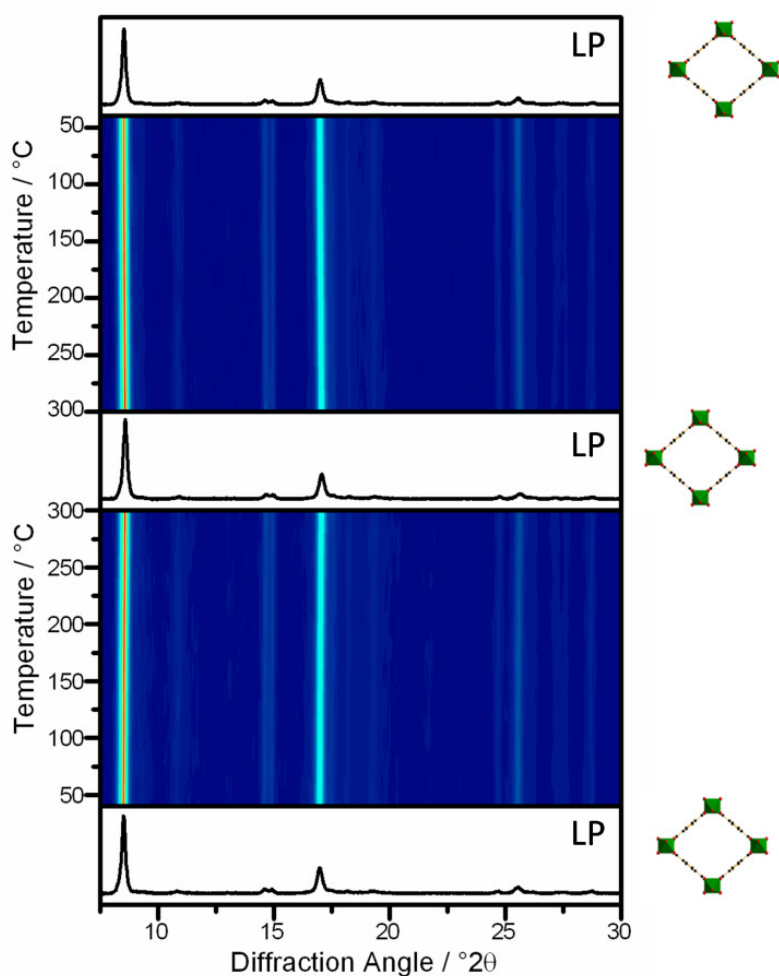


Figure 3.4.8: Thermodiffractometry of MIL-53( $\text{Fe}_{0.49}\text{V}_{0.51}$ ) showing no structural changes upon heating and cooling

### 3.4.7. Sorption of Ethanol by MIL-53( $\text{Fe}_{0.74}\text{V}_{0.26}$ )

Figure 3.4.9 shows contour plots of *in situ* energy-dispersive X-ray diffraction data (EDXRD) measured during the uptake of ethanol by MIL-53(Fe) and MIL-53( $\text{Fe}_{0.74}\text{V}_{0.26}$ ) by addition of 25:75 ethanol : water solution to suspension of the respective solid in water. Both materials initially display the Bragg peaks of the hydrated material. As the ethanol solution is added, the MIL-53( $\text{Fe}^{\text{III}}$ ) material transforms into a half-open phase (Figure 3.4.9a), as previously reported.<sup>5</sup> No change in the structure of MIL-53( $\text{Fe}_{0.74}\text{V}_{0.26}$ ), however, was seen over the timescale of this experiment (Figure 3.4.9b), although some uptake of ethanol was seen after 24 hours. Addition of 1:1 solution of ethanol/water to both

materials leads to the formation of the fully open framework for both materials after around 10 minutes. The formation of the intermediary product half-open framework is seen for the pure iron analogue (Figure 3.4.9c) but not for MIL-53( $\text{Fe}_{0.74}\text{V}_{0.26}$ ) (Figure 3.4.9d). The complete conversion of MIL-53( $\text{Fe}_{0.74}\text{V}_{0.26}$ ) from closed to fully open in one step with no intermediary products or splitting of Bragg peaks confirms again that this material is both phase pure and homogenous in nature and shows distinctly different structural flexibility than the pure Fe material.

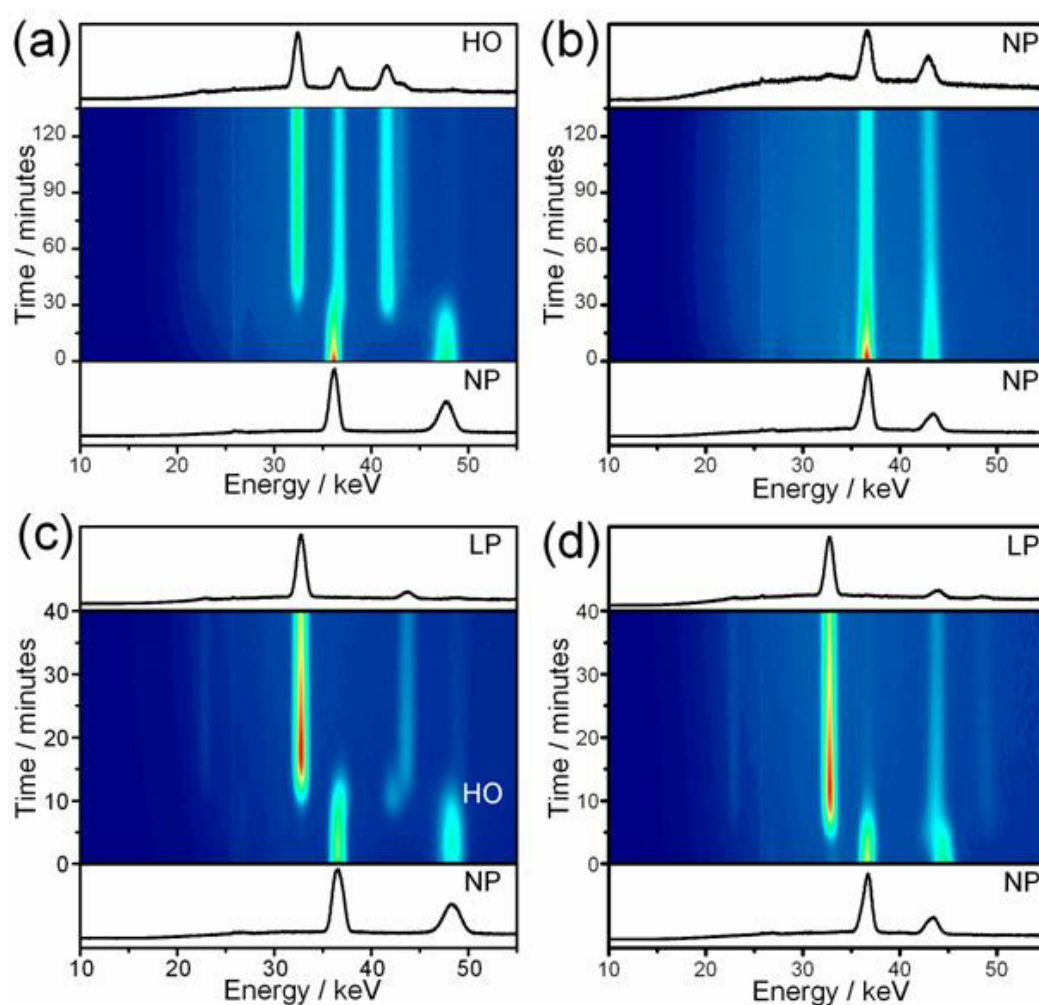


Figure 3.4.9: Time resolved EDXRD contour plots of ethanol absorption by MIL-53(Fe) and MIL-53( $\text{Fe}_{0.74}\text{V}_{0.26}$ ). a) Addition of 25% ethanol to MIL-53(Fe); b) addition of 25% ethanol to MIL-53( $\text{Fe}_{0.74}\text{V}_{0.26}$ ); c) addition of 50% ethanol to MIL-53(Fe); d) addition of 50% ethanol to MIL-53( $\text{Fe}_{0.74}\text{V}_{0.26}$ ). Data were collected on Beamline F3 at HASYLAB, DESY

### 3.4.8. Porosity Studies of MIL-53(Fe, V)

Of particular interest to any potential uses of MIL-53(Fe, V) for gas purification, the ability of MIL-53(Fe, V) to adsorb significant quantities of gas must first be investigated.

MIL-53(Fe) itself displays little porosity due to its closed structure (BET surface area of  $12 \text{ m}^2\text{g}^{-1}$ ).<sup>8</sup> MIL-47(V) with its open structure absorbs large quantities of gas, displaying a BET surface area of  $930 \text{ m}^2\text{g}^{-1}$  for nitrogen adsorption.<sup>22</sup>

Sorption studies of both materials were taken at 77 K using nitrogen as a probe molecule after activation under vacuum at 200 °C (Figure 3.4.10). MIL-53( $\text{Fe}_{0.74}\text{V}_{0.26}$ ) exhibits some porosity with slight opening of the framework at higher pressures. The measured BET surface area is  $51 \text{ m}^2\text{g}^{-1}$ ; approximately four times that of MIL-53(Fe). This is still consistent with its closed MIL-53(Fe)-like structure. MIL-53( $\text{Fe}_{0.49}\text{V}_{0.51}$ ) displays significant porosity with a measured BET surface area of  $390 \text{ m}^2\text{g}^{-1}$ . Although significantly less than that recorded for MIL-47, there remains the possibility that the structure partially closes upon cooling to 77 K. This closing of the structure with temperature has been noted for dehydrated MIL-53(Al).<sup>23</sup> Without low temperature XRD studies, it would be difficult to determine whether closing of the MIL-53( $\text{Fe}_{0.49}\text{V}_{0.51}$ ) has occurred or not.

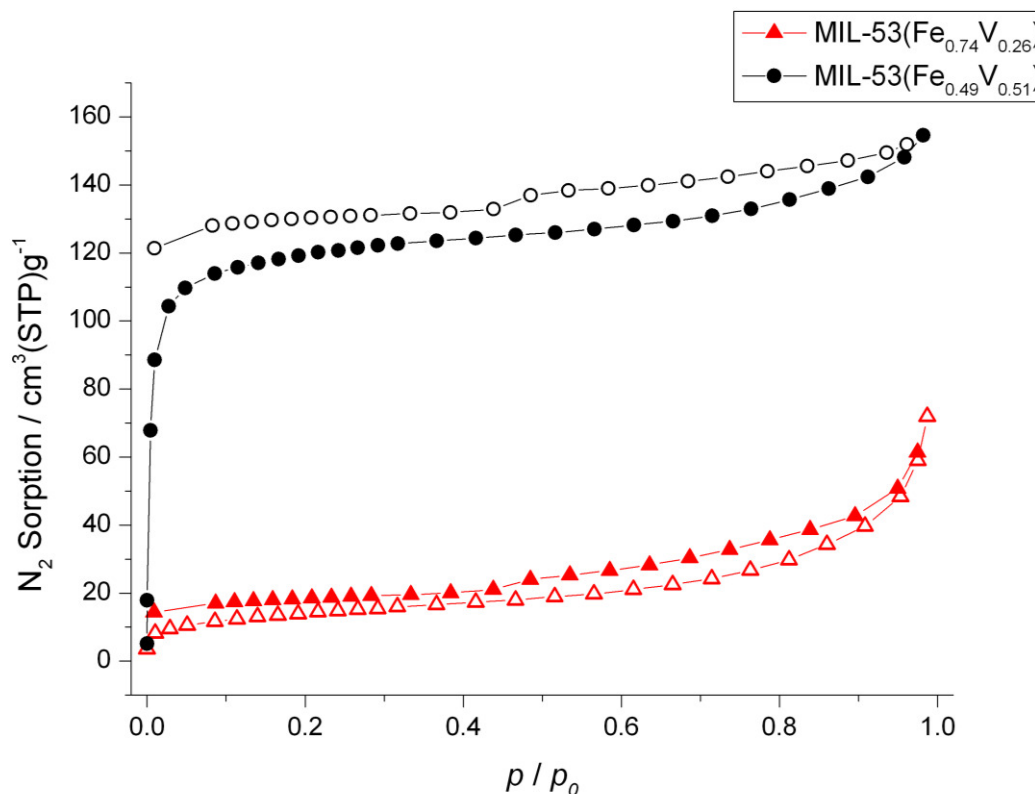


Figure 3.4.10:  $N_2$  sorption isotherm of MIL-53( $Fe_{0.74}V_{0.26}$ ) and MIL-53( $Fe_{0.49}V_{0.51}$ ) at 77 K. Filled shapes represent adsorption isotherms and hollow shapes represent desorption isotherms

### 3.4.9. Xylene sorption studies of MIL-53( $Fe_{0.74}V_{0.26}$ )

The ability of a material to resolve  $C_8H_{10}$ -aromatics into para-, meta- and ortho-xylene is of particular industrial interest due to its potential use in membrane-separation systems – an alternative to the energy-intensive fraction crystallisation method.<sup>24</sup> Both MIL-47(V) and MIL-53(Fe) are known to be able to successively resolve xylene mixtures into their separate isomers.<sup>2,6</sup> MIL-53 has selectivity in the order ortho > meta > para whereas MIL-47(V) displays para > ortho > meta selectivity for liquid phase separation. Since MIL-53(Fe, V) exhibits both MIL-53(Fe) and MIL-47(V)-like behaviour, the xylene selectivity of MIL-53(Fe, V) is of interest.

The ability of MIL-53( $Fe_{0.74}V_{0.26}$ ) adsorb each individual xylene was investigated by our collaborators in K.U. Leuven (see Figure 3.4.11). The selectivity of MIL-53( $Fe_{0.74}V_{0.26}$ ) was shown to be para > meta > ortho-xylene. This selectivity is unlike that of either MIL-

53(Fe) or MIL-47(V), further illustrating the benefits of synthesising mixed-metal MIL-53 analogues. The total weight (%) of xylene adsorbed is lower than that seen for MIL-47(V) (~40 %). This is likely due to an insufficient activation method (temperature too low) and further work is required to investigate this.

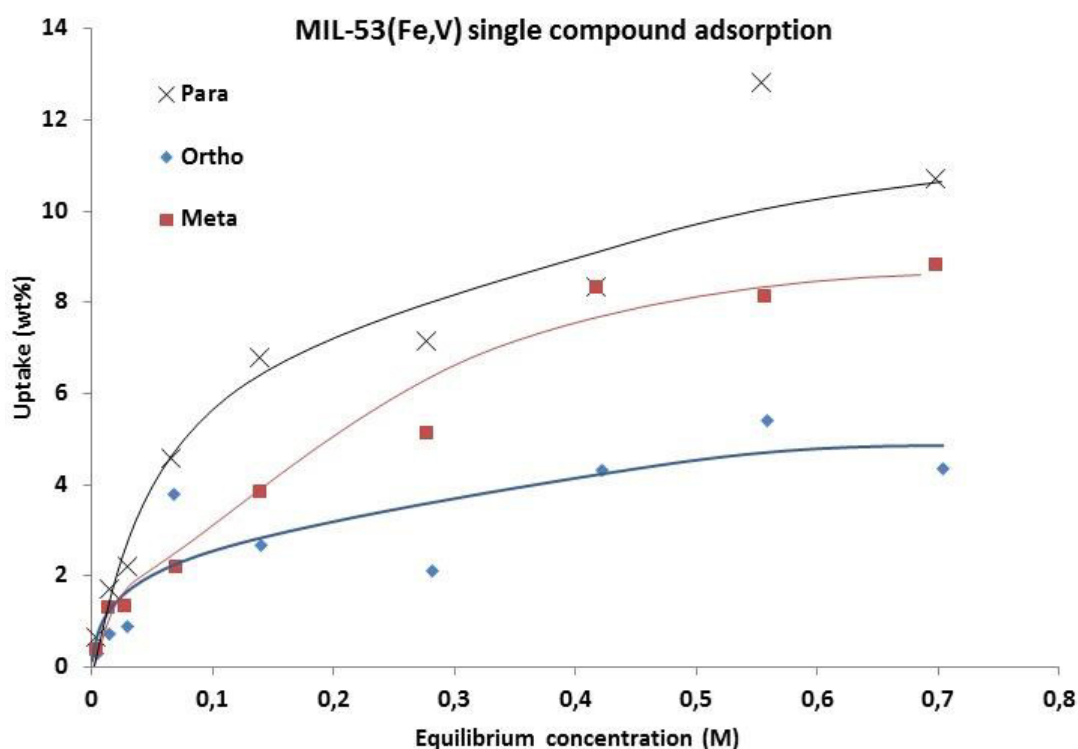


Figure 3.4.11: Single-compound adsorption on MIL-53(Fe<sub>0.76</sub>V<sub>0.24</sub>) in batch mode at 298 K: uptake of C<sub>8</sub> alkyl-aromatic compounds from hexane as a function of the bulk phase concentration

### 3.5. [(Fe, Co)(BDC)(OH, F)]<sup>0.5</sup>·0.5DMA<sup>+</sup>

#### 3.5.1. Synthesis

Anhydrous iron (III) chloride and cobalt (II) nitrate hexahydrate in molar ratio 2:1 (0.002 mol total metal) and terephthalic acid (0.002 mol) were dissolved in a mixture of 'aged' DMF (10 cm<sup>3</sup>), water (0.3 cm<sup>3</sup>) and HF (0.01 cm<sup>3</sup>). The mixture was stirred at room temperature and then transferred into Teflon liners. The liners were placed in steel autoclaves, kept at 160 °C for 72 hours and cooled to room temperature. The resulting yellow powders were isolated by suction filtration, washed with DMF and dried in air.

Incorporation of cobalt into the material was suggested by the yellow colour of the product as opposed to the orange colour of the pure iron analogue.<sup>13</sup> Attempts to increase cobalt content were unsuccessful with co-formation of Co(BDC)(DMF) observed.<sup>25</sup> Substitution of the cobalt salt from the nitrate to cobalt (II) chloride further exacerbated the formation of Co(BDC)(DMF).

Attempts to repeat the synthesis were often unsuccessful with Co(BDC)(DMF) formed as a co-product in a majority of reactions. This can likely be accounted to problems with 'aged' DMF.<sup>26</sup> Over time or as an effect of heating, dimethylformamide will hydrolyse to form dimethylammonia and formic acid. Although this property may be beneficial for formation of the pure iron and mixed iron-vanadium material, an excess (or indeed a shortage) of the hydrolysis products appears to be detrimental to the formation of the mixed iron-cobalt phase. Attempts to repeat the experiment with both fresh and 'aged' DMF were unsuccessful implying a certain degree of aging is required for successful synthesis of the product.

### 3.5.2. Structure

A profile fit of the PXRD pattern of the  $[(\text{Fe}, \text{Co})(\text{BDC})(\text{OH}, \text{F})]^{0.5-} \cdot 0.5\text{DMA}^+$  material suggests that it shares the same structure and space group (P1) as the pure iron analogue as shown in Figure 3.5.1. Substitution of iron for cobalt results in an increase in the unit cell volume seen in Table 3.5.1, consistent with the larger size of  $\text{Co}^{2+} / \text{Co}^{3+}$  with regards to the substituted iron.<sup>27</sup>

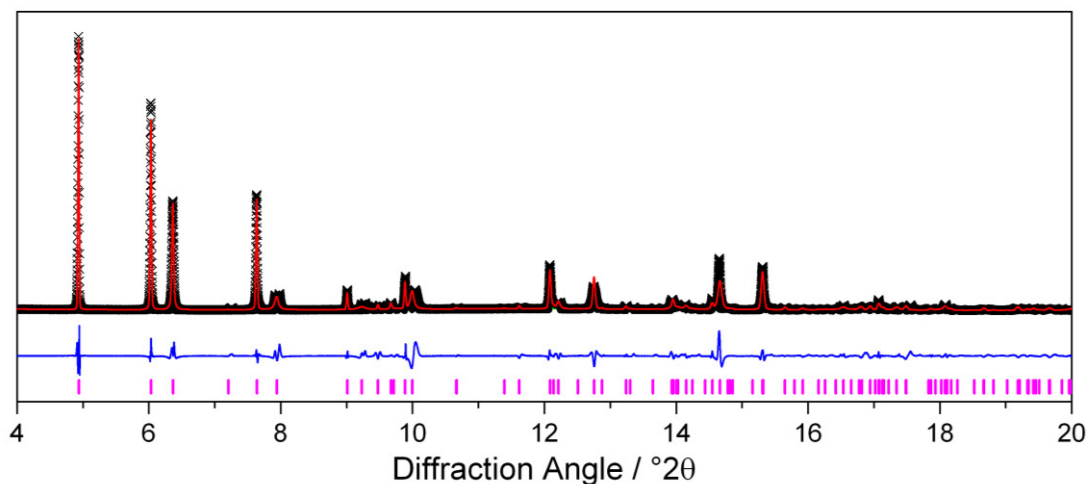


Figure 3.5.1: High resolution powder XRD pattern with profile fit of the  $[(\text{Fe}, \text{Co})(\text{BDC})(\text{OH}, \text{F})]^{0.5-} \cdot 0.5\text{DMA}^+$  material. Data was collected on Beamline I11 at Diamond ( $\lambda = 0.825164 \text{ \AA}$ ). Rata data are black crosses, the red line is the fit, the blue line is the difference and the magenta lines are tick marks.

Table 3.5.1: Comparison of unit cell parameters for those of the reported  $[(\text{Fe}(\text{BDC})(\text{OH}, \text{F}))^{0.5-} \cdot 0.5\text{DMA}^+]$  and those of the cobalt doped analogue from the profile fit.

	$a / \text{\AA}$	$b / \text{\AA}$	$c / \text{\AA}$	$\alpha / ^\circ$	$\beta / ^\circ$	$\gamma / ^\circ$	$V / \text{\AA}^3$
Fe	6.9004(14)	8.554(3)	10.380(3)	107.15(2)	100.16(2)	102.10(2)	553.6(2)
Fe-Co	6.982(3)	8.576(2)	10.358(3)	106.74(2)	99.83(5)	103.03(3)	559.8(3)

### 3.5.3. Calcination

Attempts to calcine  $[(\text{Fe}, \text{Co})(\text{BDC})(\text{OH}, \text{F}))^{0.5-} \cdot 0.5\text{DMA}^+]$  were unsuccessful with no change in structure observed after calcination at  $300^\circ\text{C}$  for several hours as evidenced by powder XRD showing a clear deviation in behaviour away from the pure iron analogue.<sup>13</sup> An increase in the calcination temperature to  $310^\circ\text{C}$  led to destruction of the material. The ability of the cobalt doped material to resist calcination when compared to the facile calcination of the pure iron and the mixed iron-vanadium materials can largely be accounted to the higher stability of cobalt (II) over that of cobalt (III). This effect is further exacerbated by the lack of any suitable ligands to stabilise the trivalent cobalt state and is observed in literature with the majority of Co(III) containing MOFs containing nitrogen-coordinating ligands.<sup>28-33</sup>

### 3.5.4. XANES

XANES at the iron K-edge show a shift in the edge position to higher energies, away from what would be expected if both metals were evenly distributed as is found in the pure iron analogue (Figure 3.5.2 (a)). The estimated oxidation state for iron in the cobalt doped material is around 2.8 implying that iron is predominately occupying the trivalent sites in the material (Figure 3.5.2(b)). This is further supported by the XANES at the Co K-edge where a shift away from an expected oxidation of 2.5 is seen (Figure 3.5.2(c)). The estimated cobalt oxidation state is around 2.1 suggesting a strong preference for divalent sites (Figure 3.5.2(d)). The preponderance of Co(II) over Co(III) in carboxylate co-ordinated materials agrees well with the literature.<sup>25,34,35</sup> The proposed chemical formula is therefore  $[\text{Fe}^{\text{III}}_{0.5}\text{Co}^{\text{II}}_{0.5}(\text{BDC})(\text{OH}, \text{F})]^{0.5-} \cdot 0.5\text{DMA}^+$ .

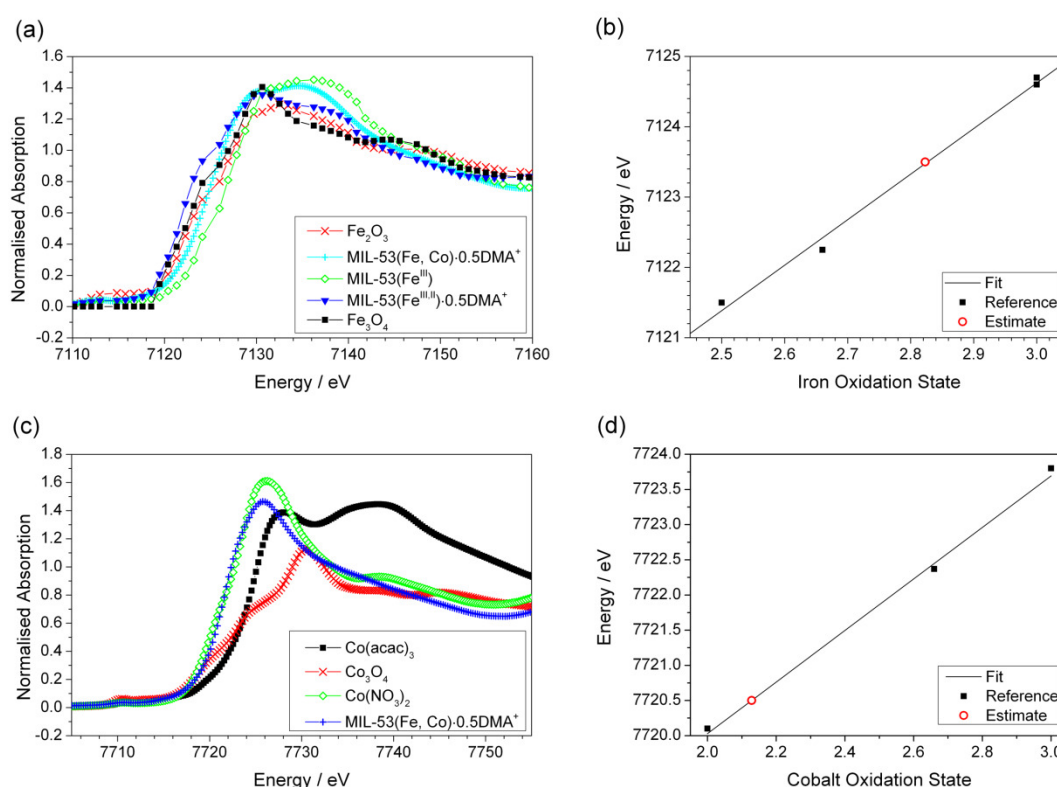


Figure 3.5.2: XANES spectra of  $[(\text{Fe}, \text{Co})(\text{BDC})(\text{OH}, \text{F})]^{0.5-} \cdot 0.5\text{DMA}^+$  material at (a) the iron K-edge and (c) the cobalt K-edge. Estimates of the oxidation states are shown in (b) and (d) for iron and cobalt respectively. Edge positions and the reference materials can be found in Table 3.5.2Table 3.5.3



Table 3.5.2: Iron K-edge positions of reference materials and [(Fe, Co)(BDC)(OH, F)]<sup>0.5-</sup>·0.5DMA<sup>+</sup>. Reference compound oxidation states in bold. Edge positions defined as the energy at which the normalised absorption is equal to 0.5

Compound	Edge Position / eV	Oxidation State
Fe <sub>2</sub> O <sub>3</sub>	7124.6	<b>3</b>
Fe <sub>3</sub> O <sub>4</sub>	7122.25	<b>2.66</b>
Fe(BDC)(OH, F) (MIL-53(Fe))	7124.7	<b>3</b>
[Fe(BDC)(OH, F)] <sup>0.5-</sup> ·0.5DMA <sup>+</sup>	7121.5	<b>2.5</b>
[(Fe, Co)(BDC)(OH, F)] <sup>0.5-</sup> ·0.5DMA <sup>+</sup>	7123.5	<b>2.82</b>

Table 3.5.3: Co K-edge positions of reference materials and [(Fe, Co)(BDC)(OH, F)]<sup>0.5-</sup>·0.5DMA<sup>+</sup>. Reference compound oxidation states in bold. Edge positions defined as the energy at which the normalised absorption is equal to 0.5

Compound	Edge Position / eV	Oxidation State
Co(acac) <sub>3</sub>	7723.8	<b>3</b>
Co <sub>3</sub> O <sub>4</sub>	7722.4	<b>2.66</b>
Co(NO <sub>3</sub> ) <sub>2</sub>	7720.1	<b>2</b>
[(Fe, Co)(BDC)(OH, F)] <sup>0.5-</sup> ·0.5DMA <sup>+</sup>	7720.5	<b>2.13</b>

## 3.6. MIL-53(Fe, Cr)

### 3.6.1. Introduction

A mixed chromium-iron MIL-53 analogue containing a 6:4 ratio of chromium to iron was synthesised by collaborators at the University of Versailles.<sup>36</sup> This material displayed breathing properties unlike those of either pure metal analogue, lending further credence to the notion of importance in investigating mixed metal systems. In order to determine whether the material was a single mixed-metal phase or a mixture of the two single metal phases, EXAFS analysis was used to determine the local environment of both the chromium and the iron atoms. Owing to the small difference in atomic number between the two metals, it is difficult to determine whether the nearest metal neighbour is iron or chromium using solely XRD. Although the structures of MIL-53(Fe) and MIL-53(Cr) are almost identical, there are differences in the intra-chain metal-metal distances (3.3889 Å for chromium<sup>37</sup>

and 3.4419 Å for iron<sup>19</sup>). If the material contains two separate single-metal phases then the iron-metal distances calculated from EXAFS will be close to that of MIL-53(Fe) and likewise for chromium. However, if the material is a true mixed-metal phase, the inter-metal distance will be between the two single phases.

### 3.6.2. Fitting Model

In order to determine the inter-metal distances, the EXAFS data were fitted to models derived from the crystal structures of the MIL-53 materials. Four models were used. The first two models were reduced versions of the crystal structure, up to and including the next nearest metal atom (see Figure 3.6.1). The second two models contain the next metal neighbours replaced by the second metal. To test the suitability of these models to calculate metal-metal distances, the iron-iron model was tested on EXAFS of MIL-53(Fe), a system where the metal-metal distances are known. An example of the MIL-53(Cr) model fit to data from the EXAFS of the Fe-Cr sample is shown in Figure 3.6.1: An example of the chromium model used to determine inter-atom distances in the MIL-53 systems. This model assumes that both nearest metal neighbours are both chromium..

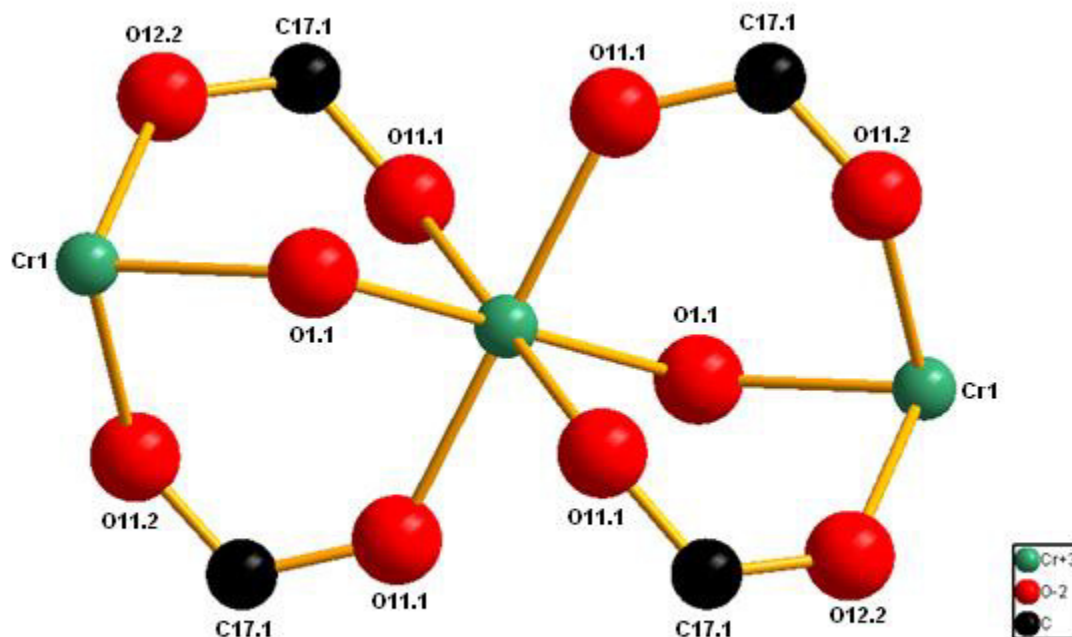


Figure 3.6.1: An example of the chromium model used to determine inter-atom distances in the MIL-53 systems. This model assumes that both nearest metal neighbours are both chromium.

The fits were performed upon the  $k^3$  weighted data. The data were fitted over a  $k$ -range of  $3\text{--}12\text{ \AA}^{-1}$  and an  $R$ -range of  $1\text{--}5\text{ \AA}$ . Initial guesses for the inter-atom distances ( $R_{\text{eff}}$ ) were taken from the crystal structures of MIL-53(Fe) and MIL-53(Cr). The mean squared variation in inter-atom distances ( $\sigma^2$ ) and the difference between the refined inter-atom distances and the initial guess ( $\Delta r$ ) were kept constant for atoms in the same shell.

Carboxylate and hydroxyl oxygens were deemed to be crystallographically distinct enough to be fitted with two different scattering events (although  $\sigma^2$  and  $\Delta r$  were kept constant – treating each event completely separate led to additional problems during the refinement.

Owing to the lower quality of the MIL-53( $\text{Cr}_{0.6}\text{Fe}_{0.4}$ ) data at the iron K-edge, fewer parameters were used to describe the oxygens (i.e. all oxygens modelled using the same  $\Delta r$  and  $\sigma^2$  values, not separate parameters for different shells)

It was found that the model used was suitable for determination of inter-metal distances after fitting of MIL-53(Fe) using the MIL-53(Fe) model with a calculated inter-metal distance of  $3.43877 \pm 0.01 \text{ \AA}$  agreeing well with the expected value of  $3.4419 \text{ \AA}$  from the crystal structure (Figure 3.6.2 and Table 3.6.1).

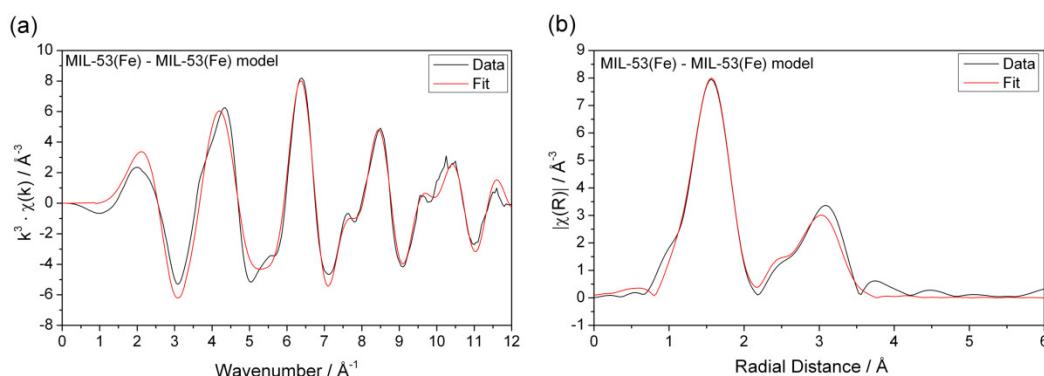


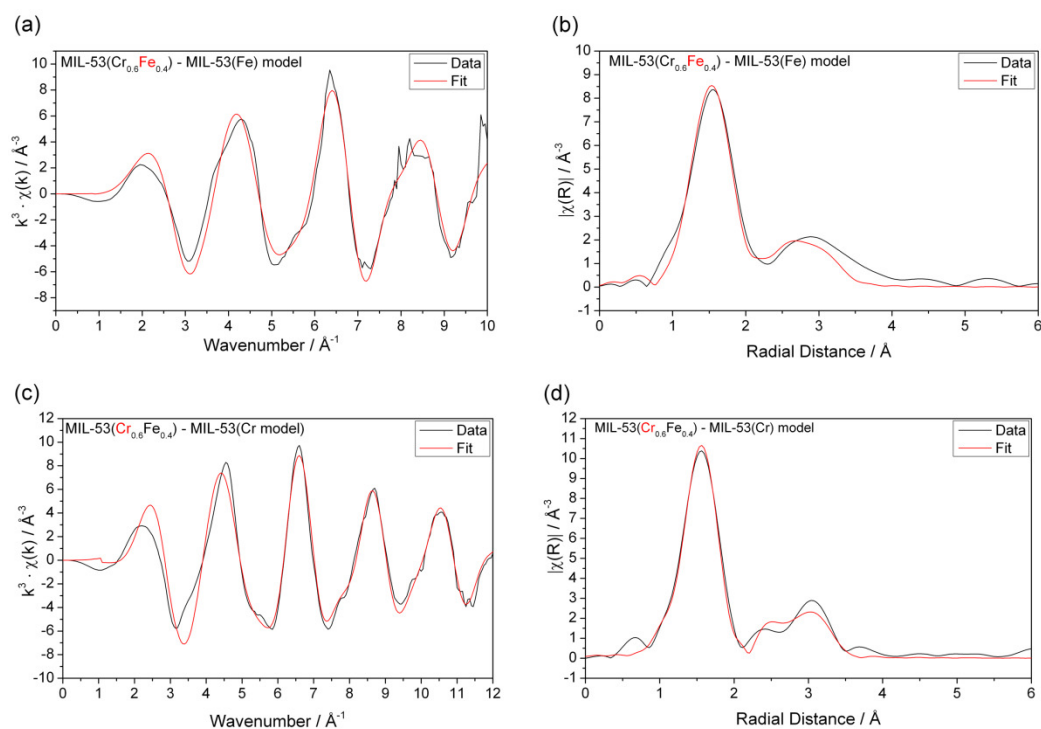
Figure 3.6.2: (a) Fit of MIL-53(Fe) EXAFS data using the 'same metal neighbour' model; (b) Fourier transform of the data and fit in R-space

Table 3.6.1: Refined inter-atom distances from the EXAFS analysis of MIL-53(Fe)

Data	Metal	Model	Atom	N	$S_0^2$	$\sigma^2$	$\delta r / \text{\AA}$	$R_{\text{eff}} / \text{\AA}$	$R / \text{\AA}$
MIL-53(Fe)	Fe	MIL-53(Fe)	O1.1	2	1.135	0.0062	0.00337	1.9441	1.94747
			O12.1	4	1.135	0.0062	0.00337	2.02	2.02337
			C17.1	4	1.135	0.0075	0.00906	2.9687	2.97776
			Fe.1	2	1.135	0.0476	-0.01313	3.4419	3.42877

### 3.6.3. EXAFS Analysis of MIL-53(Cr<sub>0.6</sub>Fe<sub>0.4</sub>)

When the single metal models were used to fit the MIL-53(Fe, Cr) EXAFS, it was found that the calculated distances deviated away from the initial values towards those to that would be expected for a solely iron-based system i.e. MIL-53(Fe) despite the high chromium content of the material (Figure 3.6.3: EXAFS fits using data collected at (a) the iron K-edge and (c) the chromium K-edge using the 'same metal neighbour' model; Fourier transforms of the data and the fit in R-space for the (b) iron and (d) chromium data. Metal studied highlighted in red. and Table 3.6.2).



**Figure 3.6.3:** EXAFS fits using data collected at (a) the iron K-edge and (c) the chromium K-edge using the 'same metal neighbour' model; Fourier transforms of the data and the fit in R-space for the (b) iron and (d) chromium data. Metal studied highlighted in red.

**Table 3.6.2:** Refined inter-atom distances from the EXAFS analysis of MIL-53(Cr<sub>0.6</sub>Fe<sub>0.4</sub>) using the 'same metal neighbour' model

Data	Metal	Model	Atom	N	S <sub>0</sub> <sup>2</sup>	σ <sup>2</sup>	δr / Å	R <sub>eff</sub> / Å	R / Å
MIL-53(Fe, Cr)	Cr	MIL-53(Cr)	O1.1	2	0.883	0.0036	0.01446	1.9295	1.94396
			O11.1	4	0.883	0.0036	0.01446	1.9732	1.98766
			C17.1	4	0.883	0.0058	0.01294	2.9522	2.96514
			Cr.1	2	0.883	0.0049	0.05014	3.3889	3.43904
MIL-53(Fe, Cr)	Fe	MIL-53(Fe)	O1.1	2	0.992	0.0037	0.00207	1.9441	1.94617
			O12.1	4	0.992	0.0037	0.00207	2.02	2.02207
			C17.1	4	0.992	0.0048	-0.02565	2.9687	2.94305
			Fe.1	2	0.992	0.0063	-0.0418	3.4419	3.4001

When the mixed metal models were used, there was strong agreement between the value calculated from the iron EXAFS (3.42926 Å) and the chromium data (3.42690 Å) (see Figure 3.6.4 and Table 3.6.3. The errors in these values are  $\sim \pm 0.02$  Å. Although these errors are significant, the distances are not that of the single metal systems but rather between the values expected for either MIL-53(Fe) or MIL-53 (Cr). While it cannot be

definitely determined what the next metal neighbour is, the strong correlation between the inter-metal distances and the fact this value is neither that of either pure metal would suggest that this MIL-53( $\text{Cr}_{0.6}\text{Fe}_{0.4}$ ) material is indeed a true mixed iron-chromium MIL-53 analogue. The complete set of refined parameters and their errors are given in Table 3.6.4,.

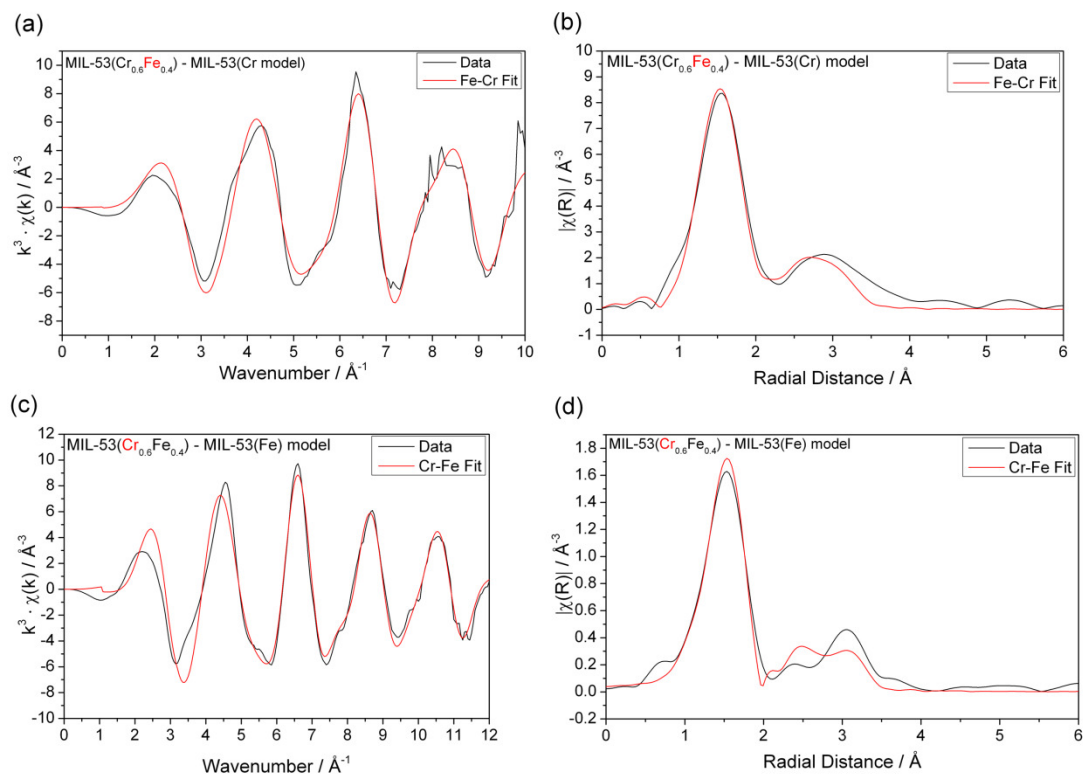


Figure 3.6.4: EXAFS fits using data collected at (a) the iron K-edge and (c) the chromium K-edge using the 'different metal neighbour' model; Fourier transforms of the data and the fit in R-space for the (b) iron and (d) chromium data. Metal studied highlighted in red.

**Table 3.6.3: Refined inter-atom distances from the EXAFS analysis of MIL-53(Cr<sub>0.6</sub>Fe<sub>0.4</sub>) using the 'different metal neighbour' model**

Data	Metal	Model	Atom	N	S <sub>0</sub> <sup>2</sup>	σ <sup>2</sup>	δr / Å	R <sub>eff</sub> / Å	R / Å
MIL-53(Fe, Cr)	Cr	Fe	O1.1	2	0.884	0.0036	0.01436	1.9295	1.94386
			O11.1	4	0.884	0.0036	0.01436	1.9732	1.98756
			C17.1	4	0.884	0.0055	0.00806	2.9522	2.96026
			Fe.1	2	0.884	0.0054	0.03028	3.3889	3.41918
MIL-53(Fe, Cr)	Fe	Cr	O1.1	2	0.985	0.0036	0.00232	1.9441	1.94642
			O12.1	4	0.985	0.0036	0.00232	2.02	2.02232
			C17.1	4	0.985	0.0049	-0.02061	2.9687	2.94809
			Cr.1	2	0.985	0.0056	-0.02276	3.4419	3.41914

**Table 3.6.4: Refined values and errors for the δr parameter**

Data	Metal	Model	δr / Å			
			O	C	Fe	Cr
MIL-53(Fe)	Fe	Fe	0.0037692 ± 0.00756457	0.00905796 ± 0.02408896	-0.01312638 ± 0.01199532	-
MIL-53(Fe, Cr)	Cr	Cr	0.01446336 ± 0.00692081	0.01294421 ± 0.02723428	-	0.05013999 ± 0.01594800
MIL-53(Fe, Cr)	Fe	Fe	0.00207006 ± 0.01324245	-0.0256532 ± 0.03794111	-0.04179983 ± 0.03025727	-
MIL-53(Fe, Cr)	Cr	Cr-Fe	0.01435636 ± 0.00708626	0.00806145 ± 0.02710409	0.03028111 ± 0.01614057	-
MIL-53(Fe, Cr)	Fe	Fe-Cr	0.0023208 ± 0.01301139	-0.02060704 ± 0.03721594	-	-0.0227623 ± 0.02999128

**Table 3.6.5: Refined values and errors for the σ<sup>2</sup> parameter**

Data	Metal	Model	σ <sup>2</sup>			
			O	C	Fe	Cr
MIL-53(Fe)	Fe	Fe	0.00618641 ± 0.00110067	0.00748344 ± 0.00313703	0.00476072 ± 0.00118498	-
MIL-53(Fe, Cr)	Cr	Cr	0.00355575 ± 0.00091890	0.00582686 ± 0.00341054	-	0.00484972 ± 0.00166277
MIL-53(Fe, Cr)	Fe	Fe	0.00369807 ± 0.00222270	0.00478459 ± 0.00558152	0.00625351 ± 0.00335743	-
MIL-53(Fe, Cr)	Cr	Cr-Fe	0.00356319 ± 0.00094055	0.00552637 ± 0.00336463	0.00537363 ± 0.00169303	-
MIL-53(Fe, Cr)	Fe	Fe-Cr	0.00363596 ± 0.00216964	0.0048747 ± 0.00548768	-	0.00561497 ± 0.00329197

**Table 3.6.6: Refined values and errors for the  $S_o^2$  and  $\Delta E_o$  parameters. Statistical values,  $\chi^2$  and the R-factor, are also included**

Data	Metal	Model	$S_o^2$	$\Delta E_o$	$\chi^2$	R-factor
MIL-53(Fe)	Fe	Fe	1.13511202 $\pm 0.13645555$	2.9352858 $\pm 1.55169902$	165855291	0.025686
MIL-53(Fe, Cr)	Cr	Cr	0.88304292 $\pm 0.09556544$	4.430445 $\pm 1.54934449$	102861827	0.026831
MIL-53(Fe, Cr)	Fe	Fe	0.99200314 $\pm 0.22191804$	2.96122567 $\pm 2.64451658$	10177741	0.041604
MIL-53(Fe, Cr)	Cr	Cr-Fe	0.88410648 $\pm 0.09798500$	4.44457432 $\pm 1.58771131$	223840795	0.028166
MIL-53(Fe, Cr)	Fe	Fe-Cr	0.98455524 $\pm 0.21490817$	3.03123833 $\pm 2.59944523$	9752763.5	0.039867

### 3.7. Summary

Through careful mediation of reaction conditions, new mixed-metal iron-vanadium MIL-53 materials have been synthesised. In addition to the expected  $Fe^{III}$  and  $V^{III}$  sites,  $Fe^{II}$  and some  $V^{II}$  were found in the materials produced. These are, to our knowledge, the first examples of metal-organic framework to contain divalent vanadium, and the unusual oxidation state is produced *in situ* during solvothermal synthesis. Calcination of  $[(Fe, V)^{II,III}(BDC)(OH, F)]^{0.5-} \cdot 0.5DMA^+$  leads to the formation of new mixed-metal MIL-53( $Fe^{III}$ ,  $V^{III}$ ) materials, for which all experimental data show the presence of phase-pure sample with mixtures of the metals on an atomic scale, albeit with some evidence for small domains of Fe- and V-rich regions. Varying the metal content of MIL-53(Fe,V) leads to large differences in both the structure and ‘breathing’ of these flexible materials, demonstrating the versatility of changing metal content to adjust properties of metal-organic frameworks. Synthesis of a mixed iron-cobalt  $[Fe(BDC)(OH, F)]^{0.5-} \cdot 0.5DMA^+$  was achieved. Although difficult to calcine and to reproduce the synthesis, the effect of divalent cobalt on the material was distinct, further displaying the potential benefits of investigations into mixed metal materials. Through analysis of the EXAFS spectra of a mixed-metal MIL-53(Fe, Cr)



samples and estimation of metal-metal bond lengths, further evidence was given towards the homogeneity of the material.

### 3.8. References

- (1) Guillou, N.; Walton, R. I.; Millange, F. *Z. Kristallogr.* **2010**, *225*, 552.
- (2) Alaerts, L.; Kirschhock, C. E. A.; Maes, M.; van der Veen, M. A.; Finsy, V.; Depla, A.; Martens, J. A.; Baron, G. V.; Jacobs, P. A.; Denayer, J. E. M.; De Vos, D. E. *Angew. Chem. Int. Ed.* **2007**, *46*, 4293.
- (3) Alaerts, L.; Maes, M.; Giebel, L.; Jacobs, P. A.; Martens, J. A.; Denayer, J. E. M.; Kirschhock, C. E. A.; De Vos, D. E. *J. Am. Chem. Soc.* **2008**, *130*, 14170.
- (4) Hamon, L.; Llewellyn, P. L.; Devic, T.; Ghoufi, A.; Clet, G.; Guillerm, V.; Pirngruber, G. D.; Maurin, G.; Serre, C.; Driver, G.; van Beek, W.; Jolimaite, E.; Vimont, A.; Daturi, M.; Férey, G. *J. Am. Chem. Soc.* **2009**, *131*, 17490.
- (5) Walton, R. I.; Munn, A. S.; Guillou, N.; Millange, F. *Chem. Eur. J.* **2011**, *17*, 7069.
- (6) El Osta, R.; Carlin-Sinclair, A.; Guillou, N.; Walton, R. I.; Vermoortele, F.; Maes, M.; de Vos, D.; Millange, F. *Chem. Mater.* **2012**, *24*, 2781.
- (7) Devic, T.; Salles, F.; Bourrelly, S.; Moulin, B.; Maurin, G.; Horcajada, P.; Serre, C.; Vimont, A.; Lavalley, J. C.; Leclerc, H.; Clet, G.; Daturi, M.; Llewellyn, P. L.; Filinchuk, Y.; Férey, G. *J. Mater. Chem.* **2012**, *22*, 10266.
- (8) Devic, T.; Horcajada, P.; Serre, C.; Salles, F.; Maurin, G.; Moulin, B.; Heurtaux, D.; Clet, G.; Vimont, A.; Greneche, J. M.; Le Ouay, B.; Moreau, F.; Magnier, E.; Filinchuk, Y.; Marrot, J.; Lavalley, J. C.; Daturi, M.; Férey, G. *J. Am. Chem. Soc.* **2010**, *132*, 1127.
- (9) Whitfield, T. R.; Wang, X. Q.; Liu, L. M.; Jacobson, A. J. *Solid State Sci.* **2005**, *7*, 1096.
- (10) Barthelet, K.; Marrot, J.; Férey, G.; Riou, D. *Chem. Commun.* **2004**, 520.
- (11) Shannon, R. D. *Acta Crystallog.* **1976**, *A32*, 751.
- (12) Combelles, C.; Ben Yahia, M.; Pedesseau, L.; Doublet, M. L. *J. Power Sources* **2011**, *196*, 3426.
- (13) Medina, M. E.; Dumont, Y.; Greneche, J. M.; Millange, F. *Chem. Commun.* **2010**, *46*, 7987.
- (14) Medina, M. E.; Dumont, Y.; Greneche, J. M.; Millange, F. *Chem. Commun.* **2010**, *46*, 7987.
- (15) Bailer, J. C.; Young, R. C.; Smith, M. E.; Moeller, T.; Gordon, P. G.; McCullough, F. In *Inorg. Synth.*; John Wiley & Sons, Inc.: 2007, p 126.
- (16) Millange, F.; Guillou, N.; Walton, R. I.; Greneche, J.-M.; Margiolaki, I.; Férey, G. *Chem. Commun.* **2008**, 4732.
- (17) Leclerc, H.; Devic, T.; Devautour-Vinot, S.; Bazin, P.; Audebrand, N.; Férey, G.; Daturi, M.; Vimont, A.; Clet, G. *J. Phys. Chem. C* **2011**, *115*, 19828.
- (18) Barthelet, K.; Marrot, J.; Riou, D.; Férey, G. *Angew. Chem. Int. Ed.* **2001**, *41*, 281.
- (19) Millange, F.; Guillou, N.; Walton, R. I.; Greneche, J.-M.; Margiolaki, I.; Férey, G. *Chem. Commun.* **2008**, 4732.
- (20) Nouar, F.; Devic, T.; Chevreau, H.; Guillou, N.; Gibson, E.; Clet, G.; Daturi, M.; Vimont, A.; Greneche, J. M.; Breeze, M. I.; Walton, R. I.; Llewellyn, P. L.; Serre, C. *Chem. Commun.* **2012**, *48*, 10237.
- (21) Hardcastle, F. D.; Wachs, I. E. *J. Phys. Chem.* **1991**, *95*, 5031.
- (22) Biswas, S.; Vanpoucke, D. E. P.; Verstraelen, T.; Vandichel, M.; Couck, S.; Leus, K.; Liu, Y.-Y.; Waroquier, M.; Van Speybroeck, V.; Denayer, J. F. M.; Van Der Voort, P. *J. Phys. Chem. C* **2013**, *117*, 22784.
- (23) Mendt, M.; Jee, B.; Stock, N.; Ahnfeldt, T.; Hartmann, M.; Himsl, D.; Pöppel, A. *J. Phys. Chem. C* **2010**, *114*, 19443.

- (24) Daramola, M. O.; Burger, A. J.; Pera-Titus, M.; Giroir-Fendler, A.; Miachon, S.; Dalmon, J. A.; Lorenzen, L. *Asia-Pac. J. Chem. Eng.* **2010**, *5*, 815.
- (25) Fu, Y. L.; Ren, J. L.; Ng, S. W. *Acta Crystallogr. Sect. E Struct. Rep. Online* **2004**, *60*, M1507.
- (26) Burrows, A. D.; Cassar, K.; Friend, R. M. W.; Mahon, M. F.; Rigby, S. P.; Warren, J. E. *CrystEngComm* **2005**, *7*, 548.
- (27) Shannon, R. D. *Acta Crystallogr. Sect. A* **1976**, *32*, 751.
- (28) Zou, J.-Y.; Shi, W.; Xu, N.; Gao, H.-L.; Cui, J.-Z.; Cheng, P. *Eur. J. Inorg. Chem.* **2014**, *2014*, 407.
- (29) Zhang, D. P.; Zhao, Z. D.; Wang, P.; Chen, X. *Bull. Korean Chem. Soc.* **2012**, *33*, 1581.
- (30) Zhao, X. Q.; Zhao, B.; Ma, Y.; Shi, W.; Cheng, P.; Jiang, Z. H.; Liao, D. Z.; Yan, S. P. *Inorg. Chem.* **2007**, *46*, 5832.
- (31) Livage, C.; Guillou, N.; Castiglione, A.; Marrot, J.; Frigoli, M.; Millange, F. *Microporous Mesoporous Mater.* **2012**, *157*, 37.
- (32) Sahu, R.; Manivannan, V. *Inorg. Chim. Acta* **2010**, *363*, 4008.
- (33) Liu, R. B.; Zhang, J. J.; Tong, B.; Liu, X.; Yang, Y.; Meng, C. G. *Z. Anorg. Allg. Chem.* **2011**, *637*, 269.
- (34) Dietzel, P. D. C.; Georgiev, P. A.; Eckert, J.; Blom, R.; Strassle, T.; Unruh, T. *Chem. Commun.* **2010**, *46*, 4962.
- (35) Munn, A. S.; Clarkson, G. J.; Millange, F.; Dumont, Y.; Walton, R. I. *CrystEngComm* **2013**, *15*, 9679.
- (36) Nouar, F.; Devic, T.; Chevreau, H.; Guillou, N.; Gibson, E.; Clet, G.; Daturi, M.; Vimont, A.; Greneche, J. M.; Breeze, M. I.; Walton, R. I.; Llewellyn, P. L.; Serre, C. *Chem. Commun.* **2012**, *48*, 10237.
- (37) Serre, C.; Millange, F.; Thouvenot, C.; Nogues, M.; Marsolier, G.; Louer, D.; Ferey, G. *J. Am. Chem. Soc.* **2002**, *124*, 13519.

## 4. Ytterbium-Organic Frameworks

### 4.1. Introduction

Lanthanide cations, typically in the 3+ oxidation state, offer facile ways to form mixed-metal and isostructural metal-organic framework structures due to their similar reactivities. However, unlike transition-metal frameworks where coordination can be rationalised from d-electron configuration, the design and prediction of lanthanide-organic frameworks is difficult to achieve due to their preference of higher coordination numbers (7, 8 and 9 are not uncommon).

Owing the ionic nature of the lanthanide ions where coordination is mainly dependent on the geometry of the ligands themselves, the coordination of lanthanide ions with carboxylate ligands can generate a vast array of potential structures. The variety of coordination modes for known ytterbium 1,4-benzenedicarboxylate are given in Figure 4.1.1. Further coordination can be achieved via bridging solvent molecules or bridging inorganic units, such as hydroxyl moieties.<sup>1-4</sup>

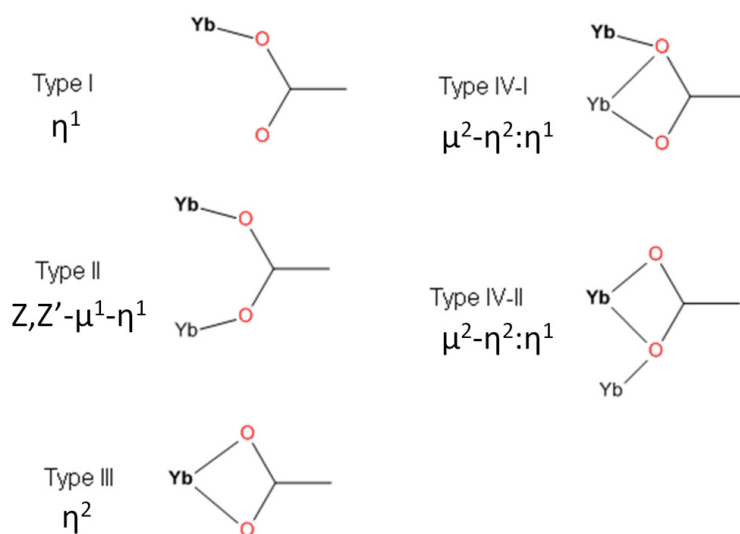


Figure 4.1.1: Examples of coordination modes known for ytterbium dicarboxylates, using notation of Batten *et al.*<sup>5</sup> Principal ytterbium atom is in bold

In this chapter, several new lanthanide-organic frameworks are described. Through mediation of the reaction solvent and subsequent calcinations, several new ytterbium-organic frameworks have been synthesised and their properties investigated. Using a solvent mixture of between 1:0 and 6:4 DMF to water leads to the formation of MB2,  $[\text{Yb}_2(\text{BDC})_3(\text{DMF})_2] \cdot 2\text{H}_2\text{O}$ , which contains ytterbium-carboxylate chains. Calcination of MB2 creates  $\text{Yb}_2(\text{BDC})_3$ , a material that exhibits permanent porosity. Further decreasing the DMF to water ratio in synthesis leads to the formation of MB3,  $[\text{Yb}_2(\text{BDC})_3(\text{DMF})_2(\text{H}_2\text{O})_2]$ , which contains ytterbium-carboxylate dimers. Although sharing similar chemical formulae, MB2 and MB3 vary greatly in terms of structure and properties. Despite of this, both MB2 and MB3 can be calcined into the same  $\text{Yb}_2(\text{BDC})_3$  material, seen from the calcination of MB2.

Attempts to create analogues of MB2 and MB3 using other lanthanides were unsuccessful with the exception of lutetium. In spite of this, doping of MB2(Yb) with other lanthanides was successful and their luminescence properties studies. Synthesis of isorecticular analogues of MB2 and MB3 were partially successful with an isorecticular analogue of MB3, MB5, being formed.

## 4.2. MB2 – $[\text{Yb}_2(\text{BDC})_3(\text{DMF})_2] \cdot 2\text{H}_2\text{O}$

### 4.2.1. Synthesis

Ytterbium (III) chloride hexahydrate (0.001 mol) and 1,4-benzenedicarboxylic acid (0.0015 mol) were dissolved in DMF (5 ml). To this,  $\text{H}_2\text{O}$  (0.15 ml) was added and the mixture stirred until complete dissolution had occurred. The reactants were heated in a 20  $\text{cm}^3$  Teflon-lined autoclave under solvothermal conditions at 100 °C for 20 hours. The resulting white crystalline solid was isolated by suction filtration. Typical reactions yields were over 90 % based on ytterbium conversion. The product was of suitable quality for single crystal XRD and the structure was resolved at 100 K (see below for further analysis). The chemical formula of this material was found to be  $[\text{Yb}_2(\text{BDC})_3(\text{DMF})_2] \cdot 2\text{H}_2\text{O}$ . This material is referred to as 'MB2'. MB2 can be formed at temperatures between 80 and 120 °C. At lower temperatures, no product was formed after two weeks whereas higher temperatures led to the formation of MB2 and an unknown impurity.

### 4.2.2. Structure

$[\text{Yb}_2(\text{BDC})_3(\text{DMF})_2] \cdot 2\text{H}_2\text{O}$  (MB2) crystallises in the monoclinic  $C2/c$  space group. Each ytterbium atom is coordinated to seven oxygens: six from singly coordinating 1,4-benzenedicarboxylate (Type II,  $Z, Z' - \mu^1 - \eta^1$ ) (BDC) linkers and one from O-coordinated DMF (Figure 4.2.1). The DMF is structurally disordered across two positions in a ratio of 0.6:0.4. Two water molecules are uncoordinated and extra-framework. A fuller view of the crystal structure is shown in Figure 4.2.2. Crystallographic data are given in Table 4.2.1 and Table 4.2.2.

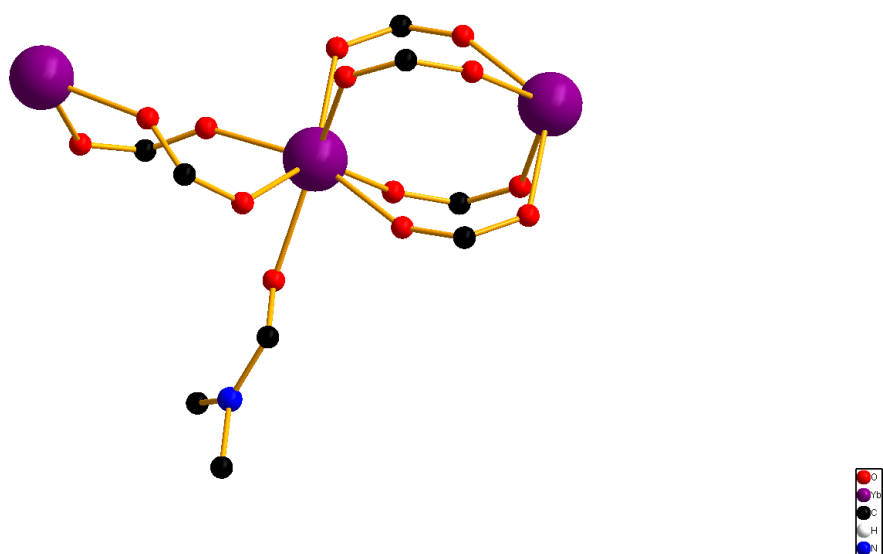


Figure 4.2.1: Coordination of ytterbium atom to its immediate neighbours. Only major position DMF included for clarity

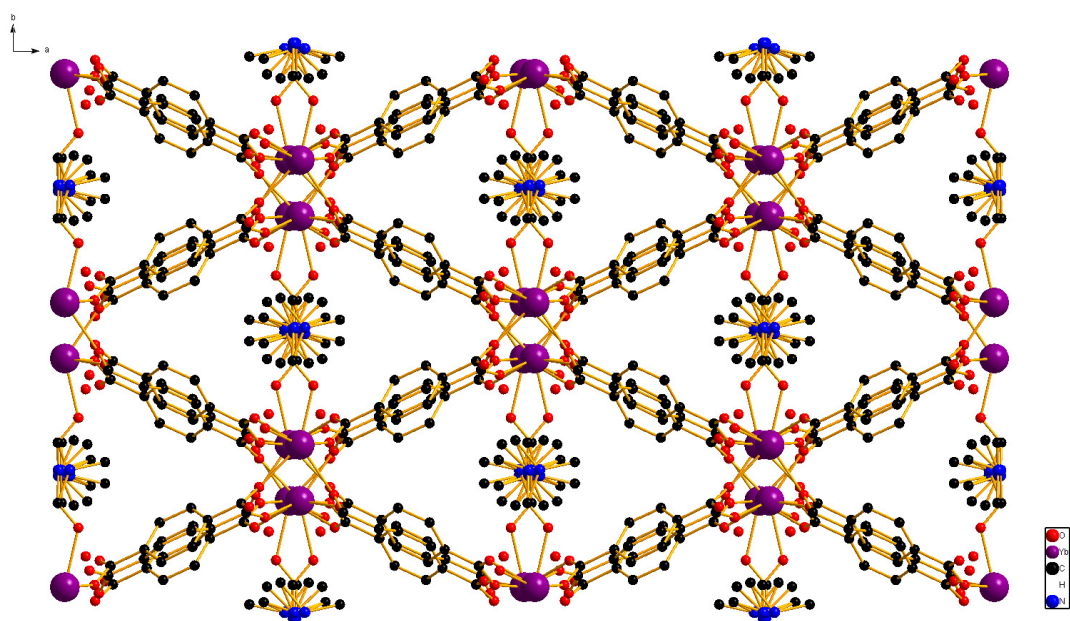


Figure 4.2.2: Crystal structure of MB2 viewed along the c-axis. Only major position DMF included for clarity

Table 4.2.1: Crystallographic data of MB2

	MB2
Formula	C <sub>30</sub> H <sub>28</sub> N <sub>2</sub> O <sub>15</sub> Yb <sub>2</sub>
Formula Weight	1002.62
Colour/Shape	Block, colourless
Size of Crystal	0.16 x 0.14 x 0.12 mm <sup>3</sup>
Temperature / K	100(2)
Crystal System	Monoclinic
Space Group	C 2/c
a / Å	18.2950(4)
b / Å	10.8482(2)
c / Å	17.3984(4)
α / °	90
β / °	101.395(2)
γ / °	90
Cell volume / Å <sup>3</sup>	3384.96
Z	4
Density (calc.) / g·cm <sup>3</sup>	1.96728

Table 4.2.2: Atomic Parameters for MB2

Atom	Wyck.	Site	S.O.F.	x/a	y/b	z/c	U [Å <sup>2</sup> ]
O109	8f	1	0.5	0.91480(15)	0.8085(2)	0.31030(15)	0.017
Yb1	8f	1		0.48899(1)	0.40160(1)	0.10202(1)	
O1	8f	1		0.5551(4)	0.2935(6)	-0.2386(4)	
O101	8f	1		0.57547(14)	0.5501(2)	0.12475(15)	
C102	8f	1		0.6134(2)	0.6078(3)	0.0831(2)	0.016
O102	8f	1		0.59664(15)	0.6197(2)	0.01028(16)	
C103	8f	1		0.6851(2)	0.6653(3)	0.1242(2)	
C104	8f	1		0.7174(2)	0.7595(4)	0.0879(2)	
H10A	8f	1		0.6939	0.7873	0.0373	0.017
C105	8f	1		0.7840(2)	0.8130(3)	0.1256(2)	
H10B	8f	1		0.8052	0.8788	0.1014	
C106	8f	1		0.8197(2)	0.7698(3)	0.1991(2)	
C107	8f	1		0.7873(2)	0.6745(3)	0.2351(2)	0.017
H10C	8f	1		0.8114	0.6448	0.285	
C108	8f	1		0.7203(2)	0.6236(4)	0.1982(2)	
H10D	8f	1		0.698	0.56	0.2233	
C109	8f	1	0.5	0.89205(19)	0.8272(3)	0.2385(2)	0.02
O110	8f	1		0.92585(15)	0.8937(2)	0.19674(16)	
O201	8f	1		0.56335(15)	0.3435(3)	0.02093(15)	
O202	8f	1		0.58337(15)	0.4227(2)	0.00100(16)	
C202	8f	1		0.6032(2)	0.3604(3)	-0.0296(2)	
C203	8f	1		0.6793(2)	0.3032(3)	-0.0147(2)	
C204	8f	1		0.7097(2)	0.2580(4)	0.0595(2)	
H20A	8f	1		0.6821	0.2637	0.1002	



Atom	Wyck.	Site	S.O.F.	x/a	y/b	z/c	U [Å <sup>2</sup> ]
C205	8f	1		0.7200(2)	0.2951(4)	-0.0746(2)	
H20B	8f	1		0.6996	0.3259	-0.1254	0.019
O301	8f	1		0.46041(16)	0.1930(2)	0.09704(16)	
C302	8f	1	0.6	0.5042(3)	0.1062(4)	0.0996(3)	0.0231(9)
H30A	8f	1	0.6	0.5544	0.1195	0.0946	0.028
N303	8f	1	0.6	0.4787(4)	-0.0100(6)	0.1098(4)	0.0229(16)
C304	8f	1	0.6	0.4036(5)	-0.0376(9)	0.1164(6)	0.036(2)
H30B	8f	1	0.6	0.38	0.0367	0.1322	0.054
H30C	8f	1	0.6	0.4039	-0.1022	0.1558	0.054
H30D	8f	1	0.6	0.3756	-0.0663	0.0656	0.054
C305	8f	1	0.6	0.5299(6)	-0.1144(7)	0.1137(6)	0.0297(19)
H30E	8f	1	0.6	0.5778	-0.0858	0.1032	0.045
H30F	8f	1	0.6	0.5085	-0.176	0.0744	0.045
H30G	8f	1	0.6	0.5375	-0.1514	0.1661	0.045
C2A	8f	1	0.4	0.5042(3)	0.1062(4)	0.0996(3)	0.0231(9)
H2AA	8f	1	0.4	0.5493	0.1288	0.0841	0.028
N3A	8f	1	0.4	0.5026(5)	-0.0093(7)	0.1187(6)	0.016(2)
C4A	8f	1	0.4	0.4343(7)	-0.046(1)	0.1452(8)	0.034(3)
H4AA	8f	1	0.4	0.4181	0.0221	0.1754	0.051
H4AB	8f	1	0.4	0.4442	-0.119	0.1784	0.051
H4AC	8f	1	0.4	0.395	-0.0638	0.0996	0.051
C5A	8f	1	0.4	0.5587(7)	-0.1000(9)	0.1125(7)	0.019(2)
H5AA	8f	1	0.4	0.6	-0.0605	0.0937	0.028
H5AB	8f	1	0.4	0.5369	-0.1645	0.0756	0.028
H5AC	8f	1	0.4	0.5773	-0.1368	0.1641	0.028

Each ytterbium is connected to adjacent ytterbiums via two and four carboxylato groups from the BDC linkers in a regular (-Yb-(O-C-O)<sub>4</sub>-Yb-(O-C-O)<sub>2</sub>-Yb-) fashion. Every carboxylate group bonds to two different ytterbium atoms in a monodentate fashion (type II) (Figure 4.1.1). This type of connectivity with only one coordination mode has not been reported in any other Yb-BDC MOFs, and leads to the formation of 1-D chains of ytterbium-carboxylate chains running along the c-axis. The coordinated DMF molecules orientate perpendicular to the dimension of the chains (Figure 4.2.3).

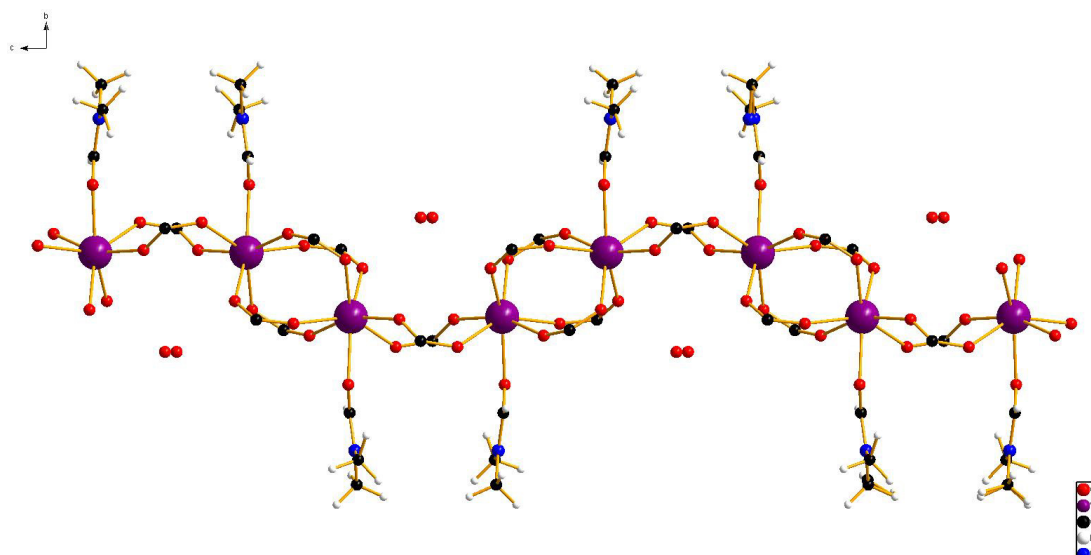
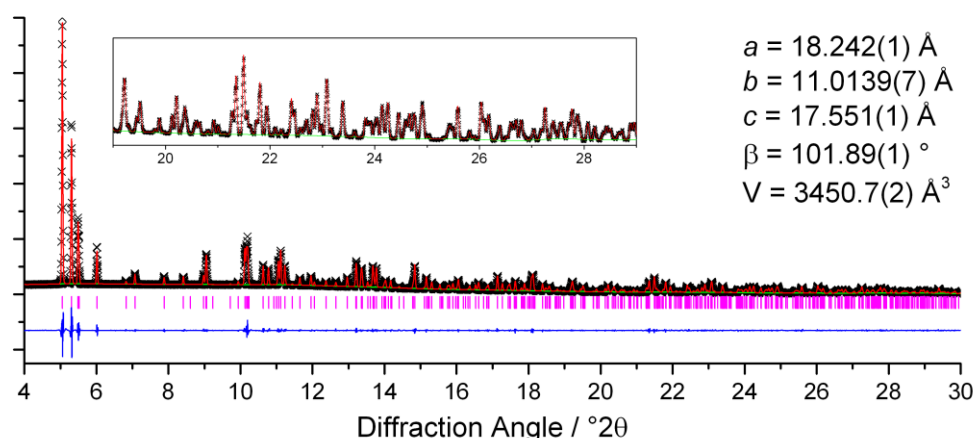


Figure 4.2.3: Ytterbium-carboxylate oxygen chain viewed along the  $a$ -axis. Only carboxylate group of linker shown. Only major DMF position shown. Extra-framework water is also shown.

Every ytterbium-carboxylate chain is connected to four other chains along the BDC linker. The linkers originating from  $(\text{Yb}-(\text{O}-\text{C}-\text{O})_4-\text{Yb})$  dimers connect to only  $(\text{Yb}-(\text{O}-\text{C}-\text{O})_2-\text{Yb})$  dimers and *vice versa*. This leads to directly connected chains having anti-periodicity with regards to one another. The periodicity of chains is restored with the next level of connectivity with adjacent chains with regards to the  $b$ -axis able to stack well with each other, resulting in regular packing of coordinated DMF along the  $c$ -axis. The overall effect of the inter-connectivity of the ytterbium-carboxylate chains leads to the formation of 1-D diamond shaped channels running along the  $c$ -axis, occupied by coordinated DMF and extra-framework water as shown in Figure 4.2.2.

Since all metal atoms are connected by organic moieties, this structure can be described as  $(\text{I}^0\text{O}^3)$  using Cheetham-Rao-Feller nomenclature.<sup>6</sup> The room temperature powder pattern can be successfully matched to the crystal data using a profile of refinement (Figure 4.2.4). An increase in the unit cell lengths can be seen for the  $b$  and  $c$  parameters whereas a decrease is seen for the  $a$  parameter when comparing the room temperature pattern with that of the crystal data collected at 100 K. The opposing behaviour of the  $a$  and  $b$  unit cell lengths can be easily rationalised since they represent the

channel cross-section – expansion in one direction must be countered by contraction in the other. Since the *b* unit cell length is roughly parallel with that of the DMF orientation, any expansion in this direction is consistent with increased steric hindrance between DMF coordinated to adjacent chains caused by increasing temperature. CHN analysis is consistent with the chemical formula of MB2 ((C 35.60%, 35.30%(calc.); H 2.47%, 2.78%(calc.); N 2.83%, 2.74%(calc.))



**Figure 4.2.4:** Profile fit of PXRD pattern of MB2 at 298 K with refined parameters. Data were collected on Beamline I11 at Diamond ( $\lambda = 0.825174$  Å). Black crosses: experimental data; Green: background; Red: profile fit; Magenta lines: allowed reflections; difference between experimental data and fit. Insert: Profile fit at higher angle

The structure of MB2 closely resembles that of  $\text{Er}_2(\text{BDC})_3(\text{DMF})_2$  reported by Zhang *et al.*<sup>7</sup> Both structures have the same connectivity and space group with the difference being the presence of occluded water in MB2. The presence of water seemingly has the effect of decreasing the Yb-Yb-Yb angle ( $148^\circ$ ) leading to a greater ‘creasing’ of the ytterbium-carboxylate chains along the *c*-axis as opposed to the flattened chains of the erbium material ( $157^\circ$ ) (Figure 4.2.5). Despite the lack of interstitial water, the erbium material has a larger unit cell volume ( $3523.93(140)$  Å<sup>3</sup>), consistent with the larger ionic radius of erbium when compared with ytterbium.<sup>8</sup> This is also reflected in the larger average Ln-O bond distances (Yb-O =  $2.268$  Å, Er-O =  $2.284$  Å).

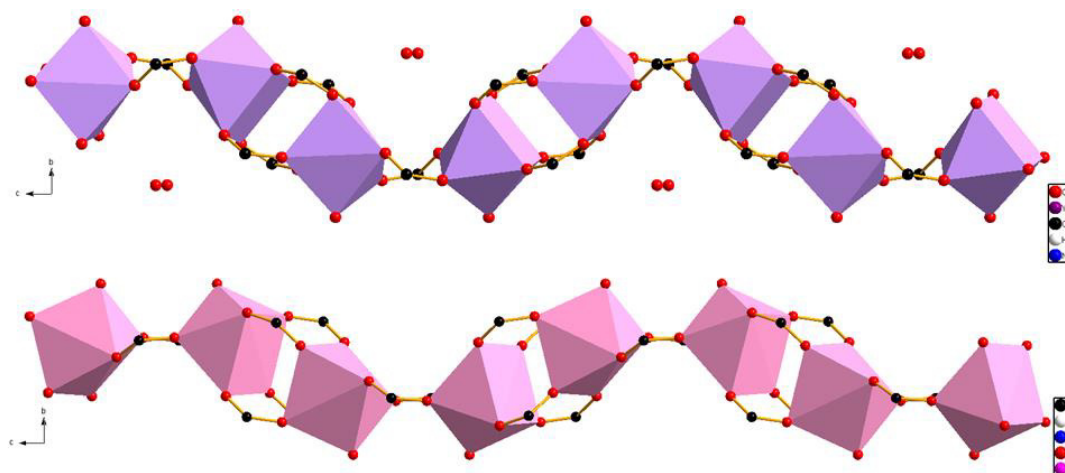


Figure 4.2.5: Comparison of the lanthanide-carboxylate chains of MB2 (top) and  $\text{Er}_2(\text{BDC})_3(\text{DMF})_2$  (bottom)

Two closely related thulium analogues of MB2 have been reported by He *et al.*<sup>9</sup> These materials display identical framework connectivity to that of MB2 with different coordinating solvent molecules.  $[\text{Tm}_2(\text{BDC})_3(\text{H}_2\text{O})_2] \cdot \text{DMF} \cdot 2\text{C}_2\text{H}_5\text{OH} \cdot 4\text{H}_2\text{O}$  contains channels partially occupied by coordinating water molecules and extra-framework DMF whereas  $[\text{Tm}_2(\text{BDC})_3(\text{H}_2\text{O})_1(\text{DMF})_1] \cdot \text{DMF} \cdot \text{H}_2\text{O}$  has alternating channels occupied by either coordinated water or DMF. These materials both display porosity when activated under vacuum. He *et al.* rationalised that the  $\text{Tm}_2(\text{BDC})_3$  material formed kept the same connectivity after removal of the solvent although without post-activation diffraction data, it is difficult to determine whether this is indeed the case or not.

### 4.2.3. Thermal Behaviour of MB2

Although MB2 itself is likely to be non-porous, the presence of apparent channels along the c-axis occupied by coordinated DMF and extra-framework water made calcination studies worthwhile. To follow the calcination of MB2, *in situ* thermodiffraction and thermogravimetric analysis were used to monitor any mass losses and phase changes associated with heating of the material.

Upon heating, the first structural change of MB2 is observed at 70 °C from the thermodiffraction (Figure 4.2.6). This can be associated to a weight loss of 3.7 % seen

by TGA (Figure 4.2.8). This corresponds to loss of two extra-framework waters (calc.: 3.6 %). The second structural change is observed at 180 °C and likely corresponds to the loss of one DMF molecule (6.2 %, calc.: 7.3 %). The third occurs at 240 °C which is accompanied by the loss of the second DMF molecule (6.3 %, calc.: 7.3 %). Combustion of the BDC linkers is observed at 500 °C, leading to formation of  $\text{Yb}_2\text{O}_3$  (40.0 %, calc.: 38.6 %) as evidenced by the PXRD pattern of MB2 heated to 600 °C (Figure 4.2.7). This weight loss profile agrees well with the initial crystal formula of  $[\text{Yb}_2(\text{BDC})_3(\text{DMF})_2] \cdot 2\text{H}_2\text{O}$ . The loss of DMF in two stages is interesting in itself since the unit cell of MB2 contains two DMF molecules in identical environments (Figure 4.2.2), suggesting that DMF should leave in a single step. However, this is not observed, implying that guest molecule departure is not a simplistic process.

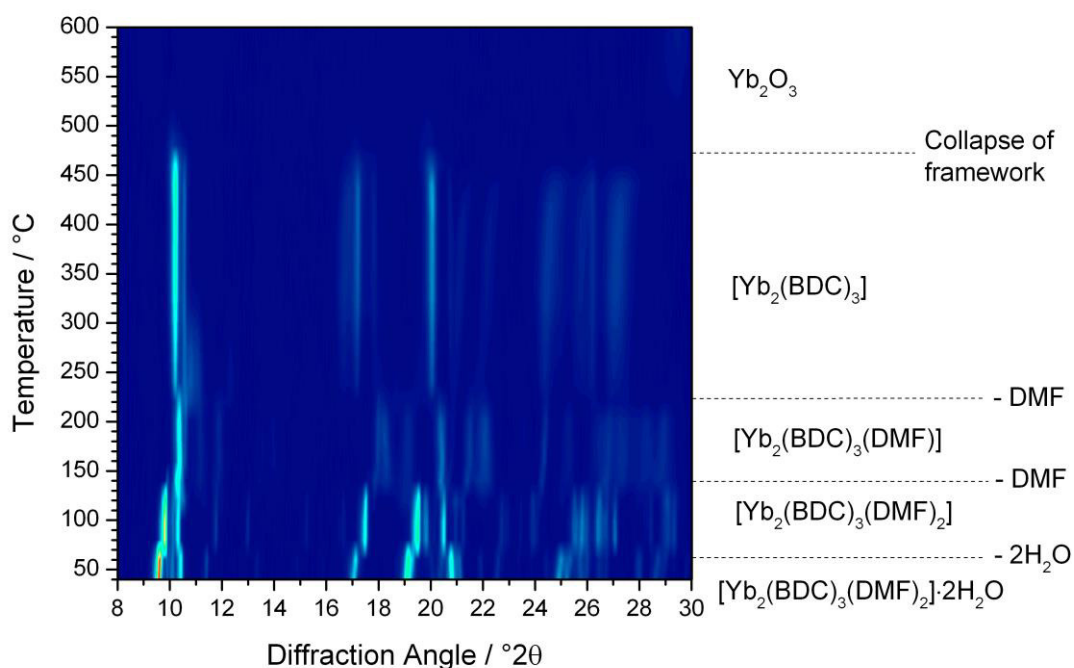


Figure 4.2.6: Thermodiffractometry of MB2 with annotated mass losses and predicted chemical formulae

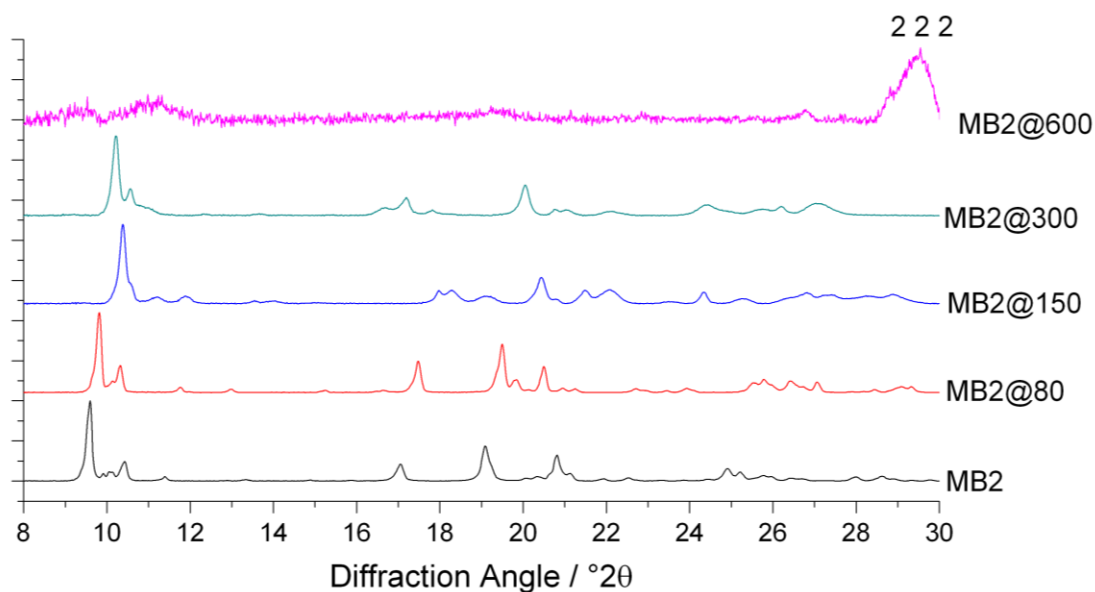


Figure 4.2.7: Comparison of PXRD patterns of MB2 after each calcination step with labelled 2 2 2 peak of ytterbium oxide

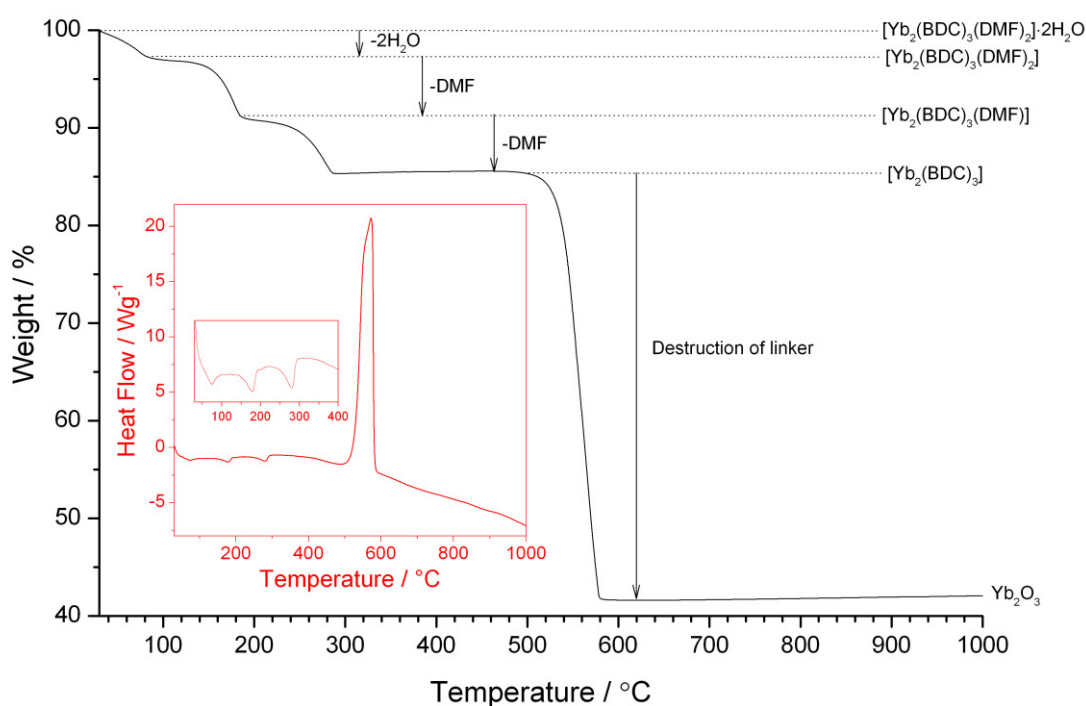


Figure 4.2.8: Main: TGA of MB2 in air; Insert: DSC curve of MB2 over same temperature range; Insert, Insert: DSC curve over temperature range of 30-400 °C showing loss of water and DMF

A comparison of the XRD patterns taken at room temperature and at 80 °C show that the loss of water leads to a contraction in the unit cell as seen in Figure 4.2.7. This is

accompanied by a small decrease in the DSC curve, consistent with the endothermic loss of solvent. The powder XRD pattern of MB2 at 80 °C (MB2@80 °C) now resembles that of the known  $\text{Er}_2(\text{BDC})_3(\text{DMF})_2$  structure showing that no collapse or rearrangement of the structure has occurred (Figure 4.2.10). This is further supported by re-absorption of water upon cooling to form the original MB2 structure (see Figure 4.2.9).

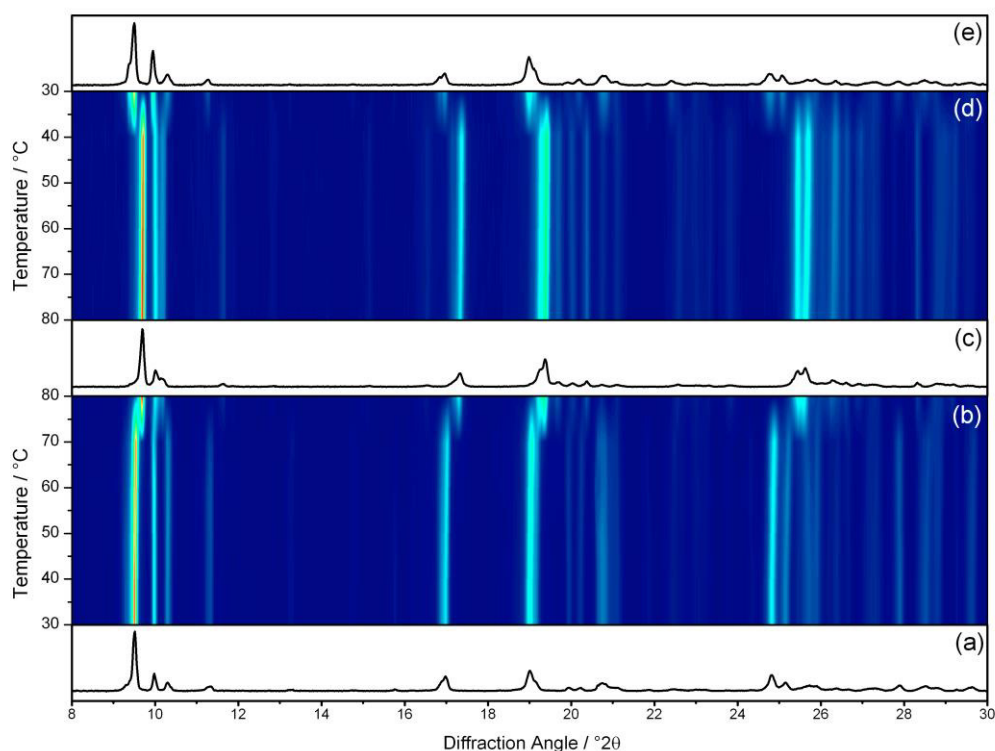


Figure 4.2.9: (a) PXRd pattern of MB2 at 30 °C; (b) Thermodiffractometry of MB2 heating to 80 °C; (c) PXRd pattern of MB2 at 80 °C; (d) Thermodiffractometry of cooling back to 30 °C in air; (e) PXRd pattern of MB2 after cooling

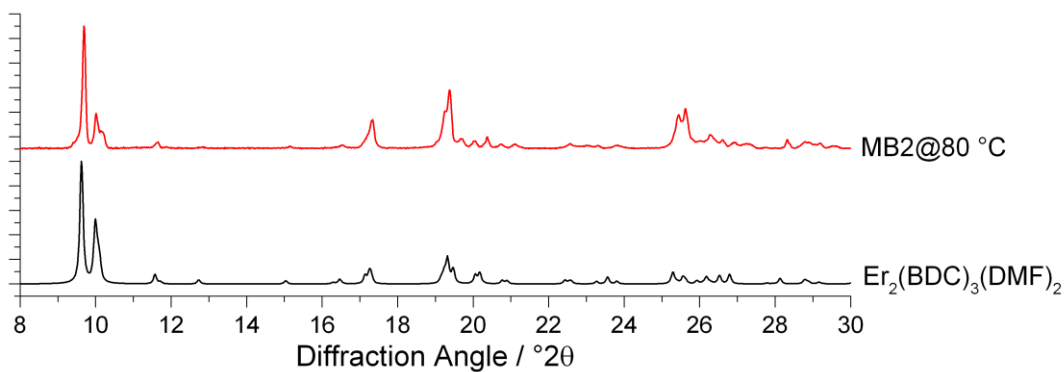
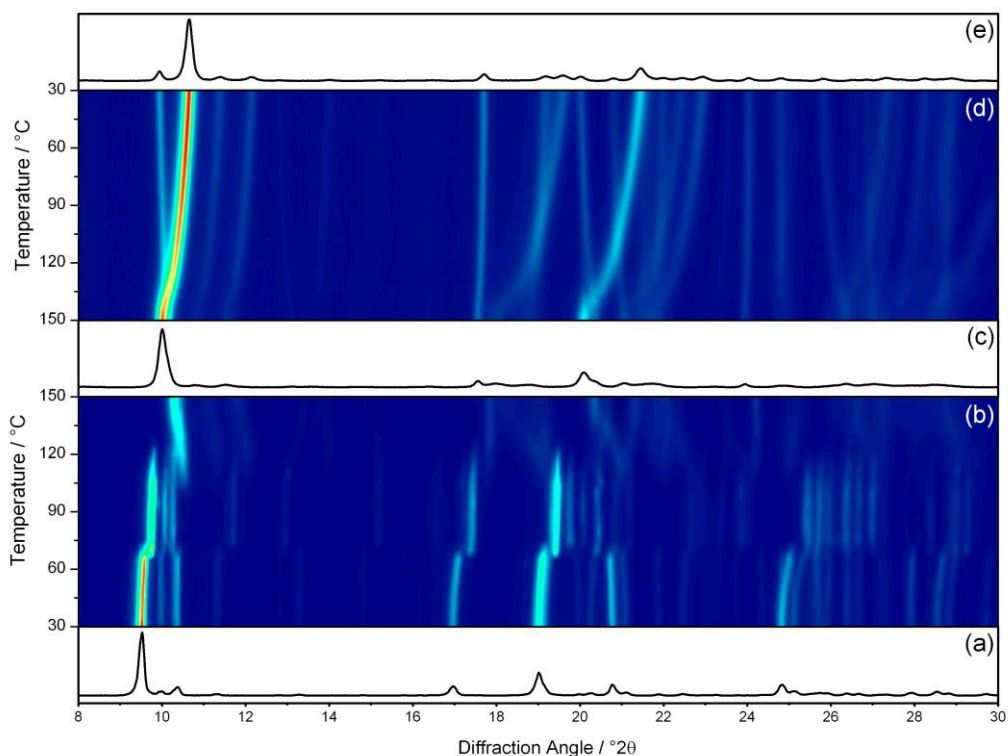


Figure 4.2.10: Comparison of the PXRd pattern of MB2 collected *in situ* at 80 °C with that of the simulated PXRd pattern of  $\text{Er}_2(\text{BDC})_3(\text{DMF})_2$

Heating of MB2 to 150 °C leads to loss of half of the coordinated DMF as evidenced by TGA and endothermic behaviour in the DSC curve. This material after cooling in air shall now be referred to as MB2-150. This loss of solvent is accompanied by a further contraction in the unit cell. Upon cooling, the material undergoes a relaxation in the structure evidenced by gradual shifts in the Bragg peaks with decreasing temperature (Figure 4.2.11). Since the diffraction pattern remains the same upon cooling in either air or dry nitrogen, possible adsorption of water by the material seems unlikely. Thermogravimetric analysis of a sample of MB2-150 produced after cooling supports this with only a small initial loss (surface water ~1.1 %) followed by loss of the remaining DMF (5.9 %, calc.: 7.9 %) (Figure 4.2.12). The PXRD patterns of MB2 heated to 150 °C (MB2@150) and MB2-150 do not match those of the known ytterbium-BDC materials. Unfortunately, the low crystallinity of these MB2-150 materials makes structural determination difficult.



**Figure 4.2.11:** (a) PXRD pattern of MB2 at 30 °C; (b) Thermodiffractometry of MB2 heating to 150 °C; (c) PXRD pattern of MB2 at 150 °C; (d) Thermodiffractometry of cooling back to 30 °C in air; (e) PXRD pattern of MB2-150 after cooling



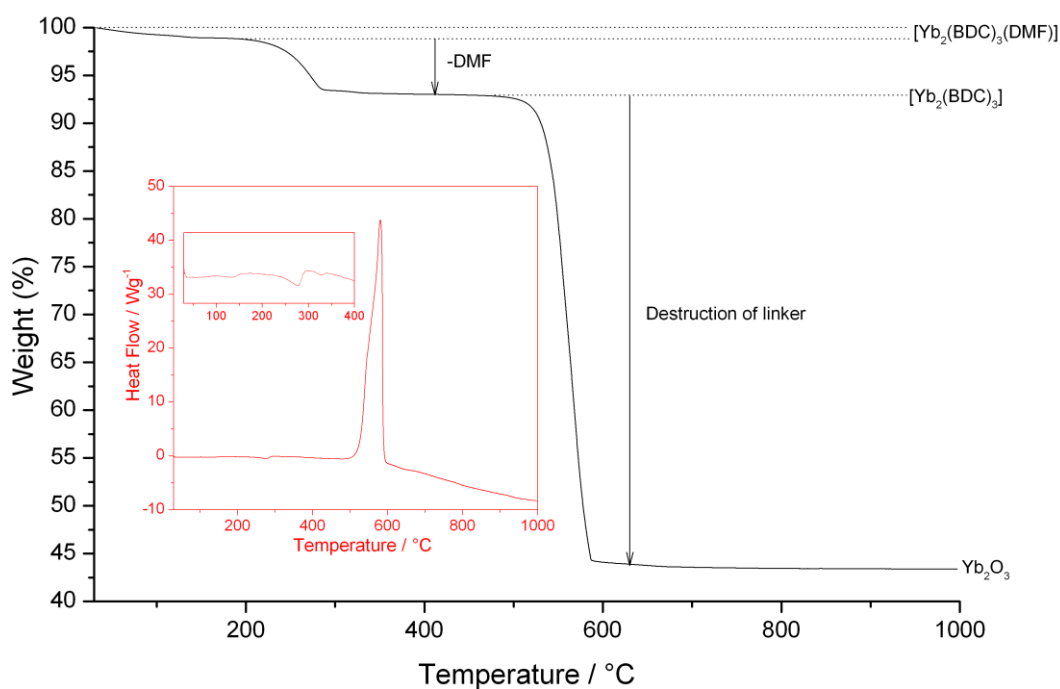


Figure 4.2.12: Main: TGA of MB2-150 in air; Insert: DSC curve of MB2 over same temperature range; Insert, Insert: DSC curve over temperature range of 30-400 °C showing loss of water and remaining DMF

Upon heating to 300°C,  $\text{Yb}_2(\text{BDC})_3$  is formed. This material undergoes a single phase change upon cooling with identical cooling profiles seen by thermodiffraction under either air or dry nitrogen, suggesting that this material does not absorb water (Figure 4.2.13). This phase change is not continuous like the previous one but occurs abruptly at around 150 °C upon cooling. Elemental analysis of  $\text{Yb}_2(\text{BDC})_3$  is consistent with this formula (C: 33.92 %, 34.38 %(calc.); H: 1.68 %, 1.44 %(calc.)). Attempts to regenerate MB2 through immersion in DMF were unsuccessful suggesting that this material no longer adopts a MB2-like connectivity.

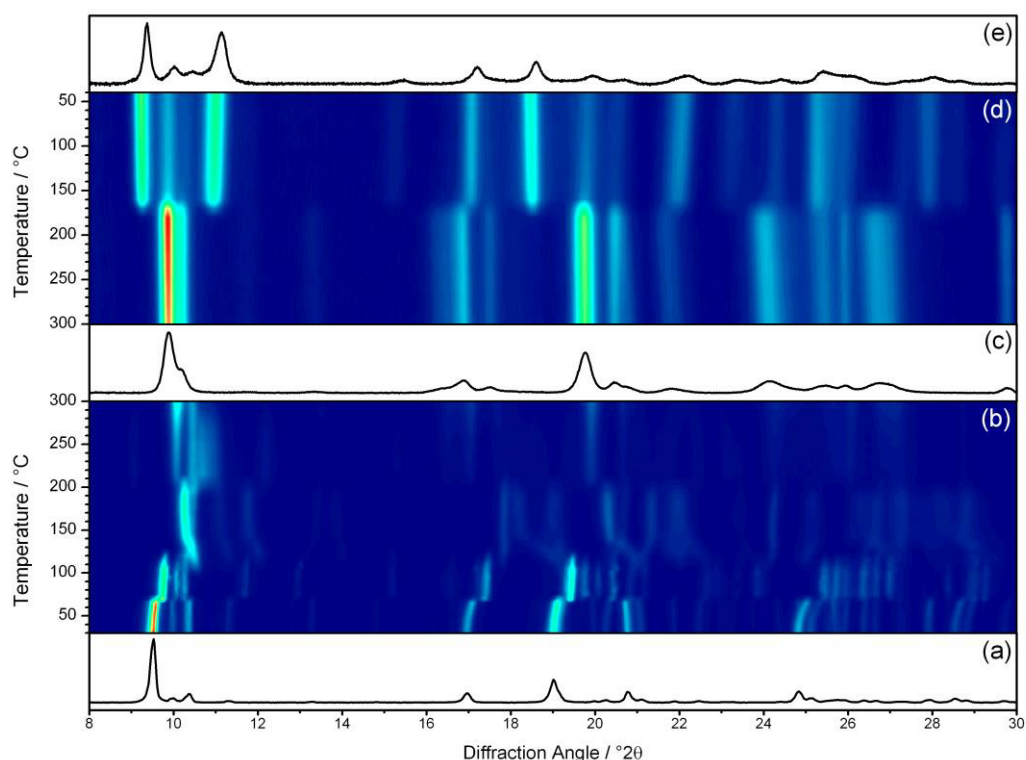


Figure 4.2.13: (a) PXRd pattern of MB2 at 30 °C; (b) Thermodiffractometry of MB2 heating to 300 °C in air; (c) PXRd pattern of MB2 at 300 °C; (d) Thermodiffractometry of cooling back to 30 °C in air; (e) PXRd pattern of MB2-300 after cooling

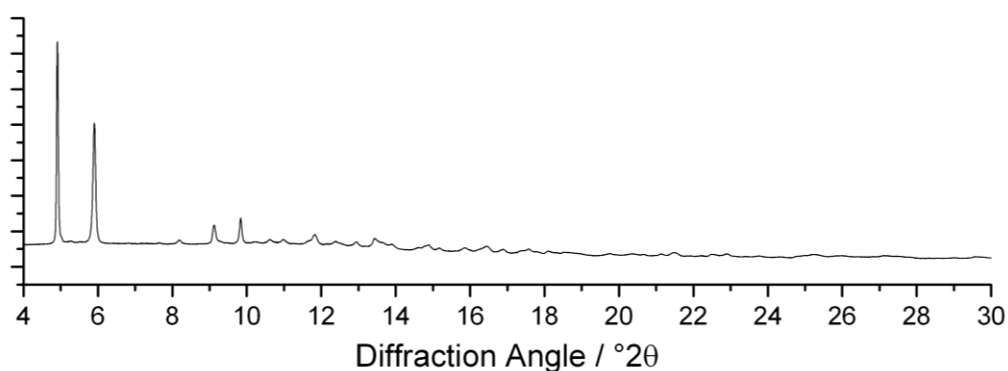


Figure 4.2.14: PXRd pattern of MB2-300. Data were collected on Beamline I11 at Diamond ( $\lambda = 0.825174 \text{ \AA}$ ). Sample was calcined slowly using a heating and cooling rate of  $0.2 \text{ }^{\circ}\text{C}\cdot\text{s}^{-1}$  and a dwell time of 6 hours.

Thermogravimetric analysis of  $\text{Yb}_2(\text{BDC})_3$  shows no significant mass losses until destruction of the linkers at around 500 °C (below). The collapse of the framework and destruction of the BDC linkers to form ytterbium (III) oxide agrees well with the weight loss of 52.5 % seen (expected: 54.0 %). This further confirms the identity of MB2 calcined at 300 °C (MB2-300) as  $\text{Yb}_2(\text{BDC})_3$ .

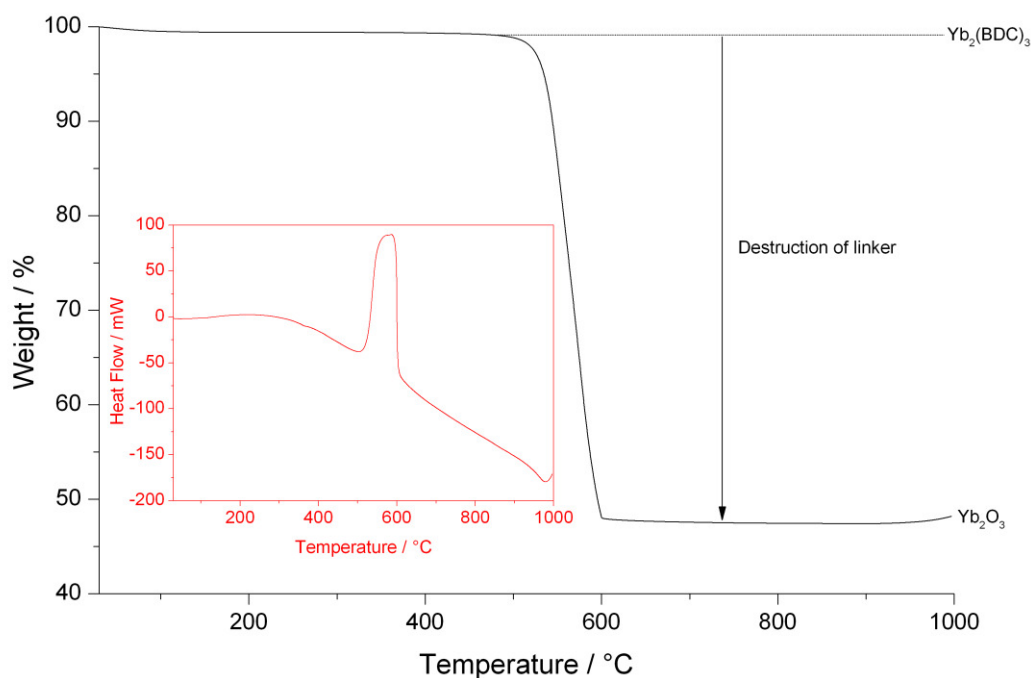


Figure 4.2.15: Main: TGA of MB2-300 in air; Insert: DSC curve of MB2-300 over same temperature range

To further investigate the apparent robustness of the  $\text{Yb}_2(\text{BDC})_3$  towards loss and regain of water,  $\text{Yb}_2(\text{BDC})_3$  was heated to 300 °C and the powder XRD pattern collected *in situ* both during and after heating in air. Unlike the initial cooling profile seen post-calcination that displayed a phase change at around 170 °C, the XRD patterns of  $\text{Yb}_2(\text{BDC})_3$  at 300 °C and at room temperature show little difference illustrating the stability of the structure (Figure 4.2.16).

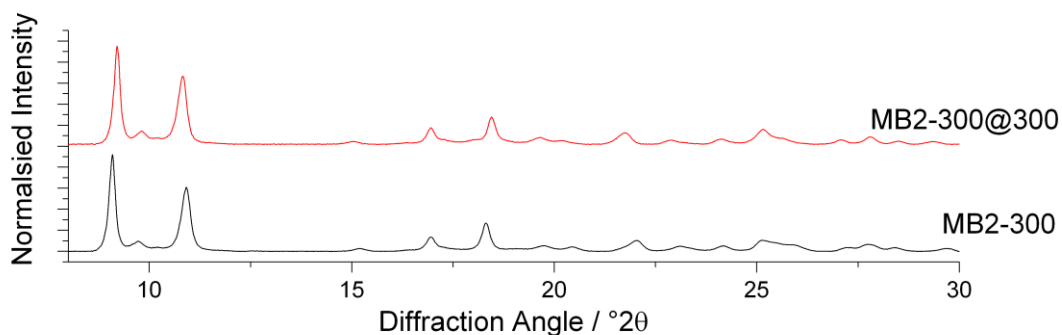


Figure 4.2.16: PXRD patterns of MB2-300 and MB2-300 collected *in situ* at 300 °C

The lack of coordinated solvent within the  $\text{Yb}_2(\text{BDC})_3$  structure should allow for a porous structure. Very few  $\text{Ln}_2(\text{BDC})_3$  materials have been reported and characterised. The

Yaghi group reported that  $\text{Tb}_2(\text{BDC})_3(\text{H}_2\text{O})_4$  could be dehydrated at elevated temperatures to form  $\text{Tb}_2(\text{BDC})_3$  with reabsorption of water upon cooling.<sup>10</sup> Further work by Daiguebonne *et al.* expanded on this and reported a isostructural series of  $\text{Ln}_2(\text{BDC})_3(\text{H}_2\text{O})_4$  ( $\text{Ln} = \text{La-Tm}$ ) materials that all displayed the same loss and reabsorption of water with temperature.<sup>11,12</sup> The lighter lanthanide materials ( $\text{Ln} = \text{La-Eu}$ ) dehydrate with no overall change in their structure whereas the smaller  $\text{Ln}_2(\text{BDC})_3(\text{H}_2\text{O})_4$  ( $\text{Ln} = \text{Tb-Tm}$ ) undergo a structural phase change. The XRD patterns of the dehydrated smaller  $\text{Ln}_2(\text{BDC})_3$  materials were indexed but not solved. Attempts to synthesise ytterbium and lutetium analogues of these materials lead to the formation of  $[\text{Er}_2(\text{BDC})_3(\text{H}_2\text{O})_8] \cdot 2\text{H}_2\text{O}$  analogues.<sup>11</sup> Pan *et al.* reported the synthesis of  $[\text{Er}_2(\text{BDC})_3(\text{H}_2\text{O})_6]$ . This material could be dehydrated to  $\text{Er}_2(\text{BDC})_3$  and but formed  $[\text{Er}_2(\text{BDC})_3(\text{H}_2\text{O})_4]$  upon reabsorption of water.<sup>13</sup> None of these dehydrated materials has powder XRD patterns that match that of MB2-300 ( $\text{Yb}_2(\text{BDC})_3$ ).

To conclude this section, several new ytterbium-organic frameworks have been made through calcination of MB2. The PXRD patterns of these materials both at calcination temperature and after cooling do not match those of any reported lanthanide-BDC materials. This aptly displays the advantage of both calcination and thermodiffraction in characterising new lanthanide-organic framework materials. A scheme for the synthesis, the calcination profile and the products formed from MB2 is given in Figure 4.2.17.

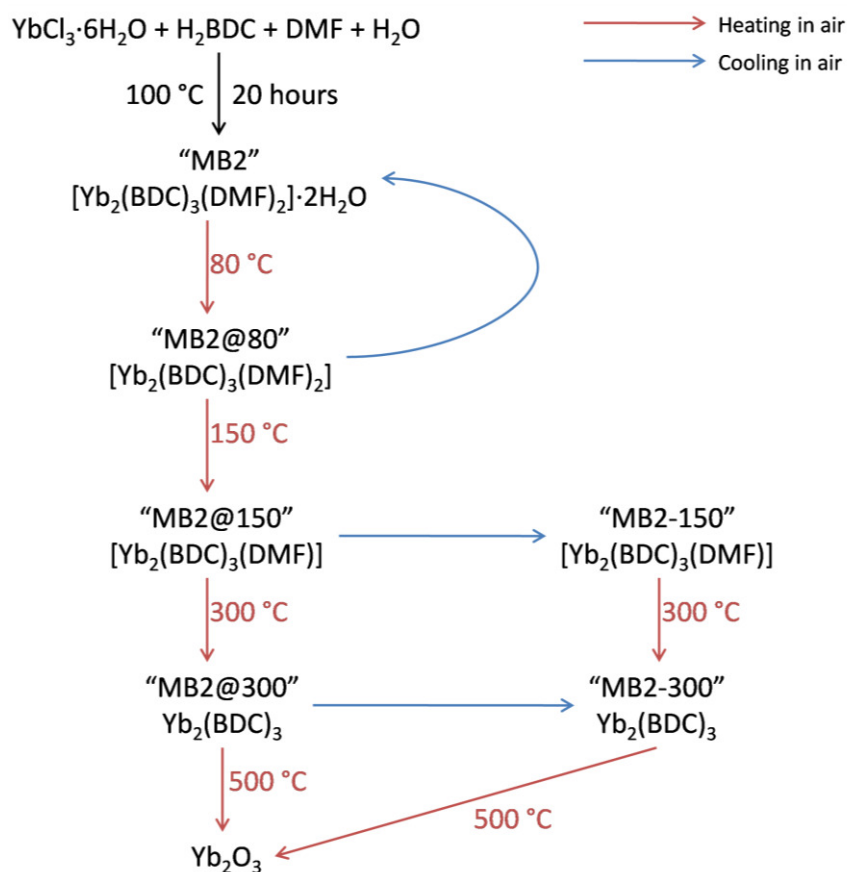


Figure 4.2.17: Reaction scheme for the synthesis of MB2 and its calcination products

#### 4.2.4. Porosity Studies of MB2

To investigate the porosity of this material and its decomposition products, MB2 was activated at 100 °C, 200 °C and 300 °C under vacuum. These three temperatures correspond well to each of the calcination steps observed in the previous section. Gas adsorption studies were made at 77 K using nitrogen as a probe molecule. The sample activated at 100 °C shows little uptake of nitrogen, which is consistent with the structure of MB2 where most of the free space in the framework is occupied by the coordinated DMF.

The samples of MB2 activated at 200 and 300 °C display type IV adsorption isotherm with H4-type hysteresis loops.<sup>14</sup> Low pressure hysteresis is indicative of strong interactions between the adsorbent and the adsorbate, possibly due to the presence of open metal sites. This hysteresis was also seen for the previously mentioned thulium materials.<sup>15</sup> The samples activated at 200 and 300 °C adsorb 80 and 100 cm<sup>3</sup> (STP) g<sup>-1</sup> of

nitrogen corresponding to BET surface areas of 218 and 305 m<sup>2</sup> g<sup>-1</sup>, respectively. To the best of our knowledge, these are the highest values reported for any lanthanide 1,4-benzenedicarboxylate material.<sup>10,15,16</sup>

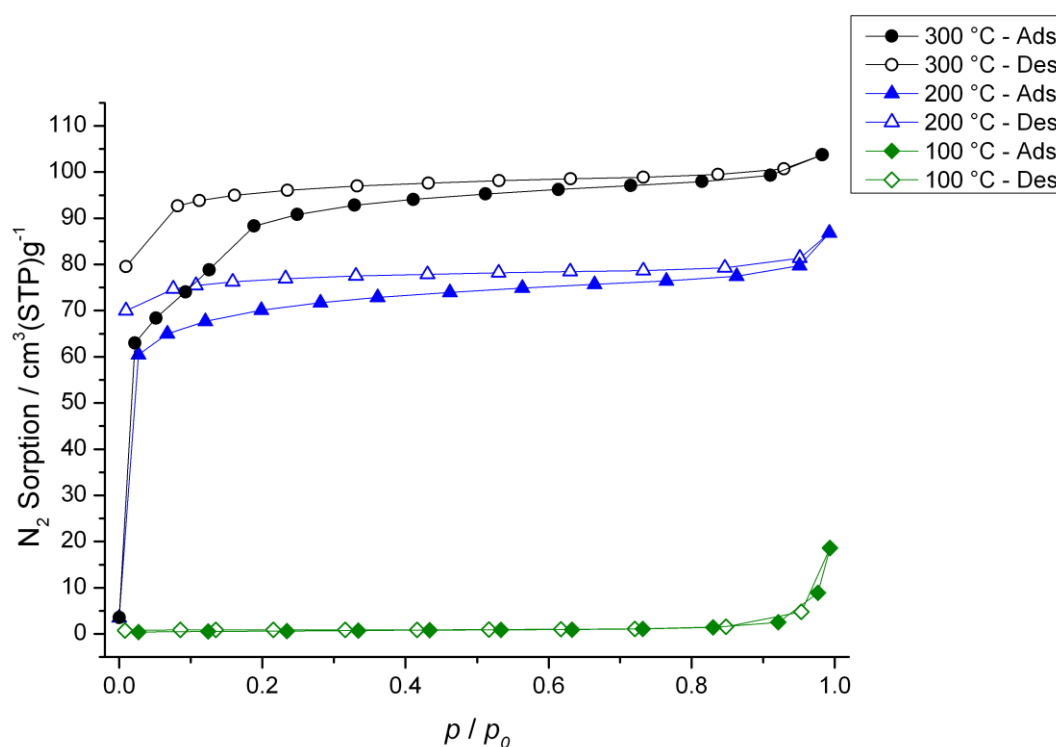


Figure 4.2.18: N<sub>2</sub> Sorption Isotherms of MB2 calcined at various temperatures under vacuum. Filled symbols: adsorption isotherm; Empty symbols: desorption isotherm

#### 4.2.5. Infrared Spectra of MB2 and Its Calcination Products

The IR spectrum of MB2, Figure 4.2.19 and Figure 4.2.20, shows the presence of both hydrogen-bonded water (3584, 3527 cm<sup>-1</sup>) and coordinated DMF (3050-2935 cm<sup>-1</sup>). The lack of a peak at 1700 cm<sup>-1</sup> corresponding to aryl-carboxylic acids implies that no free linker is present and all the 1,4-benzenedicarboxylic acid is coordinated. The peak at 1680 cm<sup>-1</sup> can be associated to the C=O stretch of DMF. Peaks at 1633-1562 cm<sup>-1</sup> and 1397-1375 cm<sup>-1</sup>, relating to the anti-symmetrical and symmetrical C-O stretches of carboxylate ions, further support this. Bands at 1108 and 1095 cm<sup>-1</sup> relate to the C-N stretch of DMF. The presence of a peak at 823 cm<sup>-1</sup> proves that no rearrangement of the 1,4-benzenedicarboxylate linkers has occurred with only para-substituted ring systems present.

The IR spectrum of MB2 calcined at 150°C (MB2-150) shows a complete disappearance of the O-H peaks from water at around 3550  $\text{cm}^{-1}$ . There is also a large decrease in intensity of the bands relating to the coordinated DMF (1680,  $\sim 1100 \text{ cm}^{-1}$ ). This suggests that some of the coordinated DMF is lost which agrees with the thermogravimetric analysis ( $\sim 50\%$  DMF lost). The peak relating to symmetrical C-O stretching has become degenerate, displaying only one peak at 1380  $\text{cm}^{-1}$  instead of the two peaks seen previously. This implies that there has been a change in the connectivity of the structure, further supporting the notion that MB2-150 no longer has the same topology as the initial material.

The IR spectrum of the material calcined at 300°C (MB2-300) shows a complete disappearance of peaks corresponding to DMF proving that it has been completely removed from the material. Of particular note is the lack of any peaks at around 3500  $\text{cm}^{-1}$ , confirming that this material does not absorb water as seen in the TGA (Figure 4.2.20). The symmetrical C-O stretch at 1380  $\text{cm}^{-1}$  seen in the IR spectrum of MB2-150 has now split into four bands between 1405 and 1360  $\text{cm}^{-1}$ , implying a further change in structure.

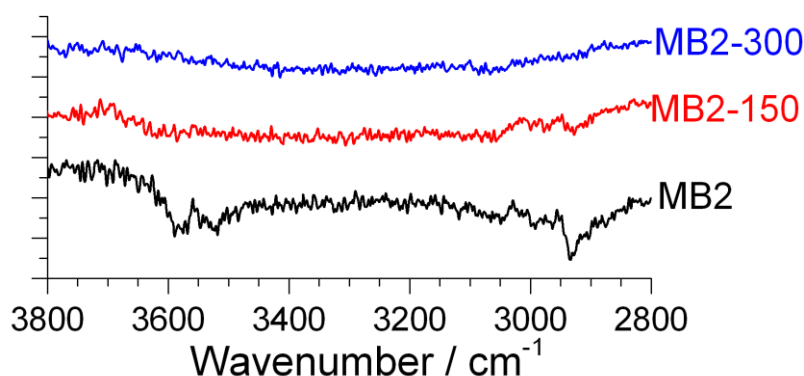


Figure 4.2.19: IR spectra of MB2 and its calcined products over the range 3800-2800  $\text{cm}^{-1}$

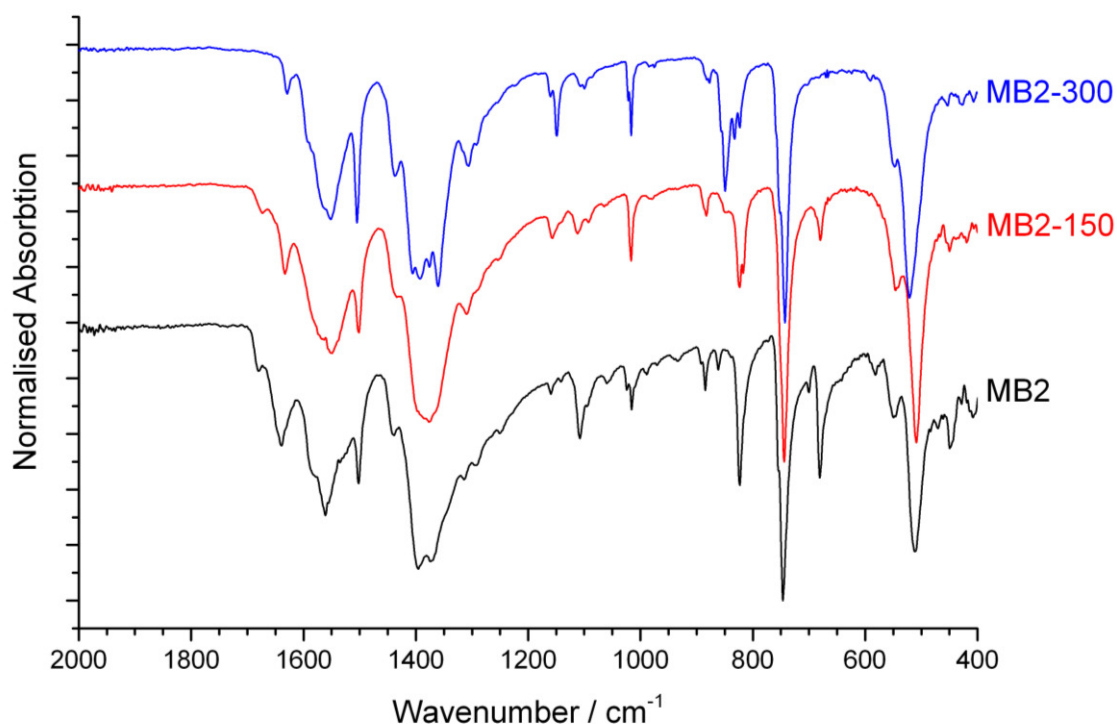


Figure 4.2.20: IR spectra of MB2 and its calcined products over the range 2000-400  $\text{cm}^{-1}$

Table 4.2.3: Assignment of IR vibrational bands of MB2 and its calcination products.<sup>17</sup> Red text indicates no band observed at that wavenumber

Absorption band / $\text{cm}^{-1}$			Strength	Assignment
MB2	MB2-150	MB2-300		
3584,3527	3584,3527	3584, 3527	w	O-H stretch (water)
3050-2935	3050-2935	3050-2935	w	C-H stretch (framework, coordinated DMF)
1680	1673	1673	m	C=O stretch (coordinated DMF)
1630-1560	1633-1548	1629-1551	s	C=O stretch (antisymmetrical carboxylate)
1502	1502	1504	s	C-H stretch (framework)
1439	1439	1437	m	-(O-C-O)-
1397,1375	1380	1405-1360	s	C=O stretch (symmetrical carboxylate)
1160	1160	1149	m	C=C stretch (framework)
1108, 1095	1108, 1095	1108, 1095	m	C-N stretch (DMF)
1016	1016	1016	m	C-O stretch (framework)
823	823	849, 832, 824	s	C-H bend (p-substituted ring systems)



#### 4.2.6. Synthesis of MB2 with other lanthanides

Owing to the similar reactivities of the lanthanide cations across the series, synthesis of MB2 with other lanthanides was expected to be relatively facile. Attempts to synthesise analogues of MB2, however, were unsuccessful for most of the lanthanides tested with the exception of lutetium (Figure 4.2.21). This can be accounted to the smaller ionic radii of ytterbium and lutetium when compared to lighter lanthanides.

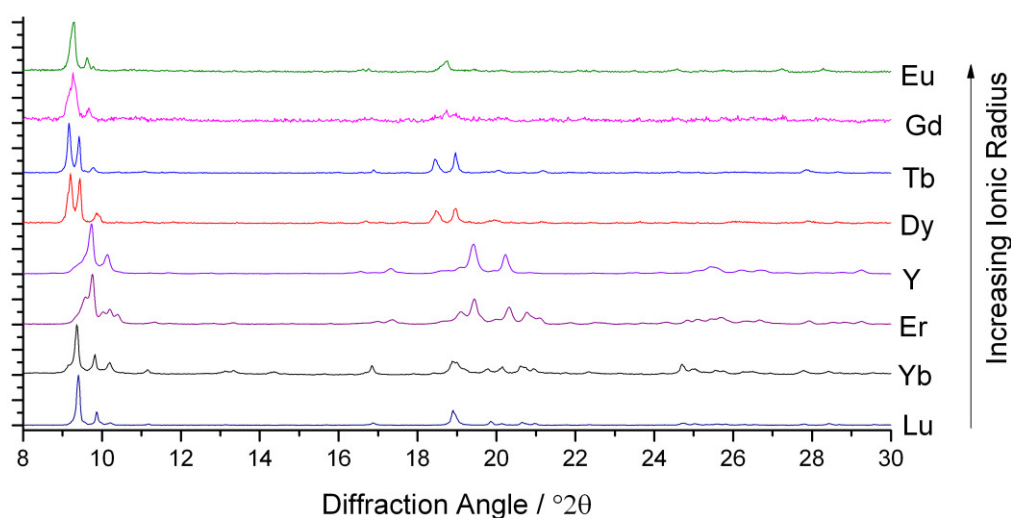


Figure 4.2.21: PXRD patterns of MB2 synthesis using other lanthanides

The lutetium analogue of MB2, MB2(Lu), displays an identical thermal profile by XRD to that of the ytterbium material supporting the notion that both the ytterbium and lutetium materials are analogues of one another(Figure 4.2.22).

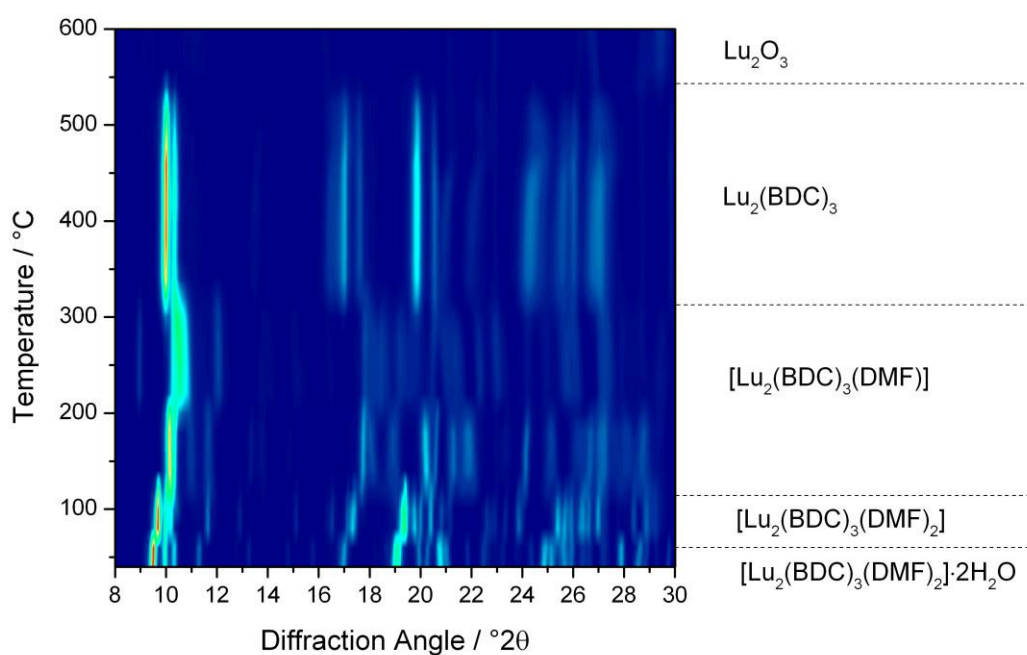


Figure 4.2.22: Thermodiffractometry of MB2(Lu)

#### 4.2.7. Doping of MB2 with other lanthanides

Although attempts to synthesise MB2 with other lanthanides were unsuccessful with other materials generated (with the exception of lutetium), it was considered to be possible to dope small amounts of other lanthanides into MB2 while maintaining the overall structure. MB2(Yb) was thus doped using erbium, terbium and europium by replacing 10% of the ytterbium (III) chloride used in the synthesis with another lanthanide source(s). A doubly doped MB2(Yb) using terbium and europium was also synthesised using 5% substitution of each lanthanide. In all cases, doped MB2(Yb, Ln) were successfully synthesised with no evidence of impurities observed by PXRD (Figure 4.2.23).

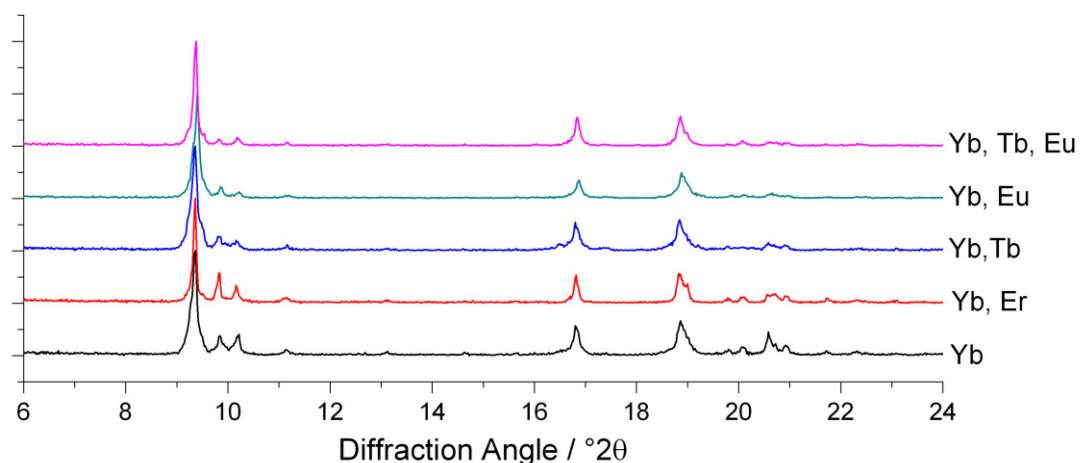


Figure 4.2.23: PXRD patterns of MB2(Yb) and its doped analogues

Photoluminescence studies of MB2(Yb) and its doped analogues were performed. A sample of MB2(Yb) was excited using a wavelength of 980 nm. This wavelength is in the infrared region and therefore unlikely to excite the BDC linker which is known to absorb at around 300 nm.<sup>18</sup> The wavelength corresponds to the excitation energy of ytterbium.<sup>19</sup> No emission peaks are observed around 300 nm. An emission peak is observed at 1070 nm (Figure 4.2.24). This can be assigned as an energy transfer between the excited ytterbium ion and the C-H vibrational band of the BDC linker.<sup>19-21</sup>

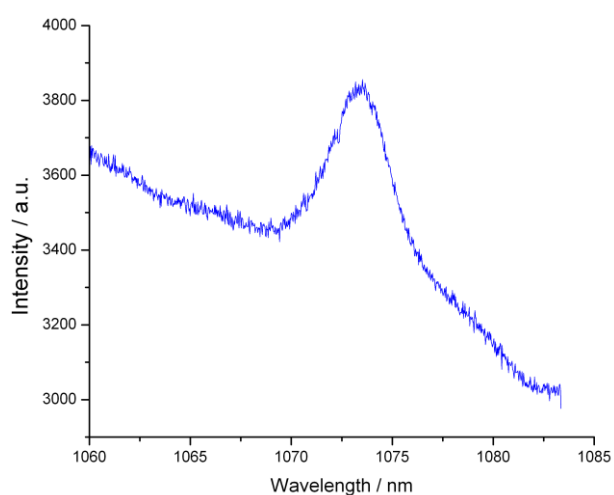
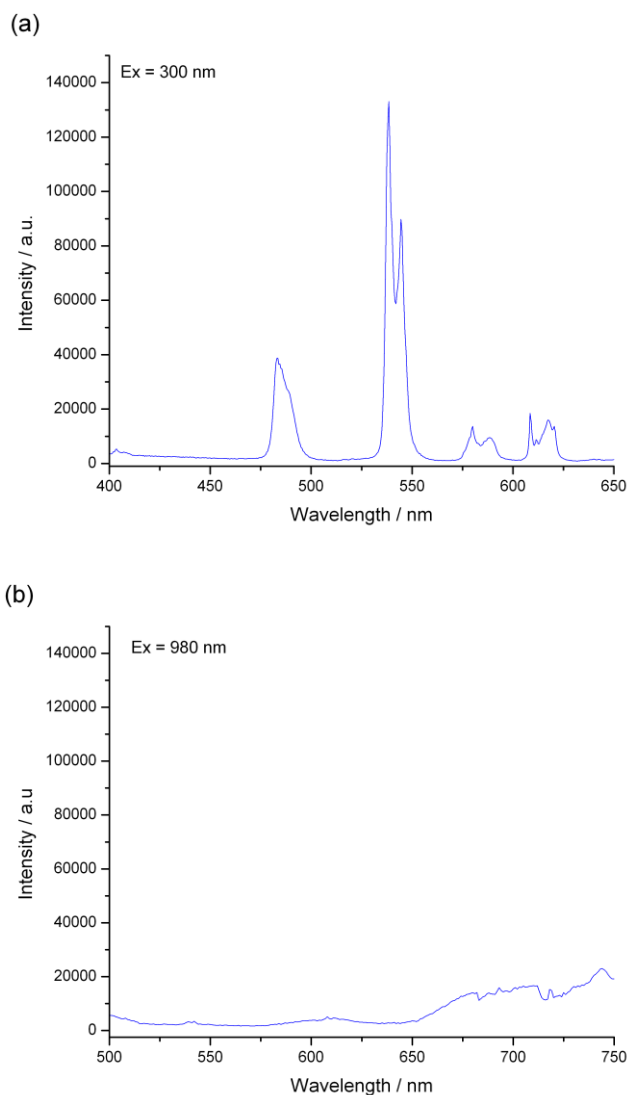


Figure 4.2.24: Emission spectrum of MB2(Yb) after excitation at 980 nm

MB2(Yb, Er) was excited using wavelengths of 300 and 980 nm. Excitation using a wavelength of 300 nm led to a series of emissions between 470 and 630 nm corresponding to excitation of the erbium ion (Figure 4.2.25(a)). This is consistent with energy transfer from the excited BDC linker. After excitation at 980 nm, no emissions were seen in the range 500-750 nm indicating that no upconversion has occurred (Figure 4.2.25(b)). Erbium is known to emit in the infrared region at 1530 nm.<sup>19</sup> It seems highly likely that excitation at 980 nm would lead to excitation of the erbium in the infrared region. Unfortunately, data were not measured over this range, although such behaviour has been seen in literature for a ytterbium-erbium doped yttrium-organic framework.<sup>22</sup>



**Figure 4.2.25: Emission spectra of MB2(Yb, Er) excited using wavelengths of (a) 300 nm and (b) 980 nm**

Excitation of MB2(Yb, Tb) with a wavelength of 300 nm leads to an emission spectrum characteristic of excited terbium (Figure 4.2.26(a)).<sup>19</sup> Excitation using 980 nm produces a small emission at 485 nm (Figure 4.2.26(b)). Since the excitation energy is less than the emission energy, this is indicative of a multi-photon absorption event - an example of upconversion. This has been reported for other lanthanide-organic frameworks.<sup>22-24</sup>

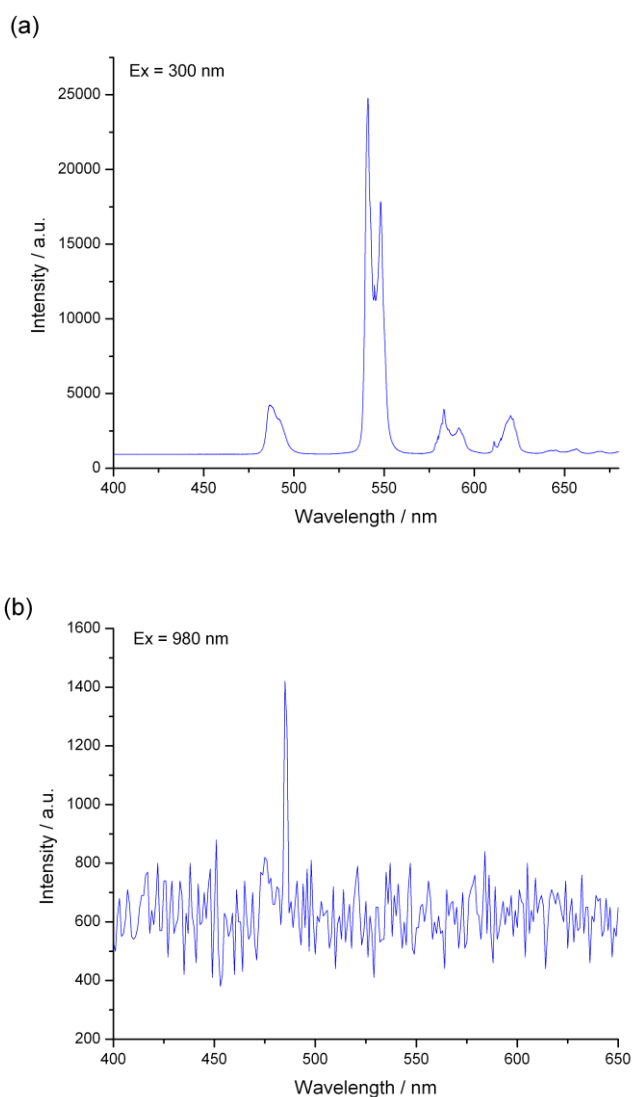


**Figure 4.2.26: Emission spectra of MB2(Yb, Tb) excited using wavelengths of (a) 300 nm and (b) 980 nm**

Excitation of MB2(Yb, Eu) using a wavelength of 305 nm leads to emission spectrum typical of trivalent europium.<sup>25</sup> The ability of MB2 to facilitate the excitation of several lanthanides makes it a good candidate for doping with multiple lanthanides.

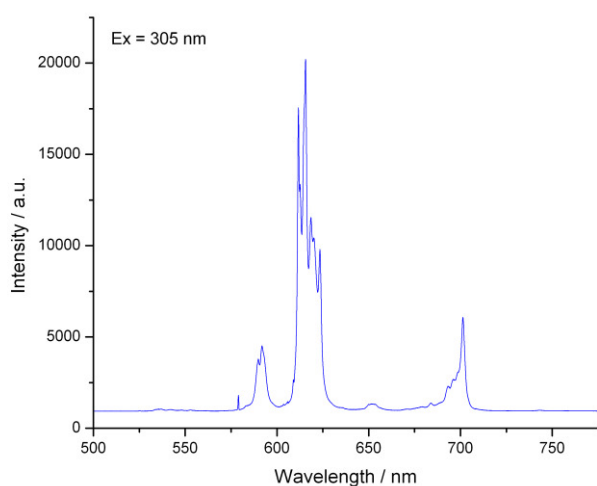


**Figure 4.2.27: Emission spectrum of MB2(Yb, Eu) excited using a wavelength of 305 nm**

The ability of lanthanide-organic frameworks to incorporate several lanthanides into the same material allow for potential ‘tuning’ of the emission spectra.<sup>26</sup> To investigate whether MB2 would be suitable for this application, MB2 was doped with both europium and terbium. Co-doping of terbium and europium is favourable due to their emissions in the green and the red regions of the visible light spectrum.<sup>27</sup> MB2(Yb, Tb, Eu) excited at 300 nm exhibits emissions from both terbium (485, 540, 548 and around 580 nm) and europium (580, 620 and 700 nm) (Figure 4.2.28(a)). Excitation at 466 nm only excites the europium with no terbium emissions seen.

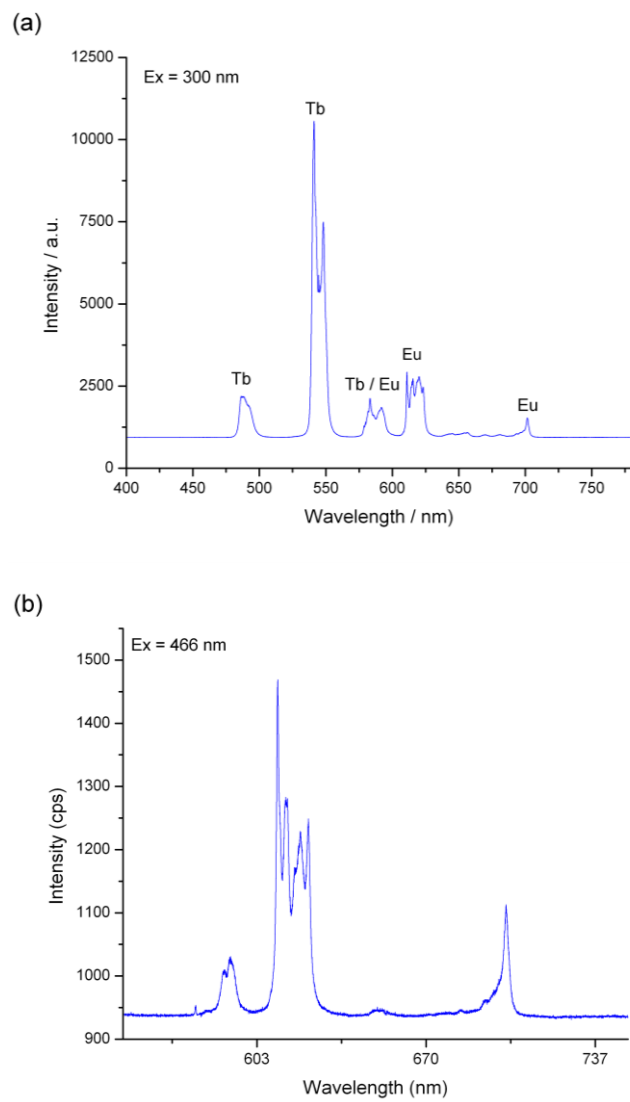


Figure 4.2.28: Emission spectra of MB2(Yb, Tb, Eu) excited using wavelengths of (a) 300 and (b) 466 nm



### 4.3. MB3 – $[\text{Yb}_2(\text{BDC})_3(\text{DMF})_2(\text{H}_2\text{O})_2]$

#### 4.3.1. Synthesis

The reaction of ytterbium (III) chloride hexahydrate with  $\text{H}_2\text{BDC}$  at temperatures between 90 and 120 °C for 20 hours was modified using varying ratios of DMF to water as solvent. It was found that using solvent compositions of 100 to 60 % DMF formed only MB2 in high quality. At compositions between 50 to 10 % DMF, the formation of a new phase was observed. This material was of suitable quality for single crystal XRD and the structure was resolved at 100 K. This structure will be referred to as 'MB3'. Using purely water as the solvent led to problems with dissolution of the hydrophobic BDC linker with no product except unreacted linker seen after heating.

#### 4.3.2. Structure of MB3

MB3,  $[\text{Yb}_2(\text{BDC})_3(\text{DMF})_2(\text{H}_2\text{O})_2]$ , crystallises in the triclinic  $P\bar{1}$  space group. Each ytterbium is coordinated to four oxygens from two *bis*-coordinating carboxylato groups, two oxygens from singly coordinated carboxylato groups and one oxygen from both DMF and water, leading to a coordination number of 8. Each ytterbium exists as part of a dimer, linked to another ytterbium by the singly coordinating carboxylato groups (Figure 4.3.1). The complete crystal structure is shown in Figure 4.3.2.

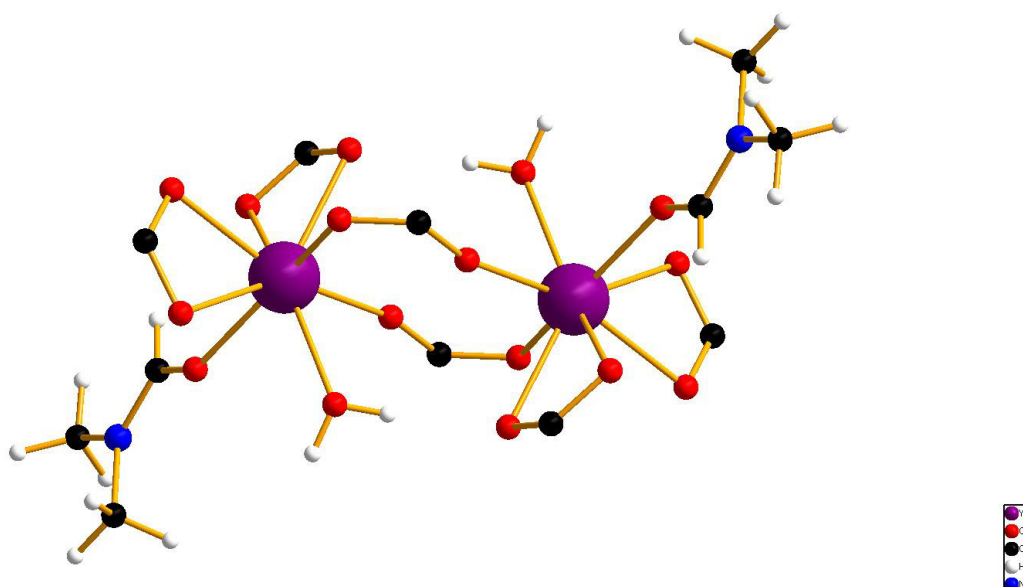


Figure 4.3.1: Ytterbium dimers found in MB3. Only carboxylate groups of BDC linkers are shown

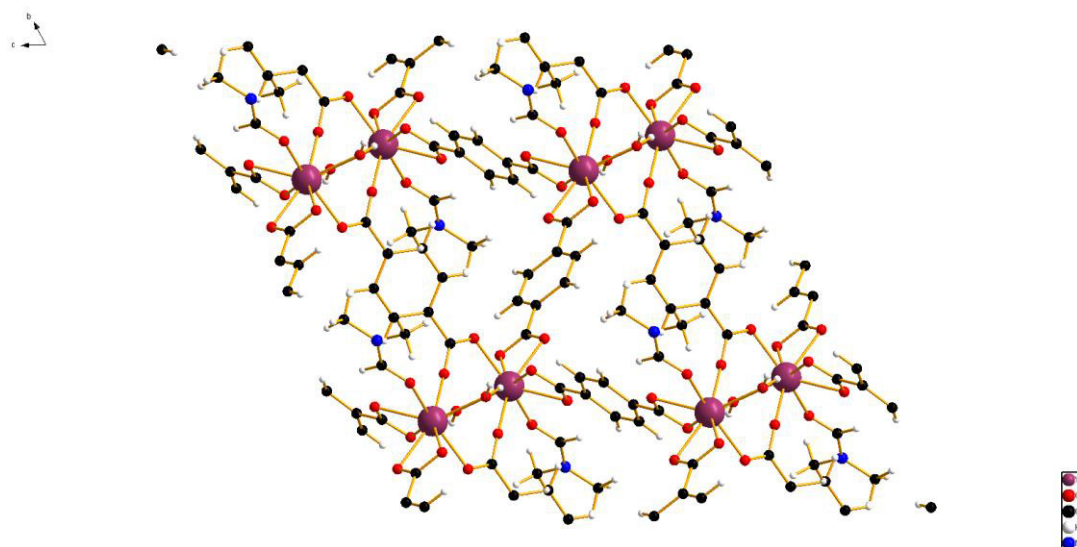


Figure 4.3.2: Crystal Structure of MB3 viewed along the  $a$ -axis. Hydrogens not shown for clarity

Each dimer is linked to six other dimers: four by each bis-coordinating linker and two by the bridging BDCs. The connectivity between dimers is such that each BDC coordinates in the same manner at both carboxylate groups *i.e.* each BDC only coordinates in a Type II or Type III manner exclusively (Figure 4.3.3). This interconnectivity leads to the overall structure of MB3. Crystallographic data are given in Table 4.3.1 and Table 4.3.2.

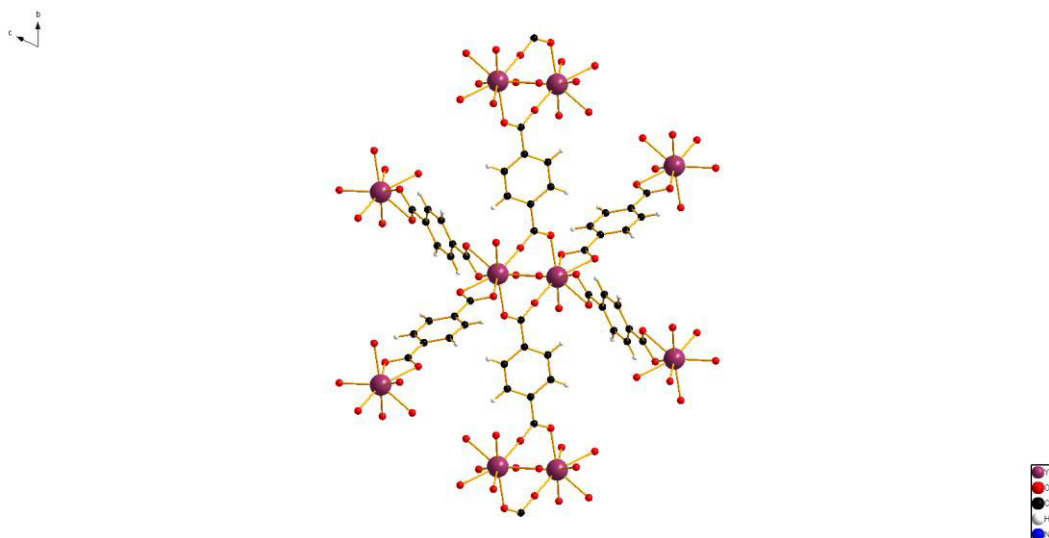


Figure 4.3.3: Connectivity of ytterbium dimers found in MB3. Only coordinating oxygens from coordinated water and DMF are shown for clarity

Table 4.3.1: Crystallographic data for MB3

	MB3
Formula	C <sub>15</sub> H <sub>15</sub> NO <sub>8</sub> Yb
Formula Weight	510.32
Colour/Shape	Block/ colourless
Temperature / K	100(2)
Crystal System	Triclinic
Space Group	<i>P</i> <b>1</b>
<i>a</i> / Å	8.5054(2)
<i>b</i> / Å	10.2435(2)
<i>c</i> / Å	10.9144(3)
$\alpha$ / °	63.350(2)
$\beta$ / °	71.042(2)
$\gamma$ / °	82.562(2)
Cell volume / Å <sup>3</sup>	803.6
<i>Z</i>	2
Density (calc.) / g·cm <sup>3</sup>	2.10878

Table 4.3.2: Atomic parameters for MB3

Atom	Ox.	Wyck.	Site	S.O.F.	x/a	y/b	z/c	U [Å <sup>2</sup> ]
Yb1		2i	1	1	0.3639	0.5659	0.3319	
O101		2i	1	1	0.5461(2)	0.5001(2)	0.1524(1)	
O102		2i	1	1	0.6538(2)	0.6276(1)	0.2241(1)	
C102		2i	1	1	0.6710(2)	0.5524(2)	0.1542(2)	
C103		2i	1	1	0.8416(2)	0.5239(2)	0.0755(2)	
C104		2i	1	1	0.8623(3)	0.4295(2)	0.0112(2)	
H10		2i	1	1	0.7688	0.3813	0.0191	0.014
C105		2i	1	1	1.0218(3)	0.4067(2)	-0.0646(2)	
H10A		2i	1	1	1.0369	0.343	-0.1093	0.013
O201		2i	1	1	0.3311(2)	0.7556(2)	0.1186(1)	
O202		2i	1	1	0.1072(2)	0.6933(2)	0.3074(1)	
C202		2i	1	1	0.1807(3)	0.7749(2)	0.1756(2)	
C203		2i	1	1	0.0864(3)	0.8933(2)	0.0865(2)	
C204		2i	1	1	0.1678(3)	0.9810(2)	-0.0575(2)	
H20		2i	1	1	0.2829	0.9681	-0.0966	0.016
C205		2i	1	1	0.0819(3)	1.0872(2)	-0.1443(2)	
H20A		2i	1	1	0.1378	1.1461	-0.2425	0.015
O301		2i	1	1	0.5018(2)	0.3748(2)	0.4598(1)	
O302		2i	1	1	0.6152(2)	0.2344(2)	0.6314(1)	
C302		2i	1	1	0.5481(2)	0.2519(2)	0.5378(2)	
C303		2i	1	1	0.5246(3)	0.1216(2)	0.5178(2)	
C304		2i	1	1	0.5173(3)	0.1384(2)	0.3853(2)	
H30		2i	1	1	0.5296	0.2328	0.3071	0.013
C305		2i	1	1	0.4924(3)	0.0180(2)	0.3681(2)	
H30A		2i	1	1	0.4868	0.03	0.2781	0.013
O401		2i	1	1	0.2097(2)	0.4076(2)	0.3220(2)	
C402		2i	1	1	0.2358(3)	0.3320(2)	0.2540(2)	
H40		2i	1	1	0.3364	0.3484	0.1777	0.015
N403		2i	1	1	0.1308(2)	0.2308(2)	0.2830(2)	
C404		2i	1	1	0.1698(3)	0.1406(2)	0.2046(2)	
H40A		2i	1	1	0.2766	0.1729	0.1291	0.031
H40B		2i	1	1	0.0823	0.1502	0.1609	0.031
H40C		2i	1	1	0.1766	0.0382	0.2713	0.031
C405		2i	1	1	-0.0287(3)	0.2073(3)	0.3946(3)	
H40D		2i	1	1	-0.0101	0.1656	0.4889	0.037
H40E		2i	1	1	-0.098	0.1397	0.392	0.037
H40F		2i	1	1	-0.0851	0.3007	0.3778	0.037
O501		2i	1	1	0.1875(2)	0.4729(2)	0.5658(1)	
H5A		2i	1	1	0.232(3)	0.439(3)	0.633(2)	0.018
H5B		2i	1	1	0.0964(18)	0.425(2)	0.603(3)	0.018

The refined unit cell agrees well with that of MB3 (Figure 4.3.4) with elemental analysis further supporting the chemical formula (C 35.24%, 35.30%(calc.); H 2.78%, 2.78%(calc.); N 2.78%, 2.74%(calc.)). An erbium analogue of this material has been reported by Chen *et al.*<sup>28</sup>

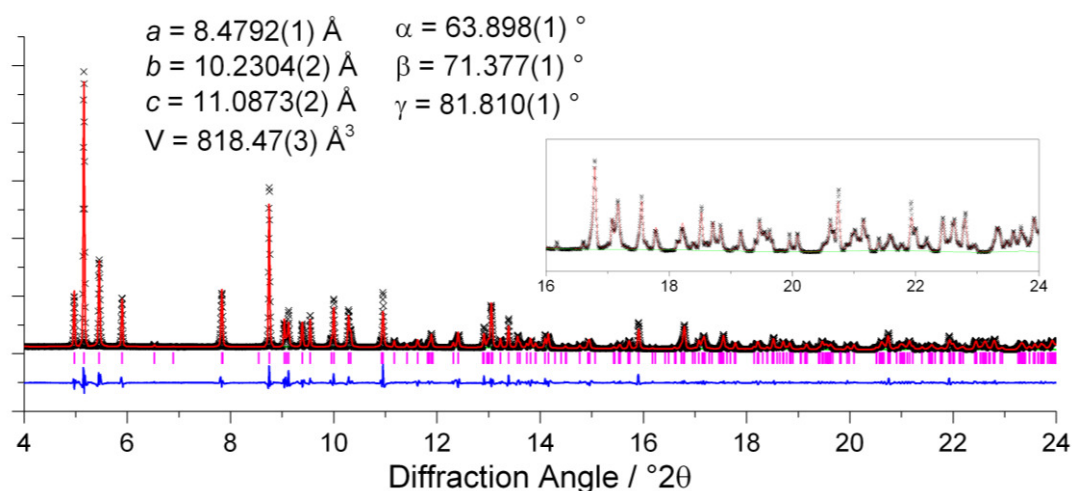


Figure 4.3.4: Profile fit of PXRD pattern of MB3 at 298 K with refined parameters. Data were collected on Beamline I11 at Diamond ( $\lambda = 0.825174 \text{ \AA}$ ). Black crosses: experimental data; Green: background; Red: profile fit; Magenta lines: allowed reflections; Blue: difference

### 4.3.3. Thermal Behaviour of MB3

Thermogravimetric analysis, Figure 4.3.5, shows an initial loss at around 140 °C of 17.2 %. This agrees well with loss of both DMF and single water in a single step (expected loss of 17.8 %). This is followed by a small further loss starting at 300 °C of 1.6 %. This loss can be attributed to the loss of the remaining water. The material begins to collapse at around 510 °C with eventual formation of  $\text{Yb}_2\text{O}_3$ .

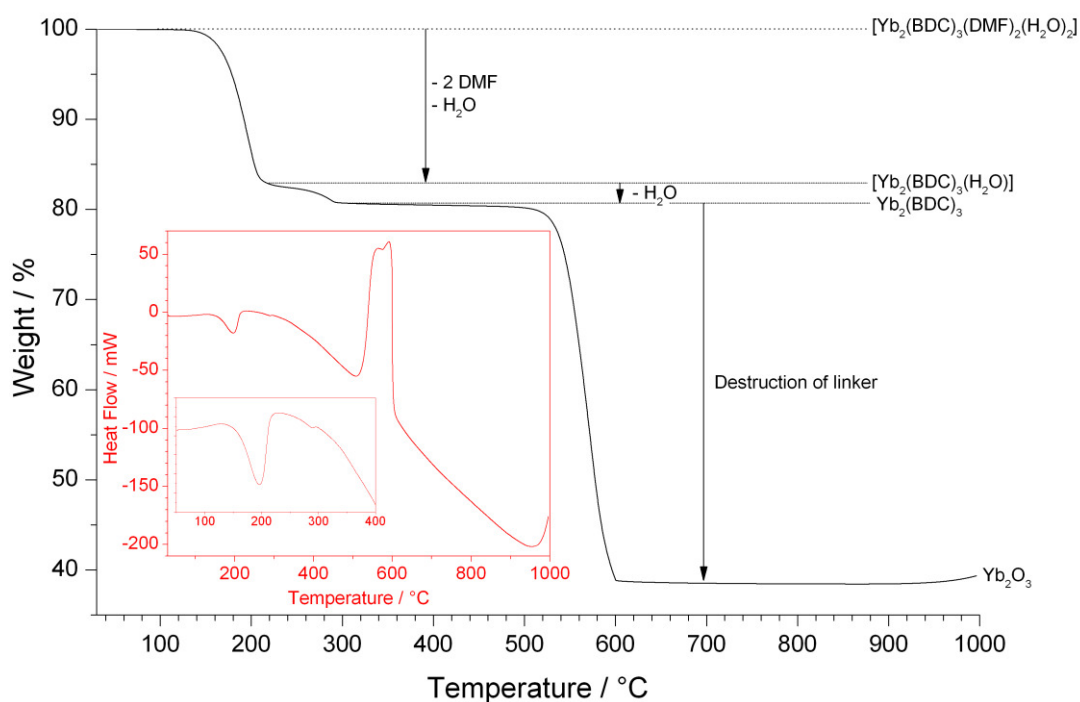


Figure 4.3.5: Main: TGA of MB3 in air; Insert: DSC curve of MB2 over same temperature range; Insert, Insert: DSC curve over temperature range of 30-400 °C showing loss of DMF and water

Thermogravimetry of MB3 shows that the material undergoes two structural changes before decomposition (Figure 4.3.6). The first change occurs at 150 °C with an associated large decrease in crystallinity. This is likely due to a rearrangement of the structure that results from the loss of both water and DMF seen by TGA. One further change is seen at 340 °C. This change could be attributed to loss of the final water evidenced by TGA and a small trough in the DSC curve. However, the large difference in temperature between these two points makes it seem unlikely. It is therefore difficult to determine whether the phase formed at 150 °C is indeed a single phase or a mixture of two phases, one of which is destroyed or converted into the other at 340 °C. The lack of mass loss and no corresponding exothermic peak in the DSC trace imply that no phase destruction occurs at 340 °C. One possibility is the transformation into the desolvated phase that is produced upon complete loss of DMF and water is a slow process, suggesting

a large difference in the structures of MB3 and the desolvated material. Owing to the low crystallinity of the material at this point, it is difficult to prove which case is correct.

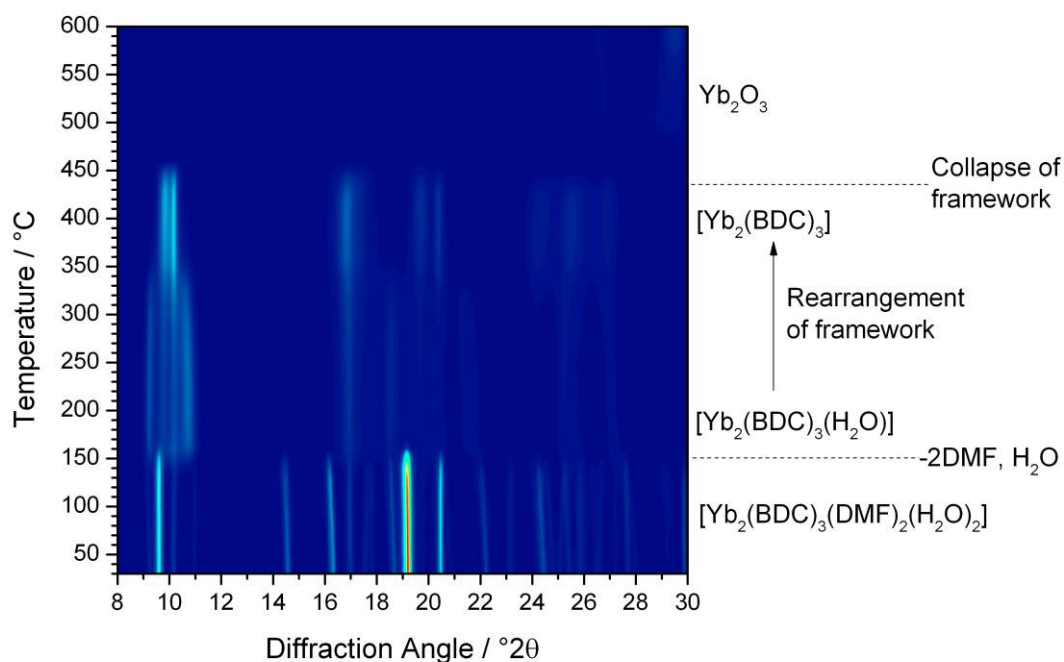
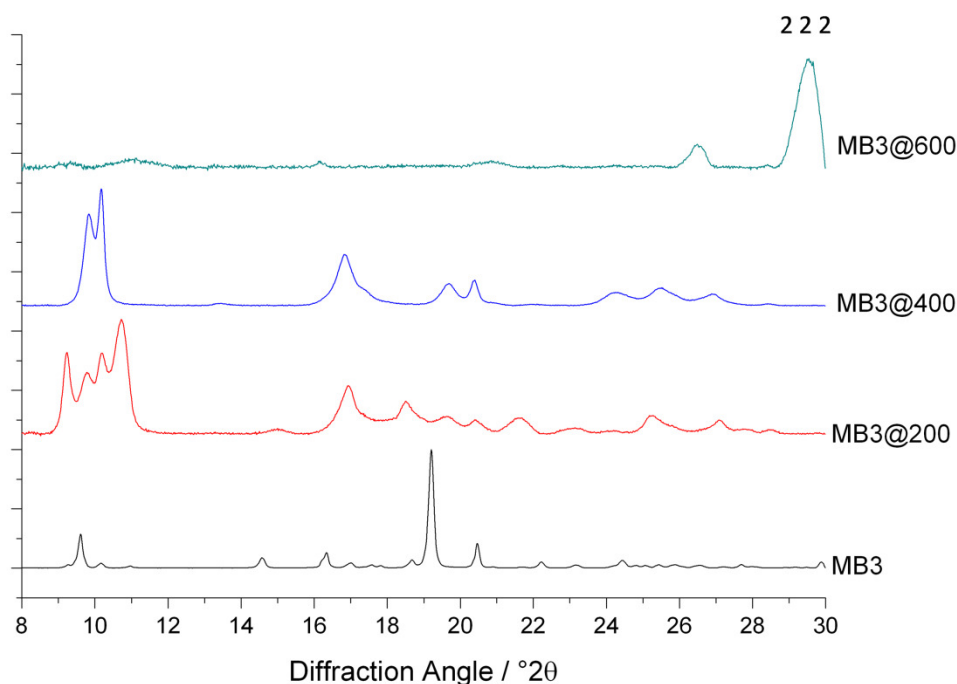


Figure 4.3.6: Thermodiffractometry of MB3 to 600°C with annotated mass losses and predicted chemical formulae



**Figure 4.3.7: Comparison of the PXRD patterns of MB3 during calcination with labelled (222) peak of ytterbium oxide. XRD pattern of MB3 shows strong preferred orientation effects due to use of stationary sample holder**

Heating MB3 to 150 °C forms  $\text{Yb}_2(\text{BDC})_3(\text{H}_2\text{O})$  (MB3@150) as evidenced by the TGA in Figure 4.3.5. During cooling, no shifts in the diffraction pattern are observed indicating that the structure is preserved (Figure 4.3.8). However, TGA of MB3 calcined at 150 °C post-cooling shows no mass loss until destruction of the material, as seen Figure 4.3.9, implying the chemical formula of MB3-150 is  $\text{Yb}_2(\text{BDC})_3$ . The discrepancy between the predicted chemical formulae at the temperatures is likely due to the differences in the calcination heating profiles (the TGA of MB3-150 was collected from a sample of MB3 calcined at 150 °C for three hours).

The final weight loss is consistent with the combustion of  $\text{Yb}_2(\text{BDC})_3$  to form ytterbium (III) oxide (52.3 %; expected: 53 %). A trough in the DSC curve at 335 °C (Figure 4.3.9) corresponds well to point where the structural transition is observed in the thermodiffractionometry of MB3 (Figure 4.3.8).



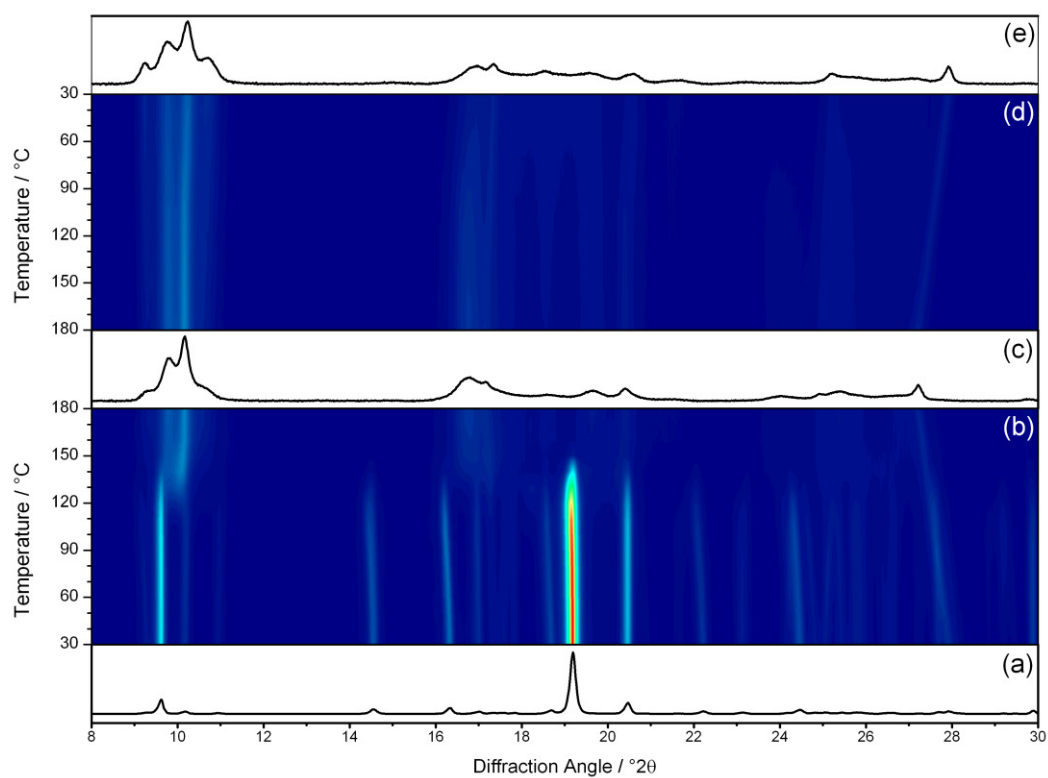


**Figure 4.3.8:** (a) PXRD pattern of MB3 at 30°C; (b) Thermodiffractometry of MB3 heating to 180 °C; (c) PXRD pattern of MB3 at 180 °C; (d) Thermodiffractometry of cooling back to 30 °C in air; (e) PXRD pattern of MB2-150 after cooling. N.B. MB3 was heated to 180 °C to ensure complete calcination of MB3 to form the product formed at 150 °C. XRD pattern of MB3 shows strong preferred orientation effects due to use of stationary sample holder

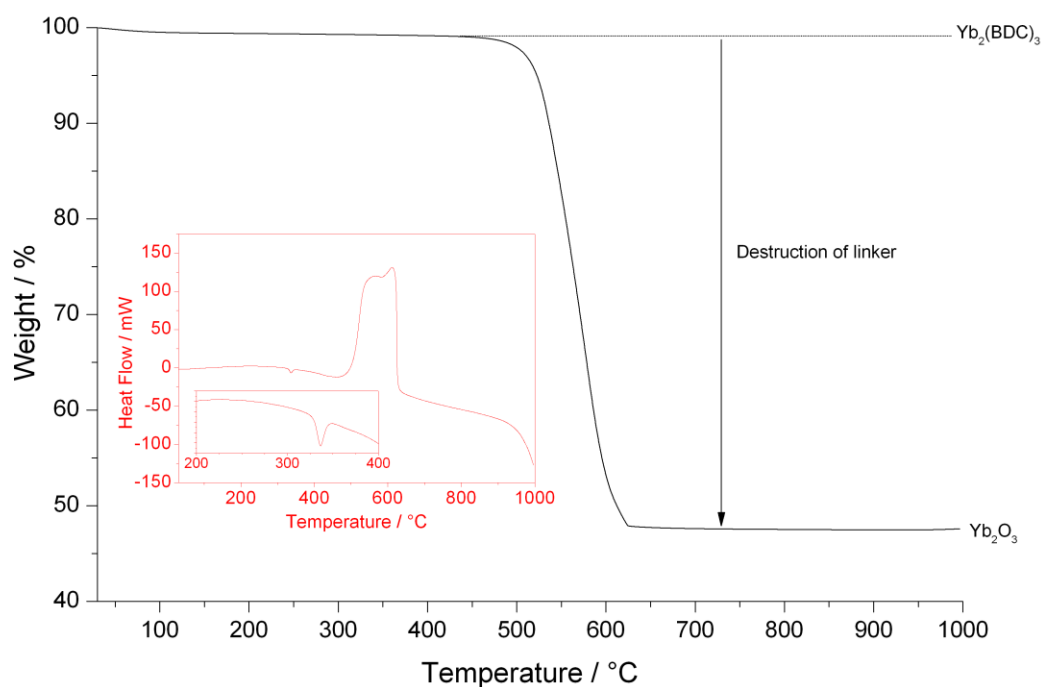


Figure 4.3.9: Main: TGA of MB3-150 in air; Insert: DSC curve of MB3-150 over same temperature range; Insert, Insert: DSC curve over temperature range of 200-400 °C showing the endothermic structural transition observed at 335 °C

Although now seemingly sharing the same chemical composition as MB2-300 ( $\text{Yb}_2(\text{BDC})_3$ ), MB3-150 appears to not have fully calcined into the  $\text{Yb}_2(\text{BDC})_3$  with a second phase present (Figure 4.3.10). It is difficult to determine the structure of the second phase impurity due to the poor crystallinity post-calcination.

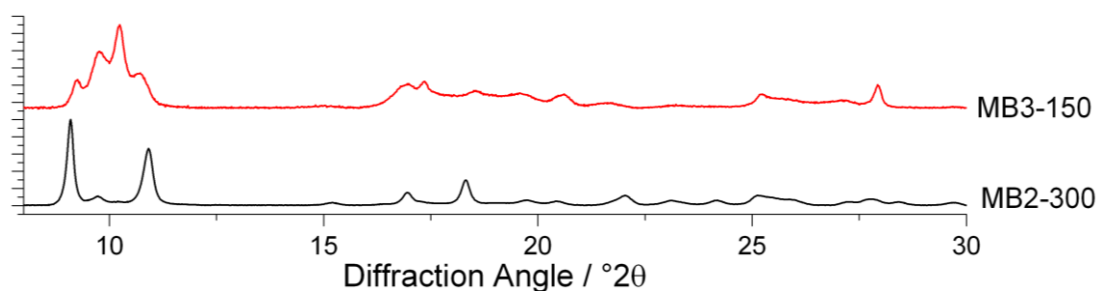


Figure 4.3.10: Comparison of PXRD patterns of MB2 and MB3 calcined at 300 and 150 °C respectively

Heating of MB3 in air at 400°C yields interesting results. At 400°C, MB3 has completely calcined into the  $\text{Yb}_2(\text{BDC})_3$  phase. As with MB3-150, this material should have the same composition as MB2-300 i.e.  $\text{Yb}_2(\text{BDC})_3$ . A comparison of the XRD patterns of MB2

and MB3 at 400°C show clear differences suggesting that at this temperature although the materials share the same chemical formula, they are not isostructural at this temperature (Figure 4.3.13).

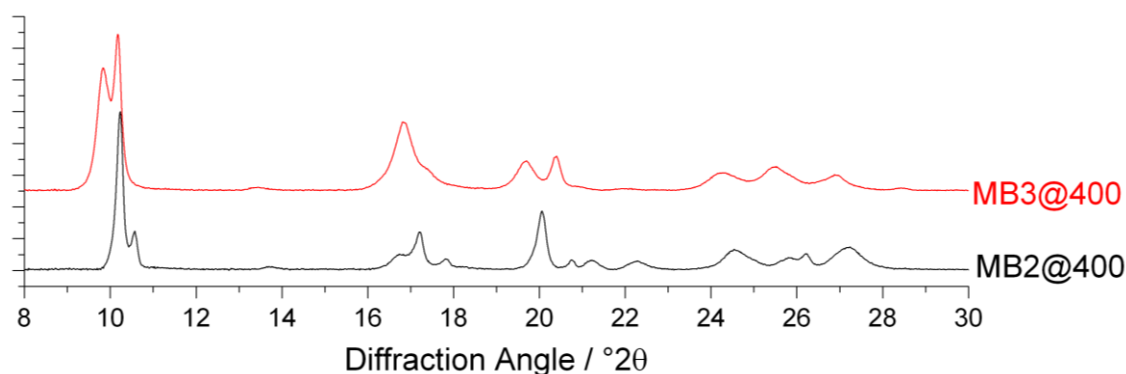


Figure 4.3.11: Comparison of PXRD pattern collected at 400°C of MB2 and MB3

Upon cooling to room temperature in air, the material undergoes a single structural transition at 200 °C (Figure 4.3.12). The material now appears to share the same structure as MB2-300 (Figure 4.3.13). This behaviour is unexpected due to the dissimilar initial structures of MB2 and MB3. MB2 and MB3, although sharing the same composition (i.e. polymorphs), vary greatly in terms of both connectivity and ytterbium coordination number. The slower transformation of MB3 into  $\text{Yb}_2(\text{BDC})_3$  when compared to MB2 suggests that the structure of the eventual  $\text{Yb}_2(\text{BDC})_3$  more closely mirrors that of MB2. This can be rationalised by more bonds and more structural rearrangement during calcination of MB3, evidenced by both the longer process and the higher temperature required for complete calcination. Further work is required to determine the structure of  $\text{Yb}_2(\text{BDC})_3$ .

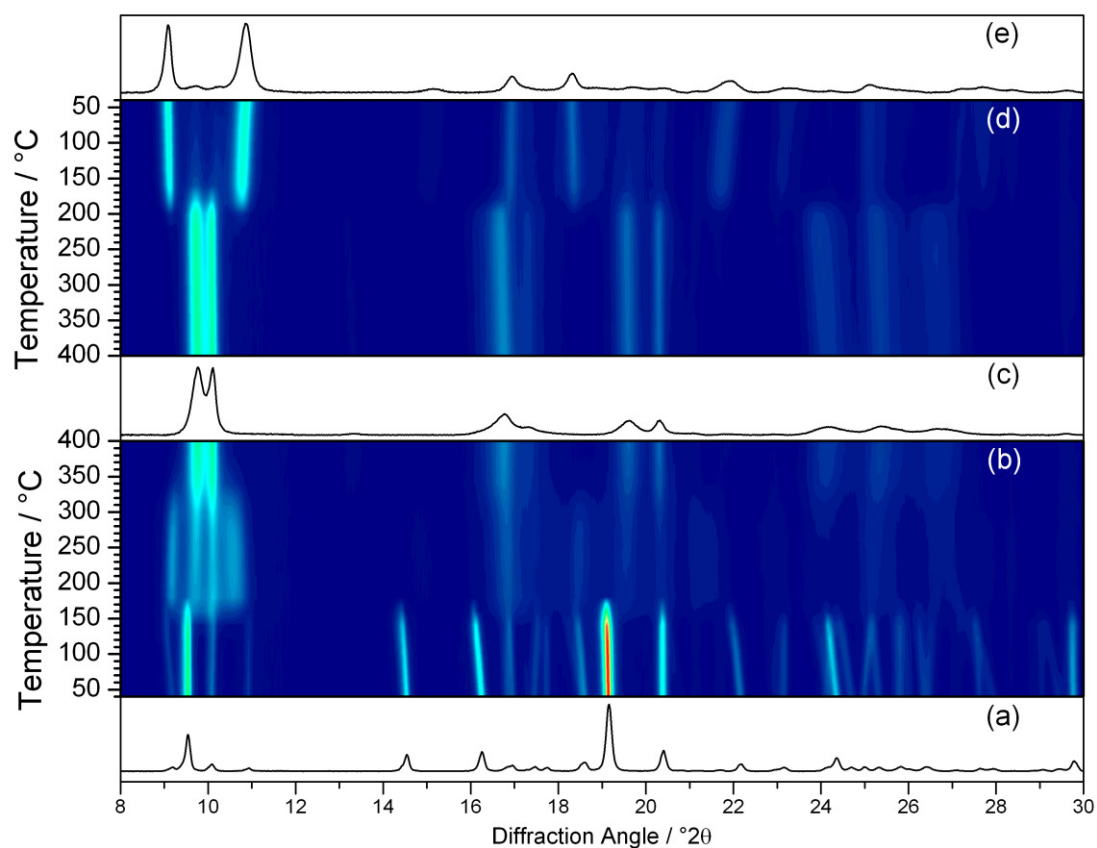


Figure 4.3.12: (a) PXRD pattern of MB3 at 30  $^{\circ}\text{C}$ ; (b) Thermogravimetric analysis of MB3 heating to 400  $^{\circ}\text{C}$ ; (c) PXRD pattern of MB3 at 400  $^{\circ}\text{C}$ ; (d) Thermogravimetric analysis of cooling back to 30  $^{\circ}\text{C}$  in air; (e) PXRD pattern of MB3-400 after cooling. N.B. MB3 was heated to 400  $^{\circ}\text{C}$  to ensure complete calcination of MB3 to form the product formed at 350  $^{\circ}\text{C}$

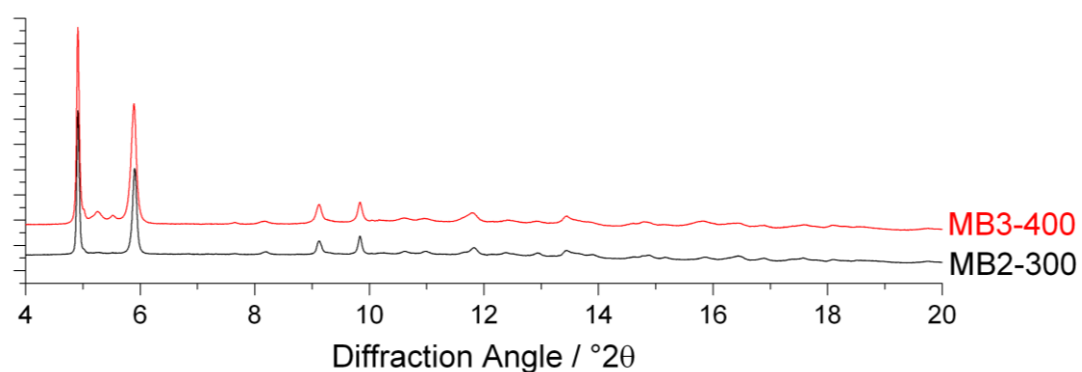


Figure 4.3.13: Comparison of PXRD patterns of MB2 calcined at 300  $^{\circ}\text{C}$  and MB3 calcined at 400  $^{\circ}\text{C}$

This ‘convergent calcination’ of two different MOFs to form a single material has not been reported before for MOFs before to the best of our knowledge. A scheme for the calcination profile of MB3 is given in Figure 4.3.14.

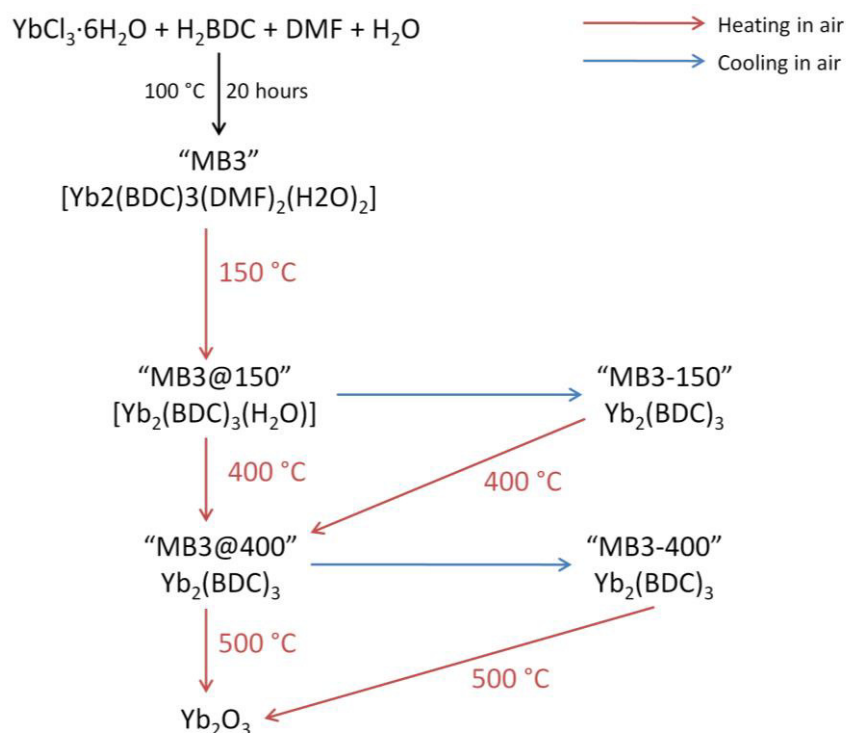


Figure 4.3.14: Reaction Scheme for the synthesis of MB3 and its calcination products

#### 4.3.4. Gas Adsorption Studies of MB3

Gas adsorption studies of MB3 show that the material treated at 100 °C does not adsorb nitrogen. This reflects the lack of free space inside the structure of MB3 as expected from the crystal structure. After treatment at 200 °C, the calcined MB3 now adsorbs nitrogen to a level similar for that that of the calcined MB2 material treated at 300 °C with a BET surface of 316 m<sup>2</sup>g<sup>-1</sup>. This is unsurprising – the calcined MB3 is now the same Yb<sub>2</sub>(BDC)<sub>3</sub> as the fully calcined MB2-300. Treatment of MB3 at 300 °C yields even higher adsorption with a BET surface area of 376 m<sup>2</sup>g<sup>-1</sup>. This is approximately 20% higher than the values found for MB2 and may be due additional defects found in the less crystalline Yb<sub>2</sub>(BDC)<sub>3</sub> formed through MB3 calcination.

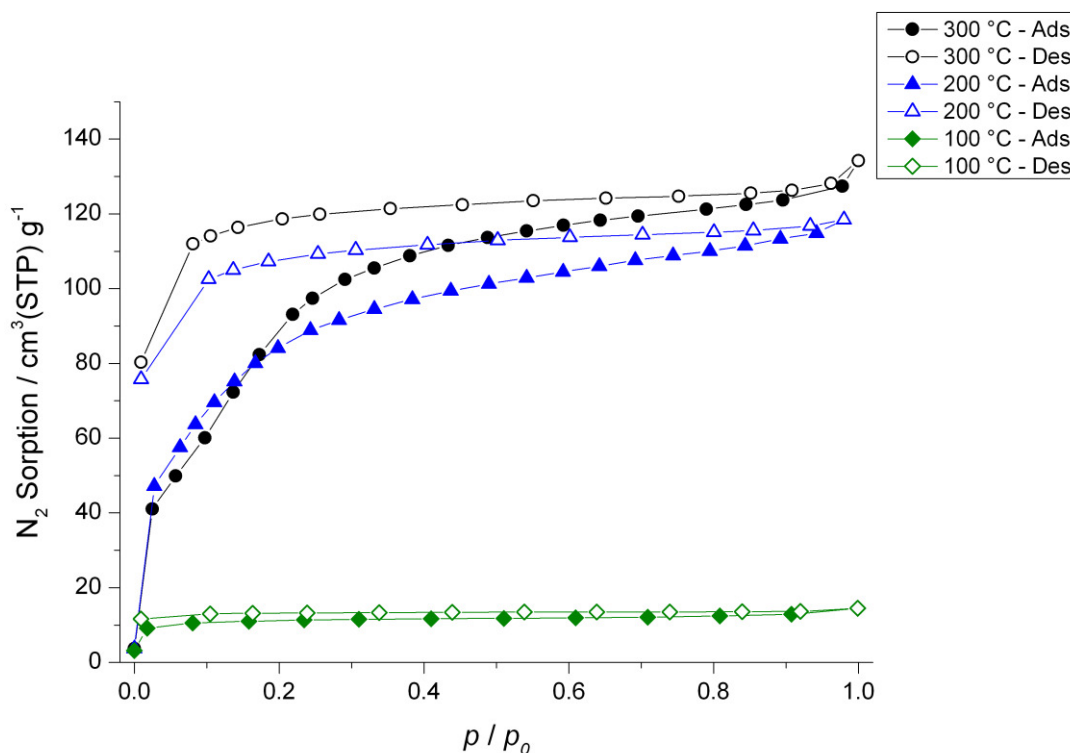


Figure 4.3.15:  $N_2$  Sorption Isotherms of MB2 calcined at various temperatures under vacuum. Filled symbols: adsorption isotherm; empty symbols: desorption isotherm

#### 4.3.5. Infrared Spectra of MB3 and Its Calcined Products

The IR spectrum of MB3 displays two sets of bands at  $\sim 3300$  and  $\sim 3000\text{ cm}^{-1}$  (Figure 4.3.16). These peaks correspond well to those expected of coordinated water and DMF respectively. Unlike the IR spectrum of MB2, no peaks relating to free extra-framework water ( $\sim 3550\text{ cm}^{-1}$ ) are seen, suggesting that only coordinated water and DMF are found in this material. A strong peak at  $1651\text{ cm}^{-1}$  represents the C=O stretch of coordinated DMF (Figure 4.3.17). Strong peaks at  $\sim 1600$  and  $\sim 1385\text{ cm}^{-1}$  relate to the anti-symmetrical and symmetrical stretches of the carboxylate groups from the BDC linker. A further peak relating to coordinated DMF is seen at  $1108\text{ cm}^{-1}$ . The peak at  $845\text{ cm}^{-1}$  is consistent with that of a para-substituted aromatic ring system confirming that no rearrangement of the BDC linker has occurred. The IR spectrum is consistent with the expected chemical formula of  $[Yb_2(BDC)_3(DMF)_2(H_2O)_2]$ .

The IR spectrum of MB3 calcined at 400 °C has no peaks relating to either coordinated or free DMF and water. This is consistent with the expected lack of coordinated solvent seen by TGA. A comparison of the IR spectra of MB2-300 and MB3-400 show virtually no difference consistent with the premise that these two materials are identical in both composition and structure (Figure 4.3.18).

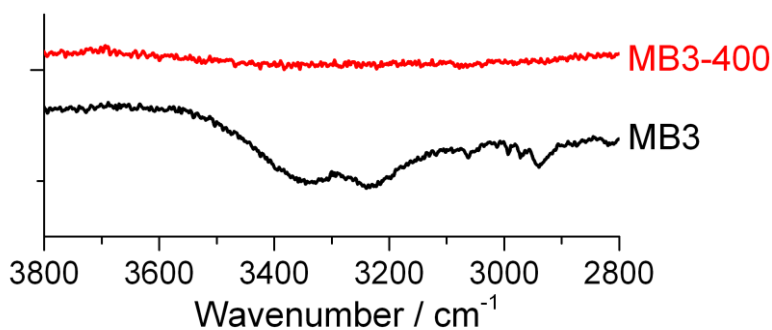


Figure 4.3.16: IR Spectra of MB3 and its calcined product between 3800 and 2800  $\text{cm}^{-1}$

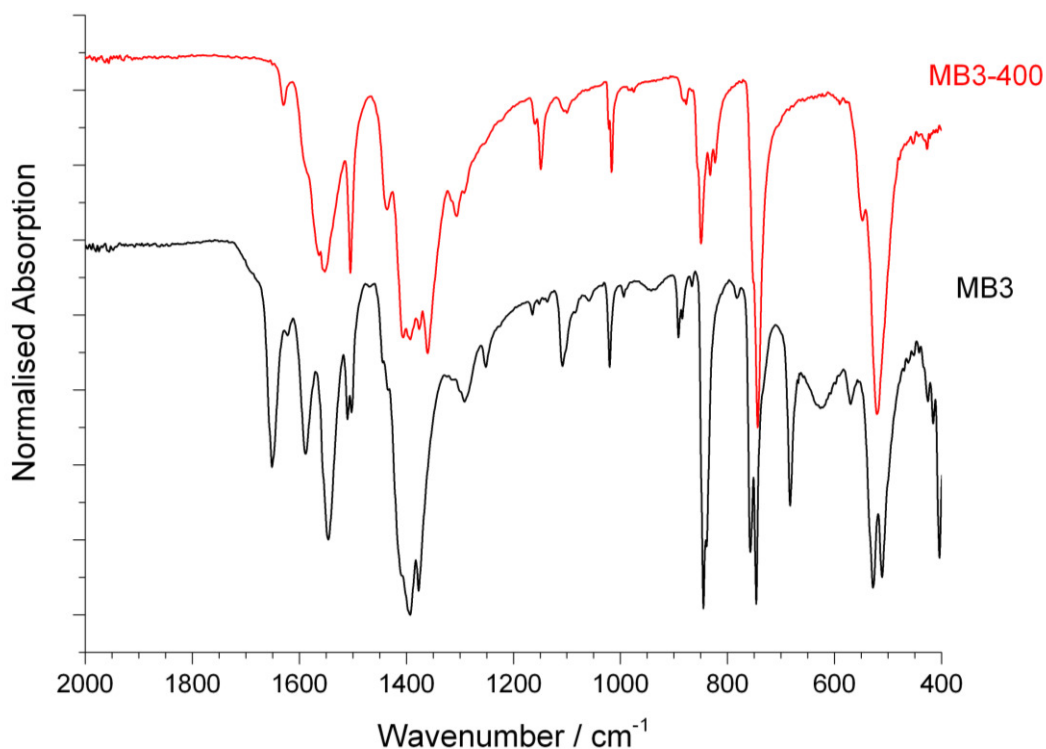


Figure 4.3.17: IR Spectra of MB3 and its calcined product between 2000 and 400  $\text{cm}^{-1}$

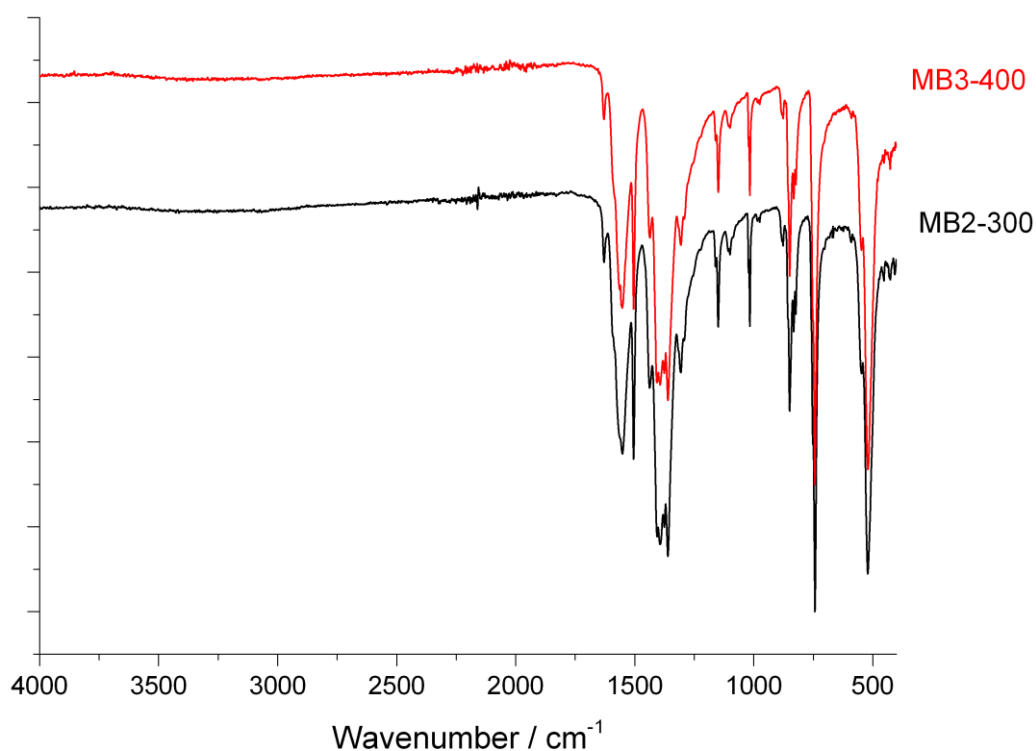


Figure 4.3.18: Comparison of the IR Spectra of MB2 and MB3 calcined at 300 and 400 °C respectively

Table 4.3.3: Assignment of vibrational bands of MB3 and its calcined product. Red text represents missing absorption bands

Absorption band / $\text{cm}^{-1}$		Strength	Assignment
MB3	MB3-400		
3337, 3233	3337, 3233	w	O-H (coordinated water)
3061-2939	3061-2939	w	C-H stretch (framework, coordinated DMF)
1651	1651	s	C=O stretch (coordinated DMF)
1623-1546	1630-1552	s	C=O stretch (antisymmetrical carboxylate)
1509, 1501	1504	m	C-H stretch (framework)
1445, 1439	1436	m	-(O-C-O)-
1394, 1376	1404-1361	s	C=O stretch (symmetrical carboxylate)
1164	1149	w	C=C stretch (framework)
1108	1108	m	C-N stretch (DMF)
1020	1016	m	C-O stretch (framework)
845	845	s	C-H bend (p-substituted ring systems)



## 4.4. Synthesis of Isorecticular Analogues of MB2 and MB3

### 4.4.1. Synthesis

As mentioned in the introduction, the ability of metal-organic frameworks to maintain their topology with complete or partial substitution of the linkers is well known.<sup>29,30</sup> This is known as isorecticular synthesis. To investigate whether the structures of MB2 and MB3 could be expanded through extension of the linkers, 1,4-benzenedicarboxylic acid ( $H_2BDC$ ) was substituted by 2,6-naphthalenedicarboxylic acid ( $H_2NDC$ ) and 4,4'-biphenyldicarboxylic acid ( $H_2BPDC$ ) in typical reactions for synthesis of MB2 and MB3. The structures of the linker precursors are given in Figure 4.4.1.

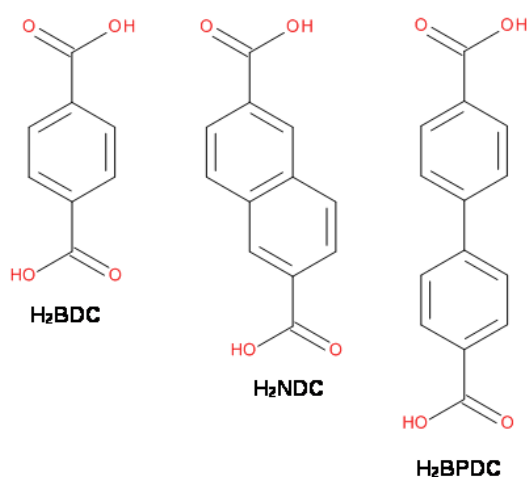
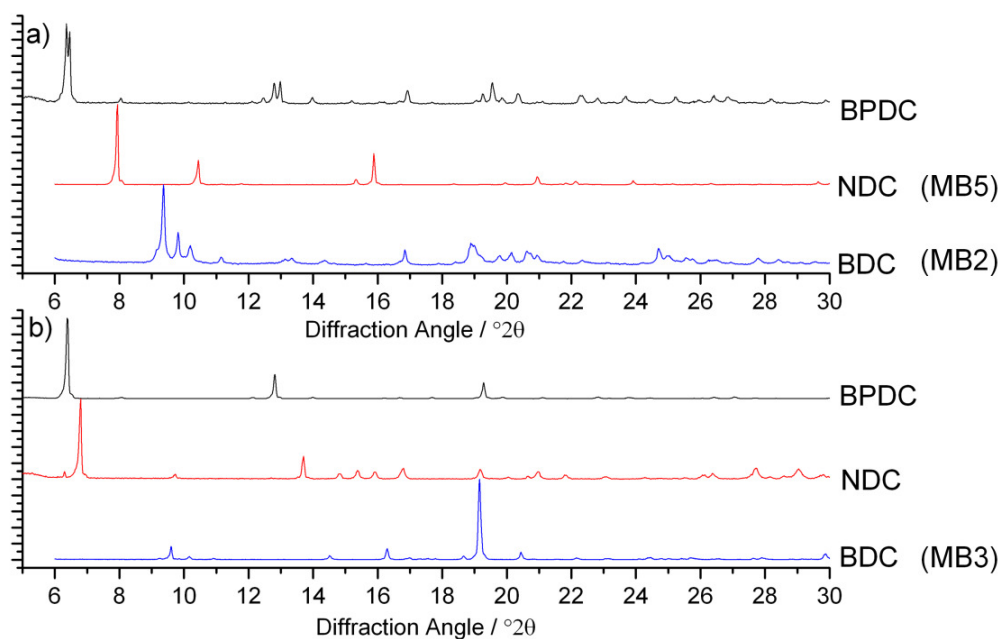


Figure 4.4.1: 'Extended' linker precursors used in the isorecticular synthesis of MB2 and MB3

The reactants were heated to 120 °C for twenty hours similar to typical reaction conditions used for MB2 and MB3 synthesis. Only partial dissolution of the extended linkers was seen prior to heating. Only after heating, complete dissolution of the linker was seen with no Bragg peaks corresponding to the linkers seen in the PXRD pattern of the products. In all four reactions, white crystalline powders were successfully synthesised. The PXRD patterns are given in Figure 4.4.2.



**Figure 4.4.2: PXRD patterns of the products formed through isoreticular synthesis of a) MB2 and b) MB3 and those from regular MB2 and MB3 synthesis using DMF-water ratios of 95:5 and 1:1 respectively**

All four reactions give products appear to be metal-organic frameworks, as evidenced by the large d-spacings seen by powder XRD patterns. Evidence for extended structures is given by the significant increase in d-spacing shown by the shift in Bragg peaks to smaller values. Only the reaction of H<sub>2</sub>NDC with MB2 conditions gave a product suitable for single crystal XRD and the structure solved. This new material shall be referred to as MB5 and will be discussed in section 4.4.2. The remaining three materials, although highly crystalline, were not suitable for single crystal XRD and subsequent attempts to synthesise suitable samples by varying reaction times, temperatures and reagent ratios were unsuccessful.

#### 4.4.2. MB5 – $[\text{Yb}_2(\text{NDC})_3(\text{H}_2\text{O})_4]\cdot 4\text{H}_2\text{O}$

MB5 was synthesised from ytterbium(III) chloride hexahydrate (0.39 g), 2,6-naphthalenedicarboxylic acid (0.324 g), DMF (5 cm<sup>3</sup>) and water (0.15 cm<sup>3</sup>). The mixture was heated to 120 °C for 20 hours before being cooled to room temperature and the white crystalline solid isolated by suction filtration. The synthesis is more like that of MB2 and MB3 with a lower ratio of water to DMF used during synthesis. The greater content of DMF is likely required to solubilise the NDC linker.

$[\text{Yb}_2(\text{NDC})_3(\text{H}_2\text{O})_4]\cdot 2\text{H}_2\text{O}$  (MB5) crystallises in the triclinic *PI* space group. Each ytterbium is coordinated to eight oxygens: two from singly coordinating 2,6-naphthalenedicarboxylate (NDC) linkers, four from two doubly coordinating NDC and two from coordinating water molecules. Two molecules of DMF are uncoordinated and extra-framework. Each ytterbium exists as part of a dimer, linked to another ytterbium by the singly coordinating carboxylato groups (Figure 4.4.3). The crystal structure of MB5 is given in Figure 4.4.4. Crystallographic data are given in Table 4.4.1: Crystallographic data for MB5Table 4.4.1 and Table 4.4.2

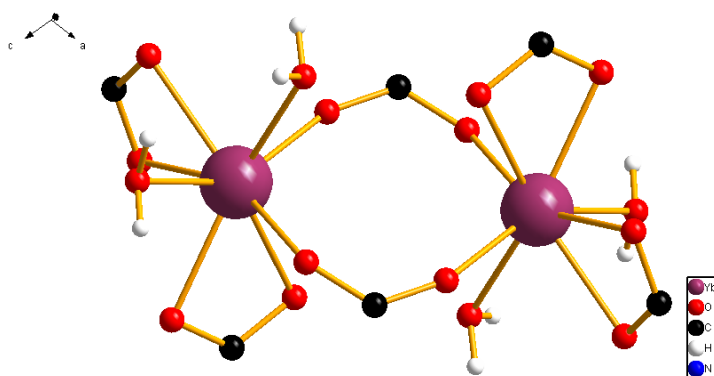


Figure 4.4.3: Ytterbium dimers present in MB5

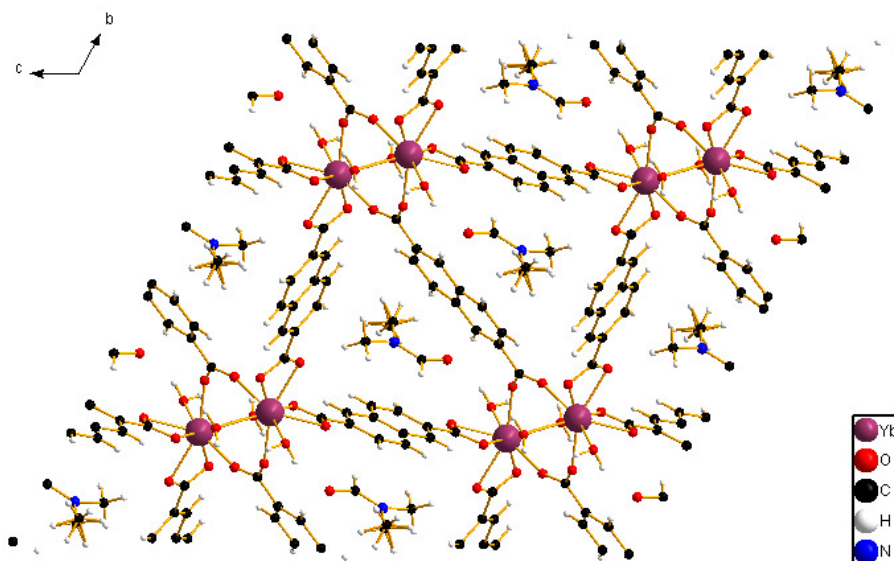


Figure 4.4.4: Crystal structure of MB5 viewed along the  $a$ -axis

Table 4.4.1: Crystallographic data for MB5

	MB5
Formula	$C_{42}H_{40}N_2O_{18}Yb_2$
Formula Weight	1206.85
Colour/Shape	Block, colourless
Size of Crystal	0.16 x 0.14 x 0.12 mm <sup>3</sup>
Temperature / K	100(2)
Crystal System	Triclinic
Space Group	$P\bar{1}$
$a$ / Å	8.4516(2)
$b$ / Å	12.3979(4)
$c$ / Å	12.5674(3)
$\alpha$ / °	110.452(2)
$\beta$ / °	102.131(2)
$\gamma$ / °	109.620(3)
Cell volume / Å <sup>3</sup>	1079.2(1)
$Z$	2
Density (calc.) / g·cm <sup>3</sup>	1.85679

Table 4.4.2: Atomic Parameters of MB5

Atom	Ox.	Wyck.	Site	S.O.F.	x/a	y/b	z/c	U [Å <sup>2</sup> ]
Yb1		2i	1	1	0.294	0.4585	0.5964	
O1A		2i	1	1	0.1389	0.2658	0.6069	
O2A		2i	1	1	-0.0275	0.3284	0.5069	
C2A		2i	1	1	-0.0141	0.2518	0.5507	
C3A		2i	1	1	-0.1823	0.1469	0.5361	
C4A		2i	1	1	-0.1701	0.0478	0.5643	
H4A		2i	1	1	-0.0557	0.0489	0.5923	-1.2
C5A		2i	1	1	-0.3231	-0.0494	0.5512	
H5A		2i	1	1	-0.315	-0.117	0.5674	-1.2
C6A		2i	1	1	-0.4933	-0.0495	0.5136	
C7A		2i	1	1	-0.6528	-0.1465	0.5035	
H7A		2i	1	1	-0.6457	-0.2118	0.5243	-1.2
O1B		2i	1	1	0.4499	0.5077	0.7989	
O2B		2i	1	1	0.5596	0.4332	0.6613	
C2B		2i	1	1	0.5696	0.4782	0.7727	
C3B		2i	1	1	0.7241	0.4967	0.8714	
C4B		2i	1	1	0.7383	0.5548	0.9941	
H4B		2i	1	1	0.6507	0.5823	1.0121	-1.2
C5B		2i	1	1	0.8772	0.5718	1.0874	
H5B		2i	1	1	0.886	0.6118	1.1695	-1.2
C6B		2i	1	1	1.0072	0.53	1.0618	
C7B		2i	1	1	1.1506	0.5444	1.1552	
H7B		2i	1	1	1.1607	0.5831	1.2378	-1.2
O1C		2i	1	1	0.2831	0.3266	0.4214	
O2C		2i	1	1	0.484	0.3418	0.3322	
C2C		2i	1	1	0.3277	0.291	0.3311	
C3C		2i	1	1	0.1835	0.1799	0.2147	
C4C		2i	1	1	0.0016	0.1353	0.2038	
H4C		2i	1	1	-0.0282	0.1735	0.2717	-1.2
C5C		2i	1	1	-0.1329	0.0373	0.0964	
H5C		2i	1	1	-0.2556	0.0098	0.0895	-1.2
C6C		2i	1	1	-0.091	-0.0234	-0.0042	
C7C		2i	1	1	-0.2267	-0.1271	-0.1168	
H7C		2i	1	1	-0.3495	-0.1602	-0.1239	-1.2
O1D		2i	1	1	0.1729	0.5781	0.7011	
H1DA		2i	1	1	0.1141	0.5989	0.6545	-1.5
H1DB		2i	1	1	0.2577	0.646	0.7624	-1.5
O1E		2i	1	1	0.1971	0.5246	0.4501	
H1EA		2i	1	1	0.169	0.5862	0.4822	-1.5
H1EB		2i	1	1	0.1031	0.461	0.3882	-1.5
O100		2i	1	1	0.3194	0.7568	-0.0753	
C101		2i	1	1	0.4244	0.7538	0.0064	
H101		2i	1	1	0.4816	0.7002	-0.0174	-1.2

Atom	Ox.	Wyck.	Site	S.O.F.	x/a	y/b	z/c	U [Å <sup>2</sup> ]
N102		2i	1	1	0.4641	0.8192	0.1248	
C103		2i	1	1	0.5978	0.8202	0.2192	
H10A		2i	1	1	0.6396	0.757	0.1815	-1.5
H10B		2i	1	1	0.5436	0.7983	0.275	-1.5
H10C		2i	1	1	0.7006	0.9061	0.265	-1.5
C104		2i	1	0.717	0.3805	0.8974	0.1643	
H10D		2i	1	0.717	0.4709	0.9801	0.2332	-1.5
H10E		2i	1	0.717	0.2867	0.855	0.1902	-1.5
H10F		2i	1	0.717	0.3255	0.912	0.0971	-1.5
C04A		2i	1	0.283	0.3226	0.8819	0.1665	0.0521
H04A		2i	1	0.283	0.3275	0.8906	0.2478	-1.5
H04B		2i	1	0.283	0.1986	0.8245	0.1072	-1.5
H04C		2i	1	0.283	0.3604	0.9667	0.1685	-1.5

Upon closer inspection, it becomes apparent that MB3 and MB5 display the similar type of ytterbium-carboxylate dimers albeit with differing coordinating molecules. Each ytterbium dimer is connected to six others in the same manner. Since both materials exhibit the same connectivity, it can be stated that MB3 and MB5 are isorecticular analogues of each other (Figure 4.4.5).

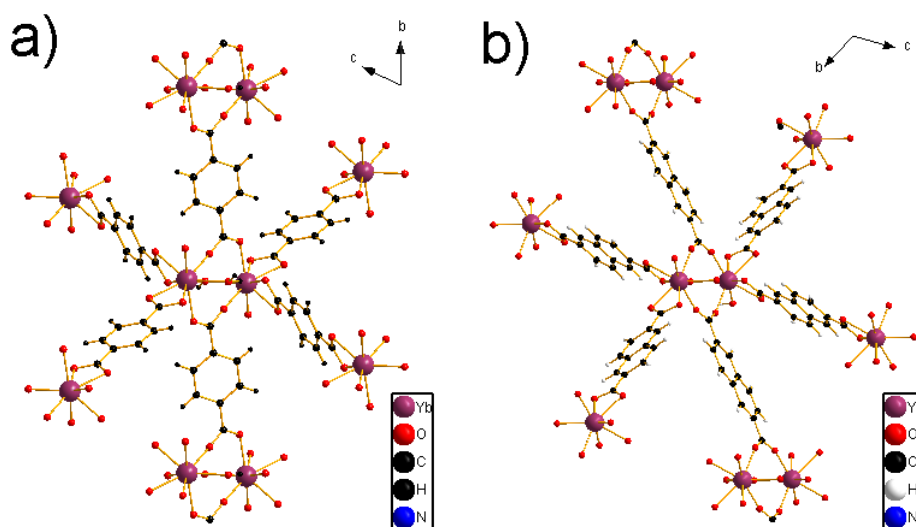


Figure 4.4.5: Connectivity of the ytterbium dimers found in a) MB3 and b) MB5. Only oxygen atoms from coordinating water and DMF shown for clarity

The simulated powder XRD pattern of MB5 is difficult to reconcile with the diffraction pattern of MB5 (Figure 4.4.6). This is likely due to differences in the temperature the crystal structure was solved and the temperature the XRD pattern was collected (100 K and 298 K respectively). Another large factor is the preferred orientation of the crystals, as seen with MB3. It is therefore difficult to fully assign the diffraction pattern of MB5 with that of its crystal structure at this point.

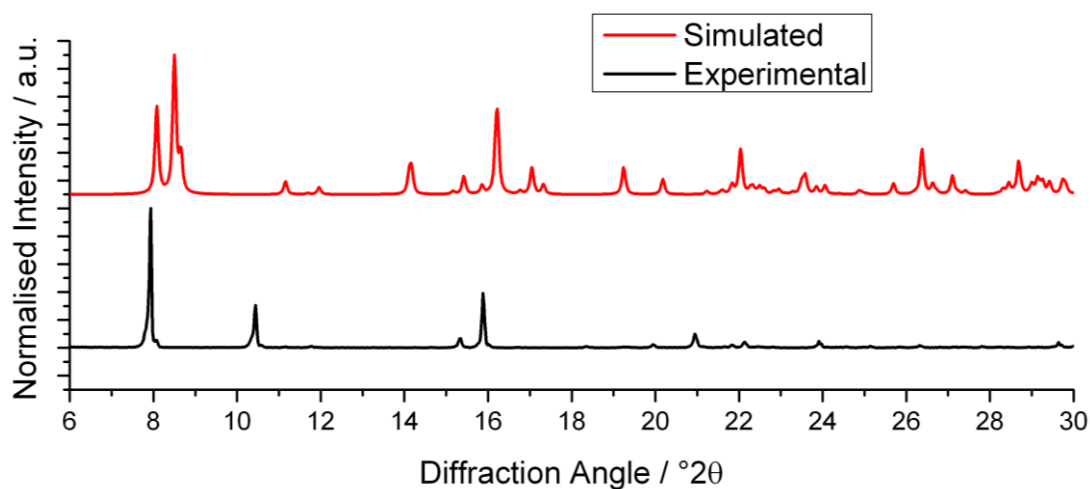


Figure 4.4.6: PXRD patterns of simulated and experimental patterns of MB5

#### 4.4.3. Thermal Behaviour of MB5

Since MB5 exhibits an expanded form of the MB3 structure, previously inaccessible voids in the MB3-type structure may become available. The presence of large voids within the structure of MB5 is given by the presence of extra-framework DMF in the pores of the framework. In MB3, access to these pores is blocked by the presence of the coordinated DMF. A representation of the potential free space in the parallelepiped pores of both frameworks is given in Figure 4.4.7.

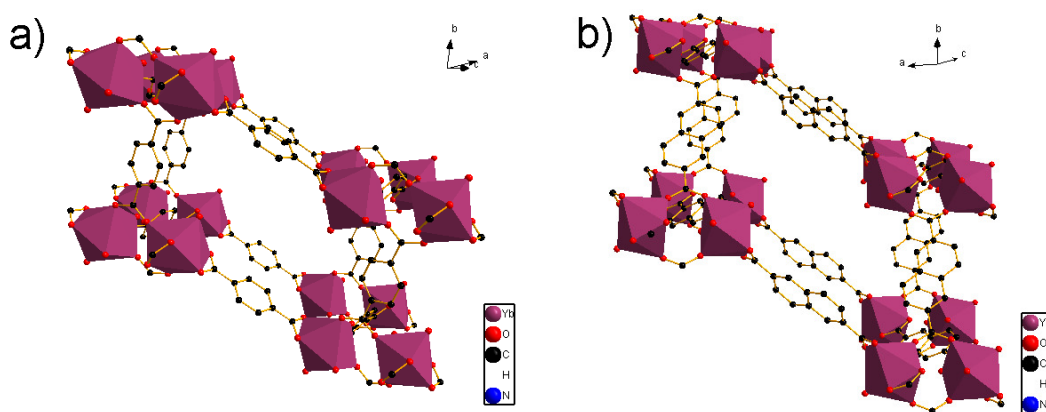


Figure 4.4.7: Parallelepiped voids within the structures of a) MB3 and b) MB5. Coordinated and uncoordinated DMF not shown for clarity

Although MB5 has the potential ability to be porous, it remains to be seen whether the pores can be evacuated and the structure remain stable or whether the structure collapses as seen in MB3. To investigate the thermal stability of MB5, both thermogravimetric analysis and thermogravimetry were performed on said material.

The thermogravimetric analysis of MB5 shows to clear losses at around 150 and 300 °C of 7.6 and 6.1 % respectively, before eventual collapse of the framework at around 600 °C (Figure 4.4.8). Assuming the same composition as the crystal structure i.e.  $[\text{Yb}_2(\text{NDC})_3(\text{H}_2\text{O})_4] \cdot 2\text{DMF}$  and loss of uncoordinated DMF following by the coordinated water, two losses of 12.1% and 6.0% would be expected. This suggests that less DMF is present than expected – this can be explained by the difference in temperatures between the start of the TGA and the temperature at which the crystal structure was solved. Assuming the structure after the first weight loss is now  $[\text{Yb}_2(\text{NDC})_3(\text{H}_2\text{O})_4]$ , the second weight loss agrees well with complete loss of coordinated water generating the fully evacuated  $\text{Yb}_2(\text{NDC})_3$  material (6.0 %, calc: 6.0 %)



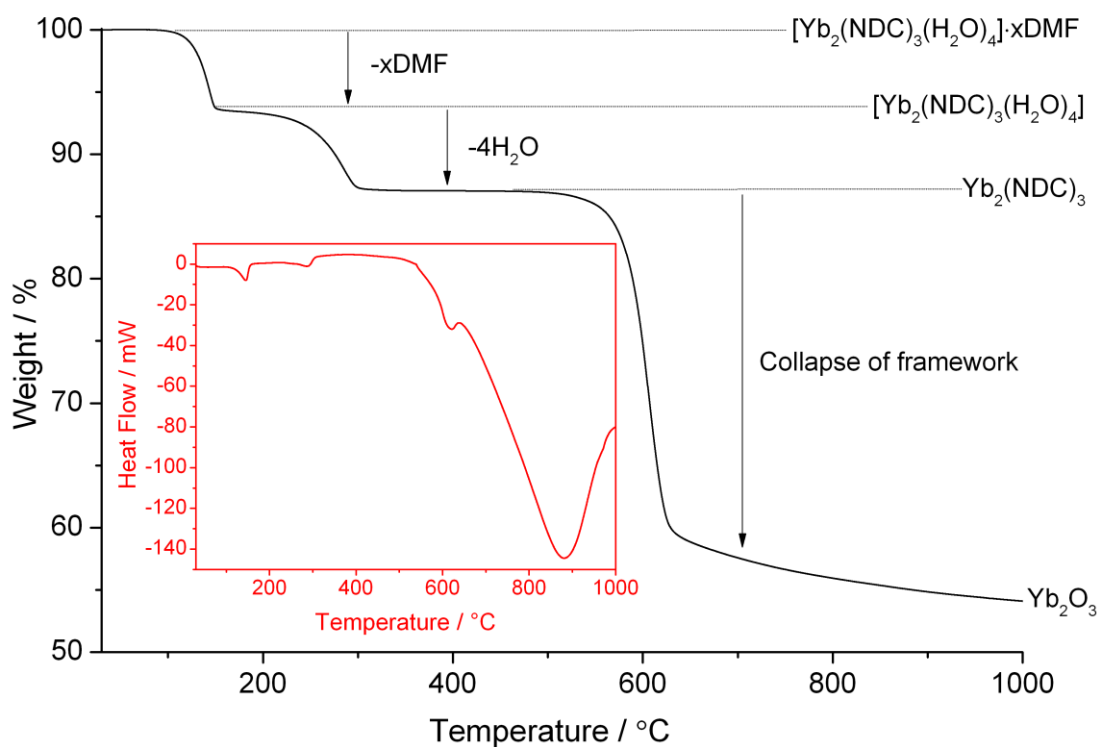


Figure 4.4.8: Main: TGA of MB5 in air; Insert: DSC curve of MB5 over same temperature range

Thermogravimetry of MB5 displays four clear structural changes before collapse of the framework (Figure 4.4.8). The first two changes agree well with the losses expected from the TGA i.e. loss of uncoordinated DMF followed by loss of coordinated water. All three of these patterns remain roughly as intense as one another suggesting no large changes in crystallinity corresponding to a significant structural rearrangement, like the one seen in MB3. Before collapse of the framework at around 540 °C, a new unexpected phase is observed at around 480 °C. These peaks in this region what would be expected for materials with high d-spacings i.e. metal-organic frameworks. The stability of these new phases upon cooling have not been investigated although be an interesting area for further investigation.

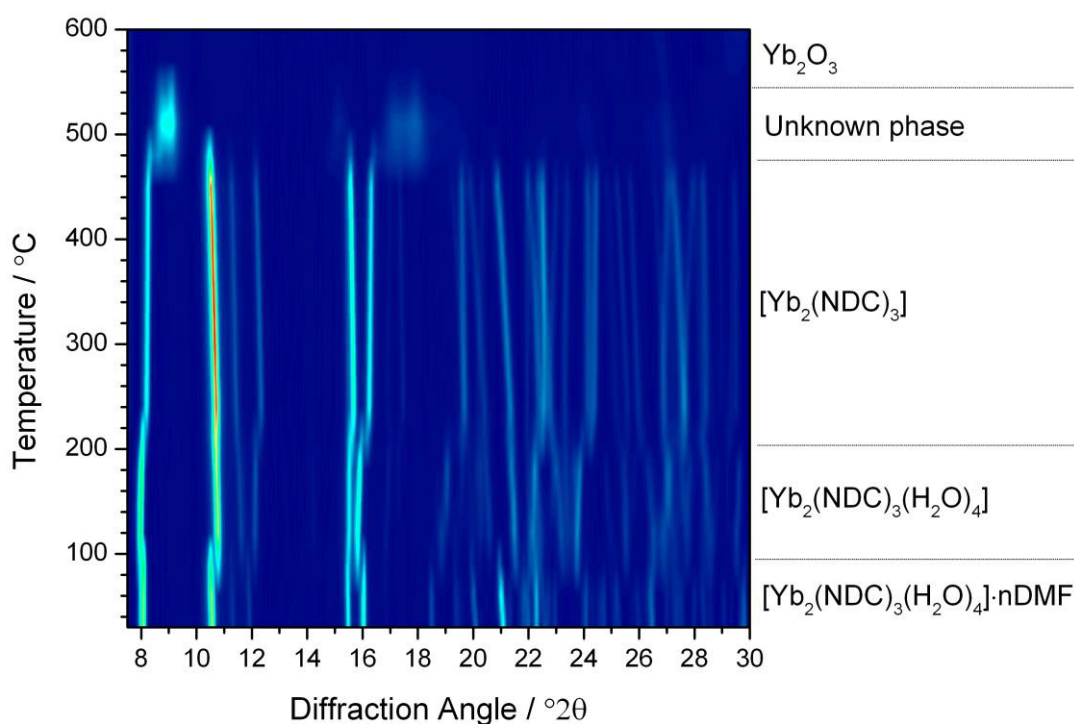


Figure 4.4.9: Thermodiffractometry of MB5 in air

## 4.5. Summary

Through mediation of the reaction solvent and subsequent calcinations, several new ytterbium-organic frameworks have been synthesised and their properties investigated. Using a solvent mixture of between 1:0 and 6:4 DMF to water leads to the formation of MB2 -  $[\text{Yb}_2(\text{BDC})_3(\text{DMF})_2] \cdot 2\text{H}_2\text{O}$  which contains ytterbium-carboxylate chains running along the *c*-axis. Calcination of MB2 creates  $\text{Yb}_2(\text{BDC})_3$ , a material that exhibits significant porosity. A lutetium analogue of MB2 was synthesised. Doping of MB2(Yb) with other lanthanides was successful with clear evidence from both XRD and photoluminescence studies. Further decreasing the DMF to water ratio leads to the formation of MB3 –  $[\text{Yb}_2(\text{BDC})_3(\text{DMF})_2(\text{H}_2\text{O})_2]$  which contains ytterbium-carboxylate dimers. Although sharing similar chemical formulae, MB2 and MB3 vary greatly in terms of structure and properties. Despite of this, both MB2 and MB3 can be calcined into the same  $\text{Yb}_2(\text{BDC})_3$  material. An

isorecticular analogue of MB3, MB5, was synthesised using the extended 2,6-naphthalenedicarboxyate linker.

## 4.6. References

- (1) Zehnder, R. A.; Renn, R. A.; Pippin, E.; Zeller, M.; Wheeler, K. A.; Carr, J. A.; Fontaine, N.; McMullen, N. C. *J. Mol. Struct.* **2011**, 985, 109.
- (2) Feng, S. *Acta Crystallogr. Sect. E. Struct. Rep. Online* **2010**, 66, M33.
- (3) Na, L.; Hua, R.; Zhang, L.; Zhang, W.; Ning, G. *J. Chem. Crystallogr.* **2009**, 39, 688.
- (4) Weng, D.; Zheng, X.; Jin, L. *Eur. J. Inorg. Chem.* **2006**, 4184.
- (5) Batten, S. R.; Neville, S. M.; Turner, D. R. *Coordination polymers : design, analysis and application*; RSC Pub.: Cambridge, 2009.
- (6) Cheetham, A. K.; Rao, C. N. R.; Feller, R. K. *Chem. Commun.* **2006**, 4780.
- (7) Zhang, Y.; Yang, J.; Li, G. D.; Zhang, F.; Chen, J. S. *J. Coord. Chem.* **2008**, 61, 945.
- (8) Shannon, R. *Acta Crystallogr. Sect. A* **1976**, 32, 751.
- (9) He, H. Y.; Ma, H. Q.; Sun, D.; Zhang, L. L.; Wang, R. M.; Sun, D. F. *Cryst. Growth Des.* **2013**, 13, 3154.
- (10) Reineke, T. M.; Eddaoudi, M.; Fehr, M.; Kelley, D.; Yaghi, O. M. *J. Am. Chem. Soc.* **1999**, 121, 1651.
- (11) Daiguebonne, C.; Kerbellec, N.; Bernot, K.; G  rault, Y.; Deluzet, A.; Guillou, O. *Inorg. Chem.* **2006**, 45, 5399.
- (12) Daiguebonne, C.; Kerbellec, N.; Guillou, O.; B  nzli, J.-C.; G  my, F.; Catala, L.; Mallah, T.; Audebrand, N.; G  rault, Y.; Bernot, K.; Calvez, G. *Inorg. Chem.* **2008**, 47, 3700.
- (13) Pan, L.; Zheng, N.; Wu, Y.; Han, S.; Yang, R.; Huang, X.; Li, J. *Inorg. Chem.* **2001**, 40, 828.
- (14) Sing, K. S. W.; Everett, D. H.; Haul, R. A. W.; Moscou, L.; Pierotti, R. A.; Rouquerol, J.; Siemieni  wska, T. *Pure Appl. Chem.* **1985**, 57, 603.
- (15) He, H.; Ma, H.; Sun, D.; Zhang, L.; Wang, R.; Sun, D. *Cryst. Growth Des.* **2013**, 13, 3154.
- (16) Guo, H. L.; Zhu, Y. Z.; Qiu, S. L.; Lercher, J. A.; Zhang, H. J. *Adv. Mater.* **2010**, 22, 4190.
- (17) Williams, D. H.; Fleming, I. *Spectroscopic methods in organic chemistry*; 6 ed. ed.; McGraw-Hill: London, 2008.
- (18) Lang, L. *Absorption Spectra in the Ultraviolet and Visible Region*, 1968.
- (19) Eliseeva, S. V.; B  nzli, J.-C. G. *Chem. Soc. Rev.* **2010**, 39, 189.
- (20) Guo, Z.; Xu, H.; Su, S.; Cai, J.; Dang, S.; Xiang, S.; Qian, G.; Zhang, H.; O'Keeffe, M.; Chen, B. *Chem. Commun.* **2011**, 47, 5551.
- (21) White, K. A.; Chengelis, D. A.; Gogick, K. A.; Stehman, J.; Rosi, N. L.; Petoud, S. p. *J. Am. Chem. Soc.* **2009**, 131, 18069.
- (22) Sun, C.-Y.; Zheng, X.-J.; Chen, X.-B.; Li, L.-C.; Jin, L.-P. *Inorg. Chim. Acta* **2009**, 362, 325.
- (23) Weng, D.; Zheng, X.; Chen, X.; Li, L.; Jin, L. *Eur. J. Inorg. Chem.* **2007**, 3410.
- (24) Weng, D.; Zheng, X.; Jin, L. *Eur. J. Inorg. Chem.* **2006**, 2006, 4184.
- (25) Mohapatra, S.; Adhikari, S.; Rij  , H.; Maji, T. K. *Inorg. Chem.* **2012**, 51, 4891.
- (26) Dang, S.; Zhang, J.-H.; Sun, Z.-M. *J. Mater. Chem.* **2012**, 22, 8868.
- (27) Haquin, V.; Etienne, M.; Daiguebonne, C.; Freslon, S.; Calvez, G.; Bernot, K.; Le Poll  s, L.; Ashbrook, S. E.; Mitchell, M. R.; B  nzli, J.-C.; Eliseeva, S. V.; Guillou, O. *Eur. J. Inorg. Chem.* **2013**, 2013, 3464.
- (28) Chen, B.; Yang, Y.; Zapata, F.; Qian, G.; Luo, Y.; Zhang, J.; Lobkovsky, E. B. *Inorg. Chem.* **2006**, 45, 8882.
- (29) Banerjee, R.; Furukawa, H.; Britt, D.; Knobler, C.; O'Keeffe, M.; Yaghi, O. M. *J. Am. Chem. Soc.* **2009**, 131, 3875.

(30) Bauer, C. A.; Timofeeva, T. V.; Settersten, T. B.; Patterson, B. D.; Liu, V. H.; Simmons, B. A.; Allendorf, M. D. *J. Am. Chem. Soc.* **2007**, *129*, 7136.

## 5. Crystallisation of Metal-Organic Frameworks

---

### 5.1. Introduction

The study of crystallisation kinetics and the observation of intermediary product crystalline phases during the formation of any material is important to understand their formation mechanism to then allow new materials to be prepared with some predictability.<sup>1</sup> If crystallinity is monitored as a function of time using a range of temperatures, information about the kinetics of the crystallisation can be extracted. These crystallisation studies can be performed using *ex situ* or *in situ* methods.

*Ex situ* crystallisation methods for solvothermal reactions involve quenching of reactions after certain time periods, recovering the solid by filtration and examining the solid product formed, usually using powder X-ray diffraction. The advantage of *ex situ* methods is their simplicity – reactions can be performed under laboratory conditions with no modification to the synthesis. Further analysis of the materials using other techniques such as TGA or IR spectroscopy is possible. However, since direct observation of the crystallisation cannot be followed (the reaction must be stopped and cooled to observe its progress), the true reaction kinetics and the presence of any high temperature intermediary products cannot be seen. The rate of sampling also affects the quality of the data derived. Also the assumption must be made that the quenched material is the same as that present at reaction conditions, *i.e.* has not irreversibly changed on cooling and filtration, which may not be the case.

*In situ* methods are non-invasive allowing for direct observation of the crystallisation process, often in real-time. *In situ* investigations of synthesis can be performed using a wide range of techniques including IR,<sup>2</sup> Raman,<sup>3</sup> NMR,<sup>4</sup> EXAFS,<sup>5</sup> SAXS,<sup>6</sup>

WAXS,<sup>7</sup> powder X-ray diffraction<sup>8</sup> and total scattering.<sup>9</sup> The challenge in this area is to build realistic reaction vessels from which diffraction data can be measured. Many of these techniques require the high intensity radiation provided by a synchrotron source to penetrate reaction vessels to directly observe syntheses. Of particular interest to MOF crystallisation are studies using powder XRD diffraction. These techniques allow for extraction of both lattice parameters and kinetic data.

Crystallisation studies using powder XRD tend to use one of two techniques. *In situ* energy dispersive X-ray diffraction (EDXRD) experiments use a white X-ray beam containing a range of energies with a fixed detector. Since data over the entire energy range are collected near simultaneously from a fixed detector, rapid data collection can be achieved, facilitating straightforward following of the crystallisation process. Although useful for monitoring crystallisation kinetics, extraction of meaningful lattice parameters is difficult and complicated, and the d-spacing resolution is inherently low so structure refinement is not possible.<sup>10,11</sup>

The second technique is *in situ* angular dispersive X-ray diffraction (ADXRD). Using a monochromatic X-ray source, the signal is measured as a function of diffraction angle, similar to laboratory X-ray diffractometers. Since the X-ray source has to be monochromated before sample exposure, the flux of the beam is typically less than that would be used for EDXRD experiments although with modern synchrotrons this is rarely a problem, especially if highly penetrating short wavelength X-rays are used. The use of ADXRD allows for detailed structural analysis with extraction of lattice parameters using Rietveld refinement possible. It is for these reasons, ADXRD was chosen as the technique to perform crystallisation studies on the metal-organic frameworks discussed in this chapter.

This chapter describes how crystallisation of several metal-organic frameworks can be followed both *ex situ* and *in situ* and how these two sets of techniques can complement one another to enable the pathways of MOF formation to be monitored.

## 5.2. Experimental Set-Up

The Oxford Diamond *In Situ* Cell (ODISC)<sup>12</sup> is a furnace for *in situ* diffraction studies with infrared heating, Figure 5.2.1 (a), (b) and (c). This furnace can provide rapid heating up to 1100 °C from room temperature in a matter of minutes. Combining this with the highly penetrating short wavelength radiation (~55 keV, equivalent to ~ 0.2 Å) provided by beamline I12 at the Diamond Light Source allows for *in situ* studies of reactions such as crystallisation in real time. Using a PEEK (poly-ether ether ketone) reaction vessel with an internal thermocouple (constructed in house by the University of Warwick mechanical workshop) permitted direct measurement of reaction temperature, Figure 5.2.1(d). The volume of the PEEK vessel used was similar to those used in typical synthesis in the laboratory (~ 5 ml). The reaction mixture was introduced to the reaction vessel and was agitated using a magnetic follower, with agitation continued during the course of reaction. A wavelength of 0.2242 Å was used and 2-D diffraction patterns collected every minute using a Pixium large area image plate detector (430 x 430 mm<sup>2</sup>) with an exposure time of 4000 ms. Collecting data over a range of temperatures allows us to observe metal-organic framework crystallisation directly. The temperatures used were between 90 and 120 °C.



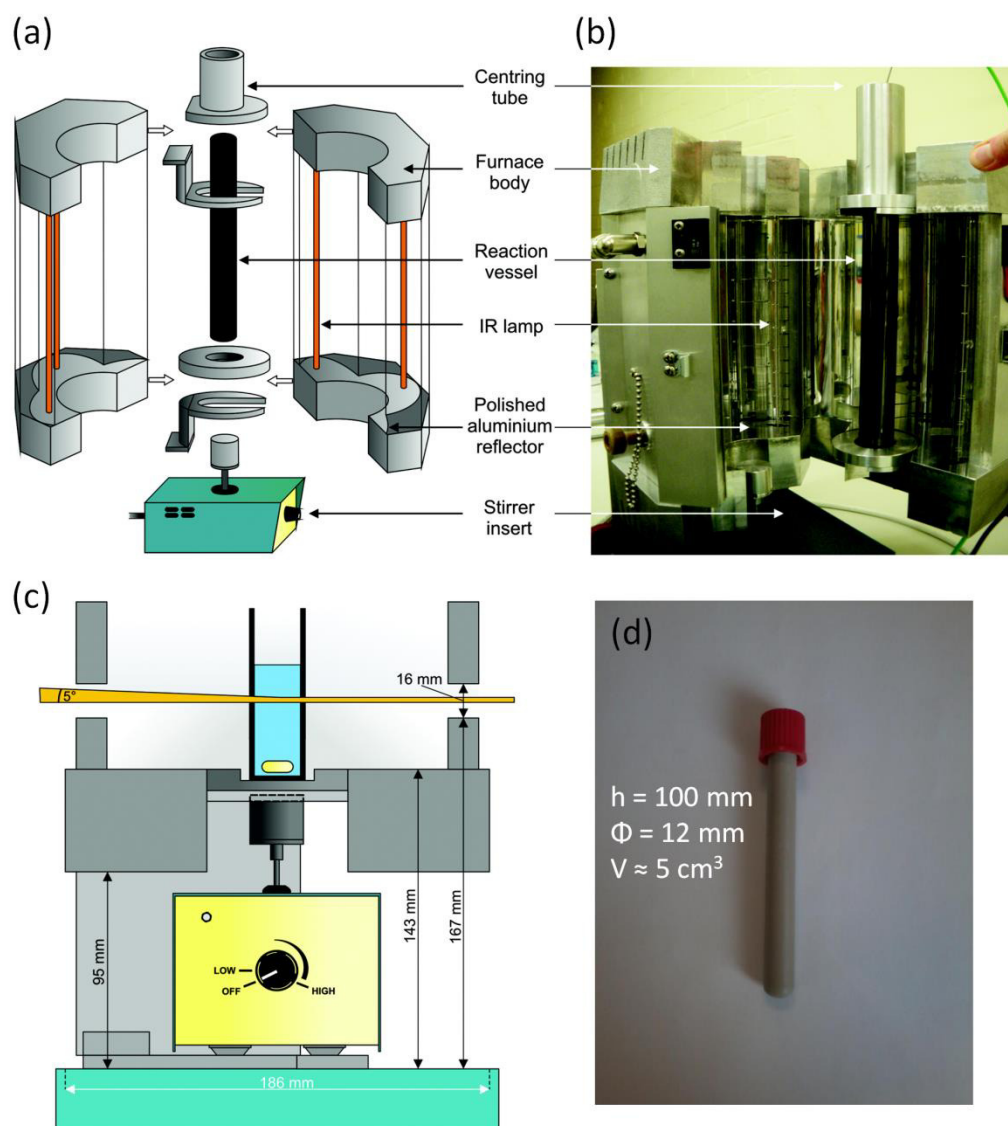


Figure 5.2.1: (a) and (b): Schematic of the ODISC furnace alongside a photograph of the internal furnace set-up; (c): Cross section of the lower section of the cell showing the beam-path and magnetic stirrer; (d): PEEK autoclave used in crystallisation studies (internal thermocouple not shown)

Diffraction images were taken every sixty seconds using a 4000 ms exposure. These 2-D diffraction patterns were integrated using the fit2d software to give 1-D diffraction patterns.<sup>13</sup> These 1-D diffraction patterns were loaded into the GSAS software,<sup>14</sup> and the diffraction patterns were refined using the Rietveld method using crystal structure models as appropriate (see below). Although the atomic positions were not refined, the refinement allowed determination of crystallographic unit cell parameters along with a scale factor. The scale factor relates to the total intensity of the Bragg peaks and can therefore be used

as a determination of the degree of crystallinity when compared to the diffraction pattern of the material at completion. Reactions were stopped when intensity of the Bragg peaks no longer appeared to be increasing. It is worth noting that while the data were recorded, there was no automated data analysis to view data while being recorded so the end-point was not necessarily easy to judge. Owing to the crystallinity of the PEEK reaction vessel used, Bragg peaks from the tube itself were observed. A comparison of the diffraction patterns at the start and finish of the reaction could be used to determine the product from the reaction vessel. The software used only fitted peaks from the metal-organic framework ignoring those from the PEEK vessel.

Owing to the large quantity of the data collected and difficulties in automating the refinement process, it was decided that a five minute interval between refinements would be sufficient to follow the crystallisation process.

### 5.3. Crystallisation of MB2 ( $[\text{Yb}_2(\text{BDC})_3(\text{DMF})_2] \cdot 2\text{H}_2\text{O}$ )

#### 5.3.1. *In Situ* Studies

To determine whether any intermediary products were formed during the synthesis of MB2, time-resolved diffraction plots were made for each reaction temperature. Time-resolved diffraction plots for the reactions at 120, 110 and 90 °C are given in Figure 5.3.1. Reactions were also performed at 100 °C but have been excluded from this analysis due to irregularities in the growth of the scale factor with time, possibly due to irregularities in sample agitation. At all the reaction temperatures studied, only direct formation of MB2 was observed with no evidence of the formation of crystalline intermediary products seen. Bragg peaks from terephthalic acid are also seen at the start of the reactions at 110 and 90 °C and gradually disappear as the reaction reaches reaction

temperature and before the product is formed. The reaction temperature is reached and maintained after around 20 minutes as evidenced by readings from the internal thermocouple shown in Figure 5.3.1d.

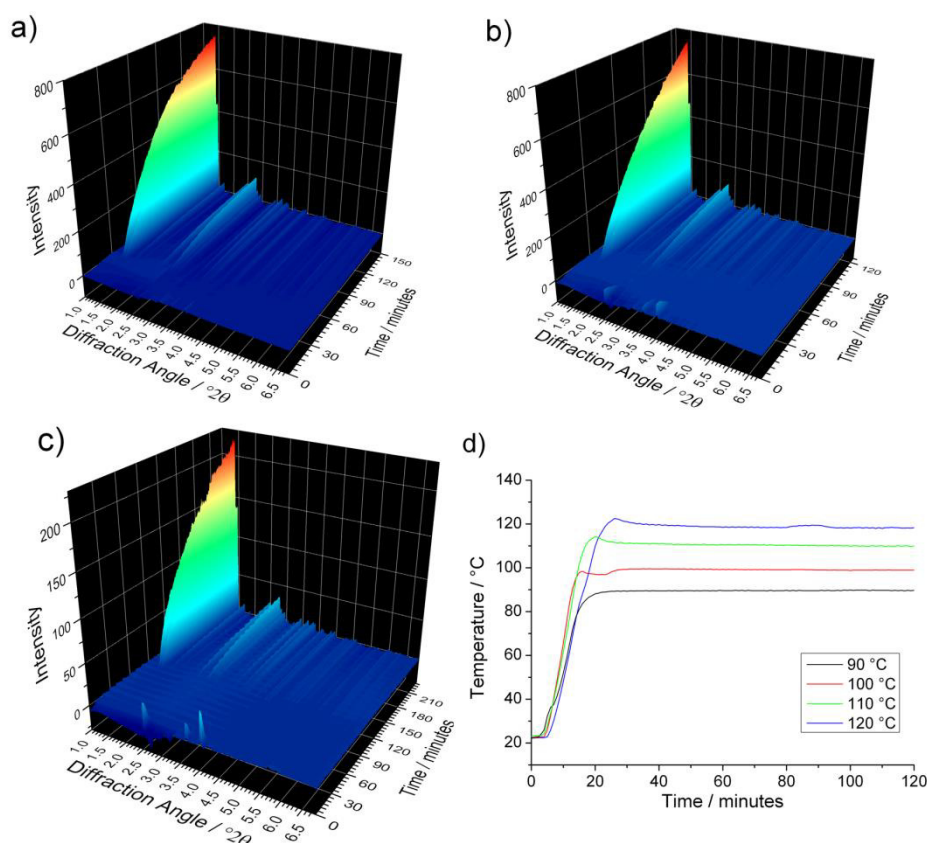


**Figure 5.3.1: 3-D Time-resolved diffraction plots of MB2 crystallisation at a) 120  $^{\circ}\text{C}$ , b) 110  $^{\circ}\text{C}$  and c) 90  $^{\circ}\text{C}$  with the backgrounds subtracted; d) Temperature profiles of the reactions recorded using the internal thermocouple.**

It was discovered that the XRD pattern of MB2 at reaction temperatures did not match that of that of the pattern at room temperature when synthesised in the laboratory, nor the simulated pattern from the single crystal structure, which had been determined at 77 K. Comparison of the measured XRD pattern with other  $\text{Ln}_2(\text{BDC})_3(\text{DMF})_x(\text{H}_2\text{O})_y$  materials found that the *in situ* diffraction patterns closely matched that of the previously reported  $\text{Er}_2(\text{BDC})_3(\text{DMF})_2$ , presumably due to its larger unit cell.<sup>15</sup> Upon cooling to room temperature, the PXRD pattern closely resembles that expected for MB2 (Figure 5.3.2).

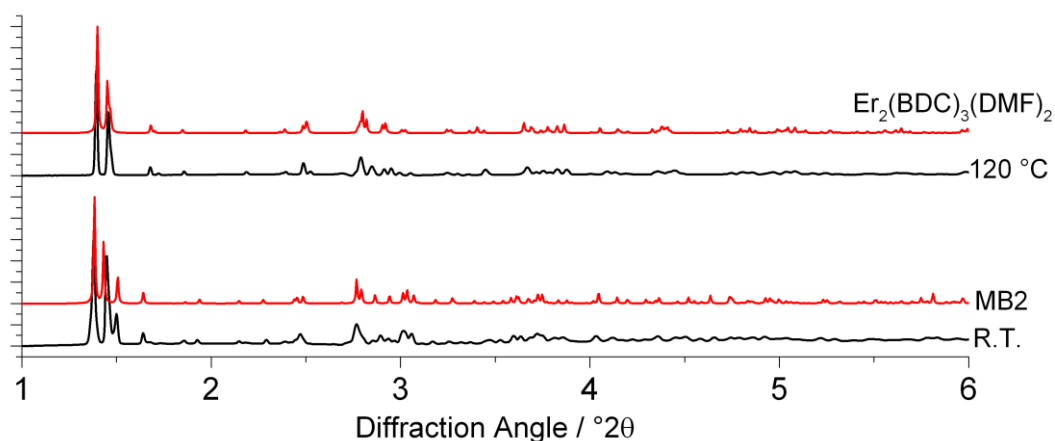
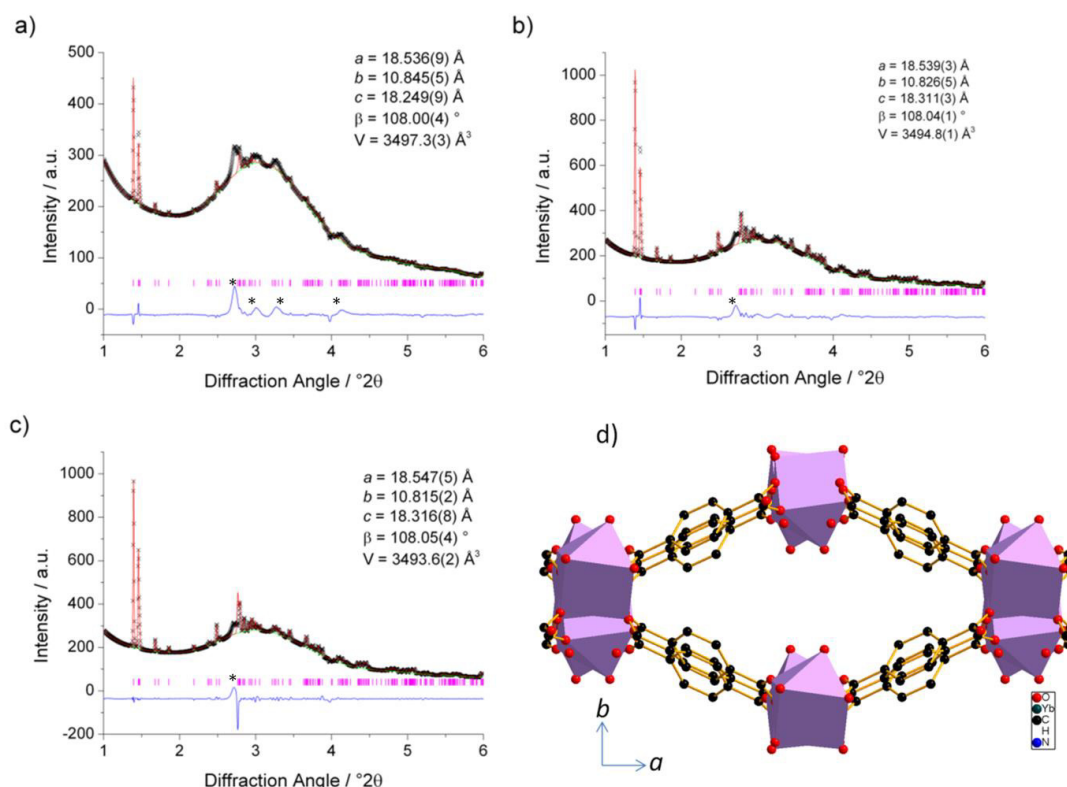


Figure 5.3.2: PXRD plot ( $\lambda = 0.2242 \text{ \AA}$ ) of MB2 measured *in situ* at 120°C and at room temperature (black) with the simulated PXRD patterns (red) of MB2 ( $a = 18.2950(4) \text{ \AA}$ ,  $b = 10.8482(2) \text{ \AA}$ ,  $c = 17.3984(4) \text{ \AA}$ ,  $\beta = 101.395(2)^\circ$ ,  $V = 3384.96(12) \text{ \AA}^3$ ) and  $\text{Er}_2(\text{BDC})_3(\text{DMF})_2$  ( $a = 18.653(4) \text{ \AA}$ ,  $b = 10.738 \text{ \AA}$ ,  $c = 18.547(4) \text{ \AA}$ ,  $\beta = 108.46(3)^\circ$ ,  $V = 3523.9(1) \text{ \AA}^3$ ) given as comparisons.

Partial Rietveld refinement of the XRD patterns from the final products collected at reaction temperatures allowed us to obtain further information on the materials *in situ*. At all of the temperatures studied, the material continues to adopt the same unit cell as the  $\text{Er}_2(\text{BDC})_3(\text{DMF})_2$  structure (Figure 5.3.3).<sup>16</sup> At high temperatures, the  $a$ -parameter increases compared to at 90 °C, whereas the  $b$ -length diminishes. Since these two lengths correspond to the diamond-shaped cross-section of the 2-D channels in MB2, it can easily be rationalised that an increase in one direction must lead to an associated decrease in the other (Figure 5.3.3d). The  $c$ -parameter that runs along the ytterbium ‘chains’ shows only a comparatively small increase with temperature consistent with a small extension in the metal-metal chain distances. The  $\beta$ -angle increases with temperature. The combined effect of this leads to a decrease in unit-cell volume. Negative thermal expansion has been observed for several metal-organic frameworks.<sup>17-20</sup>



**Figure 5.3.3:** Profile fits of PXRD patterns of MB2 taken at a) 90 °C, b) 110 °C and c) 120 °C taken *in situ* ( $\lambda = 0.2242 \text{ \AA}$ ) with refined parameters. Patterns were profiled using  $\text{Er}_2(\text{BDC})_3(\text{DMF})_2$  as a starting point. Materials crystallise in the  $C2/c$  spacegroup. Asterisks in the difference line denote regions where diffraction peaks from the PEEK sample holder are found. d): Crystal structure of MB2 viewed along the c-axis

A comparison of the scaling factor against time plots for each reaction temperature appear to show that only the reactions at 90 and 120 °C are approaching completion, as seen in Figure 5.3.3. The reaction at 110 °C has not reached completion. Despite this, useful information can be gleaned from this data since the degree of crystallinity can be fitted for incomplete reactions. The initial appearance of MB2 is unsurprisingly earliest for the reaction at 120 °C, closely followed by 110 and then 90 °C in that order.

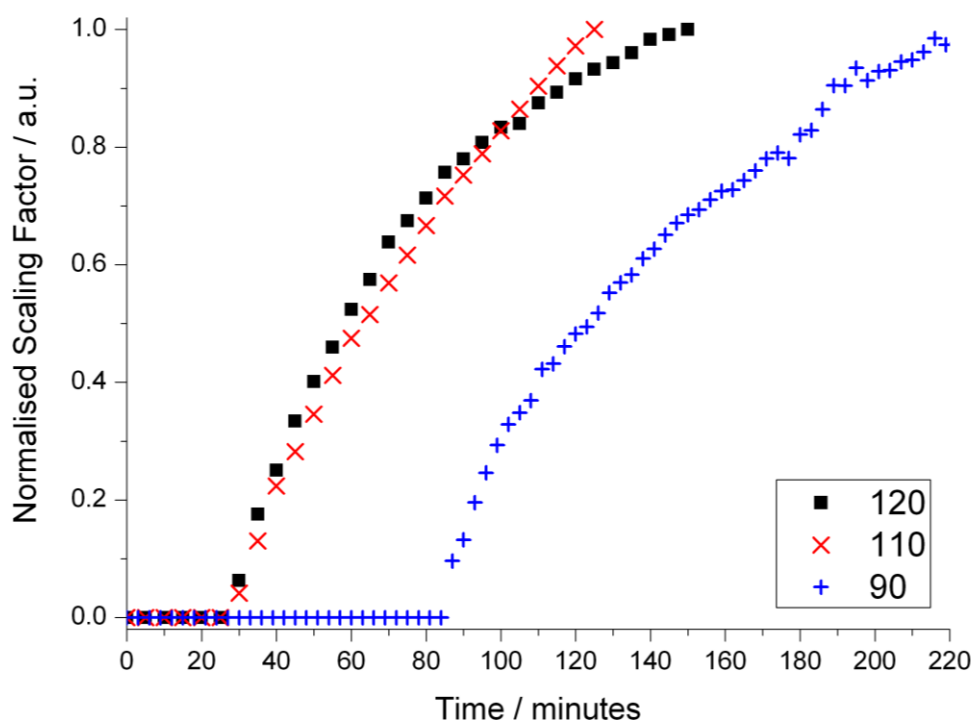


Figure 5.3.4: Plot of normalised scaling factor against time for MB2 crystallisation at varying temperatures

The Rietveld analysis allows lattice parameters to be determined as a function of reaction time. The  $a$  cell parameter increases as the reaction progresses for all three temperatures (90, 110, 120°C) with plateaus reached for 110 and 120°C. The  $a$  parameter increases as the reaction progresses. The  $b$  parameter follows an opposite trend with decreasing values both as the reaction progresses and with increasing temperature. The relationship between the structure in the  $ab$  plane with regards to that along the  $c$ -axis is shown in Figure 5.3.3d and Figure 5.3.5. This suggests that the channels along the  $c$ -axis ‘flatten’ as the reaction progresses. The  $c$  parameter remains roughly constant as the reaction progresses. This can be explained by the rigidity of the ytterbium carboxylate chains – any change in the  $c$ -axis would require re-orientation of the 1,4-benzenedicarboxylate linkers.

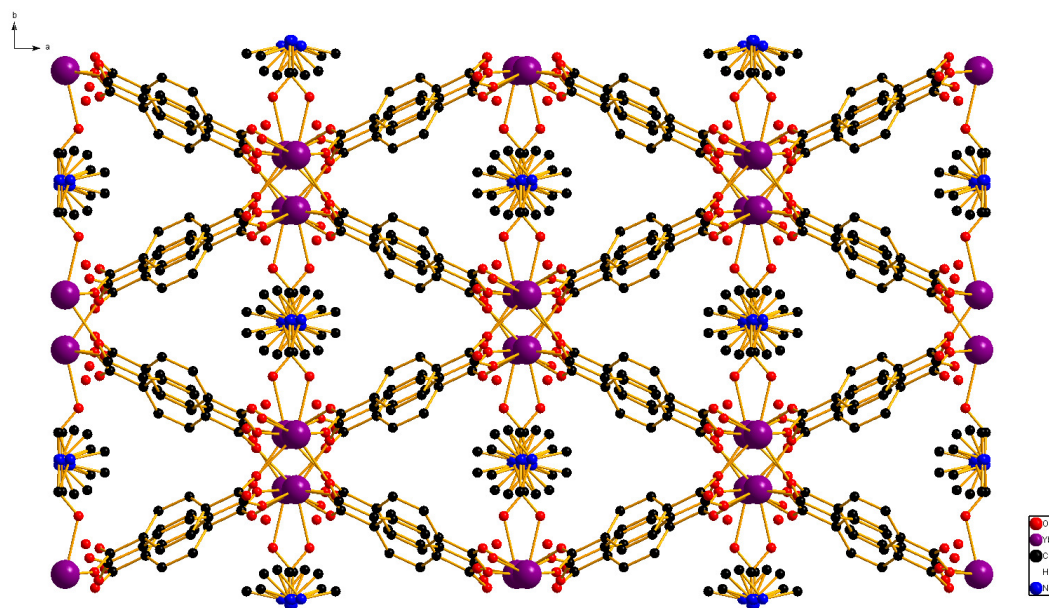


Figure 5.3.5: Crystal Structure of MB2 viewed along the c-axis. Hydrogens excluded for clarity

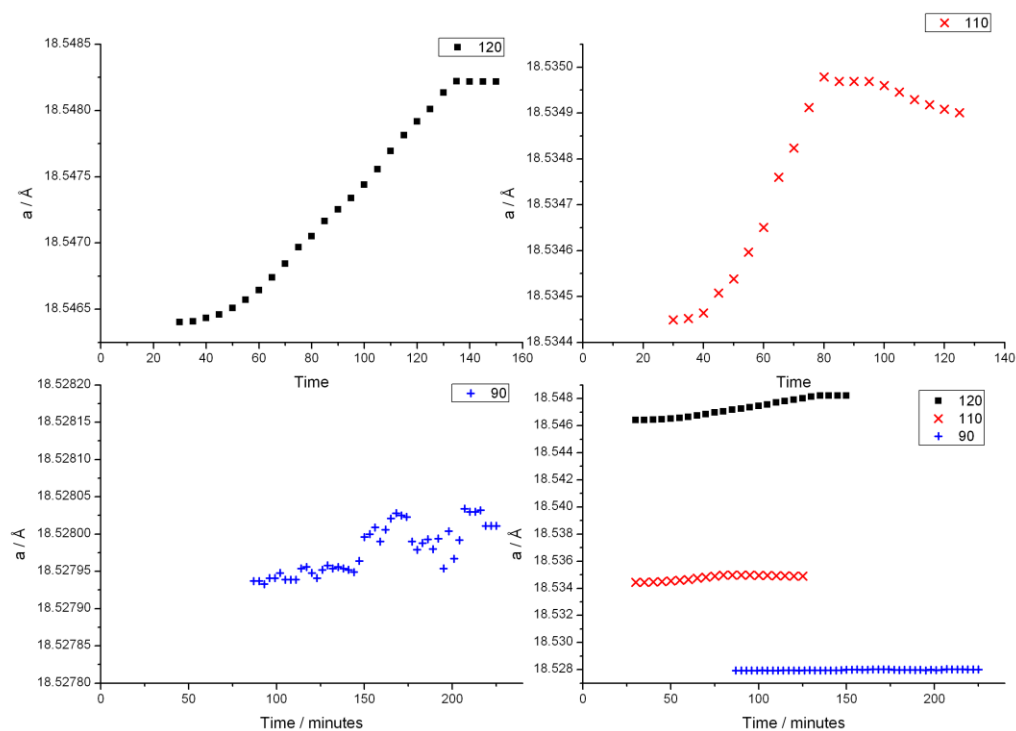


Figure 5.3.6: Evolution of  $a$ -parameter with time during MB2 crystallisation; Top left, top right, bottom left: Profiles at 120, 110 and 90°C respectively; Bottom left: All previous plots on the same axis

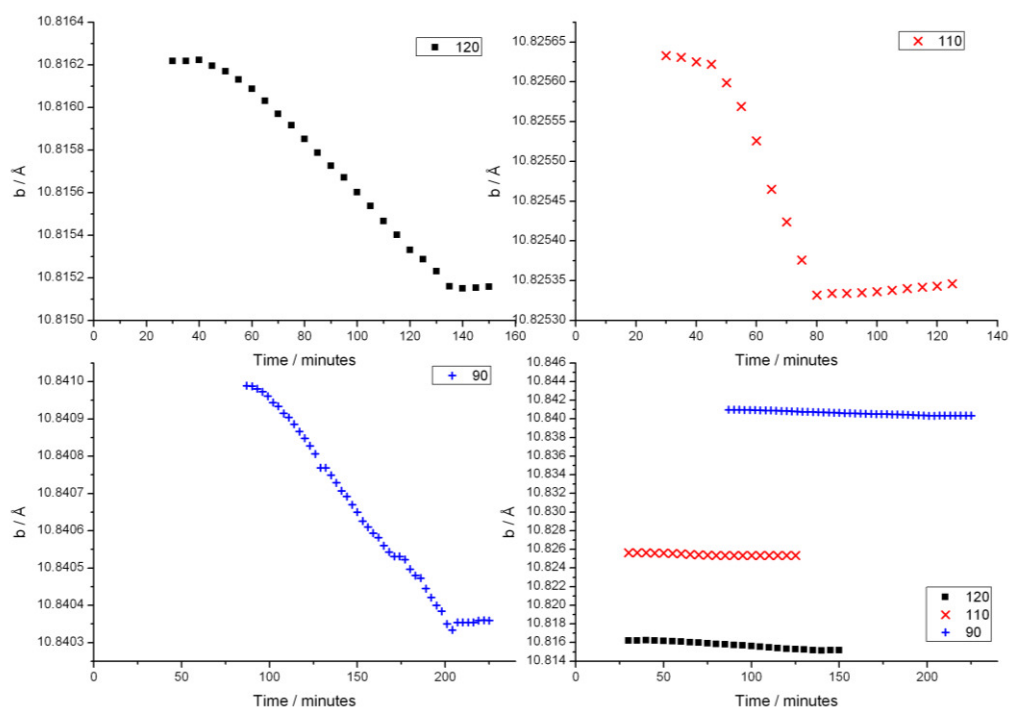


Figure 5.3.7: Evolution of b-parameter with time during MB2 crystallisation; Top left, top right, bottom left: Profiles at 120, 110 and 90°C respectively; Bottom left: All previous plots on the same axis

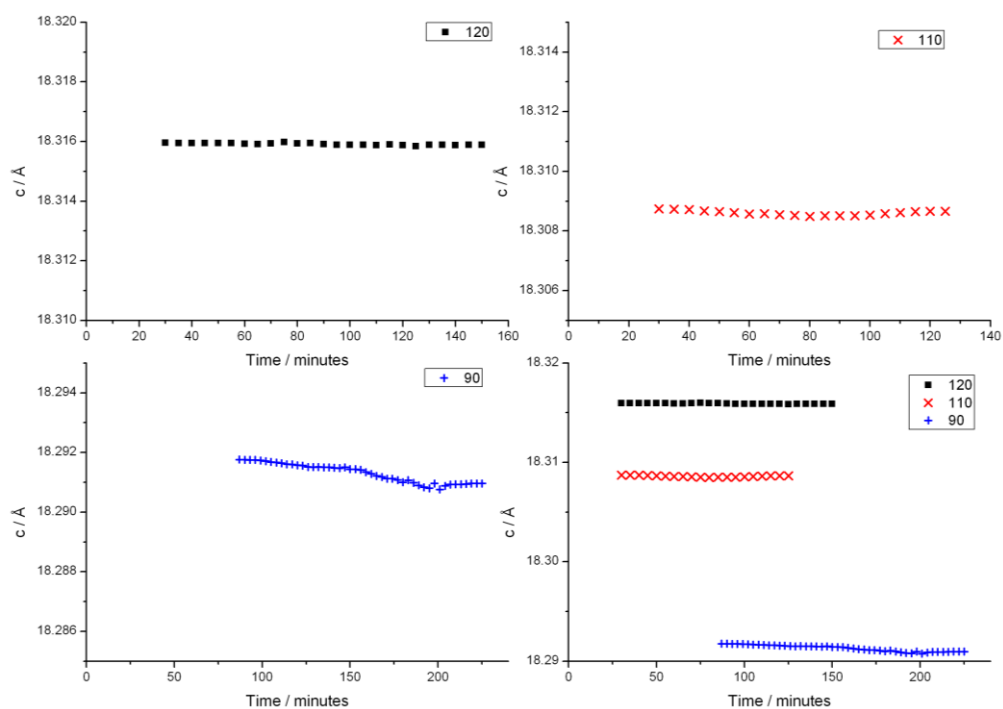


Figure 5.3.8: Evolution of c-parameter with time during MB2 crystallisation; Top left, top right, bottom left: Profiles at 120, 110 and 90°C respectively; Bottom left: All previous plots on the same axis



The  $\beta$  parameter remains relatively constant with only slight decreases observed as the reaction progresses. It increases with temperature. The  $\beta$  parameter in relates monoclinic unit cell is angle between the  $a$ -axis and  $c$ -axis. This is supported by the observation that the increase in the  $\beta$  angle with temperature is seemingly proportional to the change in temperature – the difference in the  $\beta$  parameter between 110 and 120°C is approximately half that of the difference between 90 and 110°C, likely due to the lengthening of the Yb-O bonds.

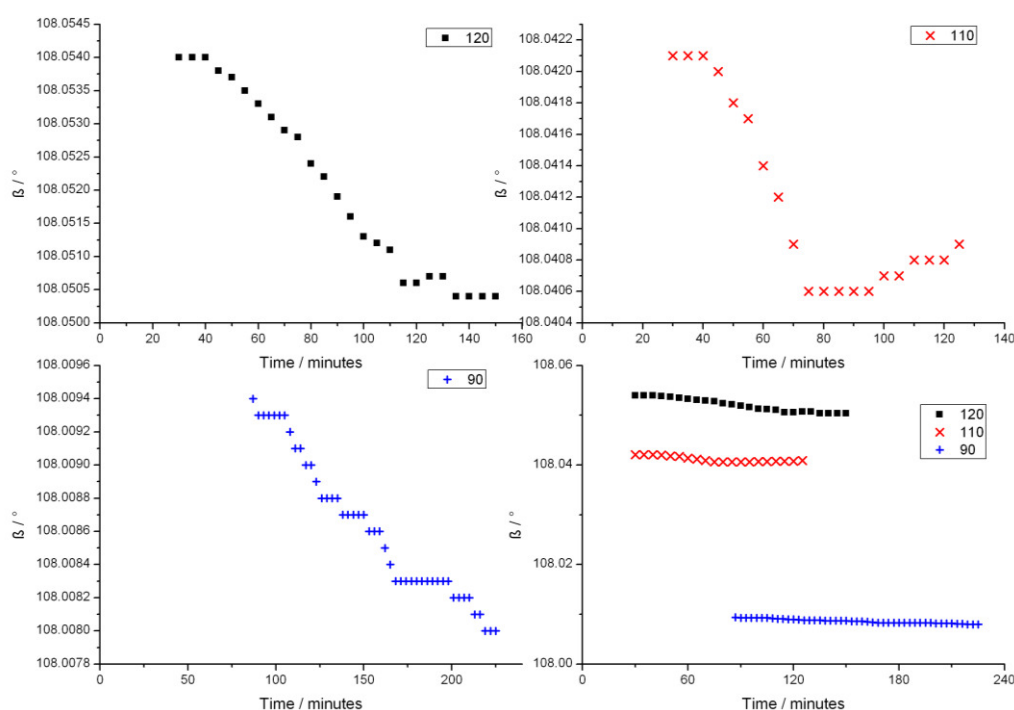


Figure 5.3.9: Evolution of  $\beta$  with time during MB2 crystallisation; Top left, top right, bottom left: Profiles at 120, 110 and 90°C respectively; Bottom left: All previous plots on the same axis

The unit cell volume slightly increases in the cases of 110 and 120 °C as the reactions progresses whereas the crystallisation at 90 °C shows a larger decrease. The differing volume changes seems irrational at first since the other unit cell parameters all seem to change in the same manner between temperatures; it stands to reason that the unit cell volume should change in the same manner. This assumption would only be correct if the relationship between changes in the unit cell parameter were all proportional

to changes in temperature. If one parameter changed faster than the others then the overall effect on the volume could lead to a non-linear relationship between temperature and volume.

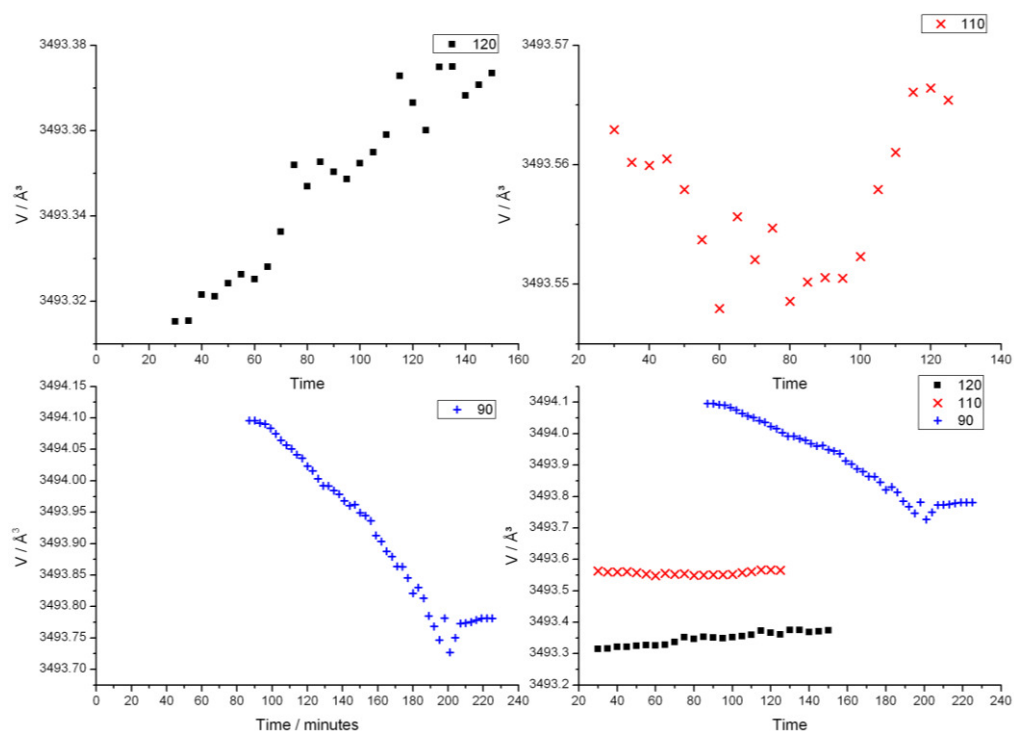


Figure 5.3.10: Evolution of unit cell volume with time during MB2 crystallisation; Top left, top right, bottom left: Profiles at 120, 110 and 90°C respectively; Bottom left: All previous plots on the same axis

### 5.3.2. *Ex Situ* Study

In order to determine whether the changes in the unit cell parameters were real and not artefacts of the refinement process, *ex situ* studies of the crystallisation of MB2 were performed. To mimic the reaction conditions present in the experimental set-up at JEEP, reactions were performed in the PEEK vessels placed into an oil bath at the reaction temperature of 120 °C. Although the rapid heating rate provided by ODISC could not be replicated, the narrow thickness of the PEEK vessels should ensure that reaction temperatures are quickly reached. The contents of these reaction tubes were agitated

using a magnetic follower and 'quenched' by removing from the oil bath after a set time (60, 90, 120 minutes) and cooled in air. This allowed investigation of the crystalline products at various stages of crystallisation on a similar timescale to those used for the *in situ* studies. The products could then be studied by XRD and their composition studied by TGA.

Profile refinement of the powder XRD (using monochromatic Cu K $\alpha$  radiation) collected for the reactions at 120 °C quenched at 60, 90 and 120 minutes show evolution of the unit cell parameters with time in a similar manner to those collected during the *in situ* studies (Figure 5.3.11a, b and c; Table 5.3.1). The cell parameters are smaller at room temperature than those collected during the *in situ* studies, as expected. The *a* length shows an increase at longer reactions whereas the *b* parameter shows a decrease. The *c* parameter remains roughly constant while the  $\beta$  angle decreases. This has the overall effect of the unit cell volume diminishing with longer reaction times. When compared to the final product *i.e.* the one synthesised conventionally after 20 hours, these trends continue (Figure 5.3.11d). This implies that the changes in the unit cell parameters seen in the *in situ* crystallisation studies are indeed actual effects and not artefacts of the refinement process.

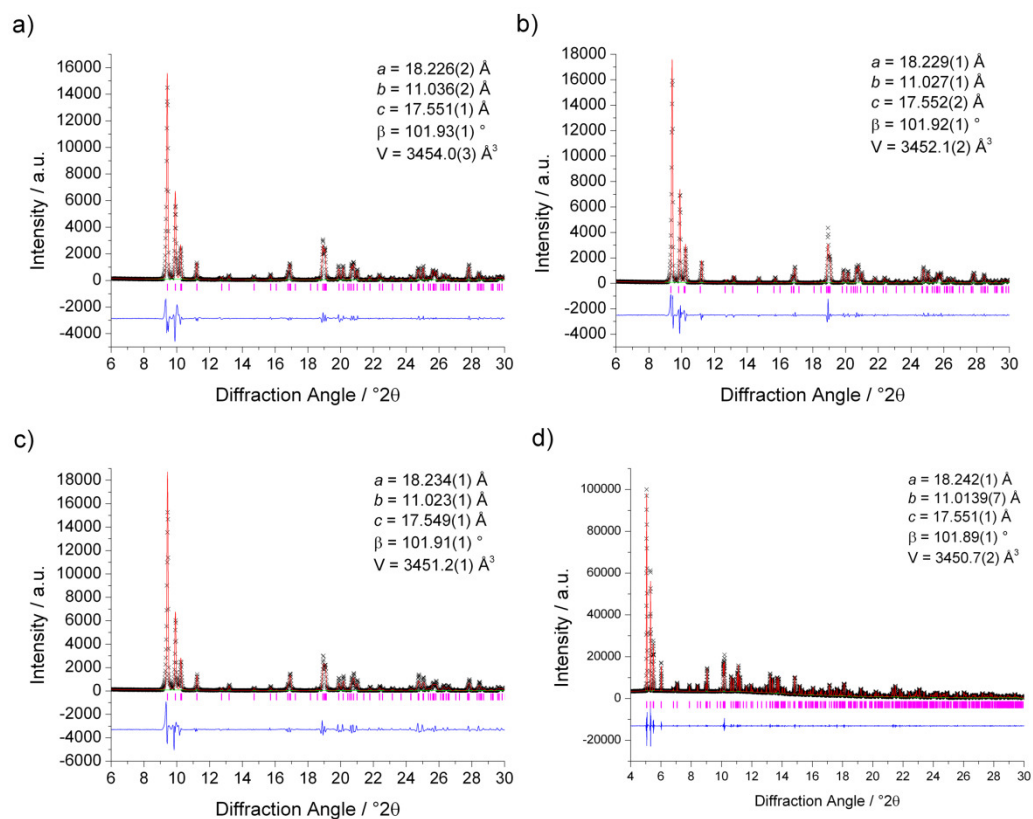


**Figure 5.3.11:** Profile fits of MB2 crystallisation products quenched after a) 60, b) 90 and c) 120 minutes; d) Profile fit of MB2 synthesised by conventional means. Refined crystallographic parameters included as inserts. Data for a), b) and c) were collected using laboratory XRD ( $\lambda = 1.5406 \text{ \AA}$ ). Data for d) were collected on Beamline I11 at Diamond ( $\lambda = 0.825174 \text{ \AA}$ ).

**Table 5.3.1: Refined lattice parameters for both *in situ* and *ex situ* crystallisation studies of MB2 synthesised at 120 °C. The lattice parameters of the final crystallisation product synthesised using a reaction time of 20 hours and those from the crystal structure (solved at 77 K) have been included as comparison**

Data Collection	Reaction Time / minutes	a / Å	b / Å	c / Å	$\beta$ / °	v / Å <sup>3</sup>
<i>In Situ</i>	60	18.546(2)	10.816(4)	18.315(5)	108.05(3)	3493.2(2)
<i>In Situ</i>	90	18.547(3)	10.816(2)	18.316(4)	108.05(1)	3493.3(2)
<i>In Situ</i>	120	18.547(2)	10.815(3)	18.316(7)	108.05(3)	3493.4(3)
<i>In Situ</i>	150	18.549(5)	10.815(2)	18.316(8)	108.05(4)	3493.6(2)
<i>In Situ</i>	After cooling	18.205(4)	10.978(1)	17.501(1)	101.93(5)	3422.1(3)
<i>Ex Situ</i>	60	18.226(2)	11.036(2)	17.551(1)	101.93(1)	3454.0(3)
<i>Ex Situ</i>	90	18.229(1)	11.027(1)	17.552(2)	101.92(1)	3452.1(2)
<i>Ex Situ</i>	120	18.234(1)	11.023(1)	17.549(1)	101.91(1)	3451.2(1)
<i>Ex Situ</i>	2400	18.244(1)	11.0139(7)	17.551(1)	101.89(1)	3450.7(2)
Crystal Structure	--	18.2950(4)	10.8482(2)	17.3984(4)	101.395(2)	3385.0(1)

Although XRD allowed us to determine that there was structural evolution during crystallisation, it gave few clues to the cause of this effect. Possible reasons include relaxation of the crystal structure allowed by reorientation of the ligands or by changes to the composition of the material. Changes of the amount of water or DMF incorporated into the material may to explain the crystallographic changes.

Thermogravimetric analysis of the quenched materials displayed the same characteristic losses as MB2 (described in Chapter 4) seen at 85, 200, 300 and 600 °C (Figure 5.3.12 main). Although losses are seen at similar temperatures, with loss of extra-framework water seen first at 85 °C, large differences in the size of the second and third mass losses are seen. This corresponds to the loss of DMF in MB2 synthesised by conventional means (see previous chapter). Since the weight percentage after the third loss is close to and roughly consistent to that of Yb<sub>2</sub>(BDC)<sub>3</sub> (measured ~83.6 %, calc: 83.5 %), it can be assumed that the differences between the second and third weight loss must be related to that of the loss of coordinated solvent and not due to impurities. Furthermore, the changes in mass loss follow at trend with the time of reaction used.

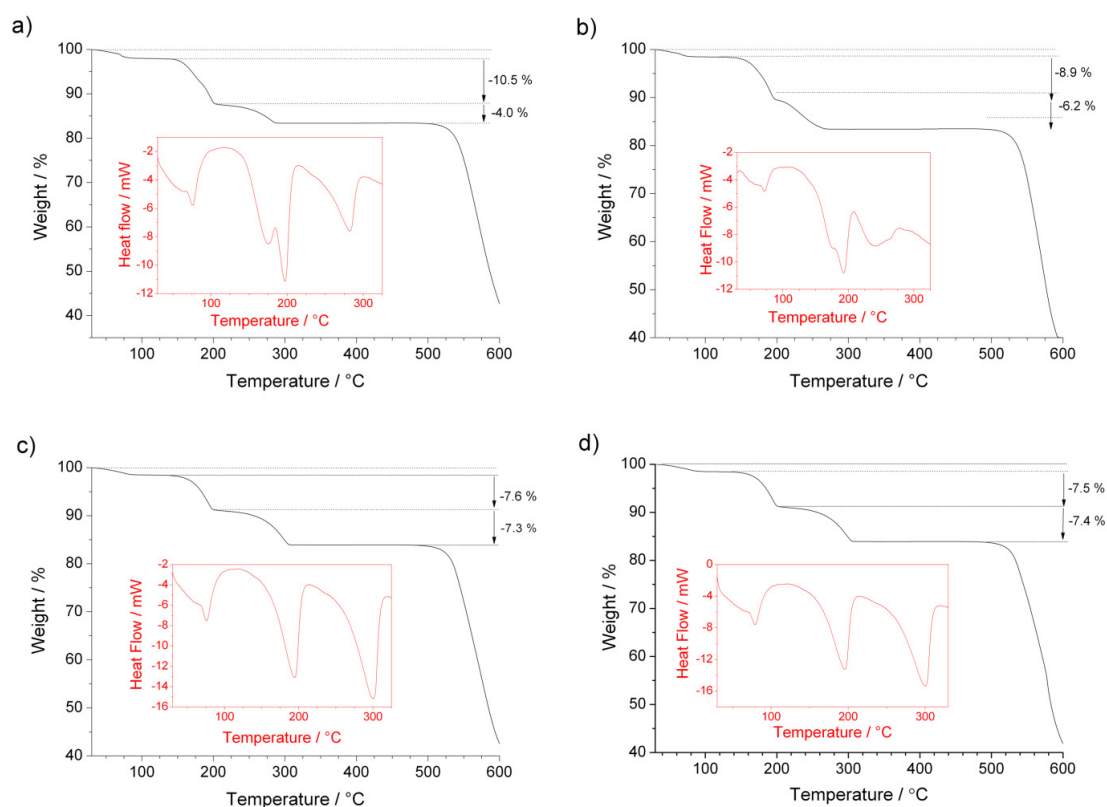


**Figure 5.3.12:** Main: TGA of MB2 crystallisation products after quenching after a) 60, b) 90, c) 120 minutes and d) final product after 20 hours; Inserts: DSC curves over temperature range 30 to 325 °C showing loss of water and DMF

The ratios of the second and third masses losses are 78:28, 59:41 and 51:49 for quenching times of 60, 90 and 120 minutes, respectively. Seeing as the ratio of these losses in the conventionally synthesised MB2 are almost 1:1 as found in the crystal structure, it can be proposed that the differences in these losses can be accounted to something coordinating in place of DMF in the material. Since the only other solvent present is water, partial substitution of DMF for water appears likely. Substitution of DMF for water has been observed for thulium analogues sharing the same connectivity as MB2.<sup>21</sup>

$[\text{Tm}_2(\text{BDC})_3(\text{H}_2\text{O})(\text{DMF})]\cdot\text{DMF}\cdot\text{H}_2\text{O}$  exhibits 50% substitution of DMF for water with channels partially occupied by either water or DMF whereas the fully water-substituted  $[\text{Tm}_2(\text{BDC})_3(\text{H}_2\text{O})_2]\cdot\text{DMF}\cdot 2\text{C}_2\text{H}_5\text{OH}\cdot 4\text{H}_2\text{O}$  contains channels occupied by a range of solvent molecules. The substitution of DMF for water in these materials has the effect of increasing the accessible pore volume for extra-framework solvent, as shown by the second example

in which ethanol fills the space occupied by DMF. This idea explains why although the mass difference between coordinated water and DMF is large and hence should show distinct differences in the total mass loss for the loss of coordinated solvent *i.e.* the second and third losses seen by TGA, no large inconsistencies are actually seen due to the incorporation of extra-solvent into the framework since the mass of one coordinated DMF and one extra-framework water is equivalent to the opposite case. Indeed, this is aptly shown in the example of  $[\text{Ti}_2(\text{BDC})_3(\text{H}_2\text{O})(\text{DMF})]\cdot\text{DMF}\cdot\text{H}_2\text{O}$  where the effective exchange of coordinated DMF for extra-framework DMF has occurred whilst maintaining the same overall mass.

Further evidence for partial water substitution is given in the DSC curves (Figure 5.3.12 inserts). In the DSC curve for the sample quenched at 60 minutes, there are four distinct troughs whereas the product quenched at 120 minutes only has three, as is seen in the curve for MB2 synthesised by conventional methods. The central two troughs in the DSC curve for the sample quenched at 90 minutes appear two have almost merged. From the DSC curve seen for conventional MB2, the first and last trough can be assigned to loss of extra-framework solvent and the final DMF respectively. The splitting of the trough in the 60 and 90 minutes cases seems to imply that two distinct solvent loss events – consistent with partial substitution of the DMF. The fact that these two events appear to merge into one as the reaction progresses supports the notion that the water is being replaced by DMF as the reaction progresses.

The substitution of DMF for water during the early crystallisation of MB2 helps to explain several aspects of the synthesis. Using solely DMF as the reaction solvent, only a poorly crystalline as yet unknown material is synthesised. Only with addition of water to the synthesis can crystalline MB2 be formed in high yield. An explanation for the presence of water in MB2 early in the crystallisation process may be due to the formation of the

partially water-substituted MB2 as the kinetic product of the reaction, converting to the more thermodynamically stable DMF-coordinated product over time.

#### 5.4. Crystallisation of MB3 - $[\text{Yb}_2(\text{BDC})_3(\text{DMF})_2(\text{H}_2\text{O})_2]$

As with MB2, crystallisation of MB3 was followed *in situ* using reaction temperatures of 120, 110, 100 and 90°C. In a typical reaction,  $\text{YbCl}_3 \cdot 6\text{H}_2\text{O}$  (0.4 g, 0.001 mol) and terephthalic acid (0.25 g, 0.0015 mol) were dissolved in DMF (2.5 ml) before addition of water (2.5 ml). Initially, Bragg peaks corresponding to terephthalic acid are observed as shown in Figure 5.4.1. This is due to the poor solubility of terephthalic acid in the DMF-water reaction solvent. As the reaction vessel heats up, these peaks disappear after around 20 minutes indicating that all of the reactants have dissolved. No intermediary products are observed with direct formation of MB3 observed. The Bragg peaks of the product seem to occur at the same point regardless of the temperature used.

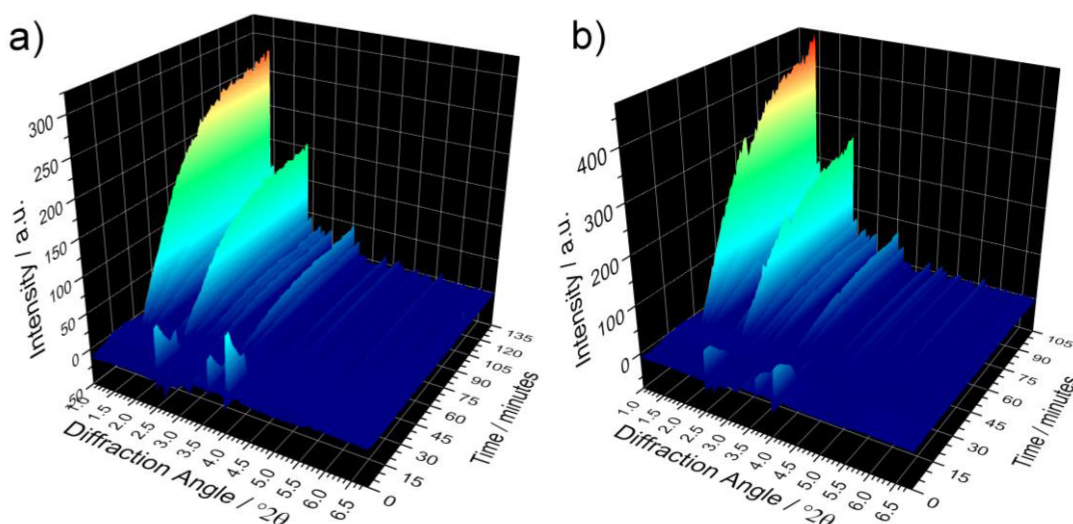


Figure 5.4.1: 3-D time-resolved diffraction plot of MB3 synthesis at a) 110 °C and b) 120°C. Reactions at 90 and 100 °C have not been shown due to discrepancies in the data (see Figure 5.4.3)

Unlike MB2 where discrepancies between the room and reaction temperature XRD patterns were observed, the XRD patterns of MB3 at each temperature correspond well with those of the crystal structure of MB3 using the *P1* spacegroup. When comparing the



lattice parameters of the reactions at the different temperatures at their furthest point of crystallisation, the lattice parameters generally show decrease with temperature leading to an overall decrease in the unit volume. Similar negative thermal expansion trends were also seen for MB2.

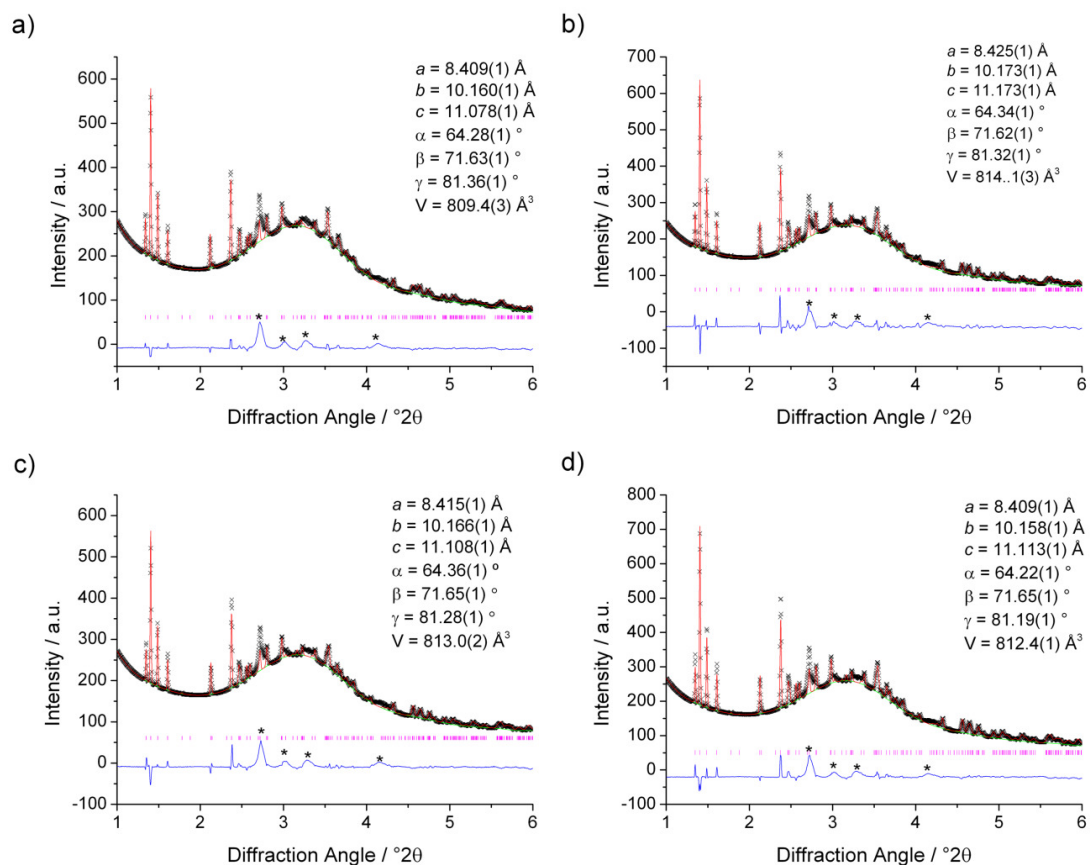


Figure 5.4.2: Profile fits of PXRD patterns of MB3 taken at a) 90 °C, b) 100 °C, c) 110 °C and d) 120 °C taken *in situ* ( $\lambda = 0.2242 \text{ \AA}$ ) with refined parameters. Materials crystallise in the  $P\bar{1}$  spacegroup. Asterisks in the difference line denote regions where diffraction peaks from the PEEK sample holder are found.

The crystallisations at 90 and 100 °C show a very different shaped extent of crystallisation curves (Figure 5.4.3). Since only the crystallisations performed at 110 and 120 °C display characteristic crystallisation progression, only the results from crystallisations at these two temperatures shall be discussed.

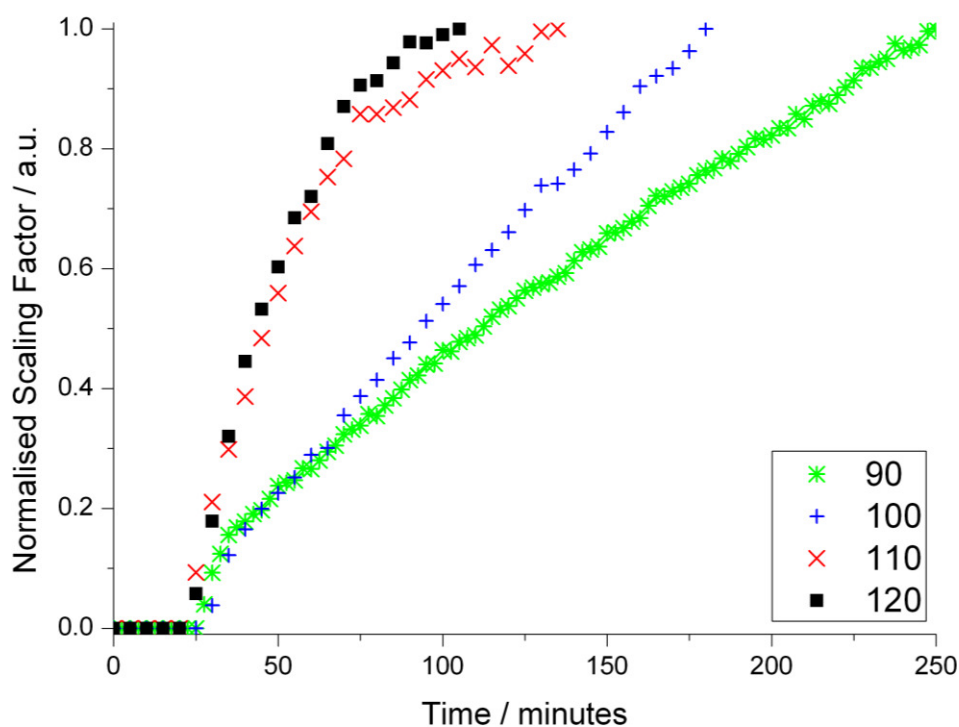


Figure 5.4.3: Plot of scaling factor against time for MB3 synthesis at various temperatures

The  $a$ -parameter initially increases and then decreases as the reaction progresses (Figure 5.4.4). The  $a$ -parameter also decreases as the temperature is increased from 100 to 120 °C. The  $b$ -parameter decreases as the reaction progresses although an increase at towards the end of the reaction is seen for both temperatures (Figure 5.4.5). The  $b$ -parameter also decreases with temperature. The  $c$ -parameter increases as the reaction progresses and begins to decrease as the reaction nears completion (Figure 5.4.6). The  $c$ -parameter also decreases with temperature.

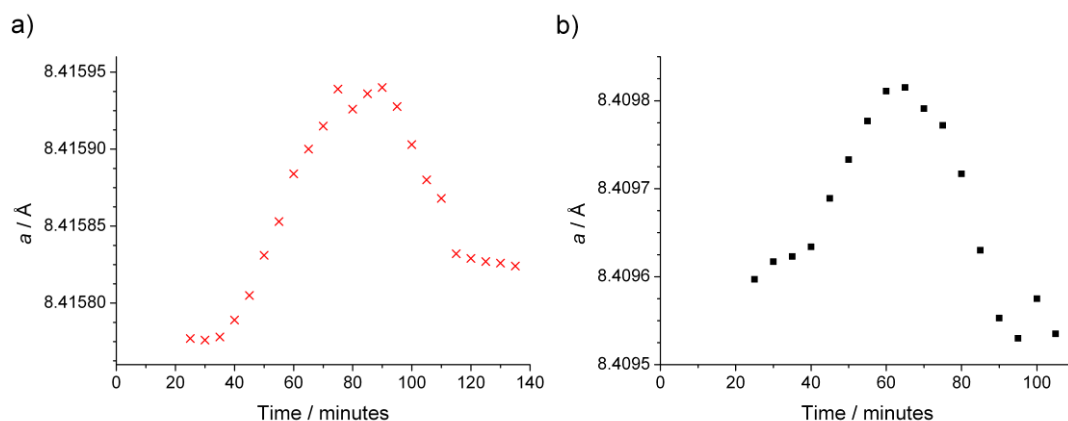


Figure 5.4.4: Evolution of the  $a$ -parameter with time during crystallisation of MB3 at a) 110 °C and b) 120 °C

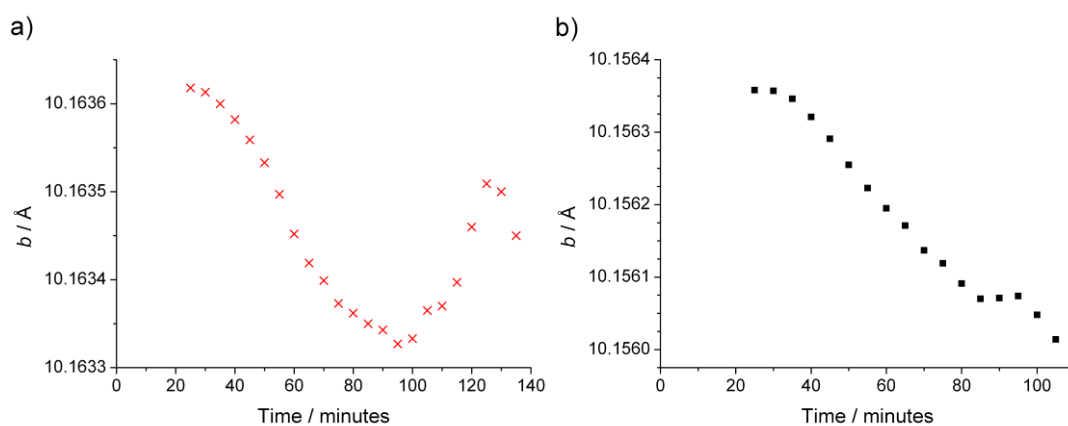


Figure 5.4.5: Evolution of the  $b$ -parameter with time during crystallisation of MB3 at a) 110 °C and b) 120 °C

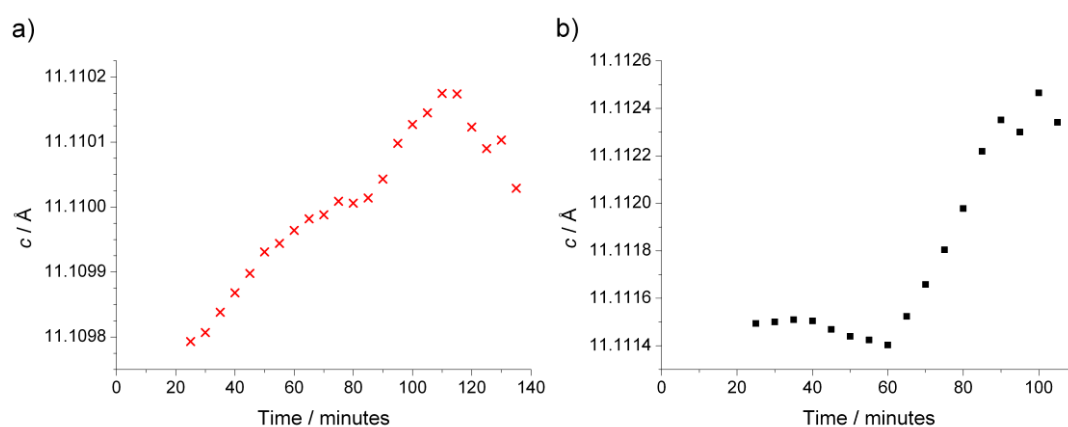


Figure 5.4.6: Evolution of the  $c$ -parameter with time during crystallisation of MB3 at a) 110 °C and b) 120 °C

The  $\alpha$  and  $\beta$  angles both increase with temperature whereas the  $\gamma$  angle decreases (Figure 5.4.7, Figure 5.4.8 and Figure 5.4.9). The angles remain roughly constant as the reaction progresses – most increases and decreases are within the range of 0.001 °. The

unit cell volume decreases with temperature with no clear relationship between time and unit cell volume (Figure 5.4.10). At present, there is no obvious explanation for the trends observed.

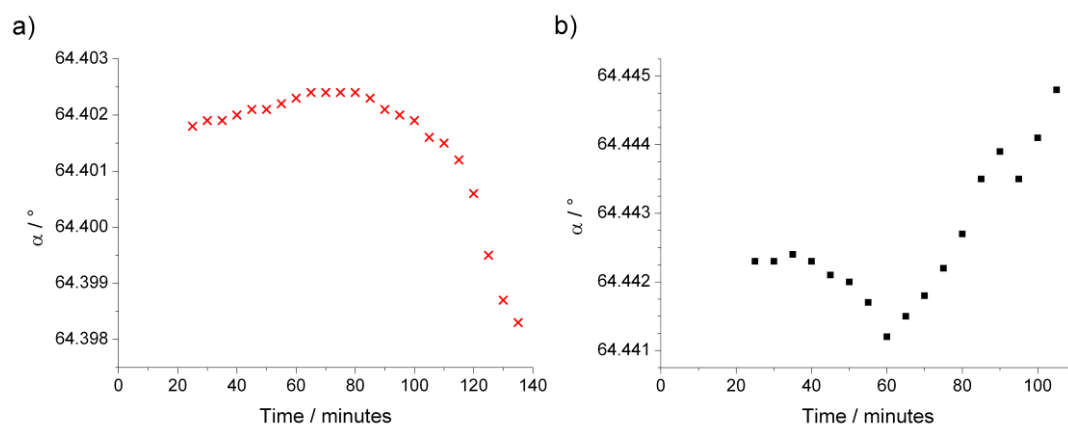


Figure 5.4.7: Evolution of  $\alpha$  with time during crystallisation of MB3 at a) 110 °C and b) 120 °C

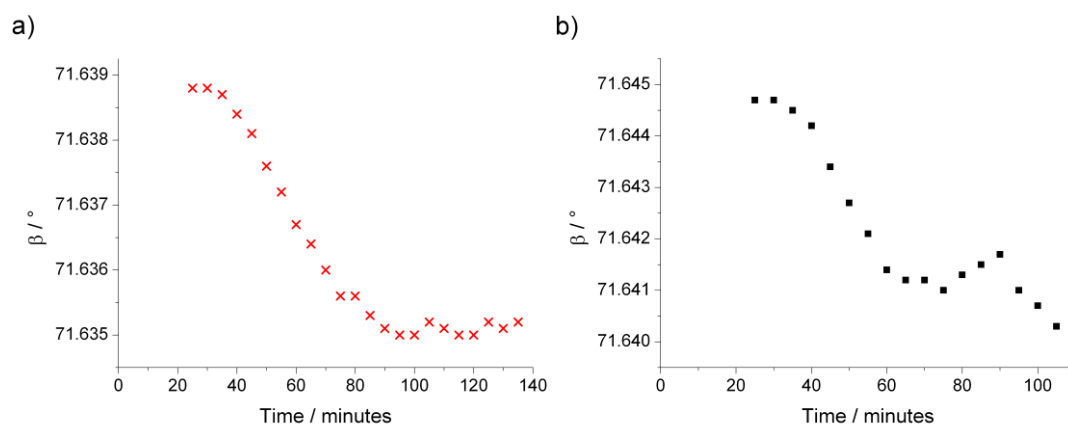


Figure 5.4.8: Evolution of  $\beta$  with time during crystallisation of MB3 at a) 110 °C and b) 120 °C

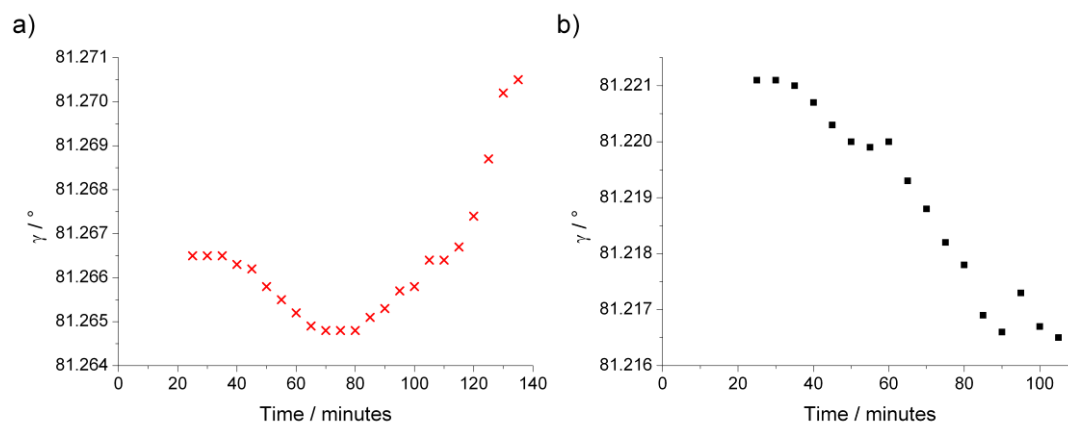


Figure 5.4.9: Evolution of  $\gamma$  with time during crystallisation of MB3 at a) 110 °C and b) 120 °C

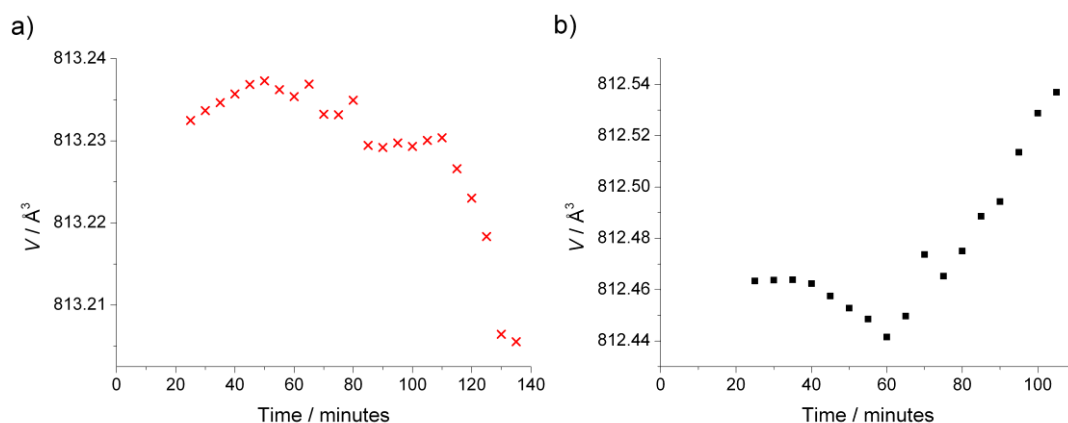


Figure 5.4.10: Evolution of the unit cell volume with time during crystallisation of MB3 at a) 110 °C and b) 120 °C

## 5.5. Crystallisation of interpenetrated MOF-5

### 5.5.1. MOF-5 and its interpenetrated form

MOF-5 or  $Zn_4O(BDC)_3$  was first synthesised by the Yaghi group.<sup>22</sup> MOF-5 crystallises in the  $Fm3m$  spacegroup and consists of 6-connected  $Zn_4O$  clusters linked by the benzenedicarboxylate linkers (Figure 5.5.1). This leads to a cubic 6-connected net system with large voids in the pores. The free space in the structure is initially occupied by solvent residual from the synthesis but this can easily be removed by heating to form a fully evacuated structure around 80 % of the structure existing as free space.<sup>23</sup>

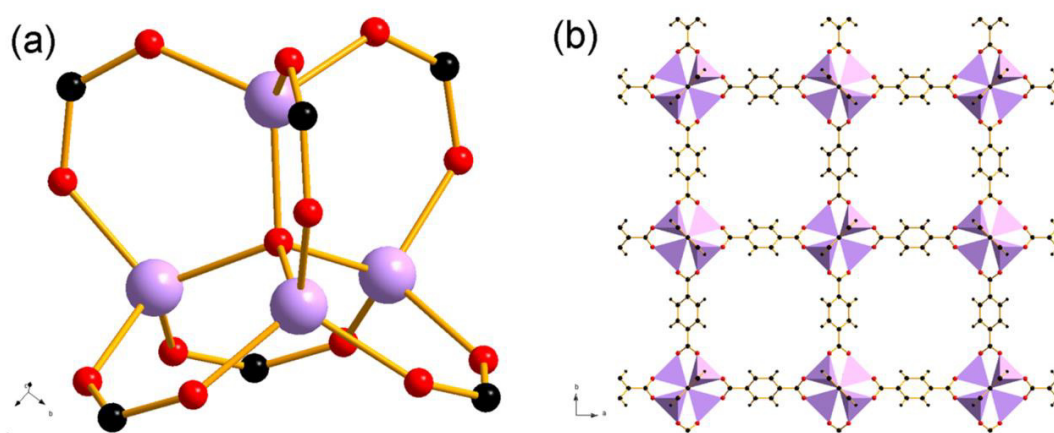


Figure 5.5.1: (a):  $Zn_4O$  cluster; (b): Crystal structure of MOF-5. Lilac atoms / polyhedra: zinc; black spheres: carbon; red spheres: oxygen; white spheres: hydrogen

Owing to the large amounts of free space within the structure of MOF-5, the co-formation of an interpenetrated MOF-5 phase is often observed, Figure 5.5.2.<sup>24</sup> Phase-pure interpenetrated MOF-5 (MOF-5int) was synthesised by Kim *et al.* by the addition of melamine to the synthesis.<sup>25</sup> Since melamine is not present in the final structure, it can be deduced that it does not act as a templating agent but to merely lower the overall pH; an effect that has also been seen for other bulky weak organic bases such as aniline and 2,4,6-tris(4-pyridyl)-1,3,5-triazine.<sup>25</sup>

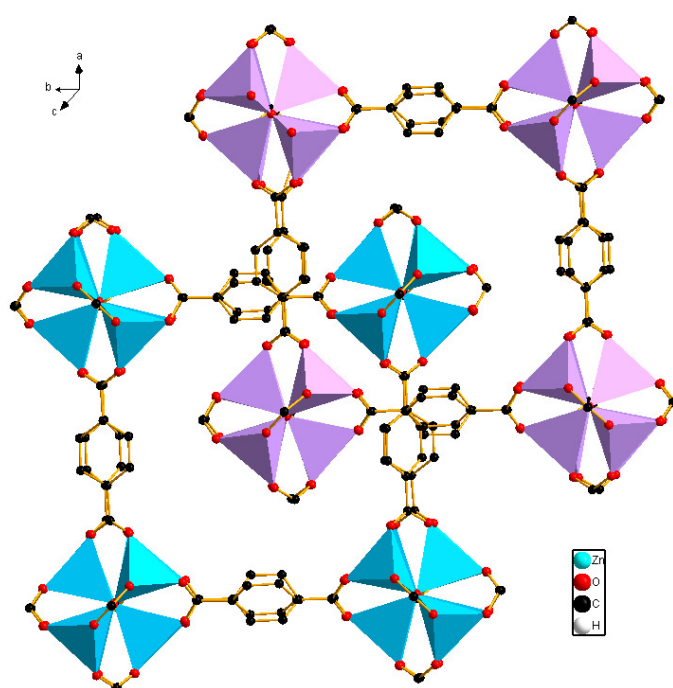


Figure 5.5.2: Crystal structure of interpenetrated MOF-5, MOF-5int. The two interpenetrated nets are given by purple or turquoise polyhedra

The formation of an interpenetrated structure for MOF-5 has beneficial effects for certain applications. Although large amounts of the free space are lost with a reduction in total surface area from 4400 to 1130 m<sup>2</sup>g<sup>-1</sup> seen, a doubling of potential absorption sites is achieved. This has the effect of increasing the gravimetric hydrogen uptake by 54 % and a tripling of the volumetric uptake due to the increased density.<sup>25</sup>

Although the crystallisation of non-interpenetrated MOF-5 has been investigated using AFM,<sup>26</sup> quenching<sup>27</sup> and SANS,<sup>28</sup> the crystallisation of interpenetrated MOF-5 has not been investigated in detail. There are three possible scenarios for the formation of MOF-5int. The first is direct formation of MOF-5int from solution with the second being crystallisation of one MOF-5 cubic net followed by a second intercalated net. The third would be formation of an intermediary product, similar to the formation of MIL-53(Fe) from MOF-235.<sup>29</sup> The formation of an intermediary product in the synthesis of non-interpenetrated MOF-5 was observed by Hausdorf *et al.* where MOF-69c ( $[\text{Zn}_3(\text{OH})_2(\text{BDC})_2]\cdot 2\text{DEF}$ ) was found to form initially which underwent redissolution and eventual formation of MOF-5 was seen.<sup>30</sup> In this section how MOF-5int crystallises is considered, using both *ex situ* and *in situ* studies.

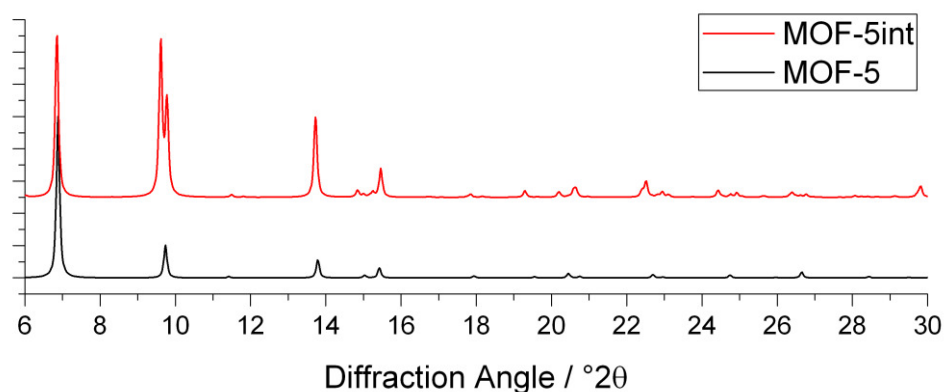


Figure 5.5.3: Comparison of the PXRD patterns of MOF-5 and its interpenetrated form. Patterns have been simulated from crystal structures

### 5.5.2. Synthesis of MOF-5int

To investigate the synthesis of MOF-5int, reactions were first studied in the laboratory, performed in glass screw-top culture tubes, heated in an oil bath to 110 °C. This had the advantages of being able to determine the onset of crystallisation by eye, impossible when using conventional steel autoclaves, and to allow agitation of the reactants with a magnetic follower, similar to the conditions that would be used in the *in situ* experiments. The ratio of the reactants used was the same as in the initial paper by

Kim *et al.* with the exception of the amount of DMF used.<sup>25</sup> In a typical reaction,  $\text{Zn}(\text{NO}_3)_2 \cdot 6\text{H}_2\text{O}$  (0.6 g, 2.0 mmol),  $\text{H}_2\text{BDC}$  (0.125 g, 0.75 mmol) and melamine (0.050g, 0.38 mmol) were dissolved in DMF (5 ml) and the reactants heated to 110 °C.

The reaction mixture showed initial signs of change after around 30 minutes in the form of a white precipitate. As the reaction progressed, this white precipitate redissolved into the reaction solvent, and has completely disappeared after around four hours. The reaction mixture remained clear until it was cooled, upon which a second white precipitate formed. The first and the second precipitates were collected after 3 and 20 hours respectively, and their crystallinity investigated by powder XRD (Figure 5.5.4).

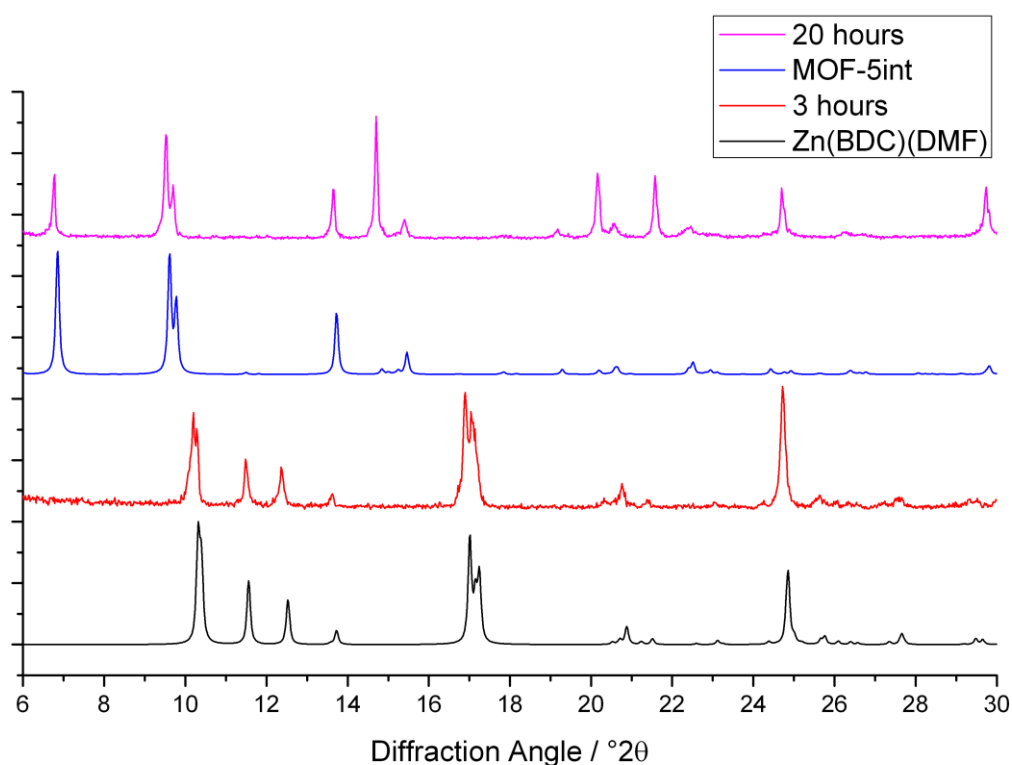


**Figure 5.5.4: PXRD patterns of the two precipitates and the simulated PXRD patterns of MOF-5int and  $\text{Zn}(\text{BDC})(\text{DMF})$  from their crystal structures**

The comparison of the powder XRD patterns of the precipitates yields several interesting results. The first point of notice is that the XRD pattern of the first precipitate, collected after 3 hours, does not match that of MOF-5int. Comparison of the pattern with



those of known zinc benzenedicarboxylate materials allowed determination of the material to be that of Zn(BDC)(DMF) (Figure 5.5.5).<sup>31</sup> This phase is not the same as the MOF-69c intermediary product phase seen by McKinstry *et al.* during MOF-5 synthesis,<sup>27</sup> suggesting clear differences between the synthesis of the non-interpenetrated and interpenetrated forms. The second point of notice is the formation of MOF-5int after 20 hours of reaction time upon cooling. This is unusual behaviour – many other MOFs crystallise from solution at reaction temperature, as based on the *in situ* diffraction studies reported so far,<sup>8,32,33</sup> as was seen for MB2 and MB3. The initial formation and subsequent disappearance of Zn(BDC)(DMF) followed by the formation of MOF-5int upon cooling a clear solution made this reaction an interesting candidate for *in situ* crystallisation studies.

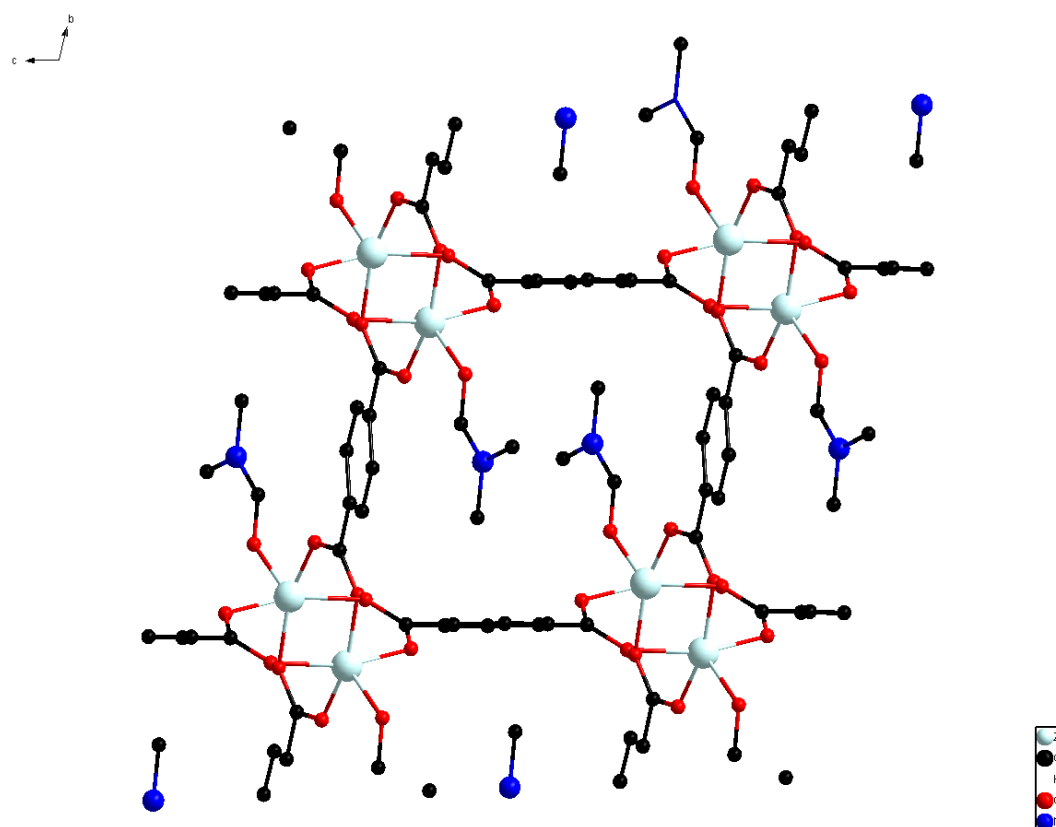
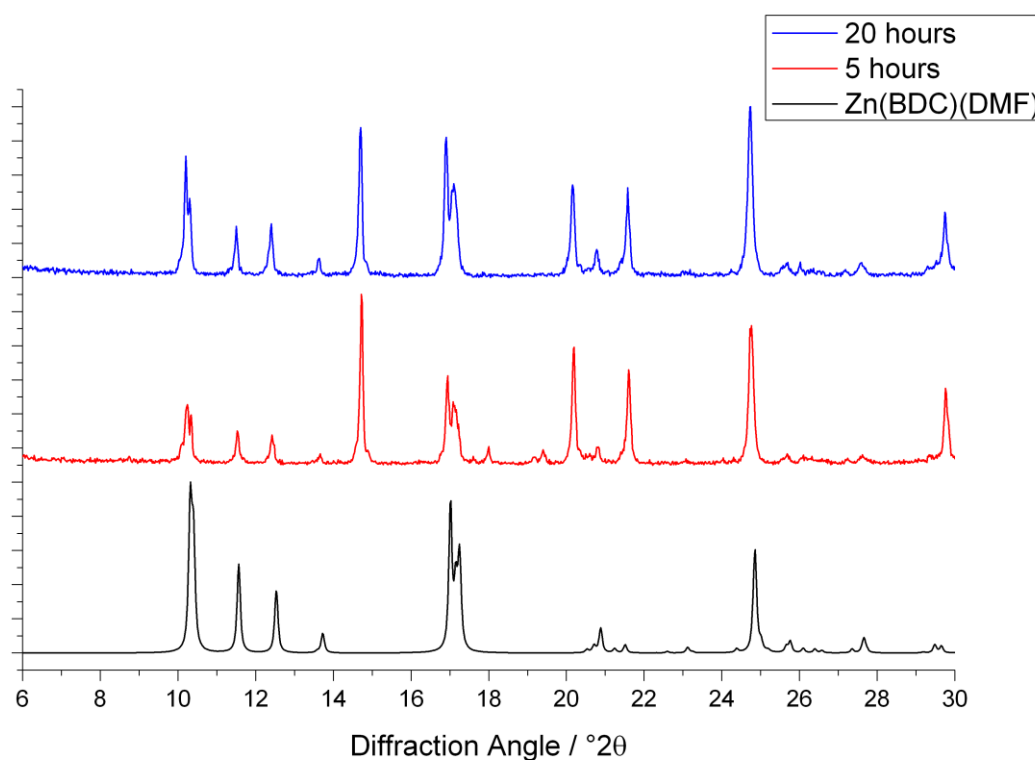


Figure 5.5.5: Crystal Structure of Zn(BDC)(DMF)

Not using melamine in the reaction mixture lead to the formation of mainly Zn(BDC)(DMF) as the initial precipitate with no subsequent re-dissolution (Figure 5.5.6),

and the product after 20 hours is still the same phase. Peaks seen at 14.7 and 29.8 °2 $\theta$  denote the presence of small amounts of unreacted terephthalic acid as an impurity. The formation of Zn(BDC)(DMF) over that of non-interpenetrated MOF-5 may be due to the reaction solvent used; DMF was used instead of DEF, which is usually used to crystallise MOF-5. .



**Figure 5.5.6: PXRD patterns of the products formed in the absence of melamine. Simulated PXRD pattern of Zn(BDC)(DMF) included for comparison**

The presence of melamine is required for the formation of MOF-5<sup>int</sup> and its removal does not lead to the formation of the non-interpenetrated form.<sup>25</sup> The synthesis of MOF-5 requires the addition of triethylamine to the reaction mixture.<sup>22</sup> This would imply that the dissolution of Zn(BDC)(DMF) requires the presence of an organic base. The formation of MOF-5 over its interpenetrated form could be affected by the size or the strength of the organic base used. Further work would be required to confirm this.

### 5.5.3. An *In Situ* Study of MOF-5<sub>int</sub> Crystallisation

Similar to the crystallisation studies of MB2 and MB3, MOF-5<sub>int</sub> crystallisation was followed *in situ* using ODISC on Beamline I12 at Diamond. Unlike the methodology used previously for MB2 and MB3, the PEEK reaction vessel was replaced with a steel autoclave. This was to remove problems with agitation of the precipitate via stirring in the PEEK tubes – the magnetic follower used in the PEEK tubes was insufficiently sized to promote enough of the solid into the path of the X-ray source. Using the steel autoclave allowed for use of a larger follower which alleviated the agitation problem but led to reduced intensity and the appearance of diffraction peaks from steel in the data collected.

Since the steel autoclave has a higher capacity (15 ml), reagent quantities were tripled to accommodate this, but concentrations were kept the same as in the smaller-scale reactions. The reactants were heated to 120 °C with the autoclave reaching reaction temperature after around 20 minutes as evidenced by the probe thermocouple.

Evidence of the first precipitate seen in the laboratory experiments is seen as diffraction peaks emerge after 50 minutes. These peaks continue to increase in intensity until 160 minutes and then begin to decrease before having completely disappeared after around 220 minutes (Figure 5.5.7). This corresponds well to the observations made in the clear glass reaction vessels.

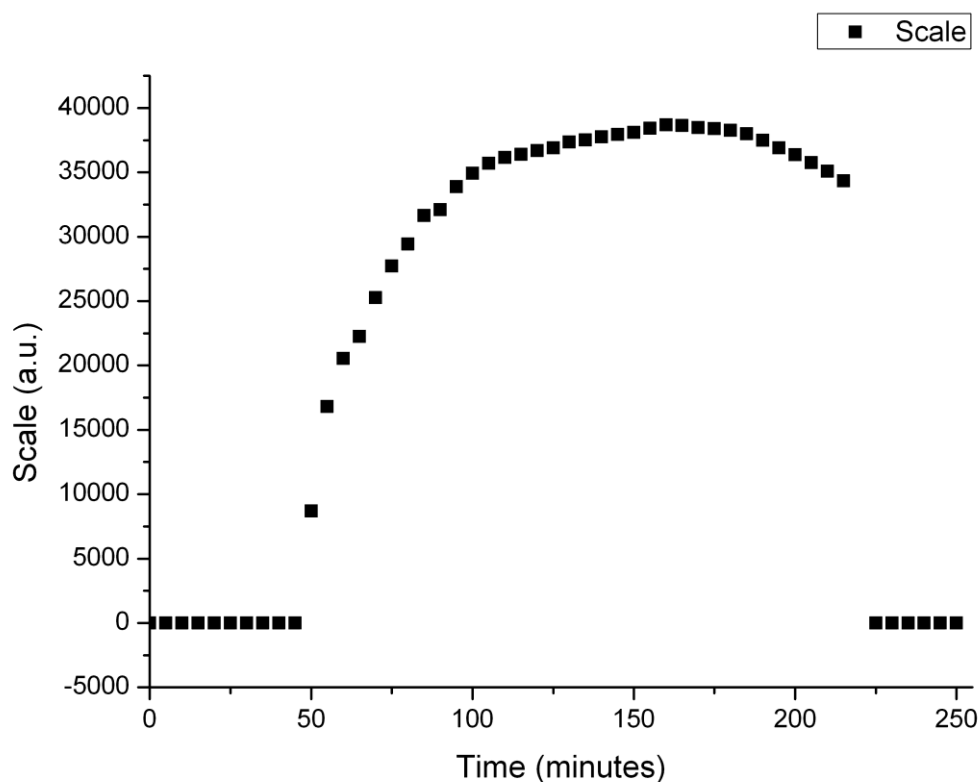


Figure 5.5.7: Plot of scale factor against time for the crystallisation of MOF-5int at 120 °C, profiled using the  $P2_1/c$  spacegroup

A comparison of the diffraction patterns taken at reaction temperature with those of the potential expected products show clear differences – the precipitate formed at reaction temperature is clearly neither that of Zn(BDC)(DMF) nor that of MOF-5 or its interpenetrated form (Figure 5.5.8).

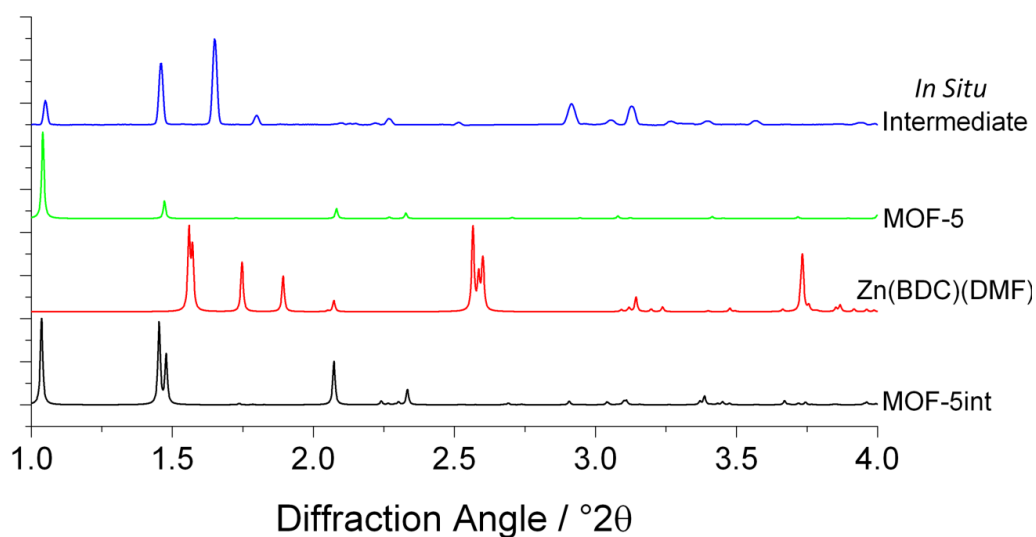


Figure 5.5.8: Comparison of the PXRD pattern of the intermediary product formed during MOF-5int synthesis at 120 °C with the simulated PXRD patterns of MOF-5, MOF-5int and Zn(BDC)(DMF). Data were collected on Beamline I12 at Diamond ( $\lambda = 0.2332 \text{ \AA}$ )

Attempts to profile the diffraction pattern of the intermediary product using the crystal structures of known zinc benzenedicarboxylates were partially successful with the  $P2_1/c$  spacegroup displaying the closest match (Figure 5.5.9). This spacegroup is shared by  $[\text{Zn}_3(\text{BDC})_3(\text{H}_2\text{O})_2] \cdot 4\text{DMF}$  which was used as a basis for refinement.<sup>31</sup> Although unit cell parameters can be extracted from the data, any further structural determination is difficult with the quality of the data. Further studies are required to both determine the structure of this intermediary product and to further understand the mechanism of the crystallisation of both MOF-5 and its interpenetrated form.

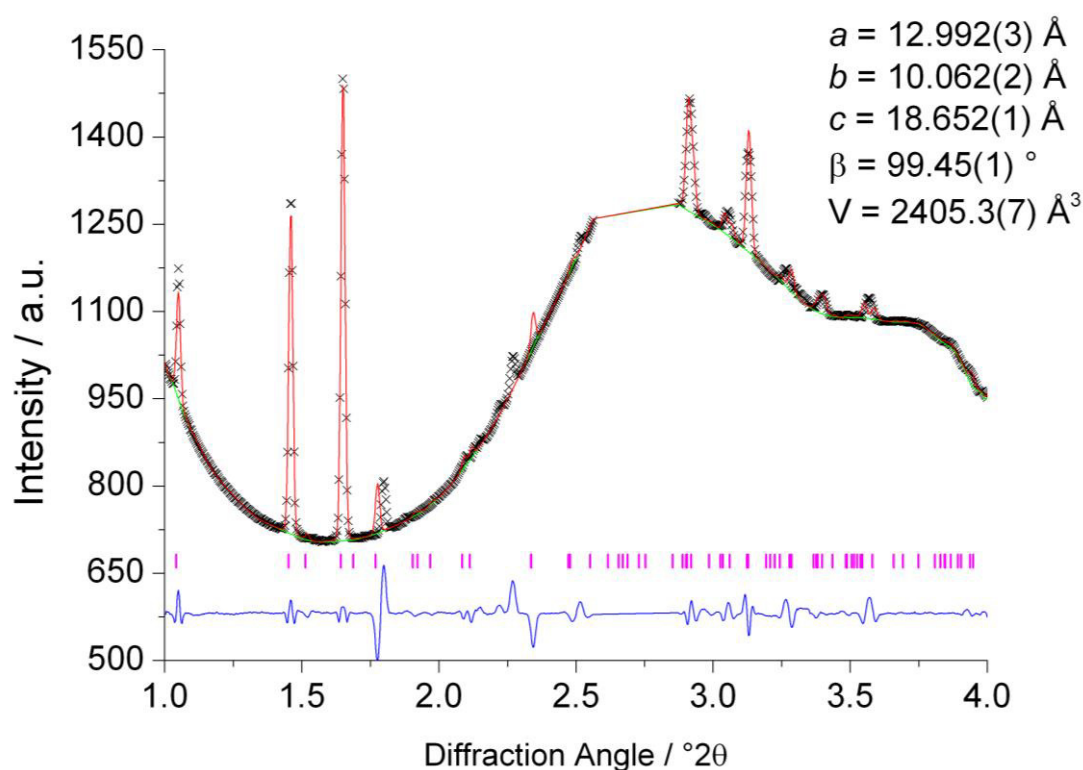


Figure 5.5.9: Profile fits of PXRD patterns of the intermediary product taken in situ at 120 °C ( $\lambda = 0.2332 \text{ \AA}$ ) with refined parameters. Material crystallises in the  $P2_1/c$  spacegroup

A proposed reaction scheme for the synthesis of MOF-5int is given in Figure 5.5.10. After an hour of heating, the as yet unidentified *in situ* intermediary product is formed at reaction temperatures. If the reaction is stopped at this point and cooled to room temperature, Zn(BDC)(DMF) can be isolated as the first product. If melamine is excluded from the reaction, this remains the sole product after longer reaction times. If both melamine and longer reaction times are used, the *in situ* intermediary product redissolves. Upon cooling after this point, MOF-5int is formed as the final product. The presence of MOF-69c as an intermediary phase during non-interpenetrated MOF-5 synthesis has been reported by McKinsty *et al.*, but this does not match the intermediary phase seen here.<sup>27</sup> An interesting aspect of both non- and interpenetrated syntheses of MOF-5 is that the  $\text{Zn}_4\text{O}$  clusters that form the secondary building units of these materials and those of its isorecticular analogues<sup>34</sup> are not present in the structures of MOF-69c or Zn(BDC)(DMF).

Indeed, this is similar to the synthesis of MIL-53(Fe) where the structurally dissimilar MOF-235 is found as an intermediary product.<sup>33</sup> The redissolution of these intermediary products may yield reactive species required to form the eventual final products, rather than the idea of having preformed building units in solution.

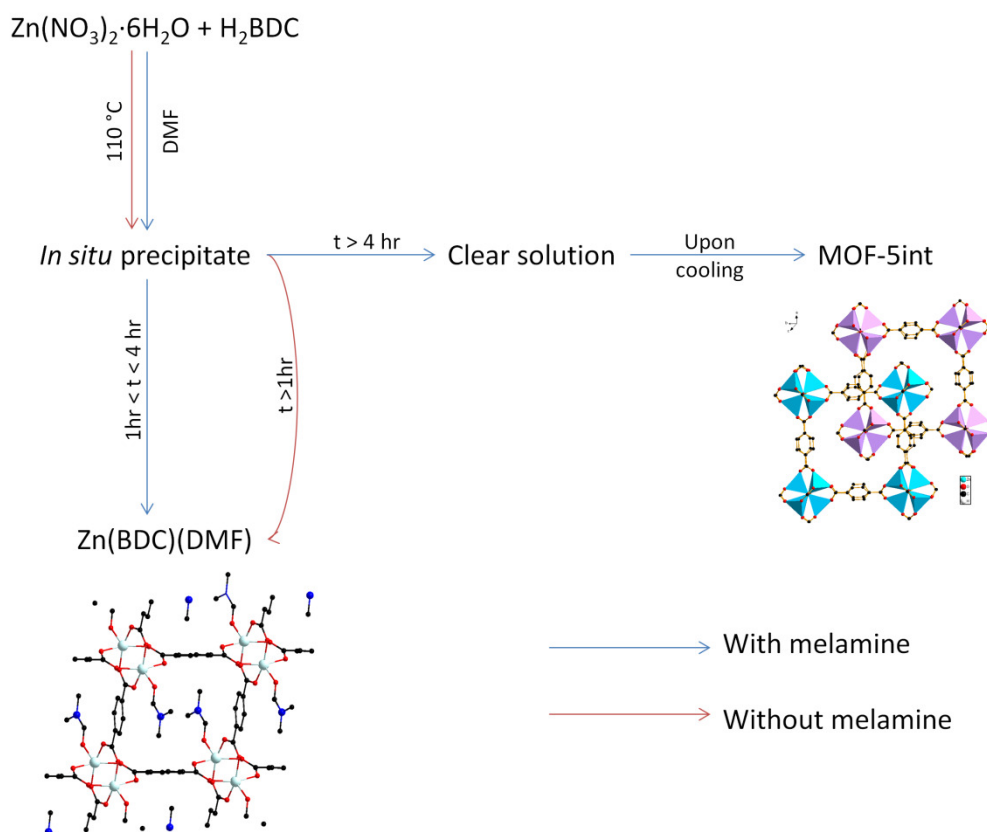


Figure 5.5.10: Reaction scheme for the synthesis of interpenetrated MOF-5

## 5.6. Summary

The crystallisation of MB2, MB3 and MOF-5int were studied both *in situ* and *ex situ*. The *in situ* investigation of the crystallisation of MB2 established that the crystal structure undergoes small changes as the crystallisation progressed. Changes in the unit cell parameters were also seen for the *ex situ* study of quenched MB2 crystallisation reactions and by using thermogravimetric analysis, clear differences were seen in the solvent loss profile suggesting differing compositions. These were accounted to varying amounts of

water and DMF in the materials. The coordination of water early in the crystallisation suggests the necessity of water in the synthesis, but this is replaced by DMF (present in excess) as the reaction proceeds. The *in situ* studies of MB3 crystallisation gave some information on structural evolution of the material but the data are inconclusive at present and more data would need to be recorded in the future. The work reported here is one of the first to make use of the ODISC cell and shows how structural information (in this case changing lattice parameters) can be measured under real reaction conditions. This is a significant advance over the previous low-resolution EDXRD work used to follow MOF crystallisation *in situ*, and it is hoped that the data would be of sufficiently quality to allow a full structure refinement to allow atomic positions to be determined. For the large volume low symmetry unit cell materials studied here this has not yet proved possible. The work is still a rare example of an *in situ* study of MOF crystallisation and more data must be measured from other materials to make systematic studies of MOF formation and to draw comparisons between the various materials in the literature.

*Ex situ* investigations of interpenetrated MOF-5 synthesis provided evidence of the existence of a crystalline intermediary product in the crystallisation. This intermediary product was formed as a precipitate that re-dissolves as the reaction progresses. MOF-5int was only formed when the reaction vessel was cooled after heating past the disappearance of the intermediary product. The intermediary product could be isolated by quenching and was determined to be Zn(BDC)(DMF); however, *in situ* studies ascertained that the intermediary product was not this material at the reaction temperatures. The preliminary results reported here suggest that further studies of the Zn<sup>2+</sup>-BDC-DMF system are needed, despite the large literature on MOF-5 and its variants.



## 5.7. References

- (1) Jensen, K. M. Ø.; Tyrsted, C.; Bremholm, M.; Iversen, B. B. *ChemSusChem* **2014**, *7*, 1594.
- (2) Sheikh, N. S.; Leonori, D.; Barker, G.; Firth, J. D.; Campos, K. R.; Meijer, A. J. H. M.; O'Brien, P.; Coldham, I. J. *Am. Chem. Soc.* **2012**, *134*, 5300.
- (3) Ou, J. Z.; Yaacob, M. H.; Breedon, M.; Zheng, H. D.; Campbell, J. L.; Latham, K.; Plessis, J. d.; Wlodarski, W.; Kalantar-zadeh, K. *Phys. Chem. Chem. Phys.* **2011**, *13*, 7330.
- (4) Miladinovic, Z. P.; Zakrzewska, J.; Kovacevic, B. T.; Miladinovic, J. M. *Microporous Mesoporous Mater.* **2014**, *195*, 131.
- (5) Zhou, Y.; Lin, Y.; Patzke, G. R. *Prog. Chem.* **2012**, *24*, 1583.
- (6) Yan, S.; Wu, Z.; Yu, H.; Gong, Y.; Tan, Y.; Du, R.; Chen, W.; Xing, X.; Mo, G.; Chen, Z.; Cai, Q.; Sun, D. *J. Phys. Chem. C* **2014**, *118*, 11454.
- (7) Philippot, G.; Jensen, K. M. O.; Christensen, M.; Elissalde, C.; Maglione, M.; Iversen, B. B.; Aymonier, C. *J. Supercrit. Fluids* **2014**, *87*, 111.
- (8) El Osta, R.; Feyand, M.; Stock, N.; Millange, F.; Walton, R. I. *Powder Diffraction* **2013**, *28*, S256.
- (9) Saha, D.; Jensen, K. M. O.; Tyrsted, C.; Bojesen, E. D.; Mamakhel, A. H.; Dippel, A.-C.; Christensen, M.; Iversen, B. B. *Angew. Chem. Int. Ed.* **2014**, *53*, 3667.
- (10) Garnier, E. *Acta Crystallog. Sect. A* **2009**, *65*, 51.
- (11) Scarlett, N. V. Y.; Madsen, I. C.; Evans, J. S. O.; Coelho, A. A.; McGregor, K.; Rowles, M.; Lanyon, M. R.; Urban, A. J. *J. Appl. Crystallogr.* **2009**, *42*, 502.
- (12) Moorhouse, S. J.; Vranješ, N.; Jupe, A.; Drakopoulos, M.; O'Hare, D. *Rev. Sci. Instrum.* **2012**, *83*.
- (13) Hammersley, A. P.; Svensson, S. O.; Hanfland, M.; Fitch, A. N.; Hausermann, D. *High Pressure Res.* **1996**, *14*, 235.
- (14) Toby, B. H. *J. Appl. Crystallogr.* **2001**, *34*, 210.
- (15) Haquin, V.; Gumy, F.; Daiguebonne, C.; Bunzli, J. C.; Guillou, O. *Eur. J. Inorg. Chem.* **2009**, 4491.
- (16) Chen, B.; Yang, Y.; Zapata, F.; Qian, G.; Luo, Y.; Zhang, J.; Lobkovsky, E. B. *Inorg. Chem.* **2006**, *45*, 8882.
- (17) Dubbeldam, D.; Walton, K. S.; Ellis, D. E.; Snurr, R. Q. *Angew. Chem. Int. Ed.* **2007**, *46*, 4496.
- (18) Han, S. S.; Goddard, W. A., III *J. Phys. Chem. C* **2007**, *111*, 15185.
- (19) Zhou, W.; Wu, H.; Yildirim, T.; Simpson, J. R.; Walker, A. R. H. *Phys. Rev. B* **2008**, *78*.
- (20) Lock, N.; Wu, Y.; Christensen, M.; Cameron, L. J.; Peterson, V. K.; Bridgeman, A. J.; Kepert, C. J.; Iversen, B. B. *J. Phys. Chem. C* **2010**, *114*, 16181.
- (21) He, H.; Ma, H.; Sun, D.; Zhang, L.; Wang, R.; Sun, D. *Cryst. Growth Des.* **2013**, *13*, 3154.
- (22) Li, H.; Eddaoudi, M.; O'Keeffe, M.; Yaghi, O. M. *Nature* **1999**, *402*, 276.
- (23) Eddaoudi, M.; Li, H.; Yaghi, O. M. *J. Am. Chem. Soc.* **2000**, *122*, 1391.
- (24) Hafizovic, J.; Bjørgen, M.; Olsbye, U.; Dietzel, P. D. C.; Bordiga, S.; Prestipino, C.; Lamberti, C.; Lillerud, K. P. *J. Am. Chem. Soc.* **2007**, *129*, 3612.
- (25) Kim, H.; Das, S.; Kim, M. G.; Dybtsev, D. N.; Kim, Y.; Kim, K. *Inorg. Chem.* **2011**, *50*, 3691.
- (26) Cubillas, P.; Anderson, M. W.; Attfield, M. P. *Chem. J. Eur.* **2012**, *18*, 15406.
- (27) McKinstry, C.; Cussen, E. J.; Fletcher, A. J.; Patwardhan, S. V.; Sefcik, J. *Cryst. Growth Des.* **2013**.
- (28) Nayuk, R.; Zacher, D.; Schweins, R.; Wiktor, C.; Fischer, R. A.; van Tendeloo, G.; Huber, K. J. *J. Phys. Chem. C* **2012**, *116*, 6127.

- (29) Guillou, N.; Walton, R. I.; Millange, F. Z. *Kristallogr.* **2010**, 225, 552.
- (30) Hausdorf, S.; Wagler, J.; Moßig, R.; Mertens, F. O. R. L. *J. Phys. Chem. A* **2008**, 112, 7567.
- (31) Hawxwell, S. M.; Adams, H.; Brammer, L. *Acta Crystallog. Sect. B* **2006**, 62, 808.
- (32) Goesten, M. G.; Magusin, P. C. M. M.; Pidko, E. A.; Mezari, B.; Hensen, E. J. M.; Kapteijn, F.; Gascon, J. *Inorg. Chem.* **2014**, 53, 882.
- (33) Millange, F.; Medina, M. I.; Guillou, N.; Ferey, G.; Golden, K. M.; Walton, R. I. *Angew. Chem. Int. Ed.* **2010**, 49, 763.
- (34) Martin, R. L.; Lin, L.-C.; Jariwala, K.; Smit, B.; Haranczyk, M. *J. Phys. Chem. C* **2013**, 117, 12159.

## 6. Conclusions

---

The conclusions and proposed future work, for the three experimental chapters presented in this thesis, are detailed in this chapter. Some of the results have been published.<sup>1,2</sup>

### 6.1. Summary

Through careful mediation of reaction conditions, new mixed-metal iron-vanadium MIL-53 materials have been synthesised. In addition to the expected Fe<sup>III</sup> and V<sup>III</sup> sites, Fe<sup>II</sup> and some V<sup>II</sup> were found in the materials produced. These are, to our knowledge, the first examples of metal-organic framework to contain divalent vanadium, and the unusual oxidation state is produced *in situ* during solvothermal synthesis. Calcination of [(Fe, V)<sup>II,III</sup>(BDC)(OH, F)]<sup>0.5</sup>·0.5DMA<sup>+</sup> leads to the formation of new mixed-metal MIL-53(Fe<sup>III</sup>, V<sup>III</sup>) materials, for which all experimental data show the presence of phase-pure sample with mixtures of the metals on an atomic scale, albeit with some evidence for small domains of Fe- and V-rich regions. Varying the metal content of MIL-53(Fe,V) leads to large differences in both the structure and ‘breathing’ of these flexible materials, demonstrating the versatility of changing metal content to adjust properties of metal-organic frameworks. Synthesis of a mixed iron-cobalt [Fe(BDC)(OH, F)]<sup>0.5</sup>·0.5DMA<sup>+</sup> was achieved. Although difficult to calcine and to reproduce the synthesis, the effect of divalent cobalt on the material was distinct, further displaying the potential benefits of investigations into mixed metal materials. Through analysis of the EXAFS spectra of a mixed-metal MIL-53(Fe, Cr) samples and estimation of metal-metal bond lengths, further evidence was given towards the homogeneity of the material.

Through mediation of the reaction solvent and subsequent calcinations, several new ytterbium-organic frameworks have been synthesised and their properties

investigated. Using a solvent mixture of between 1:0 and 6:4 DMF to water leads to the formation of MB2 -  $[\text{Yb}_2(\text{BDC})_3(\text{DMF})_2] \cdot 2\text{H}_2\text{O}$  which contains ytterbium-carboxylate chains running along the *c*-axis. Calcination of MB2 creates  $\text{Yb}_2(\text{BDC})_3$ , a material that exhibits significant porosity. A lutetium analogue of MB2 was synthesised. Doping of MB2(Yb) with other lanthanides was successful with clear evidence from both XRD and photoluminescence studies. Further decreasing the DMF to water ratio leads to the formation of MB3 -  $[\text{Yb}_2(\text{BDC})_3(\text{DMF})_2(\text{H}_2\text{O})_2]$  which contains ytterbium-carboxylate dimers. Although sharing similar chemical formulae, MB2 and MB3 vary greatly in terms of structure and properties. Despite of this, both MB2 and MB3 can be calcined into the same  $\text{Yb}_2(\text{BDC})_3$  material. An isorecticular analogue of MB3, MB5, was synthesised using the extended 2,6-naphthalenedicarboxylate linker.

Through mediation of the reaction solvent and subsequent calcinations, several new ytterbium-organic frameworks have been synthesised and their properties investigated. Using a solvent mixture of between 1:0 and 6:4 DMF to water leads to the formation of MB2 -  $[\text{Yb}_2(\text{BDC})_3(\text{DMF})_2] \cdot 2\text{H}_2\text{O}$  which contains ytterbium-carboxylate chains running along the *c*-axis. Calcination of MB2 creates  $\text{Yb}_2(\text{BDC})_3$ , a material that exhibits significant porosity. A lutetium analogue of MB2 was synthesised. Doping of MB2(Yb) with other lanthanides was successful with clear evidence from both XRD and photoluminescence studies. Further decreasing the DMF to water ratio leads to the formation of MB3 -  $[\text{Yb}_2(\text{BDC})_3(\text{DMF})_2(\text{H}_2\text{O})_2]$  which contains ytterbium-carboxylate dimers. Although sharing similar chemical formulae, MB2 and MB3 vary greatly in terms of structure and properties. Despite of this, both MB2 and MB3 can be calcined into the same  $\text{Yb}_2(\text{BDC})_3$  material. An isorecticular analogue of MB3, MB5, was synthesised using the extended 2,6-naphthalenedicarboxylic acid linker.

## 6.2. Future Work

The preliminary studies detailed in this work, such as the effect of metal ratio on the properties of MIL-53, the structure of  $\text{Yb}_2(\text{BDC})_3$  and the crystallisation of interpenetrated MOF-5, present opportunities for this work to be expanded from in future.

Since the uptake of vanadium into the structure of MIL-53(Fe) had large effects on both the structure and properties of the material, it stands to reason that further investigations into the ability to precisely control the metal ratios, *i.e.* metal uptake identical to synthesis ratio, would be beneficial to ‘tune’ the properties of the MIL-53(Fe, V) material, or indeed that of any other mixed-metal MIL-53. MIL-53( $\text{Fe}_{0.74}\text{V}_{0.26}$ ) displayed interesting single-compound xylene adsorption with behaviour unlike that of MIL-53(Fe) or MIL-47(V) albeit with comparatively low total weight adsorption due to an insufficient activation method. With further refinement of the activation methods, total adsorption and selectivity toward xylenes would likely be improved. Further investigations into the adsorption properties of this material and that of MIL-53( $\text{Fe}_{0.49}\text{V}_{0.51}$ ) would be of particular interest due to potential uses in membrane separation systems.

The structure of  $\text{Yb}_2(\text{BDC})_3$  remains unknown as of printing of this work. Although seemingly simple in its compositions, attempts to index the powder XRD pattern have been unsuccessful. Trying to rationalise its structure from the progenitor compounds, MB2 and MB3, is difficult due to the different topologies and connectivities of their structures.  $\text{Yb}_2(\text{BDC})_3$  exhibits both porosity and the ability to be doped through calcination of MB2(Yb, Ln) making it a suitable candidate for investigation of its use as a molecular sensor. Resolution of the structure and investigations into the adsorption properties of this material are required to fully understand this material.

Studies into the crystallisation of metal-organic frameworks have yielded interesting insights into the synthesis of these materials. *In situ* and *ex situ* studies into the

crystallisation of interpenetrated MOF-5 indicate the presence of a transient intermediary product at reaction temperatures early in the synthesis that yet remains unidentified. MOF-5 and its analogues remain one of the most widely studied metal-organic frameworks, making investigations into the crystallisation of these materials particularly relevant. The effect of temperature, reagent concentration and choice of organic base during the synthesis of interpenetrated MOF-5 remain fascinating subjects for further crystallisation studies.

### 6.3. References

- (1) Breeze, M. I.; Clet, G.; Campo, B. C.; Vimont, A.; Daturi, M.; Grenèche, J.-M.; Dent, A. J.; Millange, F.; Walton, R. I. *Inorg. Chem.* **2013**, 52, 8171.
- (2) Nouar, F.; Devic, T.; Chevreau, H.; Guillou, N.; Gibson, E.; Clet, G.; Daturi, M.; Vimont, A.; Grenèche, J. M.; Breeze, M. I.; Walton, R. I.; Llewellyn, P. L.; Serre, C. *Chem. Commun.* **2012**, 48, 10237.

# A. Appendix

---

## A.1. Precious Metal-Organic Frameworks

In this short section a summary of exploratory reactions to examine the possibility of making ruthenium and iridium MOFs is described. The work did not yield any significant (or publishable) conclusions, but some interesting observations were made, so it is presented here for completeness. The inherent porosity of metal-organic frameworks and the interesting catalytic, optical and magnetic properties of precious metals, especially those of the platinum group (which comprise of the second and third row elements of Groups 8,9 and 10 of the Periodic Table), makes the formation of platinum-group MOFs an interesting challenge. Difficulties in the synthesis of precious-metal-organic frameworks arise from the tendency of precious metal reactants to form oxides or reduce to their metallic forms under solvothermal conditions. Only a few examples of monometallic precious-metal MOFs have been reported, compared to the many thousands of transition-metal and lanthanide materials. Eckshtain-Levi *et al.* reported a series of osmium salicylamide MOFs with dimensionality in 1, 2 or 3 dimensions.<sup>1</sup> Kozachuk *et al.* described the preparation of a mixed-valent ruthenium analogue of HKUST-1.<sup>2</sup> Although several examples of metal-organic framework containing precious metal nano-particles have been reported,<sup>3-5</sup> few examples of precious-metal doped intra-framework metal-organic framework have been reported with the exception of metallo-ligand types.<sup>6,7</sup>

## A.2. Synthesis of iridium-organic frameworks

The attempted solvothermal synthesis of iridium-organic frameworks was performed over a range of temperatures and reaction times using iridium (III) chloride hydrate and 1,4-benzenedicarboxylic acid with DMF as the reaction solvent. Many of these reactions gave a

mixture of white needle-shaped crystals and black powder. The black powder could be assigned to iridium (IV) oxide by powder XRD.

The white needle-shaped crystals were found to be of suitable quality for structure solution by single crystal XRD. The crystals were found to not contain iridium at all and the chemical formula determined to be  $(\text{DMA}^+)(\text{HBDC}^-)$  (DMA = dimethylammonium, HBDC = 1-carboxyl-4-benzenecarboxylate, a partially deprotonated form of 1,4-benzenedicarboxylic acid). This material crystallises in the triclinic  $P\bar{1}$  spacegroup and contains chains of hydrogen-bonded HBDC running diagonal to one another. The crystal structure is given in Figure 6.3.1 and crystallographic data and atomic coordinates are given in Table 6.3.1 and 6.3.2. The structure of the same salt has been reported previously at room temperature, with different crystal symmetry.<sup>8,9</sup> The hydrolysis of DMF to form  $\text{DMA}^+$  is well known in literature with several metal-organic frameworks containing  $\text{DMA}^+$  generated *in situ* during reaction.<sup>10-14</sup> The presence of iridium can be used to catalyse the hydrolysis of DMF as reported by Curtis *et al.*<sup>15</sup>

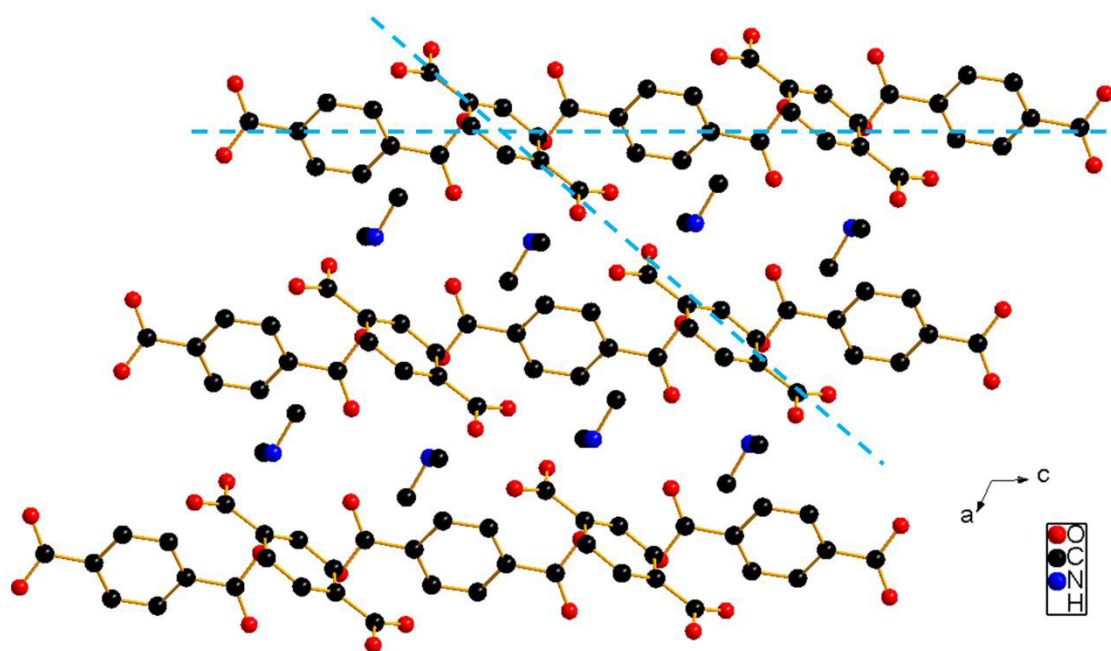


Figure 6.3.1: Crystal structure of  $(\text{DMA})(\text{HBDC})$  viewed along the  $b$ -axis. Hydrogens excluded for clarity. Blue dashed lines display chains of hydrogen-bonded HBDC



Table 6.3.1: Crystallographic data of (DMA)(HBDC)

	(DMA <sup>+</sup> )(HBDC <sup>-</sup> )
Formula	O <sub>8</sub> C <sub>20</sub> N <sub>2</sub> H <sub>26</sub>
Formula Weight	421.426
Colour/Shape	Needle
Temperature / K	100(2)
Crystal System	Triclinic
Space Group	<i>P</i> 1
<i>a</i> / Å	7.8115(11)
<i>b</i> / Å	9.0336(7)
<i>c</i> / Å	9.5942(7)
$\alpha$ / °	92.8270(59)
$\beta$ / °	13.9024(101)
$\gamma$ / °	114.0482(109)
Cell volume / Å <sup>3</sup>	546.17(13)
<i>Z</i>	2
Density (calc.) / g·cm <sup>3</sup>	1.28119

Table 6.3.2: Atomic parameters for (DMA)(HBDC).

Atom	Ox.	Wyck.	Site	S.O.F.	x/a	y/b	z/c	U [Å <sup>2</sup> ]
O3		2i	1	1	0.40006	0.97828	0.85629	
O1		2i	1	1	0.05639	0.53037	0.64199	
O2		2i	1	1	-0.2795	0.34999	0.56979	
O4		2i	1	1	0.30964	1.16066	0.92852	
C5		2i	1	1	-0.09749	0.44733	0.67142	
N1		2i	1	1	0.52712	0.71701	0.75305	
H1A		2i	1	1	0.40896	0.69184	0.66332	-1.2
H1B		2i	1	1	0.51924	0.76693	0.83216	-1.2
C7		2i	1	1	-0.04376	0.47391	0.84218	
C8		2i	1	1	0.12873	0.62048	0.95186	
H8		2i	1	1	0.21508	0.70094	0.92012	-1.2
C9		2i	1	1	0.11135	0.90876	0.54057	
H9		2i	1	1	0.18576	0.84748	0.5668	-1.2
C10		2i	1	1	0.17177	0.64643	1.10926	
H10		2i	1	1	0.28668	0.74471	1.18245	-1.2
C11		2i	1	1	0.14381	1.02926	0.657	
C12		2i	1	1	-0.03269	0.87986	0.3846	
H12		2i	1	1	-0.05484	0.79831	0.30697	-1.2
C13		2i	1	1	0.29449	1.06002	0.82731	
C14		2i	1	1	0.53165	0.55981	0.78285	
H14A		2i	1	1	0.52961	0.50126	0.69545	-1.5
H14B		2i	1	1	0.40997	0.49065	0.79511	-1.5
H14C		2i	1	1	0.65833	0.58512	0.87741	-1.5
C15		2i	1	1	0.70974	0.83553	0.73936	
H15A		2i	1	1	0.71656	0.78528	0.65251	-1.5
H15B		2i	1	1	0.83678	0.86469	0.83508	-1.5
H15C		2i	1	1	0.6963	0.93478	0.72147	-1.5

A comparison of the powder XRD pattern of (DMA)(HBDC) with that simulated from the crystal structure show reasonable agreement when considerations such as thermal (the structure was determined at 100 K but the powder studied at room temperature) and preferred orientation effects are taken into account (Figure 6.3.2).

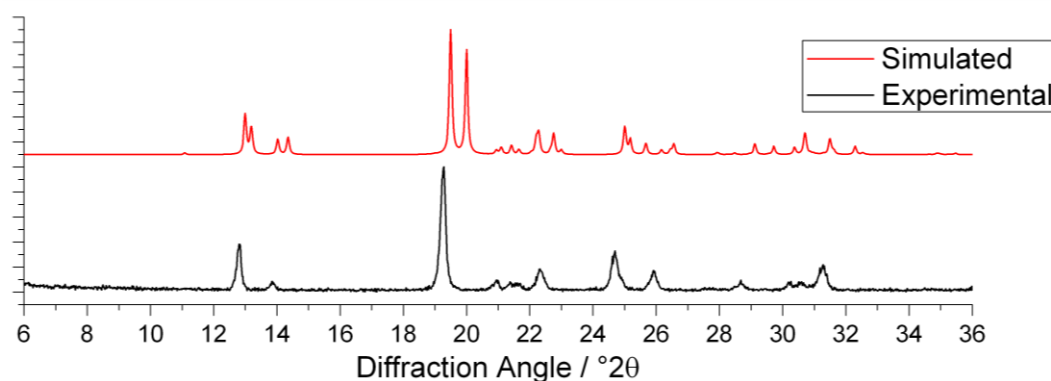


Figure 6.3.2: Comparison of the PXRD patterns of (DMA)(HBDC) with that simulated from the crystal structure

Since dimethylformamide (DMF) is susceptible to hydrolysis, other chemically-related solvents, but with known robustness to hydrolysis, were used to replace DMF in the synthesis. These included dimethylacetamide (DMAC), tetramethylurea (TMU) and N-methyl-2-pyrrolidone (NMP). These solvents have been used by others for metal-organic framework synthesis.<sup>16-18</sup> The structures of these solvents are shown in Figure 6.3.3. None of these reactions formed any solid products, with clear dark red (Ru) or yellow solutions (Ir) produced.

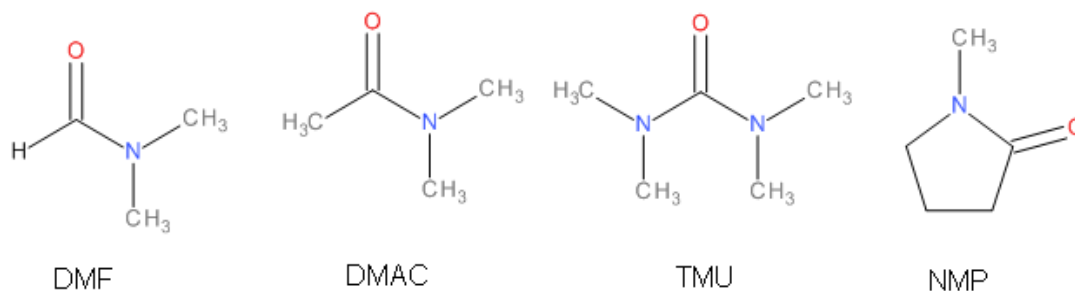
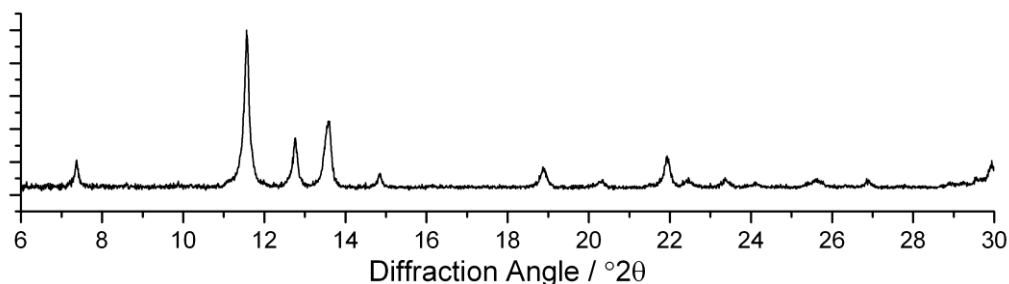


Figure 6.3.3: Structure of DMF and similar ligands

### A.3. Synthesis of ruthenium-organic frameworks

In a similar manner to that used for iridium, solvothermal reactions were performed over a range of temperatures and reaction times using ruthenium(III) chloride hydrate as a metal source. As was found for iridium, reactions using DMF led to the formation of (DMA)(HBDC) and ruthenium(IV) oxide. DMF was substituted for the solvents shown in

Figure 6.3.3 The reaction using ruthenium(III) chloride hydrate and 1,4-benzenedicarboxylic acid in tetramethylurea (TMU) performed at 100 °C for twenty hours lead to the formation of a dark black-blue powder. The powder XRD pattern of this material is shown in Figure 6.3.4.



**Figure 6.3.4: PXRD pattern of the product formed during the solvothermal reaction of ruthenium (III) chloride hydrate and 1,4-benzenedicarboxylic acid in the presence of TMU at 100 °C for 20 hours**

The powder XRD pattern of this material initially piqued interest due to the presence of a Bragg peak at 7.3 °2θ, denoting that this material exhibits d-spacing in the range that would be expected for a metal-organic framework-like material. The pattern does not match any of the known transition-metal BDC materials reported in the literature. The reaction was repeated with the absence of 1,4-benzenedicarboxylic acid with no change in the product formed. Without the presence of the BDC linkers, it seems unlikely that this material is indeed a metal-organic framework. This material shall be referred to as Ru-TMU.

In order to attempt to determine the identity of this Ru-TMU phase, thermogravimetric analysis was performed upon the material. One major loss is seen starting at 200 °C of 54.5 wt% total. Assuming that the final decomposition product is ruthenium(IV) oxide, this would be indicative of a formula weight of around 292 g mol<sup>-1</sup>. The atomic and formula weights of ruthenium and TMU are 101 and 166 g mol<sup>-1</sup>, respectively. With the assumption that ruthenium and TMU are present in a 1:1 ratio, as in the synthesis, the remaining 75 g mol<sup>-1</sup> can be assigned to two chloride ions (total

molecular weight =  $71 \text{ g mol}^{-1}$ ). The proposed chemical formula for this material is likely the 1:1 complex of  $\text{RuCl}_2$  with TMU,  $\text{RuCl}_2 \cdot \text{TMU}$ . It is impossible to determine whether this material exists as a monomer, a dimer or an extended structure, without a crystallographic investigation.

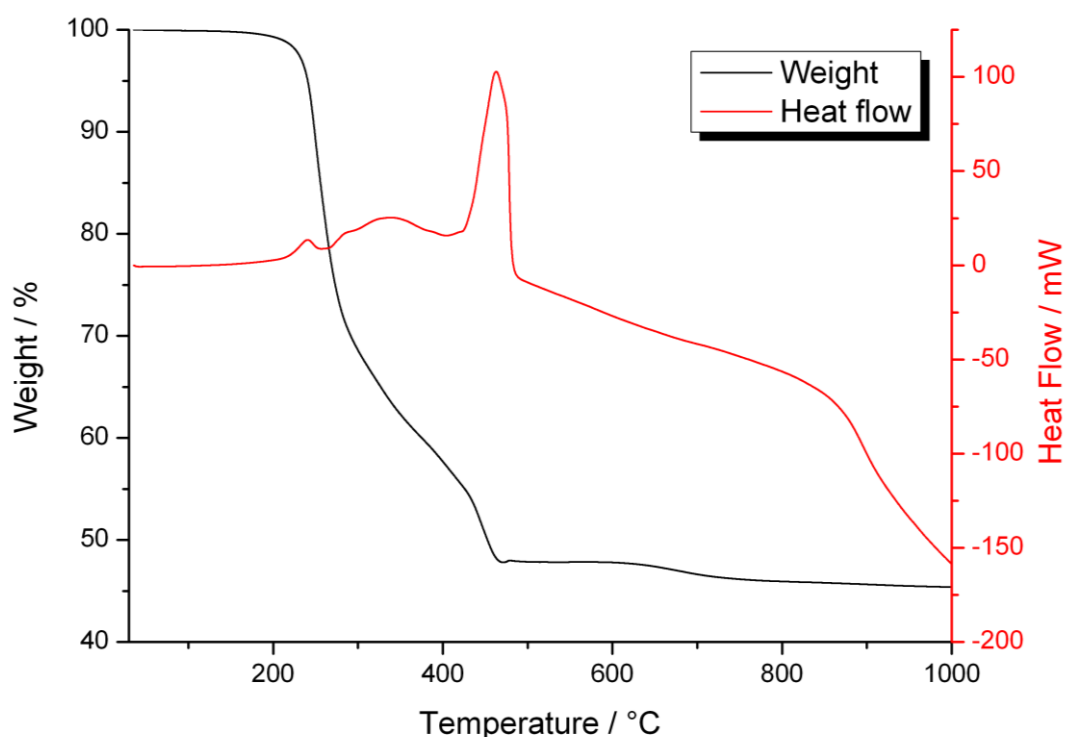


Figure 6.3.5: TGA and DSC of Ru-TMU in air

The presence of ruthenium(II) in this material is supported by its dark black-blue colour. The reduction of ruthenium(III) to (II) is facilitated through hydrolysis of the TMU ligand. Wilkinson *et al.* described the preparation of several ruthenium(II) chloride complexes with a variety of ligands with many of them displaying deep-blue colouration, although no ligands with amide functionality were investigated.<sup>19</sup> This lends further credence to the identity of the Ru-TMU material as  $\text{RuCl}_2 \cdot \text{TMU}$ .

#### A.4. Synthesis of precious-metal doped MOFs

Since MIL-53 is known to be able to incorporate a range of metals with oxidation states of 2+ to 4+, and the work in Chapter 3 showed that mixed-metal forms of the material are possible, it was chosen as a candidate structure for precious-metal doping. The ionic radii of octahedral trivalent and tetravalent ruthenium and iridium are 82 and 76 pm, and 82 and 76 pm, respectively, close to that of Fe(III) (78.5 pm).<sup>20</sup> It was for these reasons that doping seemed viable.

The synthesis was based on the published conditions for MIL-53(Fe).<sup>21</sup> Reactions were performed using a 9:1, 8:2, 7:3, 6:4 and 1:1 ratios. synthesis molar ratio of iron(III) chloride hexahydrate to precious metal(III) chloride hydrate (0.001 mol total metal). This and 1,4-benzenedicarboxylic acid (0.001 mol) were added to DMF (5 cm<sup>3</sup>), HF (0.05 cm<sup>3</sup>) and water (0.15 cm<sup>3</sup>), and the solution stirred until dissolution had occurred. The reaction solution was introduced into a Teflon liner, sealed in a steel autoclave and heated solvothermally at 150 °C for 20 hours. Reactions using ratios of Fe:Ru/Ir ratios higher and including 8:2 were unsuccessful forming the same (DMA)(HBDC) material seen previously. Reactions using the 9:1 Fe:Ru/Ir ratio formed red-orange and yellow-brown powders for the ruthenium and iridium reactions, respectively. These materials were deemed to be phase-pure and iso-structural by powder XRD diffraction and initially appeared to be similar in structure to the fully open MIL-47 structure (the vanadium(IV) analogue of MIL-53). Attempts to extract lattice parameters from these materials were unsuccessful suggesting that they do not share the same *Pnma* spacegroup as MIL-47.

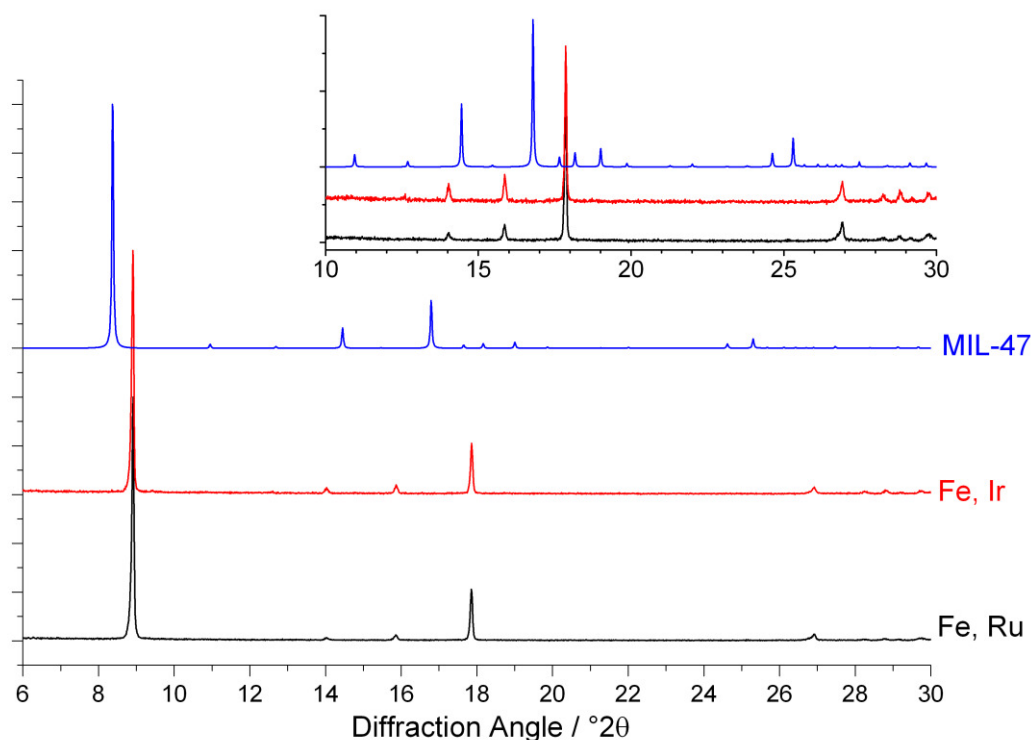


Figure 6.3.6: PXRD patterns of the 9:1 iron:ruthenium/iridium BDC materials and that of the simulated XRD pattern of MIL-47(V<sup>IV</sup>).

TGA of the 9:1 Fe:Ru supported an open MIL-47 like structure with no major weight losses seen until structure collapse beginning at 400 °C with an associated weight loss of 55.2 wt% (Figure 6.3.7). This value is less than what would be expected for MIL-53(Fe) (Fe(BDC)(OH)) (66.3 wt% loss assuming formation of Fe<sub>2</sub>O<sub>3</sub> post-decomposition). This would be consistent with incorporation of some ruthenium into the material due to ruthenium's higher mass and that it forms RuO<sub>2</sub> instead of Ru<sub>2</sub>O<sub>3</sub>, although the mass loss seen is less than what would be expected for the decomposition of (Fe<sub>0.9</sub>Ru<sub>0.1</sub>)(BDC)(OH) (64.7 %).

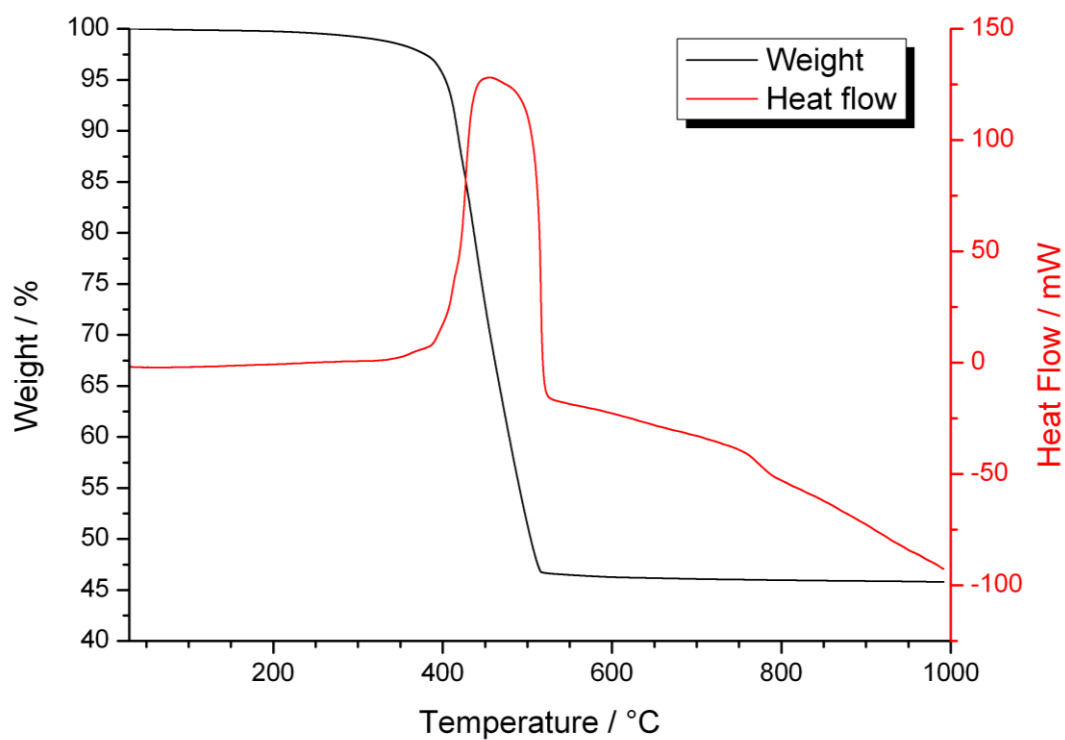
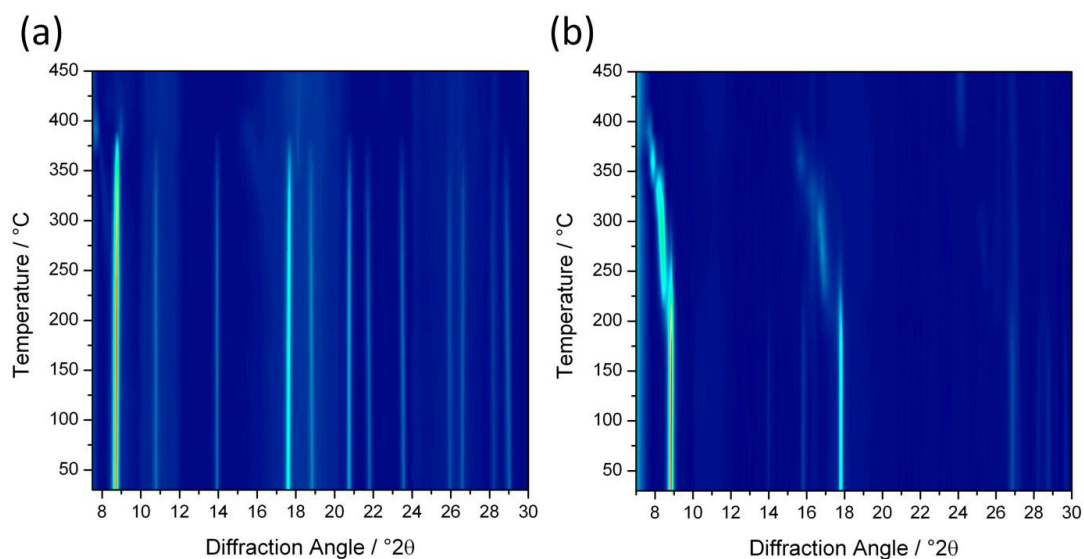


Figure 6.3.7: TGA and DSC of the 9:1 Fe:Ru BDC materials

Thermodiffractometry suggests clear differences between the two precious-metal doped samples. The Fe:Ru 9:1 materials shows behaviour agreeing well with that seen from the TGA with no structure changes seen until collapse of the framework.

Thermodiffractometry of the iridium-doped material undergoes two structural changes at 220 and 350 °C before eventual collapse of the framework at around 400 °C.





**Figure 6.3.8: Thermodiffractometry of (a) ruthenium-doped material and (b) iridium-doped iron BDC materials**

XANES at the iron K-edge yields a surprising result; in both materials, the iron oxidation state is close to +2, with estimated iron oxidation states of 2.06 and 2.09 for the ruthenium and iridium doped samples respectively (Figure 6.3.9). This does not agree with the expected value of +3 that would be expected for a MIL-53(Fe) material suggesting that this material might not be a MIL-53 analogue after all.

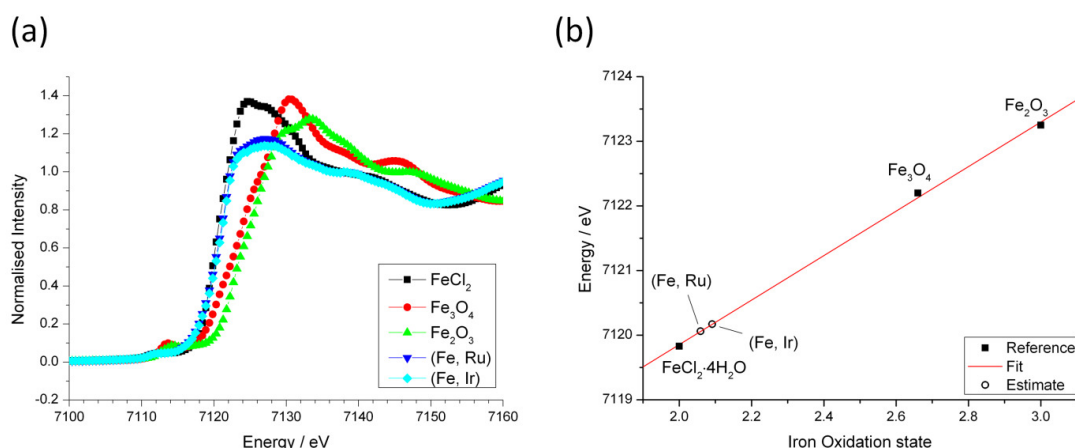


**Figure 6.3.9(a): XANES at the iron K-edge; (b) Estimates of the iron oxidation state using the edge position. Edge positions and the reference materials used are given in Table 6.3.3**

**Table 6.3.3: Iron K-edge positions of reference materials and the precious-metal doped materials. Reference compound oxidation states in bold. Edge positions defined as the energy at which the normalised absorption is equal to 0.5**

Compound	Edge Position	Oxidation State
<b>FeCl<sub>2</sub>·4H<sub>2</sub>O</b>	7119.8	2
<b>Fe<sub>3</sub>O<sub>4</sub></b>	7122.2	2.66
<b>Fe<sub>2</sub>O<sub>3</sub></b>	7123.25	3
Fe, Ru	7120.05	2.06
Fe, Ir	7120.15	2.09

XANES at the ruthenium K-edge give an estimated oxidation state of 1.63, close to that of the divalent iron seen earlier (Figure 6.3.10). The stability of Ru(II) in carboxylate linker MOFs has also been seen for the mixed valent Ru(III,II) HKUST-1 analogue reported by Kozachuk *et al.*<sup>2,22,23</sup>

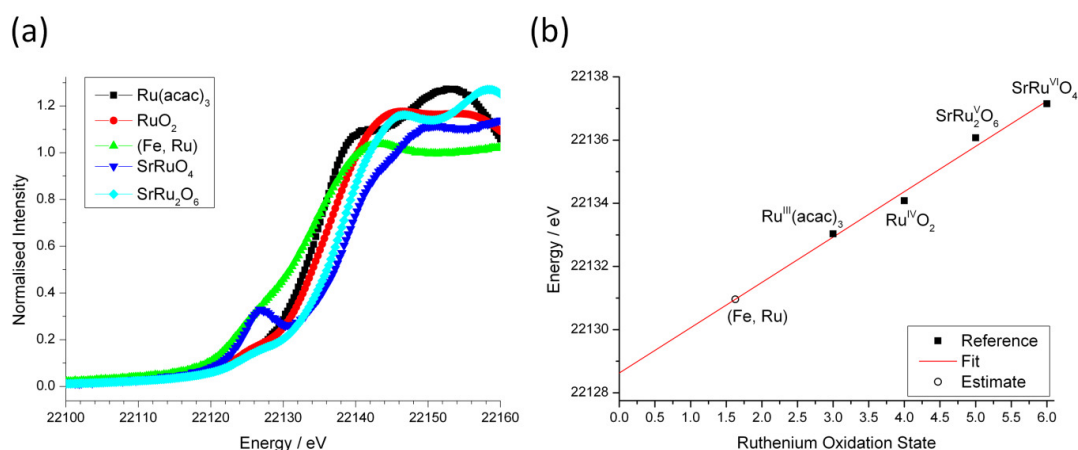


**Figure 6.3.10(a): XANES at the ruthenium K-edge; (b) Estimates of the ruthenium oxidation state using the edge position. Edge positions and the reference materials used are given in Table 6.3.1**

**Table 6.3.4: Ruthenium K-edge positions of reference materials and the ruthenium-doped material. Reference compound oxidation states in bold. Edge positions defined as the energy at which the normalised absorption is equal to 0.5**

Compound	Edge Position	Oxidation State
<b>Ru(acac)<sub>3</sub></b>	22133.03	3
<b>RuO<sub>2</sub></b>	22134.08	4
<b>SrRu<sub>2</sub>O<sub>6</sub></b>	22136.07	5
<b>SrRuO<sub>4</sub></b>	22137.15	6
Fe, Ru	22129.93	1.63

XANES at the iridium L(III) edge yields further interesting results. The estimated oxidation state is 4.14, far higher than the values seen for iron and ruthenium previously (Figure 6.3.11). This suggests that the iridium is not incorporated into the structure in the same manner that the iron and ruthenium. One possible reason for this is that iridium is incorporated into the material as an impurity and its main role is to catalyse the DMF hydrolysis required to form this material and not MIL-53 that would be expected from the synthesis conditions. The lack of impurities evidenced by PXRD seems to discredit this. An alternative solution would be that iridium(IV) may substitute two of the divalent iron in the material. This would help to explain the differing thermal behaviours of the ruthenium and the iridium doped materials.

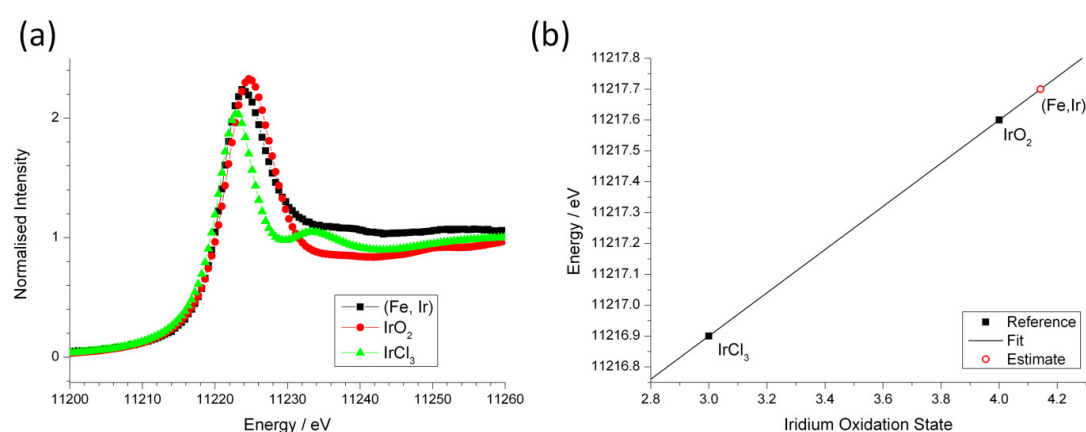


Figure 6.3.11(a): XANES at the iridium L(III)-edge; (b) Estimates of the iridium oxidation state using the edge position. Edge positions and the reference materials used are given in Table 6.3.5

Table 6.3.5: Iridium L(III)-edge positions of reference materials and the iridium-doped material. Reference compound oxidation states in bold. Edge positions defined as the energy at which the normalised absorption is equal to 0.5

Compound	Edge Position	Oxidation State
IrCl <sub>3</sub>	11216.9	3
IrO <sub>2</sub>	11217.6	4
Fe, Ir	11217.7	4.14

The infrared spectra of the two doped material show several differences to the IR spectrum of MIL-53(Fe). The broad O-H stretch band at 3620 cm<sup>-1</sup> for MIL-53(Fe) is shifted

downwards to  $3598\text{ cm}^{-1}$  (Figure 6.3.12) in the new materials and is also much sharper. This suggests that the OH functionality is still there albeit not interacting with extra-framework solvent.

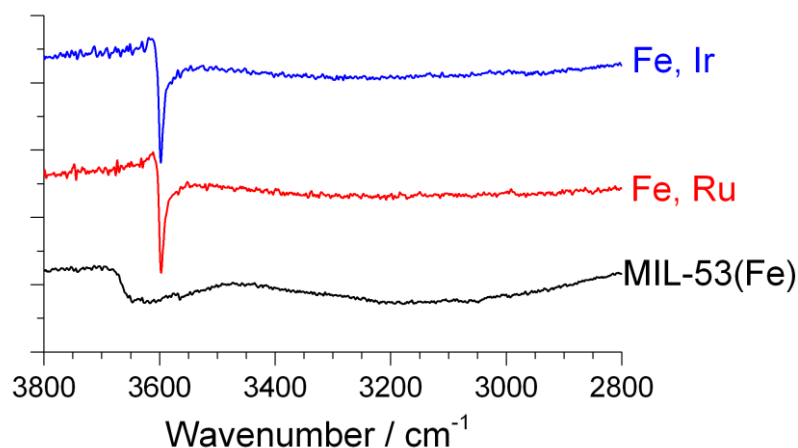


Figure 6.3.12: IR spectra of MIL-53(Fe) and the two doped materials over the range  $3800\text{-}2800\text{ cm}^{-1}$

The C=O stretch of the framework at  $1520\text{ cm}^{-1}$  for MIL-53(Fe) is found at higher wavenumbers for the doped material ( $1578\text{ cm}^{-1}$ ) (Figure 6.3.13), further implying that these two materials do not share the same structure. This strengthening of the carbonyl bond is consistent with the lower oxidation state of the metal in the doped materials. Bands at  $\sim 1150$  (C=C stretch),  $1012$  (C-O stretch) and  $820\text{ cm}^{-1}$  (C-H bend, para-substituted ring systems) suggests that no structural rearrangement of the linker have occurred. No C=O stretch is seen at  $\sim 1670\text{ cm}^{-1}$  indicating that DMF is not present in either of the doped materials. The presence of a potential C-N stretch, indicative of the presence of dimethylammonium, at around  $1100\text{ cm}^{-1}$  is seen in the spectra although definite assignation of this peak is impossible due to the presence of a peak at similar positions in the MIL-53(Fe) spectrum.

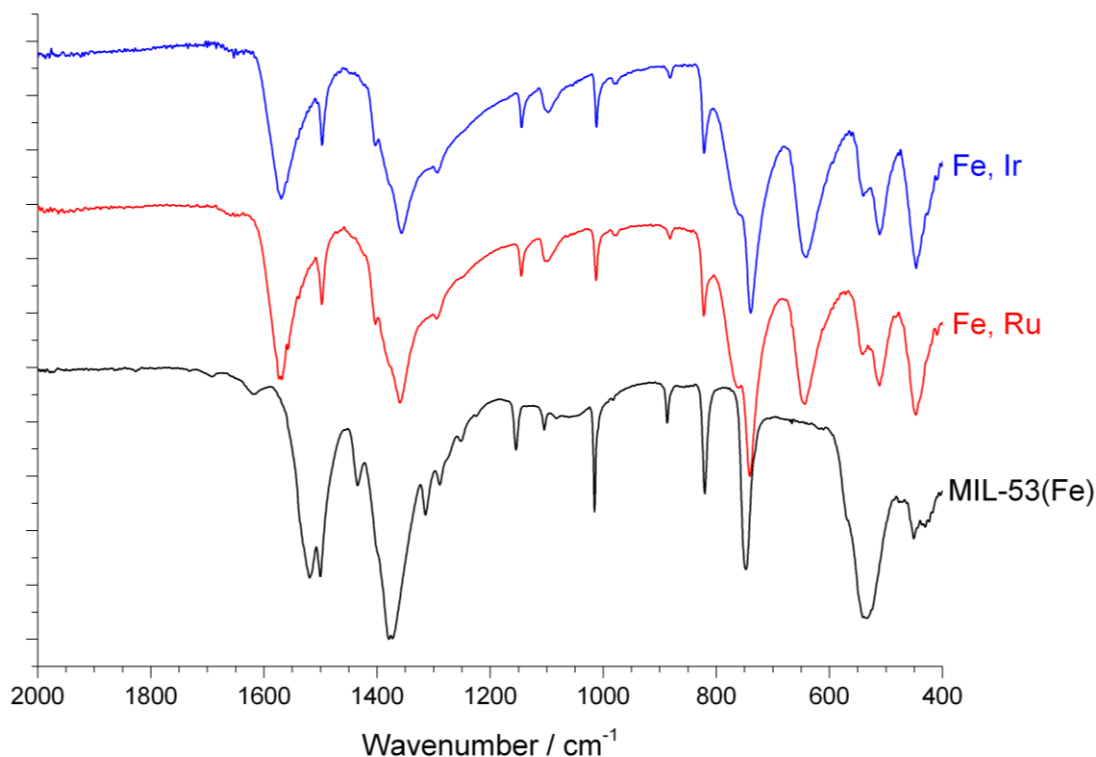


Figure 6.3.13: IR spectra of MIL-53(Fe) and the two doped materials over the range 2000-400  $\text{cm}^{-1}$

Table 6.3.6: Assignment of IR bands of MIL-53(Fe) and the two doped materials

Absorption band / $\text{cm}^{-1}$			Strength	Assignment
Fe	Fe, Ru	Fe, Ir		
3622	3596	3598	w, broad	O-H stretch (framework, water)
3100	3100	3100	w, broad	C-H stretch (framework)
1520, 1500	1578, 1498	1578, 1500	s	C-H stretch (framework)
1435	1403	1404	m	-(O-C-O)-
1374-1290	1377-1296	1377-1298	s	O-H bend (framework, water)
1154	1155	1145	m	C=C stretch (framework)
1015	1012	1013	s	C-O stretch
888	880	882	m	Fe-O stretch
820	820	821	s	C-H bend (p-substituted ring systems)

## A.5. Summary

Although no precious-metal-organic frameworks were positively identified, four new materials were synthesised. The reaction of trivalent iridium or ruthenium salts with DMF leads to the formation of (DMA)(HBDC), a material formed via hydrolysis of the solvent itself. The reaction of  $\text{RuCl}_3 \cdot x\text{H}_2\text{O}$  with tetramethylurea (TMU) led to the formation of a

dark blue powder. This material is to be likely  $\text{RuCl}_2\cdot\text{TMU}$ , although further work is required to determine this. Attempts to synthesise doped analogues of MIL-53(Fe) using precious metals lead instead to two new isostructural materials formed. These materials contain divalent iron and ruthenium and tetravalent iridium. The lower oxidation states, IR spectra and PXRD patterns suggest that these two materials are not analogous to MIL-53. Again, further work is needed to understand the structures of these materials and it would be especially advantageous if single crystals could be grown for structural characterisation.

## A.6. References

- (1) Eckshtain-Levi, M.; Yufit, D.; Shimon, L. J. W.; Kirillov, A. M.; Benisvy, L. *Cryst. Growth Des.* **2014**, *14*, 2703.
- (2) Kozachuk, O.; Yusenkov, K.; Noei, H.; Wang, Y.; Walleck, S.; Glaser, T.; Fischer, R. A. *Chem. Commun.* **2011**, *47*, 8509.
- (3) Jiang, H.-L.; Liu, B.; Akita, T.; Haruta, M.; Sakurai, H.; Xu, Q. *J. Am. Chem. Soc.* **2009**, *131*, 11302.
- (4) Gu, X. J.; Lu, Z. H.; Jiang, H. L.; Akita, T.; Xu, Q. *J. Am. Chem. Soc.* **2011**, *133*, 11822.
- (5) Liu, L. L.; Zhang, X.; Gao, J. S.; Xu, C. M. *Chinese J. Catal.* **2012**, *33*, 833.
- (6) Kozachuk, O.; Luz, I.; Xamena, F.; Noei, H.; Kauer, M.; Albada, H. B.; Bloch, E. D.; Marler, B.; Wang, Y. M.; Muhler, M.; Fischer, R. A. *Angew. Chem. Int. Ed.* **2014**, *53*, 7058.
- (7) Humphrey, S. M.; Angliss, T. J. P.; Aransay, M.; Cave, D.; Gerrard, L. A.; Weldon, G. F.; Wood, P. T. Z. *Anorg. Allg. Chem.* **2007**, *633*, 2342.
- (8) Karpova, E. V.; Zakharov, M. A.; Gutnikov, S. I.; Alekseyev, R. S. *Acta Crystallog. Sect. E. Struct. Rep. Online* **2004**, *60*, O2491.
- (9) Zhao, W.-X.; Gao, Y.-X.; Dong, S.-F.; Li, Y.; Zhang, W.-P. *Acta Crystallog. Sect. E. Struct. Rep. Online* **2007**, *63*, O2728.
- (10) Medina, M. E.; Dumont, Y.; Greneche, J. M.; Millange, F. *Chem. Commun.* **2010**, *46*, 7987.
- (11) Amarante, T. R.; Neves, P.; Valente, A. A.; Almeida Paz, F. A.; Fitch, A. N.; Pillinger, M.; Goncalves, I. S. *Inorg. Chem.* **2013**, *52*, 4618.
- (12) Chaudhari, A. K.; Mukherjee, S.; Nagarkar, S. S.; Joarder, B.; Ghosh, S. K. *CrystEngComm* **2013**, *15*, 9465.
- (13) Lin, Z.-J.; Han, L.-W.; Wu, D.-S.; Huang, Y.-B.; Cao, R. *Cryst. Growth Des.* **2013**, *13*, 255.
- (14) Burrows, A. D.; Cassar, K.; Friend, R. M. W.; Mahon, M. F.; Rigby, S. P.; Warren, J. E. *CrystEngComm* **2005**, *7*, 548.
- (15) Curtis, N. J.; Sargeson, A. M. *J. Am. Chem. Soc.* **1984**, *106*, 625.
- (16) Zhang, J.; Bu, J. T.; Chen, S.; Wu, T.; Zheng, S.; Chen, Y.; Nieto, R. A.; Feng, P.; Bu, X. *Angew. Chem. Int. Ed.* **2010**, *49*, 8876.
- (17) Yang, H.; Li, T. H.; Kang, Y.; Wang, F. *Inorg. Chem. Commun.* **2011**, *14*, 1695.
- (18) Zhu, M.; Fu, W.; Zou, G. *J. Coord. Chem.* **2012**, *65*, 4108.
- (19) Gilbert, J. D.; Rose, D.; Wilkinson, G. *J. Chem. Soc. A* **1970**, 2765.
- (20) Shannon, R. D. *Acta Crystallogr. Sect. A* **1976**, *32*, 751.
- (21) Ferey, G.; Millange, F.; Morcrette, M.; Serre, C.; Doublet, M. L.; Greneche, J. M.; Tarascon, J. M. *Angew. Chem. Int. Ed.* **2007**, *46*, 3259.
- (22) Kozachuk, O.; Meilikhov, M.; Yusenkov, K.; Schneemann, A.; Jee, B.; Kuttatheyil, A. V.; Bertmer, M.; Sternemann, C.; Poepl, A.; Fischer, R. A. *Eur. J. Inorg. Chem.* **2013**, *2013*, 4546.
- (23) Noei, H.; Kozachuk, O.; Amirjalayer, S.; Bureekaew, S.; Kauer, M.; Schmid, R.; Marler, B.; Muhler, M.; Fischer, R. A.; Wang, Y. M. *J. Phys. Chem. C* **2013**, *117*, 5658.